Shells of the bivalve *Pecten maximus* as high-resolution multi-proxy archives to reconstruct phytoplankton dynamics

Dissertation zur Erlangung des Grades "Doktor der Naturwissenschaften"
im Promotionsfach Geowissenschaften/Paläontologie

Am Fachbereich 09 für Chemie, Pharmazie, Geographie und
Geowissenschaften der Johannes Gutenberg-Universität Mainz

Lukas Fröhlich
geb. in Pirmasens

Mainz, 2025

1. Gutachter: Removed for reasons of data protection
2. Gutachter: Removed for reasons of data protection

Tag der mündlichen Prüfung: Removed for reasons of data protection

Hiermit erkläre ich, dass ich die vorliegende Arbeit selbstständig verfasst und keine anderen als die angegebenen Quellen und Hilfsmittel benutzt habe.

Lukas Fröhlich

Abstract

The significance of phytoplankton in the oceans is becoming increasingly evident, as they contribute significantly to global oxygen production, reduce atmospheric CO_2 levels, control biogeochemical cycles and provide food for the vast majority of marine life from higher trophic levels. Understanding how phytoplankton species respond to various natural and anthropogenic changes in the past is crucial for assessing their future developments and trends which is of particular interest in the light of changing climate and enhanced anthropogenic pressures on marine ecosystems. However, reconstructing the past dynamics of primary producers is extremely challenging, as in-situ and remote sensing data are scarce or only available for a few decades. Employing biogenic proxy archives such as bivalve shells to obtain geochemical data indicative of phytoplankton of the surrounding water offers enormous potential for reconstructing their dynamics, e.g., species abundance, community composition and phenology. Yet, the complex nature of the primary producers and the small number of calibration studies largely complicate and restrict the applicability of such geochemical proxies as tools for the reconstruction of phytoplankton dynamics. This work aimed to develop a profound understanding of the element-to-calcium ratios of barium (Ba/Ca_{shell}), molybdenum (Mo/Ca_{shell}) and lithium (Li/Ca_{shell}) measured in shells of the fast-growing scallop *Pecten maximus*, and their potential as geochemical phytoplankton dynamic proxies. To this avail, the Bay of Brest (France) was selected as a study location due to its well-characterized ecosystem and long history of environmental monitoring, providing important background information on the complex nature of phytoplankton phenology, the composition of communities and their role in biogeochemical cycling of elements in the water column. Shells of live-collected *P. maximus* were analyzed by means of LA-ICP-MS (Laser Ablation - Inductively Coupled Plasma - Mass Spectrometery) to obtain highly resolved geochemical profiles that were temporally aligned with high precision and contextualized with detailed information on biological and physicochemical properties of the water. Building on such datasets from multiple years, common patterns between potential environmental signals and geochemical responses were statistically evaluated and systematically addressed with a high level of details about the dynamics of various phytoplankton taxa. Together, these studies contribute to advancing the use of bivalve shells as multi-proxy archives for the reconstruction of phytoplankton dynamics.

In the first manuscript, the focus was placed on Ba/Ca_{shell} variations from *P. maximus*

shells from two successive years (2011 and 2012) contextualized with the concurrent phytoplankton abundance. Peaks occurring in the Ba/Ca_{shell} record could be related to the blooms of specific phytoplankton taxa, particularly diatoms. Neither bulk chlorophyll *a* concentrations nor the total cell abundance of diatoms or dinoflagellates adequately explained the measured Ba/Ca_{shell} variations. Instead, after considering a short time lag of several days between blooms of certain phytoplankton species and shell barium enrichments, the geochemical patterns matched closely the timing of the primary producers. However, not all taxa coincided with the formation of Ba/Ca_{shell} peaks, supporting the assumption that *P. maximus* selectively retains and ingests its food items. To achieve a high running similarity between Ba/Ca_{shell} profiles and primary producer dynamics, species-specific weighting factors were statistically determined and applied, demonstrating that barium associated with different phytoplankton species varies among taxa. Accordingly, patterns in the Ba/Ca_{shell} profiles reflect the occurrence and abundance of specific phytoplankton species.

The second manuscript targeted Ba/Ca_{shell}, Mo/Ca_{shell} and Li/Ca_{shell} chronologies of scallop shells from three years (2011, 2012 and 2019). The application of a pseudo-random sampling approach allowed the approximation of time lags and phytoplankton taxa-specific trace element loads that were involved in the formation of distinct trace element enrichments in the shells of *P. maximus*. The outcomes suggested that peaks in Ba/Ca_{shell}, Mo/Ca_{shell} and Li/Ca_{shell} profiles were most likely induced by the dietary uptake of respective elements following blooms of specific primary producers that occurred about one to two weeks earlier. Ba/Ca_{shell} peaks were attributed to the blooms of ingestible diatom and dinoflagellates, while Mo/Ca_{shell} peaks matched the timing and magnitude of the dinoflagellate *Gymnodinium* spp. and potentially the occurrence of diatom aggregation events. Large diatom blooms of *Chaetoceros* spp. or neurotoxin-producing diatom taxa (*Pseudo-nitzschia* spp.) were proposed to cause the formation of Li/Ca_{shell} peaks in *P. maximus*.

The third manuscript aimed to test and validate the previously proposed uptake and incorporation mechanisms of barium and molybdenum into scallop shell carbonate by coupling shell geochemistry with an extensive environmental monitoring survey in 2021. Comparing specimens grown in a cage above the sediment-water interface with those naturally living on the seafloor corroborated earlier interpretations that synchronous Ba/Ca_{shell} and Mo/Ca_{shell} enrichments are linked to barium and molybdenum bound to organic matter in the water column. It is quantitatively shown that the Ba/Ca_{shell} and Mo/Ca_{shell} peak magnitudes can be sufficiently explained by the ingestion of Ba-enriched diatoms and dinoflagellate cells con-

taining Mo, respectively. Furthermore, it is demonstrated that growth and filtration rates of the bivalves influence the incorporation of trace elements into the shell, accounting for the observed differences in peak magnitudes between cage-grown and sediment-lived scallops. The lack of distinct Li/Ca_{shell} enrichments in scallop shells from this year precluded the quantitative assessment of potential relationships to phytoplankton dynamics, highlighting the need for further research.

The fourth manuscript systematically evaluated different sclerochronological techniques, crucial to employ long-lived bivalve shells as high-resolution geochemical proxy archives for reconstructing environmental variables, from a theoretical perspective. Digital models that numerically simulated incremental shell growth were employed to assess how different sampling strategies and alignment methods affect the reliability of environmental reconstructions. The findings demonstrated that both the sampling strategy and temporal alignment method significantly influence the accuracy of shell proxy–based reconstructions. Furthermore, an improved alignment approach was introduced that accounts for temporally overlapping sample spots and growth-increment morphology, providing a more robust temporal contextualization of geochemical data compared to conventional techniques. The methodological framework developed in this study facilitates the use of high-resolution geochemical proxies from slow-growing bivalve shells, thereby improving the reconstruction of highly dynamic environmental variables like phytoplankton dynamics.

In summary, the findings presented throughout this thesis demonstrate that the trace element-to-calcium ratios of Ba/Ca, Mo/Ca and Li/Ca measured in *P. maximus* shells are strongly associated with the primary producer dynamics of the ecosystem in which the bivalves lived. These trace element profiles capture bloom events of different phytoplankton species, providing insights into complementary aspects of the primary producers. Therefore, shells of these bivalves inherit the great potential to serve as multi-proxy biogenic archives for the reconstruction of past phytoplankton dynamics. The vast underlying complexity associated with the occurrence of these photoautotrophic organisms, however, requires detailed calibration effort and understanding of the mechanisms involved in the uptake and incorporation of geochemical signals from the environment into the shell matrix. The hypotheses and methodologies described herein provide a basis for future studies to extend and apply the geochemical proxies on (sub)fossil shell material as well as other bivalve taxa, to advance and unleash the full potential of geochemical proxies from bivalve shells for the reconstruction of phytoplankton dynamics.

Zusammenfassung

Die zentrale Bedeutung des Phytoplanktons in den Ozeanen wird zunehmend offensichtlich, da es maßgeblich zur globalen Sauerstoffproduktion beiträgt, die Reduktion des CO_2-Gehalts der Atmosphäre steuert, biogeochemische Kreisläufe beeinflusst und die Nahrungsgrundlage für einen Großteil des marinen Lebens bildet. Um zukünftige Entwicklungen und Trends dieser Primärproduzenten abschätzen zu können, ist es entscheidend zu verstehen, wie das Phytoplankton auf verschiedene natürliche und anthropogene Veränderungen in der Vergangenheit reagiert hat. Dies ist insbesondere im Hinblick auf die aktuellen Klimaänderungen sowie die zunehmenden menschlichen Einflüsse auf marine Ökosysteme von großer Relevanz. Die Rekonstruktion der Dynamiken der Primärproduzenten ist jedoch äußerst herausfordernd, da direkte Beobachtungs- oder Fernerkundungsdaten nur spärlich vorhanden bzw. nur für wenige Jahrzehnte verfügbar sind. Biogene Proxy-Archive, wie beispielsweise Schalen von Muscheln, können daher genutzt werden, um geochemische Daten zu sammeln. Diese erlauben Rückschlüsse auf das im Wasser vorkommende Phytoplankton, wie etwa die Menge und die Vergesellschaftung der verschiedenen Phytoplanktonarten und die saisonale Abfolge von Algenblüten. Die zugrunde liegende Komplexität der Primärproduzenten sowie die geringe Anzahl an Kalibrierungsstudien erschweren und begrenzen die Anwendbarkeit solcher geochemischer Indikatoren als Werkzeuge zur Rekonstruktion der Phytoplanktondynamik jedoch maßgeblich. In dieser Arbeit wurden die Element-zu-Calcium Verhältnisse von Barium (Ba/Ca_{shell}), Molybdän (Mo/Ca_{shell}) und Lithium (Li/Ca_{shell}) in Schalen der schnell wachsenden Jakobsmuschel *Pecten maximus* untersucht und das Potenzial dieser Element-Calcium Verhältnisse als geochemische Indikatoren für Phytoplanktondynamiken bewertet. Als Untersuchungsgebiet diente die Bucht von Brest (Frankreich), die sich aufgrund ihres detailliert erforschten Ökosystems und ihrer langen Historie umfassender Umweltbeobachtungsdaten besonders hierfür eignet. Diese Daten bieten eine wertvolle Grundlage an Hintergrundinformationen über die komplexe Natur der vorherrschenden Phytoplanktonphänologie, die Zusammensetzung der Phytoplanktongemeinschaften und deren Rolle in den biogeochemischen Elementkreisläufen der Wassersäule. Schalen lebend gesammelter Jakobsmuscheln wurden mittels LA-ICP-MS (Laser Ablation - Inductively Coupled Plasma - Mass Spectrometery) analysiert, um hochaufgelöste geochemische Profile zu erhalten, die mit hoher Präzision zeitlich kontextualisiert und im Rahmen der biologischen sowie physikochemischen Eigenschaften des Wassers interpretiert wurden. Auf Grundlage mehrjähriger geochemischer Zeitreihen

wurden Zusammenhänge zwischen potenziellen Umweltsignalen und geochemischen Mustern statistisch ausgewertet und in bislang unerreichter Detailtiefe systematisch untersucht. Somit leistet diese Studie einen wichtigen Beitrag zur Weiterentwicklung der Nutzung von Muschelschalen als Multi-Proxy-Archive zur Rekonstruktion vergangener Phytoplanktondynamiken.

Im ersten Manuskript lag der Fokus auf den Ba/Ca_{shell} Variationen in den Schalen von *P. maximus* aus zwei aufeinanderfolgenden Jahren (2011 und 2012), die im Zusammenhang mit der zeitgleichen Phytoplanktonhäufigkeit untersucht wurden. Deutliche Ba/Ca_{shell} Peaks in den Schalen konnten mit den Blüten bestimmter Phytoplanktontaxa, insbesondere von Diatomeen, in Verbindung gebracht werden. Weder die Chlorophyll *a* Konzentrationen noch die Gesamtmenge an Diatomeen oder Dinoflagellaten in der Wassersäule konnten die gemessenen Ba/Ca_{shell} Muster ausreichend erklären. Stattdessen zeigten sich enge Übereinstimmungen zwischen den Blüten bestimmter Arten und der vermehrten Anreicherung von Barium in den Schalen, nach Berücksichtigung einer kurzen zeitlichen Verzögerung von einigen Tagen. Allerdings fielen nicht alle Phytoplanktonblüten mit der Bildung der Ba/Ca_{shell} Spitzen in den Schalen zusammen, was die Annahme stützte, dass *P. maximus* seine Nahrungspartikel selektiv auswählt. Um eine hohe Übereinstimmung zwischen den Ba/Ca_{shell} Profilen und der Dynamik der Primärproduzenten zu erzielen, mussten artspezifische Gewichtungsfaktoren statistisch bestimmt und angewendet werde. Dies legt nahe, dass der mit verschiedenen Phytoplanktonarten assoziierte Bariumanteil zwischen den Taxa variiert und dementsprechend die Muster in den Ba/Ca_{shell} Profilen die zeitliche Abfolge und Häufigkeit spezifischer Algenblüten widerspiegeln.

Das zweite Manuskript befasste sich mit den Ba/Ca_{shell}, Mo/Ca_{shell} und Li/Ca_{shell} Chronologien aus drei Jahren (2011, 2012 und 2019). Mittels Monte-Carlo-Experimenten auf Basis pseudozufälliger Stichproben konnten die zeitlichen Verzögerungen sowie die artspezifischen Spurenelementbeiträge abgeschätzt werden, die an der Bildung ausgeprägter Spurenelementanreicherungen in den Schalen von *P. maximus* beteiligt waren. Die Ergebnisse deuten darauf hin, dass die Spitzen in den Ba/Ca_{shell}, Mo/Ca_{shell} und Li/Ca_{shell} Profilen höchstwahrscheinlich durch die mit der Nahrung aufgenommenen Elemente infolge von Blüten bestimmter Primärproduzenten verursacht wurden, die sich etwa ein bis zwei Wochen zuvor entwickelten. Ba/Ca_{shell} Anreicherungen konnten dem Vorkommen bestimmter Diatomeen und Dinoflagellaten zugeschrieben werden, während die Mo/Ca_{shell} Spitzen zeitlich und in ihrer Ausprägung mit der Dinoflagellatenart *Gymnodinium* spp. sowie möglicherweise mit der Bildung von Aggregaten übereinstimmten. Als mögliche Ursache für die Bildung von

Li/Ca_{shell} Spitzen wurde das massenhafte Vorkommen von *Chaetoceros* spp. oder neurotoxinbildenden Diatomeen (*Pseudo-nitzschia* spp.) in Betracht gezogen.

Die zuvor beschriebenen Aufnahmemechanismen sowie die Einlagerung von Barium und Molybdän in das Schalenkarbonat der Jakobsmuscheln wurden im dritten Manuskript überprüft und getestet. Dazu wurde die geochemische Zusammensetzung von *P. maximus* Schalen mit detaillierten Umweltdaten, die infolge einer umfangreichen Monitoring-Kampagne im Jahr 2021 gesammelt wurden, verknüpft. Der Vergleich zwischen im Käfig aufgezogenen Muschelschalen (oberhalb der Sedimentoberfläche) und natürlich am Meeresboden lebenden Exemplaren bestätigte frühere Interpretationen, wonach gleichzeitige Ba/Ca_{shell} und Mo/Ca_{shell} Anreicherungen mit an organischem Material gebundenem Barium und Molybdän in der Wassersäule in Verbindung stehen. Es konnte quantitativ gezeigt werden, dass die Ausprägung der Ba/Ca_{shell} und Mo/Ca_{shell} Spitzen hinreichend durch die Aufnahme von Ba-angereicherten Diatomeen bzw. Mo-haltigen Dinoflagellatenzellen erklärt werden können. Darüber hinaus konnte gezeigt werden, dass die Wachstums- und Filtrationsraten der Muscheln maßgeblich die Einlagerung von Spurenelementen in die Schalen beeinflussen, was die beobachteten Unterschiede in den Peakhöhen zwischen käfig- und bodenlebenden Individuen erklären konnte. Das Fehlen ausgeprägter Li/Ca_{shell} Anreicherungen in den Muschelschalen aus diesem Jahr (2021) erschwerte eine quantitative Bewertung möglicher Zusammenhänge mit der Phytoplanktondynamik und betonte den Bedarf weiterführender Studien.

Im vierten Manuskript wurden verschiedene sklerochronologische Techniken, die für die Nutzung langlebiger Muschelschalen als hochauflösende geochemische Proxy-Archive zur Rekonstruktion von Umweltvariablen entscheidend sind, aus theoretischer Perspektive beleuchtet. Um zu untersuchen, wie unterschiedliche Beprobungsstrategien und zeitliche Alignierungsmethoden die Rekonstruktionsgenauigkeit von Umweltparameter beeinflussen, wurden digitale Modelle verwendet, die das inkrementelle Schalenwachstum numerisch simulierten. Die Ergebnisse zeigten, dass sowohl die Wahl der Beprobungsstrategie als auch die Methode der zeitlichen Kontextualisierung die Genauigkeit schalenbasierter Rekonstruktionen wesentlich beeinflussen kann. Darüber hinaus wurde eine neue Methode zur zeitlichen Einordnung geochemischer Proben eingeführt, die die potenziell zeitliche Überlappung von Proben sowie die Morphologie der Wachstumsinkremente berücksichtig. Im Vergleich zu herkömmlichen Verfahren bietet diese Methode das Potenzial, eine robustere zeitliche Kontextualisierung geochemischer Proben zu ermöglichen. Die in dieser Studie präsentierte methodische Grundlage erleichtert die Anwendbarkeit hochauflösender geochemischer Indikatoren aus langsam

wachsenden Muschelschalen und verbessert dadurch die Rekonstruktionsmöglichkeiten hochdynamischer Umweltvariablen wie die des Phytoplanktons.

Die in dieser Arbeit vorgestellten Ergebnisse zeigen, dass die in den Schalen von *P. maximus* gemessenen Spurenelement-zu-Calcium Verhältnisse (Ba/Ca, Mo/Ca und Li/Ca) eng mit der Dynamik der im Wasser vorkommenden Primärproduzenten verbunden sind. Profile dieser Spurenelemente archivieren die Blüten verschiedener Phytoplanktonarten und ermöglichen dadurch Einblicke in komplementäre Aspekte der Primärproduzenten. Somit besitzen diese Muscheln ein großes Potenzial als biogene Multi-Proxy Archive für die Rekonstruktion vergangener Phytoplanktondynamiken. Aufgrund der zugrunde liegenden Komplexität der photoautotrophen Organismen sind jedoch detaillierte Kalibrierungsstudien und ein tiefgreifendes Verständnis der Mechanismen, die an der Aufnahme und Einlagerung von Spurenelementen aus der Umwelt in die Muschelschale beteiligt sind, erforderlich. Die beschriebenen Hypothesen und methodischen Ansätze bilden die Grundlage für zukünftige Studien, in denen die geochemischen Proxys auch auf (sub-)fossiles Schalenmaterial sowie auf andere Muschelarten übertragen werden. Dadurch kann das volle Potenzial für eine hochaufgelöste Rekonstruktion der marinen Primärproduktion auf Basis von Muschelschalen erschlossen werden.

Acknowledgements

Removed for reasons of data protection

Table of Contents

List of Figures

List of Tables

1 Introduction

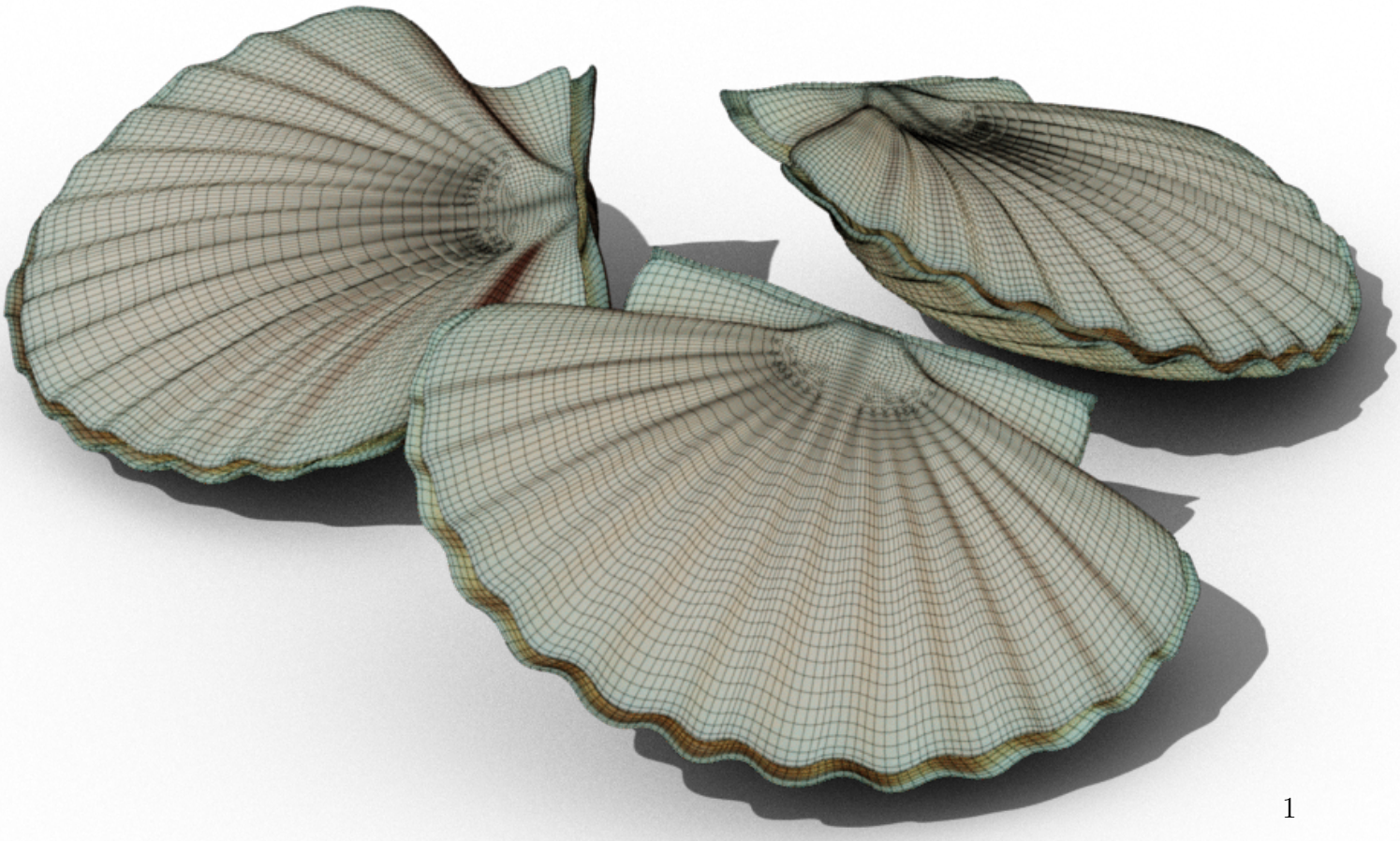

1.1 Marine phytoplankton – A valuable yet complex component of the ocean

> *"The phytoplankton in our oceans are less visible than the trees and grasses we see in our daily lives, but their influence is profoundly underappreciated."* – Falkowski (2012)

Marine environments cover approx. 71% of the surface of the Earth, providing critical benefits to the planet, including climate regulation and the provision of essential resources for humans. Within these vast aquatic ecosystems, a diverse assemblage of microscopic phytoplankton forms the foundation of marine life. There are probably more than 10,000 marine phytoplankton species estimated in the ocean (de Vargas et al., 2015), of which approx. 4000 species have been described (Sournia et al., 1991; Tett and Barton, 1995). These photosynthetic organisms harness sunlight as a primary energy source to convert inorganic carbon into organic, energy-rich carbon compounds. This process of photoautotrophic biomass synthesis, known as primary production, constitutes the basis of the food web by supplying energy to organisms from higher trophic levels, and thus largely regulates the functioning of entire ecosystems. Although these organisms represent less than 1% of the global photosynthetic biomass, they contribute to nearly half of the global net primary production (Bidle and Falkowski, 2004; Falkowski, 2012). Phytoplankton species not only play a crucial role as primary producers at the base of the food chain, but also contribute significantly to global biogeochemical cycles, such as the carbon cycle. At an annual marine primary production of approx. 50 Pg C (Field et al., 1998; Cavan et al., 2019), considerable amounts of carbon dioxide (CO_2) are removed from the atmosphere via the air-sea gas exchange, while more than half of the globally produced oxygen is released back into the atmosphere. Parts of the biologically fixed carbon (approx. 10 Pg C yr^{-1} Nowicki et al., 2022) that is not utilized by zooplankton or microbial processes is exported to the deep ocean through the biological pump, where it can be sequestered for centuries. This process makes phytoplankton a key contributor to the reduction of atmospheric CO_2 levels.

The predominant and most diverse groups of primary producers, diatoms and dinoflagellates, account for approx. 80% of the total phytoplankton (Simon et al., 2009). While numerous dinoflagellate species are photoautotrophic, many taxa are mixotrophs, combining photosynthesis with heterotrophic food uptake (e.g., Hansen, 2011). These groups display striking morphological variations in terms of shape, volume and size (e.g., compare Boxes 1, 2, 3, 4). Approx. 91% of diatoms are cylindrical or prismatic in shape, whereas about 87% of dinoflagellates exhibit ellipsoidal or conical forms (Ryabov et al., 2021). Their cell dimensions span several orders of magnitude, from less than 2 µm to more than 2 mm in length, and average cell volumes from 10^2 to 10^{13} µm^3 in diatoms and 10^2 to 10^8 µm^3 in dinoflagellates (Finkel et al., 2010). Phytoplankton cell morphology has a significant impact on functional traits. Cell size and shape of these organisms influence carbon fixation rate, nutrient uptake and storage, respiration and survival against predation (e.g., Edwards et al., 2012; Irion et al., 2021; Hillebrand et al., 2022). Beyond morphology, physiological traits such as photosynthesis rate, protein synthesis rate, carbon excretion rate and photoacclimation time differ largely among species (e.g., Omta et al., 2017), while species-specific life cycles determine their phenological traits. Collectively, these traits shape the ecological performance (Violle et al., 2007) and determine the composition of the phytoplankton community within an ecosystem.

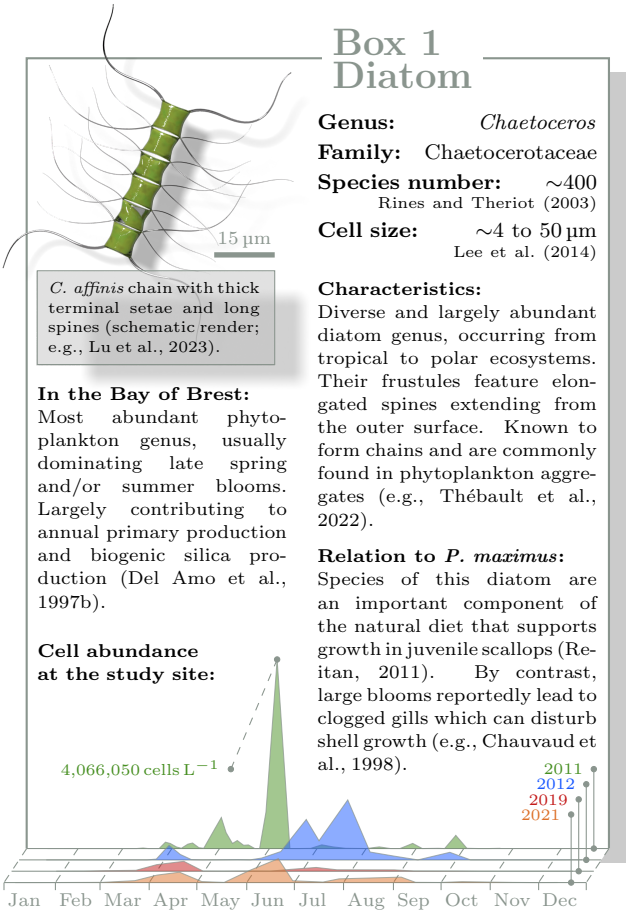

Phytoplankton dynamics are also regulated by external factors like water temperature, nutrient supply, light availability and water currents (e.g., Fernández-González et al., 2022; Poppeschi et al., 2022). For instance, temperature and nutrient conditions, particularly the nitrogen, phosphorus and silicon availability, can influence the metabolic rates of phytoplankton (e.g., Marañón et al., 2018), whereas light availability and ocean currents sub-

stantially affect the spatial and depth distribution of phytoplankton cells. In addition to these abiotic factors, the interactions and competitions among species, including pressures from higher trophic levels, play a major role in shaping phytoplankton communities. For example, the cell growth of one phytoplankton species is inhibited by another competing algae (e.g., due to allelopathic interactions Legrand et al., 2003) or the enhanced filtration activity of suspension-feeding organisms that lead to an alteration in phytoplankton biomass (e.g., Alpine and Cloern, 1992). These factors contribute to the extremely high diversity and coexistence of phytoplankton within a seemingly homogenous environment (i.e., the water column), a phenomenon known as 'the paradox of the plankton' (Hutchinson, 1961). This paradox emphasizes the inherent complexity associated with the dynamics of phytoplankton. Additionally, studies have shown that variations in phytoplankton communities follow a chaotic nature, making their dynamics extremely difficult to model which substantially affects the predictability of such systems (e.g., Benincá et al., 2008).

Box 2 Dinoflagellate

Gymnodinium spp. cell with transverse and longitudinal flagella (schematic render; e.g., Jeong et al., 2010).

Genus: *Gymnodinium*
Family: Gymnodiniaceae
Species number: ~230
Thessen et al. (2012)
Cell size: 5 to 200 µm
Guiry and Guiry (2024)

Characteristics:
Unarmored dinoflagellate occurring in both marine and freshwater ecosystems. Many species are photosynthetic, while others are mixotrophic or heterotrophic (e.g., Jakobsen and Hansen, 1997; You et al., 2020). Multiple taxa are known to produce neurotoxins and form harmful algal blooms (Wang, 2008).

In the Bay of Brest:
Bloom-forming genus that commonly occurs in the bay. These dinoflagellates form toxic algal blooms (Chauvaud et al., 1998) that emerge after the collapse of diatom blooms (Del Amo et al., 1997b) and induce phytoplankton aggregation events (Siebert et al., 2024).

Relation to *P. maximus*:
Toxic blooms of *Gymnodinium* have been reported to reduce the growth rate of *P. maximus* while having lethal effects on juveniles (e.g., Chauvaud et al., 1998). Further, blooms can inhibit feeding activity of the scallops (Chauvaud et al., 2001).

Cell abundance at the study site:

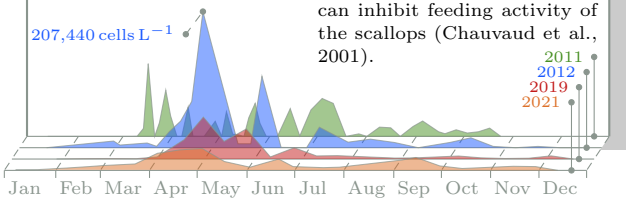

Coastal ecosystems constitute a particularly vital subset of marine realms. They are recognized for their high productivity, contributing to approx. one-fourth of the total marine primary production (Longhurst et al., 1995; Geider et al., 2001), and their importance in providing various ecological goods and services for millions of people (Barbier et al., 2011). Unlike the open ocean, where phytoplankton taxa dominate, coastal areas host a wide variety of benthic primary producers, including macroalgae and microphytobenthos. The close benthic-pelagic link occurring at coastal ecosystems affects the phytoplankton abundance in the water column, e.g., through grazing pressure by benthic organisms (e.g., Cloern, 1982), nutrient cycling at the sediment-water interface (SWI) (e.g., Ragueneau et al.,

2005), and/or the provision of benthic resting stages that seed phytoplankton blooms (e.g., Shikata et al., 2008). Moreover, the delicate interplay between processes at the SWI and other influences at the land-sea interface, such as riverine nutrient and freshwater inputs as well as coastal upwelling, generates highly variable patterns in phytoplankton dynamics in these settings (e.g., Cloern and Jassby, 2010; Carstensen et al., 2015).

Increasing anthropogenic activities coupled with a growing population pose significant threats to marine habitats (e.g., Harley et al., 2006; Boehm et al., 2017; He and Silliman, 2019). Phytoplankton species are particularly sensitive to such disturbances, as these organisms react rapidly to environmental changes. Predominantly, water pollution (e.g., caused by sewage discharge, industrial effluents and agricultural runoffs) affects phytoplankton in multiple ways. For instance, excess nitrogen input from artificial fertilizers causes imbalanced nutrient levels that fuel the development of massive phytoplankton blooms (Beman et al., 2005), drive eutrophication (Nixon, 1995; Cloern, 2001), promote harmful algal blooms (e.g., Gobler, 2020) and lead to oxygen depletion in bottom waters due to enhanced microbial respiration, thereby threatening benthic life (e.g., Rabalais et al., 2002; Diaz and Rosenberg, 2008). Climate change further intensifies these pressures. Ocean warming and stronger stratification reduce nutrient exchange between surface and deep waters, altering bloom phenology (Wiltshire and Manly, 2004) and net primary production (Bopp et al., 2013). Ocean acidification shifts the competitive fitness among phytoplankton taxa modifying their community compositions (Dutkiewicz et al., 2015). Additionally, human exploitation and biological invasions also reshape phytoplankton dynamics through the alteration of food web structures. Overfishing, for example, reduces populations of top predators, enabling zooplankton to proliferate, intensifying graz-

Box 3 Diatom

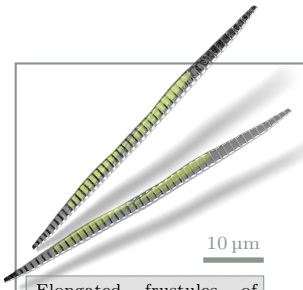

Elongated frustules of *Pseudo-nitzschia* spp. with chloroplasts (schematic render; e.g., Rhodes et al., 2016).

Genus: *Pseudo-nitzschia*

Family: Bacillariaceae

Species number: ~50
Bates et al. (2018)

Cell size: ~20 to 130 µm
Parsons et al. (2012)

Characteristics:
Chain-forming diatom genus with a widespread distribution, typically found along coastlines and upwelling systems (Trainer et al., 2012). Tolerant to a broad range of environmental conditions (e.g., Clark et al., 2019). Some species of *Pseudo-nitzschia* spp. produce the neurotoxin domoic acid (DA), responsible for amnesic shellfish poisoning (e.g., Clark et al., 2019).

In the Bay of Brest:
Yearly occurring diatoms, with some species reported to form harmful algal bloom events (Nézan et al., 2010), that have increased in frequency in recent decades (Husson et al., 2016). Increased nutrient availability favor blooms of this diatom (Claquin et al., 2010).

Relation to *P. maximus*:
Reportedly feed on *Pseudo-nitzschia* and can accumulate DA (Sauvey et al., 2021). Chains hamper shell growth due to gill clogging (Liu et al., 2008; Thébault and Chauvaud, 2013).

Cell abundance at the study site:

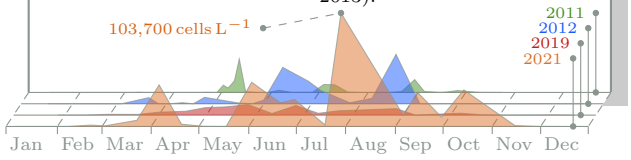

ing pressure on phytoplankton (e.g., Jackson et al., 2001; Jurgensone et al., 2011). Invasive filter-feeding organisms, such as the gastropod *Crepidula fornicata* in the Bay of Brest, can disrupt biogeochemical cycles (see section 1.5) and trophic interactions, thereby influencing phytoplankton dynamics (e.g., Chauvaud et al., 2000; Laruelle et al., 2009).

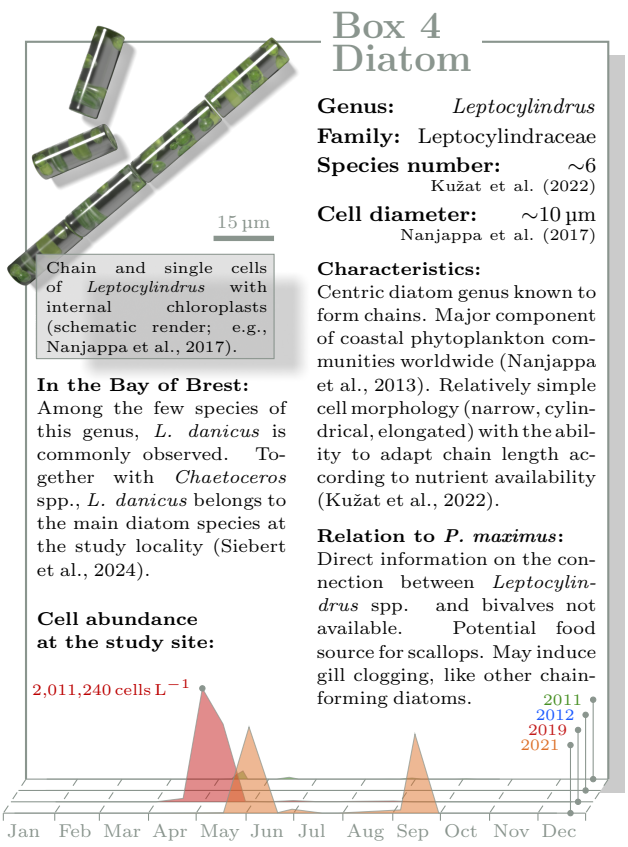

In summary, marine phytoplankton play a critical role in ecological and biogeochemical processes on global, regional and local scales. Their diverse morphological and physiological properties, combined with interactions across various environmental factors, govern the high diversity of phytoplankton communities and the complex nature of their dynamics. Coastal ecosystems are highly susceptible to anthropogenic influences that perturb food webs, biogeochemical cycles and ecosystem functioning. To address future trends in phytoplankton under climate change and intensifying human pressures, it is essential to decipher their past dynamics. Understanding how phytoplankton communities have responded to environmental variables in the past is crucial for predicting their future trajectories under global change and for refining models of ecosystem responses to various stressors. However, reliably reconstructing phytoplankton dynamics through time remains extremely challenging.

1.2 Unraveling past phytoplankton dynamics – A challenging task

Collecting historical information about phytoplankton dynamics can be achieved in multiple ways. The most accurate and detailed data come from direct observations and instrumental analyses of in-situ collected water samples. These methods involve measuring phytoplankton-indicative parameters such as fluorescence pigment analyses (e.g., chlorophyll *a* (Chl *a*) and pheophytin concentrations), microscopy, digital imaging, flow cytometry, high performance liquid chromatography and genome sequencing (e.g., Lorenzen, 1967; Phinney and Cucci, 1989; Li et al., 2023). Such data can be complemented by additional parameters of the water column, including temperature, pH, salinity, currents, nutrient concentrations as well as measurements on the total organic carbon and nitrogen, to generate a comprehensive picture of the status and dynamics of the phytoplankton community at a specific location. However, collected water samples and/or long-term observations are evidently scarce, spatially limited and temporally confined to a few decades (e.g., Cadée and Hegeman, 2002; Edwards and Richardson, 2004). Since individual water samples capture only snapshots of the ecosystem, the frequency of sampling is critical, as short-lived phytoplankton blooms may remain undetected. The combination of time-consuming, labor-intensive analyses and the need for high sampling resolution often make long-term monitoring impractical or even impossible. Alternatively, data on primary production derived from remote sensing satellite missions (e.g., CZCS, SeaWiFS and Aqua/MODIS) provide extensive spatial coverage but are only available from the late 20^{th} century onwards (Blondeau-Patissier et al., 2014).

Environmental reconstructions extending far into the past are typically achieved through the analysis of geochemical properties in natural archives such as sediment cores, which preserve a wealth of geochemical information indicative of historical phytoplankton dynamics and associated environmental conditions. Total organic carbon, accumulation rates of $CaCO_3$, opal abundance, marine barite and elemental ratios like Ba/Ti or Al/Ti, provide insights into past primary productivity and its corresponding temporal variability (e.g., Averyt and Paytan, 2004; Gutiérrez et al., 2009). Furthermore, the distribution and assemblages of marine microfossils such as calcareous foraminifera and coccoliths, siliceous skeletons of radiolarians and diatoms or organic remains of dinoflagellates can provide insights into the paleo-community structure and composition of planktonic organisms (e.g., Witkowski et al., 2014). In addition, sedimentary biomarkers such as pigments from algae and cyanobacteria

can serve as indicators of the abundance of concurrent phytoplankton (e.g., Bjorndahl et al., 2022). Such data can be further refined using environmental DNA metabarcoding techniques, which allow for the extraction and analysis of DNA fragments from past organisms preserved in the sediment (Pedersen et al., 2015). This method enables both the qualitative and the quantitative evaluation of past pelagic and benthic communities (e.g., Sinniger et al., 2016; Barrenechea Angeles et al., 2020), providing potential insights into historical primary producers and overall ecosystem dynamics. Nevertheless, the use of sediment core analysis is associated with certain limitations. Processes such as the dissolution of fossils, sediment redistribution by bottom currents and bioturbation increase time-averaging and introduce dating uncertainties (Boltovskoy, 1994; Trauth et al., 1997). In addition, silica-undersaturated seawater can dissolve biogenic silica, e.g., diatom frustules, which results in only a minor fraction of siliceous skeletons being preserved in the sediment (e.g., Zielinski and Gersonde, 1997). Calcareous microfossils are similarly impacted by dissolution, which is primarily influenced by depth (i.e., the carbonate compensation depth at approx. 4.6 km at present; Pälike et al., 2012). In contrast, remains of organic-walled organisms are resistant to dissolution, but remain susceptible to oxidation (Zonneveld et al., 1997; Zonneveld et al., 2001). These taphonomic processes can strongly bias and complicate the assessment of species abundance and diversity from sediment deposits. One of the most significant challenges in reconstructing phytoplankton dynamics from sediment cores is the temporal contextualization and resolution of obtained data. The dating control relies on age-depth models, which are constructed using techniques such as radiometric dating, stratigraphic alignment using stable isotopes signatures and orbital tuning (e.g., Hodell et al., 2015; Lisiecki et al., 2022). Despite potential discrepancies between the different dating methods, the temporal resolution for individual samples taken from sediment cores can vary considerably, ranging from a few years to several hundreds of years (e.g., Böll et al., 2014; Wörmer et al., 2014). While such a resolution may be sufficient to address general, long-term trends in primary production and broad shifts in phytoplankton community compositions, it is too coarse to reliably resolve sub-seasonal phytoplankton dynamics (c.f., Sonnet et al., 2024), making detailed reconstructions of short-term variability from sediment cores extremely difficult.

Notably, biogenic archives from calcifying organisms such as corals, macroalgae and mollusk shells can provide highly temporally resolved environmental information. As they grow, these organisms record ambient environmental conditions in the form of geochemical properties into their skeletal or shell material. While such archives have been widely applied in

paleotemperature reconstructions through stable oxygen isotopes and element ratio analyses (e.g., McCulloch et al., 1994; Schöne et al., 2005a; Halfar et al., 2008), they also hold potential for reconstructing other environmental variables, including phytoplankton dynamics. For instance, analyses of stable nitrogen and carbon isotopes, together with phytoplankton-indicative elements such as barium (Ba) in coral skeletons can shed light on past phytoplankton and nutrient dynamics (LaVigne et al., 2016; Saha et al., 2018; Glynn et al., 2019). Shells of mollusks constitute another valuable set of environmental proxy archives. Their hard parts are widespread across aquatic habitats, with their remains being both well-preserved and largely abundant in the fossil record (e.g., Gutiérrez et al., 2003; Fortunato, 2015; Immenhauser et al., 2016). Among the mollusk taxa, bivalves, specifically their calcified shells, constitute the most promising geochemical archives for reconstructing past phytoplankton dynamics (see section 1.3). However, the applicability of biogenic materials as paleoenvironmental archives remains constrained, as underlying processes, e.g., the transfer of geochemical signals from the ambient environment, their uptake and eventual incorporation into the shell material, are still the subject of ongoing research (e.g., Trofimova et al., 2020). Concurrently, recent advances in analytical techniques permit geochemical sampling at exceptionally fine spatial scales, requiring only minimal sample quantities. These developments enable the retrieval of highly resolved geochemical records, thereby improving the precision and details of paleoenvironmental reconstructions.

1.3 Bivalve shells as multi-proxy archives for reconstructing phytoplankton dynamics

Bivalves present remarkable biological proxy archives and preserve environmental variables in their shells in a wide range of geochemical and physical properties. Their shell is composed of the calcium carbonate polymorphs calcite, aragonite and more rarely vaterite (e.g., Bøggild, 1930; Kennedy et al., 1969; Jacob et al., 2008), alongside with small quantities (up to 5 wt%) of organic matter (Marin et al., 2007; Marin et al., 2012; Agbaje et al., 2017). The shell biominerals are precipitated within a narrow gap between the mantle and the shell (i.e., extrapallial space), filled with an extrapallial fluid or gel enriched in calcium and bicarbonate ions, as well as other ions and organic compounds (e.g., Louis et al., 2022). Different parts of the mantle secrete distinct shell layers with characteristic ultrastructures, including the inner

shell layer (ISL) and the outer shell layer (OSL) (Bøggild, 1930; Kennedy et al., 1969), the latter of which can be further subdivided based on ultrastructural differences into an inner (iOSL) and outer (oOSL) sublayer (e.g., Schöne et al., 2013; Trofimova et al., 2018). These mineralized shell structures are overlain by an organic periostracum that covers the external shell surface (Bøggild, 1930; Kennedy et al., 1969). Generally, ions from the surrounding environment enter the bivalve through the gills or the digestive system and are transported by the hemolymph, the circulatory fluid of bivalves, to the site of calcification where new shell material is precipitated (Takesue et al., 2008; Marin et al., 2012). Such ions are subsequently incorporated into the crystal lattice by substituting calcium in the biominerals (Okumura and Kitano, 1986; Dromgoole and Walter, 1990; Kastner, 1999; Marriott et al., 2004; Iglikowska et al., 2016; Soldati et al., 2016; Piwoni-Piórewicz et al., 2021). Alternatively, the ions may bind to the organic fraction of the shell matrix or to inorganic nanoparticles (Carriker et al., 1980; Foster et al., 2008; Takesue et al., 2008; Schöne et al., 2010). In this way, chemical signals from the ambient environment are sequentially archived in the shell material as the bivalve grows.

By extracting and analyzing the temporally constrained geochemistry of the shells, it is therefore possible to obtain information about past environmental variables. This concept of utilizing accretionary hard parts of organisms to temporally constrain their physical or chemical characteristics is known as sclerochronology. To reliably integrate such data within a temporal framework, the growth pattern of the studied bivalve needs to be evaluated. An essential step in this process is the identification of the internal rhythms that governs shell formation. Most bivalves exhibit distinct growth features, such as growth lines, darker and lighter bands or morphological patterns on the shell surface, which typically develop at regular intervals (e.g., Pannella and MacClintock, 1968; Evans, 1972; Jones, 1980; Richardson et al., 1980; Jones and Quitmyer, 1996; Owen et al., 2002; Killam and Clapham, 2018). For example, annual slowdowns or cessations of shell growth, driven by endogenous drivers (clock genes controlling biological rhythms such as reproductive cycles), and/or exogenous factors like changes in temperature and food availability, lead to the formation of annual growth lines (e.g., Thompson et al., 1980; Schöne, 2008; Killam and Clapham, 2018). These growth lines serve as precise chronological markers, enabling the accurate temporal placement of shell-derived proxy data. Although many bivalve species are long-lived (e.g., *Arctica islandica* can attain a lifespan of more than 500 years; Schöne et al., 2005a; Wanamaker et al., 2008; Butler et al., 2013), individual proxy records from a single specimen captures only

a snapshot spanning from multiple years to decades. By applying crossdating techniques (Butler et al., 2010; Marali et al., 2017; Reynolds et al., 2021), proxy data from multiple specimens can be matched and temporally aligned, generating continuous, high-resolution time-series that extend far into the past (Butler et al., 2013; Reynolds et al., 2017b; Reynolds et al., 2022). Alternatively, shell proxies from radiometrically dated fossil shells yield valuable insights into past environmental conditions from discrete windows in time, albeit with larger temporal uncertainties.

Shells of filter-feeding bivalves are promising candidates for reconstructing phytoplankton dynamics. Most marine bivalves obtain their nutrition by filtering suspended particles, including phytoplankton as the primary food source (Ward and Shumway, 2004; Hawkins et al., 2013). Their low trophic position ensures that signals from phytoplankton undergo little modification through trophic transfer, while direct ingestion promotes the rapid signal incorporation into the shell carbonate. Several geochemical and morphological properties of bivalve shells have been proposed to extract information on phytoplankton from these archives. The following two sections provide a brief overview of some potential phytoplankton proxies, with emphasis on the shell content of the three trace elements Ba, Mo (molybdenum) and Li (lithium), which are the main focus of the present study.

1.3.1 Trace elements: Barium, Molybdenum and Lithium

The element chemical composition of bivalve shells, i.e., the chemical impurities of the shell carbonate, can serve as valuable indicators for various ecosystem-related parameters (e.g., Vihtakari et al., 2017; Peharda et al., 2021; Schöne et al., 2023). However, the mechanisms that govern the uptake of trace elements from the environment, their transport through body fluids and their subsequent incorporation into shell matrices are not fully understood. These processes are further complicated by 'vital effects', i.e., biological controls that can alter geochemical signals independently of the environmental conditions (e.g., Carré et al., 2006; Barrat et al., 2023; Schöne et al., 2023). Still the occurrence of certain elements within the shell material appears to be influenced by external environmental forcings, as suggested by the synchronous geochemical patterns observed among contemporaneously living bivalves from the same habitat (e.g., Marali et al., 2017; Schöne et al., 2023). Among these elements, temporal variations observed in shell barium-to-calcium ratios (Ba/Ca_{shell}) commonly display remarkably coherent patterns, characterized by a constant background

that is episodically punctuated by erratic, sharp peaks (Stecher et al., 1996; Vander Putten et al., 2000; Gillikin et al., 2006; Gillikin et al., 2008). While the background Ba/Ca_{shell} signal is presumably controlled by the dissolved Ba concentration of the ambient water (Gillikin et al., 2006; Barats et al., 2009), the formation of distinct Ba/Ca_{shell} peaks is proposed to be associated with the dietary uptake of particulate Ba. A potential mechanism involves the ingestion of barite ($BaSO_4$) crystals which form in sulfate-rich microenvironments that develop in assemblages of decaying phytoplankton cells after large blooms (Dehairs et al., 1980; Bishop, 1988; Stecher and Kogut, 1999). However, calculations by Thébault et al. (2009a) demonstrated that although the ingestion of $BaSO_4$ crystals may contribute to the formation of Ba/Ca_{shell} peaks, this mechanism alone cannot sufficiently explain the elevated Ba content observed in shells of the fast-growing pectinid *Comptopallium radula*. Instead, the authors proposed a more direct link between blooms of Ba-enriched phytoplankton cells (i.e., diatoms) and their dietary uptake by the bivalves. Supporting this, culture experiments have demonstrated the precipitation of Ba onto cell walls of diatoms (Sternberg et al., 2005) and that cellular Ba concentrations vary widely among marine phytoplankton species (Roth and Riley, 1971; Martin and Knauer, 1973; Fisher et al., 1991). Consequently, temporally aligned Ba/Ca_{shell} profiles can theoretically serve as indicators for the timing and magnitude of some phytoplankton blooms that occur in the water column. Several studies have examined this relationship primarily by comparing Ba/Ca_{shell} ratios with phytoplankton biomass proxies, i.e., Chl *a* pigment concentration, yet the results remain ambiguous. While some studies have reported a positive correlation between Chl *a* and Ba/Ca_{shell} (Thébault et al., 2009a; Marali et al., 2017; Doré et al., 2020), others could not establish such a clear relationship to phytoplankton biomass (Gillikin et al., 2006; Barats et al., 2009; Poitevin et al., 2022) or observed correspondence between the geochemistry and Chl *a* only after accounting for a temporal lag (Gillikin et al., 2008). Thus, the underlying mechanisms that shape Ba/Ca_{shell} profiles remain uncertain, limiting their reliability as direct geochemical proxies for phytoplankton dynamics.

In addition to Ba/Ca_{shell}, the Mo content of bivalve shells (expressed as molybdenum-to-calcium ratios Mo/Ca_{shell}) has been proposed as another potential proxy for phytoplankton dynamics. Mo/Ca_{shell} profiles measured in fast-growing bivalves (e.g., *Pecten maximus* and *C. radula*) exhibit flat background levels alternating with episodes of strong Mo/Ca_{shell} elevations (Thébault et al., 2009a; Barats et al., 2010). Similar to the synchronous Ba/Ca_{shell} peaks observed in specimens from the same habitat, Mo/Ca_{shell} profiles show similar char-

acteristics indicative of external forcings (Barats et al., 2007; Thébault et al., 2009a; Barats et al., 2010). However, variations in Mo/Ca_{shell} differ from those of Ba/Ca_{shell} which implies a different mechanism that governs the formation of Mo/Ca_{shell} peaks (Barats et al., 2007; Thébault et al., 2009a). This suggests that Mo/Ca_{shell} may serve as a phytoplankton proxy complementary to Ba/Ca_{shell}. Although research on the use of Mo/Ca_{shell} as an environmental proxy remains limited, three hypotheses have been proposed to explain the signals of Mo/Ca ratios in bivalve shells in the context of phytoplankton dynamics. First, peaks in Mo/Ca_{shell} profiles may form after phytoplankton blooms composed of phytoplankton cells enriched in Mo. Elevated Mo concentrations in phytoplankton cells could be associated with the presence of molybdoenzymes that are involved in the nitrogen fixation of the primary producers (Collier, 1985; Marino et al., 2003). A second hypothesis links Mo/Ca_{shell} peaks to the release of molybdate ions (MoO_4^{2-}) from pore waters under hypoxic environments that may develop following large phytoplankton blooms (Chaillou et al., 2002; Waeles et al., 2013). Third, under stressful conditions such as nutrient limitation, turbulence or reduced light availability, phytoplankton cells release extracellular polysaccharides that facilitate the formation of phytoplankton aggregates, commonly referred to as 'marine snow' (Alldredge and Gotschalk, 1989; Thornton, 2002). These aggregates can scavenge dissolved Mo from the water column (Dellwig et al., 2007) and sink to the SWI, where the bivalves may ingest those Mo-enriched aggregates leading to an increased incorporation of Mo into the shell material (Thébault et al., 2009a).

Lithium-to-calcium ratios measured in scallop shells (Li/Ca_{shell}) have been proposed as the third potential element chemistry-based proxy for reconstructing diatom bloom dynamics (Thébault and Chauvaud, 2013; Thébault et al., 2022), based on the highly synchronous Li/Ca_{shell} profiles of contemporaneous shells suggesting a common external driver. A key process in the ocean that governs the removal of Li from marine water is the production of biogenic opal (Coplen et al., 2002), the substance composing diatoms frustules. Thus, elevated Li/Ca_{shell} levels may arise from the direct ingestion of Li-containing diatom cells and/or the dissolution of Li-rich frustules at the SWI following large blooms. However, prior to the application of Li/Ca_{shell} as a reliable proxy for phytoplankton dynamics, the effect of shell growth rate needs to be taken into account as it can influence Li/Ca_{shell} levels in bivalve shells (Thébault et al., 2009b).

1.3.2 Other shell-derived proxies

In addition to trace elements, several other shell-based proxies have been explored to gain information about past phytoplankton dynamics. The stable carbon isotope composition of the mineral phase ($CaCO_3$) of the shell ($\delta^{13}C_{shell}$) was initially proposed to reflect the isotopic composition of the dissolved inorganic carbon ($\delta^{13}C_{DIC}$) from the ambient water (Mook and Vogel, 1968). Accordingly, elevated $\delta^{13}C_{shell}$ signals would reflect the timing of increased primary production (Goodwin et al., 2012; Schöne, 2013; Reynolds et al., 2017a; Peharda et al., 2019), because phytoplankton preferentially assimilate the lightest naturally occurring stable isotope of carbon (^{12}C) relative to the heavier isotope (^{13}C), leading to an increased $\delta^{13}C_{DIC}$ signal. However, the carbon incorporated into the shell carbonate not only originates from dissolved inorganic carbon but also of a proportion of metabolically sourced carbon derived from dietary input, which varies seasonally as well as throughout ontogeny (McConnaughey and Gillikin, 2008; Chauvaud et al., 2011; Marchais et al., 2015), thereby complicating the overall interpretation of $\delta^{13}C_{shell}$ signals.

Furthermore, the $\delta^{13}C_{shell}$ signal of the shell-bound organic matter revealed the potential for distinguishing between different carbon sources in coastal ecosystems. For instance, the more depleted C_3-derived terrestrial debris versus the more enriched signatures of marine phytoplankton (O'Donnell et al., 2003). Recently, advances in compound-specific stable isotope analysis have enabled the assessment of carbon isotope composition of individual amino acids (Larsen et al., 2013; Larsen et al., 2020). Because essential amino acids have complex biosynthetic pathways that generate distinct $\delta^{13}C$ 'fingerprints' in different groups of primary producers (e.g., microalgae and bacteria; Larsen et al., 2013), these isotopic signatures can propagate through the food webs mostly unmodified, as animals generally incorporate essential amino acids directly from their diet (Vane et al., 2025). Consequently, the $\delta^{13}C$ fingerprints of essential amino acids in the animal tissues, including carbonate-bound organic matter in bivalve shells, provide a powerful tool to differentiate among primary producers, even between phytoplankton taxa such as diatoms and dinoflagellates (Stahl et al., 2023).

The occurrence and abundance of shell pigments, such as carotenoids, may provide additional information on phytoplankton dynamics, as both the quality and composition of available food can influence shell coloration (Hedegaard et al., 2006). Although research on this subject is extremely limited, Marchais et al. (2017) successfully demonstrated in con-

trolled feeding experiments that the diet affects the shell coloration of mollusks, supporting its potential as a novel yet largely unexplored proxy. However, the substantial diversity of shell colors both across and within mollusk taxa (e.g., Williams, 2017; Grant and Williams, 2018) require further research and calibration to better understand of the relationship between food quality and quantity, pigment uptake and synthesis, and their incorporation into the shell matrix, before shell pigments can be used as dietary indicators, and thus potentially phytoplankton-related proxies.

Variations in growth increment widths in bivalve shells are not only the foundation for crossdating techniques (Butler et al., 2010; Butler et al., 2013; Reynolds et al., 2021), but can also provide information on past environmental conditions. For instance, the rate of shell formation of the long-lived *A. islandica* is mediated by factors such as seawater temperature and food availability, as well as by hydrographic conditions such as seasonal stratification and currents (Witbaard et al., 1999; Schöne et al., 2003; Schöne et al., 2005b). Although food abundance is not the only driver of shell growth, periods associated with broader annual growth increments may be linked with increased food availability, i.e., induced by enhanced primary production, and can thus provide insights into ecological changes through time (Wanamaker et al., 2009; Butler et al., 2013; Reynolds et al., 2022). In fact, research on the siphon activity of *A. islandica* in relation to food supply supported the notion that shell growth is primarily controlled by the availability of food (Ballesta-Artero et al., 2017; Ballesta-Artero et al., 2018). Interestingly, other studies demonstrated that enhanced primary production does not necessarily correspond with increased shell growth rates but can, in fact, have the opposite effect, i.e., slow down or even cessation of shell growth (Lorrain et al., 2000; Chauvaud et al., 2001; Matras et al., 2022). This phenomenon is attributed to exceedingly high algal cell concentrations at the SWI during or after intense phytoplankton blooms, which can clog the gills of the bivalves and consequently disrupt the formation of new shell material.

Finally, a more recent and still relatively unexplored approach involves examining the crystal fabrics of bivalve shells at the scale of individual biomineral units (BMUs) using scanning electron microscopy (e.g., Schöne et al., 2013; Milano et al., 2017). The ultrastructure of shells collected from sites with limited seasonal temperature variability (2 °C) appears to be controlled by food availability (Höche et al., 2022). In such environments, the BMUs may serve as indicators for sub-annual fluctuations in phytoplankton abundance within the water column, providing information on the timing and, to some extent, the magnitude of

phytoplankton blooms. However, the direct use of BMUs for reconstructing phytoplankton dynamics remains limited, as their morphology is primarily governed by temperature (Höche et al., 2022).

1.3.3 Challenges and limitations of phytoplankton proxies from bivalve shells

Although multiple and distinctly different structural and chemical properties have been explored in shells of various bivalves as potential phytoplankton proxies (see above), their application in palaeoecological studies remains limited due to several reasons. (1) The highly variable spatial and temporal patterns of phytoplankton species complicate the interpretation and calibration of shell-derived proxy signals. (2) Physiological processes such as metabolism and filtering activity, which are also externally influenced by temperature, turbidity and nutrient availability, can modify the uptake and incorporation of respective geochemical signals. (3) Resolving geochemical patterns at sub-annual scales can be particularly challenging, especially for long-lived bivalve species that form relatively narrow annual increments, when precise information about the relationship between shell growth rates and timing (i.e., the seasonal growth model) is not fully constrained. (4) Calibration studies remain scarce because they are time-consuming, technically challenging, and often constrained by the difficulty replicating natural environmental conditions in controlled settings. (5) Proxies that have been successfully established in one bivalve species may not be directly transferable to other taxa, given inter-specific differences in physiology as well as habitat characteristics. These complexities highlight the need for calibration and validation studies to fully unlock the potential of bivalve shells as archives for reconstructing photoautotrophic organisms throughout the past.

1.4 *Pecten maximus* – The great scallop

Among various bivalve species that have been examined in sclerochronological studies, shells of the fast-growing and short-lived *P. maximus* (see Box 5) have emerged as a particularly valuable sclerochronological archive, due to their well-characterized physiology and suitability for high-resolution geochemical analyses (see below). As an ecologically and economically important species, notably for commercial fisheries, *P. maximus* has attracted a broad range of scientific interest. The family Pectinidae (scallops) comprises approx. 400 living species, among which *P. maximus* (also known as the great scallop or the king scallop) is one of the best studied species that is mainly distributed along the eastern coast of the North Atlantic (Brand, 2006; Kenny et al., 2020). *P. maximus* typically occurs in shallow waters (i.e., between 20 to 45 m) but can also inhabit deeper regions of almost 200 m depth (Brand, 2006). These bivalves live on the seafloor in shallow depressions within the sediment, with the

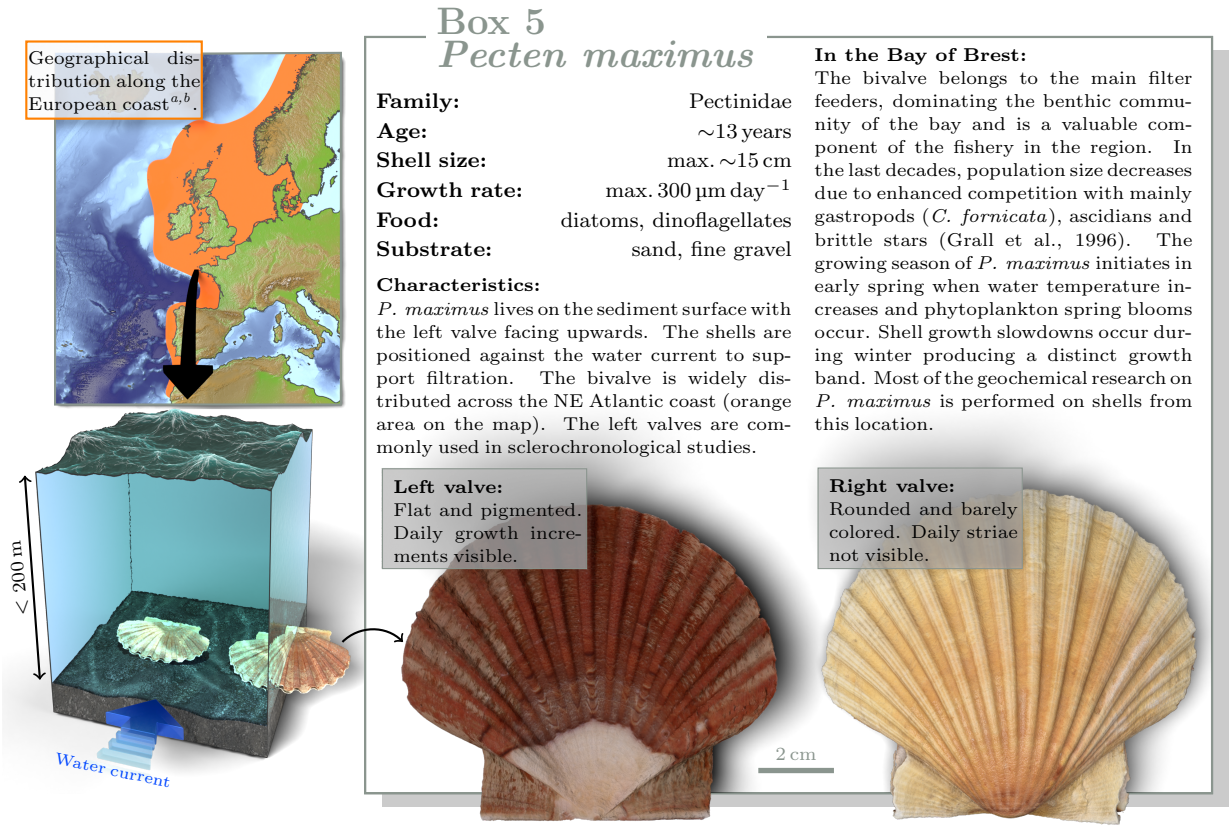

[a]Bathymetric data obtained from GEBCO Compilation Group (2025) GEBCO 2025 Grid [b]Approximated spatial distribution of *P. maximus* based on Brand (2006) and Kenny et al. (2020)

upper (left) valve aligned or slightly below the sediment surface (Baird, 1958; Hartnoll, 1967). When threatened, they can actively swim several meters by rapidly clapping their valves, expelling a water jet near the dorsal hinge to escape predators or unfavorable sediment conditions (Thomas and Gruffydd, 1971; Robson et al., 2012; Guderley and Tremblay, 2016). This swimming behavior is energetically costly and is therefore only used occasionally.

Like many bivalves, scallops feed primarily on small, living algal cells, i.e., mainly diatoms and dinoflagellates (Lorrain et al., 2000; Chauvaud et al., 2001; Lavaud et al., 2014), by filtering particulate matter from the surrounding water. Notably, *P. maximus* is capable of selectively retaining specific food items based on their size and nutritional value (e.g., Beninger et al., 2004; Beninger and Decottignies, 2005) and can actively orient its body in response to prevailing water currents to enhance particle capture and filtration (Hartnoll, 1967; Mathers, 1976). Moreover, their filtration rates are regulated in response to surrounding phytoplankton concentrations, either actively, through physiological regulation, or passively, when high cell densities lead to gill clogging or reduced oxygen availability (Lorrain et al., 2000). In addition, toxic algal blooms have been reported to hamper their filtration efficiency (Chauvaud et al., 2001). Because the deposition of new shell material in bivalves requires open valves and the mantle to be extended (Pannella and MacClintock, 1968), shell growth is disrupted during periods of reduced filtration. Consequently, episodes of intense phytoplankton blooms (particularly those dominated by toxic algae) can disturb the shell growth patterns of *P. maximus*, a phenomenon that has been frequently observed (Chauvaud et al., 1998; Lorrain et al., 2000; Chauvaud et al., 2001).

A remarkable characteristic of *P. maximus* (and other scallops) is the formation of distinct daily growth increments and lines (also known as striae; Roux et al., 1990; Schein et al., 1991; Owen et al., 2002) resulting in fine-scaled records of shell accretion (Antoine, 1978; Chauvaud et al., 1998). These daily growth marks not only allow to accurately associate fluctuations in shell growth rates with environmental changes, such as large phytoplankton blooms that disrupt shell growth, but also provide an ideal sclerochronological foundation for the precise temporal alignment of geochemical data (e.g., Chauvaud et al., 2005; Barats et al., 2009). Unlike the shells of other bivalves, the great scallop possesses two asymmetrical valves (∼15 cm shell length) of which the right, less colored valve is more convex compared to the relatively flat, stronger pigmented left valve. Both valves are composed of foliated calcite (Kennedy et al., 1969; Grefsrud et al., 2008) and are characteristically sculptured with radial ribs and prominent grooves. The daily microgrowth increments are particularly

visible on the shell surface of the left valve, where they appear as overlapping calcite ridges extruding from the outer shell surface. During the second year of growth (also reported as shells of age class 1), *P. maximus* exhibit the highest growth rates (up to 300 µm day^{-1}), after which both the daily growth rate and the number of annual growing days gradually decline (Chauvaud et al., 2012). Thus, geochemical analyses on the shell carbonate of *P. maximus* are typically performed on the shell portions of ontogenetically young specimens (i.e., age class 1), which provide the highest temporal resolution compared to older shell portions.

To precisely assign calendar dates to sampled shell material, a common technique is back-dating from the last visible striae at the ventral margin that corresponds to the date of death, when the specimen was collected alive during the growing period (e.g., Chauvaud et al., 2005; Gillikin et al., 2008). Alternatively, variations in shell growth rates can be cross-matched with known growth patterns of contemporaneous specimens from a similar age class. For historical shell pieces recovered from archeological sites, neither the date of death nor reference shells with known growth patterns are available. In such cases, oxygen isotope analyses of the shell carbonate can be employed to reconstruct past bottom water temperatures (Chauvaud et al., 2005). These reconstructed temperatures can be aligned with a theoretical seasonal temperature curve (e.g., sinusoidal seasonal cycle) to temporally contextualize different shell portions. The daily striae extending from the outer shell surface of *P. maximus* are clearly visible in well-preserved specimens but often become obscured in older shell material, impeding the identification of the daily growth increments and hindering the sub-annual alignment of geochemical samples. To overcome this limitation in (sub)fossil scallops, strontium-to-calcium ratios can be employed as a potential proxy for calcification rate, allowing to approximate daily variations of shell growth (Lorrain et al., 2005). The possibility of performing geochemical analyses with high temporal resolution, coupled with the precise alignment of data at sub-annual scales, promotes shells of *P. maximus* as highly valuable biogenic archives that are especially suited for reconstructing short-term environmental variabilities, such as phytoplankton dynamics.

As outlined in section 1.3.1, specific trace element impurities in bivalve shells are hypothesized to be indicative of the phytoplankton dynamics in the ambient water. To explore the potential of these proxies and better constrain the underlying mechanisms, several studies have combined the sclerochronological advantages of *P. maximus* shells with trace element analyses to produce highly resolved and accurately dated Ba/Ca_{shell}, Mo/Ca_{shell} and

Li/Ca_{shell} profiles (Barats et al., 2007; Gillikin et al., 2008; Barats et al., 2009; Barats et al., 2010; Thébault and Chauvaud, 2013). All studies have reported trace element profiles characterized by flat background signals interrupted by distinct peaks. These patterns were highly synchronous across individuals and years and, in the case of Ba/Ca_{shell}, closely resembled geochemical chronologies observed in other bivalve species (see section 1.3.1). Demonstrably, the timing and magnitude of the peaks vary considerably from year to year indicating that the underlying environmental drivers (hypothesized trace element uptake mechanisms presented in Box 6) shaping these geochemical patterns also change annually. For example, Ba/Ca_{shell} peaks have been related to complex benthic-pelagic interaction processes at the SWI following summer phytoplankton bloom conditions (Barats et al., 2009), while peaks in the Mo/Ca_{shell} profiles have been associated with diatom spring bloom dynamics (Barats et al., 2010). Similarly, elevated Li/Ca_{shell} ratios are potentially attributed to the ingestion and subsequent dissolution of diatom frustules by the scallops (Thébault and Chauvaud, 2013). Although these sub-seasonal trace element chronologies derived from *P. maximus* shells provide an ideal temporal resolution for calibrating respective proxies, consistent patterns between environmental signals and geochemical records remain yet to be conclusively identified. This underscores the complexity of the processes governing the formation of trace element peaks and highlights the need for further calibration work.

Box 6
Uptake hypotheses

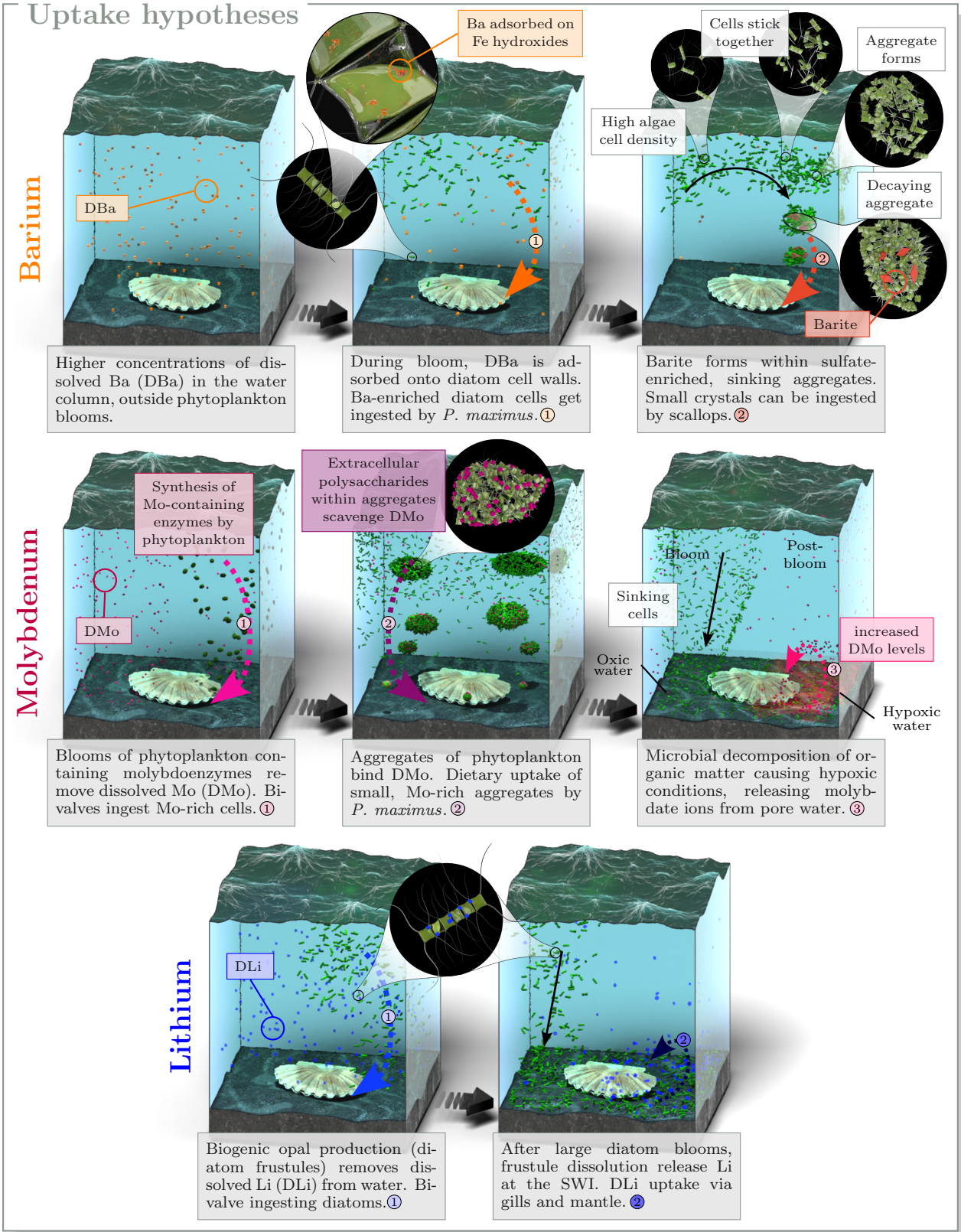

1.5 The Bay of Brest – A natural laboratory

To reliably calibrate geochemical signals derived from bivalve shells, a thorough understanding of the physical environment in which the organism lived is crucial. In the case of primary production proxies, such as trace element compositions of *P. maximus* shells (see above), the Bay of Brest in northwest France represents an ideal study site. The bay hosts a naturally abundant population of *P. maximus*, which represents a significant resource for regional commercial fisheries (e.g., Gourault et al., 2019). It is a shallow (approx. 8 to 15 m depth), semi-enclosed coastal ecosystem covering about 180 km^2, connected to the northeastern Atlantic through a narrow opening of about 2 km to the Iroise Sea. Its hydrology is influenced by the two main rivers, Aulne and Élorn, which together account for about 80% of the freshwater inputs and affect the seasonal variability of nutrients and primary production (e.g., Queguiner and Tréguer, 1984; Del Amo et al., 1997a; Labry et al., 2016). The water column is well-mixed due to strong tidal currents and exhibits pronounced seasonal successions of phytoplankton blooms and communities (e.g., Ragueneau et al., 1994; Le Pape and Menesguen, 1997).

Diatoms generally represent the most abundant phytoplankton taxa in the bay, with large spring blooms fueled by high levels of silicic acid and other nutrients (e.g., Del Amo et al., 1997a). These early blooms rapidly deplete nutrient stocks, leading to the subsequent collapse of the spring blooms. Under decreased nutrient conditions, secondary blooms emerge, consisting of both silicified taxa like diatoms and non-siliceous species such as dinoflagellates (Del Amo et al., 1997a; Del Amo et al., 1997b). While silicon and phosphate are typically the limiting nutrients for primary production until autumn, later phytoplankton blooms are constrained by the availability of nitrogen (Del Amo et al., 1997a). In addition to nutrient levels, the initiation of phytoplankton blooms in the Bay of Brest also depends on the water temperature (i.e., above 10 °C) as well as the light availability governed by water turbidity and solar radiation (Poppeschi et al., 2022). The substantial inter-annual variability in the phytoplankton community composition and phenology (see the seemingly chaotic abundance and annual patterns of four dominating phytoplankton groups at the study site presented in Box 1 to 4), reflects the underlying complexity of the primary producer dynamics in the Bay of Brest. Following large phytoplankton blooms, stressful conditions (i.e., nutrient limitations, hydrographic shifts, temperature and light conditions) can induce the phytoplankton cells to stick together and form rapidly sinking aggregates. Such events frequently occur in

the Bay of Brest and have been shown to alter biogeochemical cycles (Siebert et al., 2024) as well as the filtration activity of benthic organisms (e.g., Lorrain et al., 2000).

The benthic community in the bay is largely dominated (97% of suspension feeder biomass) by the filter feeding slipper limpet, *C. fornicata*, an invasive gastropod species that was introduced into the Bay of Brest in 1949 (e.g., Ragueneau et al., 2018). During spring blooms, this species trap silica-containing diatom frustules in its pseudo-feces, acting as a 'silicic acid pump' that retains silicon within the bay and limits its export into the Atlantic (Del Amo et al., 1997b; Chauvaud et al., 2000; Ragueneau et al., 2002; Ragueneau et al., 2005). Elevated temperatures and bacterial activity in late spring and summer favor the dissolution and recycling of the retained biogenic silica, providing essential nutrients for the development of secondary diatom blooms (Chauvaud et al., 2000). However, the proliferation of *C. fornicata* in the Bay of Brest has negative ecological consequences on local species like *P. maximus*, e.g., by competing for space with the bivalves (e.g., Ragueneau et al., 2018).

The Bay of Brest serves as a natural laboratory considering its relatively long history of environmental monitoring with a strong research focus on marine biodiversity and ecosystem functioning. Phytoplankton dynamics, for example, have been recorded and extensively studied for more than two decades through the SOMLIT-Brest monitoring program. Furthermore, nearly all geochemical analyses on *P. maximus* have been performed on shells obtained from this ecosystem (see section 1.4). Likewise, most of the work presented herein (Chapter 2, 3 and 4) is based on shells of live-collected *P. maximus* specimens from Lanvéoc, located in the southern part of the bay. These data were generated as part of the HIPPO (HIgh-resolution Primary Production multi-prOxy archives) program and, together with detailed information on environmental variables (e.g., nutrients, water chemistry, organic matter, phytoplankton dynamics). All datasets are archived in open-access repositories and are publicly available (see details in Siebert et al., 2023). This extensive and interdisciplinary dataset promotes the Bay of Brest as an ideal platform for future comparative and synthesis studies across various research disciplines.

1.6 Research objectives and motivations

This work focuses on the calibration, development and refinement of geochemical proxies and sclerochronological techniques that are essential for reconstructing past phytoplankton dynamics. Specifically, the present thesis pursued the following main objectives:

1. Understanding the variations of Ba/Ca, Mo/Ca and Li/Ca ratios in *P. maximus* shells in the context of environmental variables and bulk primary production.
2. Establishing a methodological framework to statistically evaluate potential links between high-resolution trace element variations and blooms of specific phytoplankton species.
3. Identification of previously unresolved patterns linking geochemistry with environmental data that can sufficiently explain observed geochemical variations in the shells.
4. Refining existing hypotheses to gain a better understanding of the transfer pathways of trace elements from the water column to the shell.
5. Evaluating to which extent trace element variations can serve as quantitative proxies.
6. Assessing the influence of specimen-specific physiological parameters on the inter-specimen reproducibility of geochemical profiles.
7. Testing and improving temporal alignment methods of geochemical samples to facilitate the extraction of high-resolution profiles necessary for phytoplankton dynamics reconstructions.

In the general introduction (**Chapter 1**), the scientific setting of the work was outlined, highlighting the vast complexity of phytoplankton in marine ecosystems. Further, major challenges involved in the reconstruction of past primary producer dynamics were described, presenting bivalve shells as valuable proxy archives for paleoenvironmental reconstructions. Among various geochemical proxies, the Ba/Ca_{shell} ratio was identified as a particularly promising indicator related to phytoplankton dynamics. However, the exact relationship between the respective trace element and phytoplankton biomass remains unclear.

Accordingly, **Chapter 2** addresses this knowledge gap by examining the seasonal variability of Ba/Ca_{shell} ratios from *P. maximus* shells alongside concurrent phytoplankton dynamics

from two years. This includes detailed information on both bulk primary producer biomass and the phenology of major taxonomic groups of diatoms and dinoflagellates. Furthermore, a pseudo-random sampling method is applied to statistically disentangle how Ba/Ca_{shell} signals respond to the abundance of individual phytoplankton species and their combinations, providing a more refined interpretation of the link between environmental signals and shell chemistry.

Chapter 3 builds upon the findings of the previous chapter and the contemporaneous study by Thébault et al. (2022) by extending the analysis to Ba/Ca, Mo/Ca and Li/Ca profiles measured in *P. maximus* shells from three different years. By refining the statistical framework presented in Chapter 2, the patterns in the time-series of the three trace elements are related to the key phytoplankton species monitored at the sampling site. Particular attention is given to potential time lags between environmental signals and geochemical responses as well as species-specific differences in trace element contents associated with the various phytoplankton taxa.

Although the variations of Ba/Ca_{shell}, Mo/Ca_{shell} and Li/Ca_{shell} profiles could be qualitatively related to the timing and magnitude of species-specific phytoplankton blooms, uncertainties remain regarding the quantities the phytoplankton cells contribute to the measured shell chemistry, and which pathways are involved. Therefore, **Chapter 4** addresses these uncertainties by exploring the element cycling of Ba and Mo within the water column in relation to phytoplankton dynamics and their incorporation into the shell chemistry of *P. maximus*. In order to evaluate if the proposed uptake mechanisms are adequately constrained by variations of phytoplankton blooms within the water column, trace element chronologies from scallops living naturally on the sediment floor are compared with those from contemporaneous specimens deployed in a cage above the SWI. Then, a model is employed to estimate whether the proposed uptake mechanisms sufficiently explain the observed trace element profiles in the shells of *P. maximus*. Finally, inter-specimen variability in shell chemistry is contextualized with respective physiological characteristics of the analyzed bivalves to better understand their potential influence on the trace element incorporation into the shell carbonate.

Chapter 5 shifts the focus from high-resolution trace element profiles in *P. maximus* shells to lower-resolved chronologies, with the objective of developing a theoretical framework for a more precise temporal alignment of geochemical samples. This is particularly relevant for bivalve species that exhibit slow growth and limited sub-annual growth marks

that facilitate the temporal alignment of geochemical data, such as the daily striae in scallops (see section 1.4). By generating digital shell models filled with synthetic environmental data, Chapter 5 systematically examines different sampling strategies and traditional alignment methods and introduced a novel technique that increases the accuracy of proxy-based environmental reconstructions. This study aims to provide a methodological foundation for employing trace element proxies such as Ba/Ca_{shell} ratios in shells with lower temporal resolution, thereby extending their potential for reconstructing phytoplankton dynamics on seasonal scales.

Finally, **Chapter 6** summarizes the main findings of this work and their broader implications for past phytoplankton reconstructions from trace element profiles measured in bivalve shells. Further, remaining uncertainties and limitations of the research are briefly described and contextualized with future perspectives.

References

Agbaje, O. B. A., Thomas, D. E., McInerney, B. V., Molloy, M. P., Jacob, D. E., 2017. Organic macromolecules in shells of *Arctica islandica*: Comparison with nacroprismatic bivalve shells. Marine Biology 164, 208.

Alldredge, A. L., Gotschalk, C. C., 1989. Direct observations of the mass flocculation of diatom blooms: Characteristics, settling velocities and formation of diatom aggregates. Deep Sea Research Part A, Oceanographic Research Papers 36, 159–171.

Alpine, A. E., Cloern, J. E., 1992. Trophic interactions and direct physical effects control phytoplankton biomass and production in an estuary. Limnology and Oceanography 37, 946–955.

Antoine, L., 1978. La croissance journalière chez *Pecten maximus* (L.)(Pectinidae, Bivalvia). Haliotis 9, 627–636.

Averyt, K. B., Paytan, A., 2004. A comparison of multiple proxies for export production in the equatorial Pacific. Paleoceanography 19, PA4003.

Baird, R. H., 1958. On the swimming behaviour of escallops (*Pecten maximus* L.) Journal of Molluscan Studies 33, 67–71.

Ballesta-Artero, I., Janssen, R., van der Meer, J., Witbaard, R., 2018. Interactive effects of temperature and food availability on the growth of *Arctica islandica* (Bivalvia) juveniles. Marine Environmental Research 133, 67–77.

Ballesta-Artero, I., Witbaard, R., Carroll, M. L., van der Meer, J., 2017. Environmental factors regulating gaping activity of the bivalve *Arctica islandica* in Northern Norway. Marine Biology 164, 116.

Barats, A., Amouroux, D., Chauvaud, L., Pécheyran, C., Lorrain, A., Thébault, J., Church, T. M., Donard, O. F., 2009. High frequency barium profiles in shells of the great scallop *Pecten maximus*: A methodical long-term and multi-site survey in Western Europe. Biogeosciences 6, 157–170.

Barats, A., Amouroux, D., Pécheyran, C., Chauvaud, L., Thébault, J., Donard, O. F. X., 2010. Spring molybdenum enrichment in scallop shells: A potential tracer of diatom productivity in temperate coastal environments (Brittany, NW France). Biogeosciences 7, 233–245.

Barats, A., Pécheyran, C., Amouroux, D., Dubascoux, S., Chauvaud, L., Donard, O. F. X., 2007. Matrix-matched quantitative analysis of trace-elements in calcium carbonate shells by laser-ablation ICP-MS: Application to the determination of daily scale profiles in scallop shell (*Pecten maximus*). Analytical and Bioanalytical Chemistry 387, 1131–1140.

Barbier, E. B., Hacker, S. D., Kennedy, C., Koch, E. W., Stier, A. C., Silliman, B. R., 2011. The value of estuarine and coastal ecosystem services. Ecological Monographs 81, 169–193.

Barrat, J. A., Chauvaud, L., Olivier, F., Poitevin, P., Rouget, M. L., 2023. Trace elements in bivalve shells: How 'vital effects' can bias environmental studies. Chemical Geology 638, 121695.

Barrenechea Angeles, I., Lejzerowicz, F., Cordier, T., Scheplitz, J., Kucera, M., Ariztegui, D., Pawlowski, J., Morard, R., 2020. Planktonic foraminifera eDNA signature deposited on the seafloor remains preserved after burial in marine sediments. Scientific Reports 10, 20351.

Bates, S. S., Hubbard, K. A., Lundholm, N., Montresor, M., Leaw, C. P., 2018. *Pseudo-nitzschia*, *Nitzschia*, and domoic acid: New research since 2011. Harmful Algae 79, 3–43.

Beman, J. M., Arrigo, K. R., Matson, P. A., 2005. Agricultural runoff fuels large phytoplankton blooms in vulnerable areas of the ocean. Nature 434, 211–214.

Benincá, E., Huisman, J., Heerkloss, R., Jöhnk, K. D., Branco, P., Van Nes, E. H., Scheffer, M., Ellner, S. P., 2008. Chaos in a long-term experiment with a plankton community. Nature 451, 822–825.

Beninger, P. G., Decottignies, P., 2005. What makes diatoms attractive for suspensivores? The organic casing and associated organic molecules of *Coscinodiscus perforatus* are quality cues for the bivalve *Pecten maximus*. Journal of Plankton Research 27, 11–17.

Beninger, P. G., Decottignies, P., Rincé, Y., 2004. Localization of qualitative particle selection sites in the heterorhabdic filibranch *Pecten maximus* (Bivalvia: Pectinidae). Marine Ecology Progress Series 275, 163–173.

Bidle, K. D., Falkowski, P. G., 2004. Cell death in planktonic, photosynthetic microorganisms. Nature Reviews Microbiology 2, 643–655.

Bishop, J. K. B., 1988. The barite-opal-organic carbon association in oceanic particulate matter. Nature 332, 341–343.

Bjorndahl, J. A., Gushulak, C. A. C., Mezzini, S., Simpson, G. L., Haig, H. A., Leavitt, P. R., Finlay, K., 2022. Abrupt changes in the physical and biological structure of endorheic upland lakes due to 8-m lake-level variation during the 20th century. Limnology and Oceanography 67, 1022–1039.

Blondeau-Patissier, D., Gower, J. F. R., Dekker, A. G., Phinn, S. R., Brando, V. E., 2014. A review of ocean color remote sensing methods and statistical techniques for the detection, mapping and analysis of phytoplankton blooms in coastal and open oceans. Progress in Oceanography 123, 123–144.

Boehm, A. B., Ismail, N. S., Sassoubre, L. M., Andruszkiewicz, E. A., 2017. Oceans in peril: Grand challenges in applied water quality research for the 21st century. Environmental Engineering Science 34, 3–15.

Bøggild, O. B., 1930. The shell structure of the mollusks. Det Kongelige Danske Videnskabernes Selskabs Skrifter. Naturvidenskabelig og Mathematisk Afdeling, Raekke 9 2, 231–326.

Böll, A., Lückge, A., Munz, P., Forke, S., Schulz, H., Ramaswamy, V., Rixen, T., Gaye, B., Emeis, K. C., 2014. Late Holocene primary productivity and sea surface temperature variations in the northeastern Arabian Sea: Implications for winter monsoon variability. Paleoceanography 29, 778–794.

Boltovskoy, D., 1994. The sedimentary record of pelagic biogeography. Progress in Oceanography 34, 135–160.

Bopp, L., Resplandy, L., Orr, J. C., Doney, S. C., Dunne, J. P., Gehlen, M., Halloran, P., Heinze, C., Ilyina, T., Séférian, R., Tjiputra, J., Vichi, M., 2013. Multiple stressors of ocean ecosystems in the 21st century: Projections with CMIP5 models. Biogeosciences 10, 6225–6245.

Brand, A. R., 2006. Scallop ecology: Distributions and behaviour. Developments in Aquaculture and Fisheries Science 35, 651–744.

Butler, P. G., Richardson, C. A., Scourse, J. D., Wanamaker, A. D., Shammon, T. M., Bennell, J. D., 2010. Marine climate in the Irish Sea: Analysis of a 489-year marine master chronology derived from growth increments in the shell of the clam *Arctica islandica*. Quaternary Science Reviews 29, 1614–1632.

Butler, P. G., Wanamaker, A. D., Scourse, J. D., Richardson, C. A., Reynolds, D. J., 2013. Variability of marine climate on the North Icelandic Shelf in a 1357-year proxy archive based on growth increments in the bivalve *Arctica islandica*. Paleogeography, Palaeoclimatology, Palaeoecology 373, 141–151.

Cadée, G. C., Hegeman, J., 2002. Phytoplankton in the Marsdiep at the end of the 20th century; 30 years monitoring biomass, primary production, and *Phaeocystis* blooms. Journal of Sea Research 48, 97–110.

Carré, M., Bentaleb, I., Bruguier, O., Ordinola, E., Barrett, N. T., Fontugne, M., 2006. Calcification rate influence on trace element concentrations in aragonitic bivalve shells: Evidences and mechanisms. Geochimica et Cosmochimica Acta 70, 4906–4920.

Carriker, M. R., Palmer, R. E., Sick, L. V., Johnson, C. C., 1980. Interaction of mineral elements in sea water and shell of oysters (*Crassostrea virginica* (Gmelin)) cultured in controlled and natural systems. Journal of Experimental Marine Biology and Ecology 46, 279–296.

Carstensen, J., Klais, R., Cloern, J. E., 2015. Phytoplankton blooms in estuarine and coastal waters: Seasonal patterns and key species. Estuarine, Coastal and Shelf Science 162, 98–109.

Cavan, E. L., Belcher, A., Atkinson, A., Hill, S. L., Kawaguchi, S., McCormack, S., Meyer, B., Nicol, S., Ratnarajah, L., Schmidt, K., Steinberg, D. K., Tarling, G. A., Boyd, P. W., 2019. The importance of Antarctic krill in biogeochemical cycles. Nature Communications 10, 4742.

Chaillou, G., Anschutz, P., Lavaux, G., Schäfer, J., Blanc, G., 2002. The distribution of Mo, U, and Cd in relation to major redox species in muddy sediments of the Bay of Biscay. Marine Chemistry 80, 41–59.

Chauvaud, L., Donval, A., Thouzeau, G., Paulet, Y. M., Nézan, E., 2001. Variations in food intake of *Pecten maximus* (L.) from the Bay of Brest (France): Influence of environmental factors and phytoplankton species composition. Comptes Rendus de l'Académie des Sciences - Series III - Sciences de la Vie 324, 743–755.

Chauvaud, L., Jean, F., Ragueneau, O., Thouzeau, G., 2000. Long-term variation of the Bay of Brest ecosystem: Benthic-pelagic coupling revisited. Marine Ecology Progress Series 200, 35–48.

Chauvaud, L., Lorrain, A., Dunbar, R. B., Paulet, Y. M., Thouzeau, G., Jean, F., Guarini, J. M., Mucciarone, D., 2005. Shell of the great scallop *Pecten maximus* as a high-frequency archive of paleoenvironmental changes. Geochemistry, Geophysics, Geosystems 6, Q08001.

Chauvaud, L., Patry, Y., Jolivet, A., Cam, E., Le Goff, C., Strand, Ø., Charrier, G., Thébault, J., Lazure, P., Gotthard, K., Clavier, J., 2012. Variation in size and growth of the great scallop *Pecten maximus* along a latitudinal gradient. PLoS ONE 7, e37717.

Chauvaud, L., Thébault, J., Clavier, J., Lorrain, A., Strand, Ø., 2011. What's hiding behind ontogenetic δ^{13}C variations in mollusk shells? New insights from the great scallop (*Pecten maximus*). Estuaries and Coasts 34, 211–220.

Chauvaud, L., Thouzeau, G., Paulet, Y. M., 1998. Effects of environmental factors on the daily growth rate of *Pecten maximus* juveniles in the Bay of Brest (France). Journal of Experimental Marine Biology and Ecology 227, 83–111.

Claquin, P., Longphuirt, S. N., Fouillaron, P., Huonnic, P., Ragueneau, O., Klein, C., Leynaert, A., 2010. Effects of simulated benthic fluxes on phytoplankton dynamic and photo-

synthetic parameters in a mesocosm experiment (Bay of Brest, France). Estuarine, Coastal and Shelf Science 86, 93–101.

Clark, S., Hubbard, K. A., Anderson, D. M., McGillicuddy Jr., D. J., Ralston, D. K., Townsend, D. W., 2019. *Pseudo-nitzschia* bloom dynamics in the Gulf of Maine: 2012-2016. Harmful Algae 101656, 88.

Cloern, J. E., 2001. Our evolving conceptual model of the coastal eutrophication problem. Marine Ecology Progress Series 210, 223–253.

Cloern, J. E., 1982. Does the benthos control phytoplankton biomass in South San Francisco Bay? Marine Ecology Progress Series 9, 191–202.

Cloern, J. E., Jassby, A. D., 2010. Patterns and scales of phytoplankton variability in estuarine-coastal ecosystems. Estuaries and Coasts 33, 230–241.

Collier, R. W., 1985. Molybdenum in the Northeast Pacific Ocean. Limnology and Oceanography 30, 1351–1354.

Coplen, T. B., Böhlke, J. K., De Bièvre, P., Ding, T., Holden, N. E., Hopple, J. A., Krouse, H. R., Lamberty, A., Peiser, H. S., Révész, K., Rieder, S. E., Rosman, K. J. R., Roth, E., Taylor, P. D. P., Vocke, R. D., Xiao, Y. K., 2002. Isotope-abundance variations of selected elements (IUPAC Technical Report). Pure and Applied Chemistry 74, 1987–2017.

de Vargas, C., Audic, S., Henry, N., Decelle, J., Mahé, F., Logares, R., Lara, E., Berney, Ć., Le Bescot, N., Probert, I., Carmichael, M., Poulain, J., Romac, S., Colin, S., Aury, J. M., Bittner, L., Chaffron, S., Dunthorn, M., Engelen, S., Flegontova, O., Guidi, L., Horák, A., Jaillon, O., Lima-Mendez, G., Lukeš, J., Malviya, S., Morard, R., Mulot, M., Scalco, E., Siano, R., Vincent, F., Zingone, A., Dimier, C., Picheral, M., Searson, S., Kandels-Lewis, S., Acinas, S. G., Bork, P., Bowler, C., Gorsky, G., Grimsley, N., Hingamp, P., Iudicone, D., Not, F., Ogata, H., Pesant, S., Raes, J., Sieracki, M. E., Speich, S., Stemmann, L., Sunagawa, S., Weissenbach, J., Wincker, P., Karsenti, E., 2015. Ocean plankton. Eukaryotic plankton diversity in the sunlit ocean. Science 348, 1261605.

Dehairs, F., Chesselet, R., Jedwab, J., 1980. Discrete suspended particles of barite and the barium cycle in the open ocean. Earth and Planetary Science Letters 49, 528–550.

Del Amo, Y., Le Pape, O., Tréguer, P., Quéguiner, B., Ménesguen, A., Aminot, A., 1997a. Impacts of high-nitrate freshwater inputs on macrotidal ecosystems. I. Seasonal evolution of nutrient limitation for the diatom-dominated phytoplankton of the Bay of Brest (France). Marine Ecology Progress Series 161, 213–241.

Del Amo, Y., Quéguiner, B., Tréguer, P., Breton, H., Lampert, L., 1997b. Impacts of high-nitrate freshwater inputs on macrotidal ecosystems. II. Specific role of the silicic acid pump in the year-round dominance of diatoms in the Bay of Brest (France). Marine Ecology Progress Series 161, 225–237.

Dellwig, O., Beck, M., Lemke, A., Lunau, M., Kolditz, K., Schnetger, B., Brumsack, H. J., 2007. Non-conservative behaviour of molybdenum in coastal waters: Coupling geochemical, biological, and sedimentological processes. Geochimica et Cosmochimica Acta 71, 2745–2761.

Diaz, R. J., Rosenberg, R., 2008. Spreading dead zones and consequences for marine ecosystems. Science 321, 926–929.

Doré, J., Chaillou, G., Poitevin, P., Lazure, P., Poirier, A., Chauvaud, L., Archambault, P., Thébault, J., 2020. Assessment of Ba/Ca in *Arctica islandica* shells as a proxy for phytoplankton dynamics in the Northwestern Atlantic Ocean. Estuarine, Coastal and Shelf Science 237, 106628.

Dromgoole, E. L., Walter, L. M., 1990. Inhibition of calcite growth rates by Mn^{2+} in $CaC1_2$ solutions at 10, 25, and 50°C. Geochimica et Cosmochimica Acta 54, 2991–3000.

Dutkiewicz, S., Morris, J. J., Follows, M. J., Scott, J., Levitan, O., Dyhrman, S. T., Berman-Frank, I., 2015. Impact of ocean acidification on the structure of future phytoplankton communities. Nature Climate Change 5, 1002–1006.

Edwards, K. F., Thomas, M. K., Klausmeier, C. A., Litchman, E., 2012. Allometric scaling and taxonomic variation in nutrient utilization traits and maximum growth rate of phytoplankton. Limnology and Oceanography 57, 554–566.

Edwards, M., Richardson, A. J., 2004. Impact of climate change on marine pelagic phenology and trophic mismatch. Nature 430, 881–884.

Evans, J. W., 1972. Tidal growth increments in the cockle *Clinocardium nuttalli*. Science 176, 416–417.

Falkowski, P., 2012. Ocean Science: The power of plankton. Nature 483, S17–S20.

Fernández-González, C., Tarran, G. A., Schuback, N., Woodward, E. M. S., Arístegui, J., Marañón, E., 2022. Phytoplankton responses to changing temperature and nutrient availability are consistent across the tropical and subtropical Atlantic. Communications Biology 5, 1035.

Field, C. B., Behrenfeld, M. J., Randerson, J. T., Falkowski, P., 1998. Primary production of the biosphere: Integrating terrestrial and oceanic components. Science 281, 237–240.

Finkel, Z. V., Beardall, J., Flynn, K. J., Quigg, A., Rees, T. A. V., Raven, J. A., 2010. Phytoplankton in a changing world: Cell size and elemental stoichiometry. Journal of Plankton Research 32, 119–137.

Fisher, N. S., Guillard, R. R. L., Bankston, D. C., 1991. The accumulation of barium by marine phytoplankton grown in culture. Journal of Marine Research 49, 339–354.

Fortunato, H., 2015. Mollusks: Tools in environmental and climate research. American Malacological Bulletin 33, 310–324.

Foster, L. C., Finch, A. A., Allison, N., Andersson, C., Clarke, L. J., 2008. Mg in aragonitic bivalve shells: Seasonal variations and mode of incorporation in *Arctica islandica*. Chemical Geology 254, 113–119.

Geider, R. J., Delucia, E. H., Falkowski, P. G., Finzi, A. C., Grime, J. P., Grace, J., Kana, T. M., La Roche, J., Long, S. P., Osborne, B. A., Platt, T., Prentice, I. C., Raven, J. A., Schlesinger, W. H., Smetacek, V., Stuart, V., Sathyendranath, S., Thomas, R. B., Vogelmann, T. C., Williams, P., Woodward, F. I., 2001. Primary productivity of planet earth: Biological determinants and physical constraints in terrestrial and aquatic habitats. Global Change Biology 7, 849–882.

Gillikin, D. P., Dehairs, F., Lorrain, A., Steenmans, D., Baeyens, W., André, L., 2006. Barium uptake into the shells of the common mussel (*Mytilus edulis*) and the potential for estuarine paleo-chemistry reconstruction. Geochimica et Cosmochimica Acta 70, 395–407.

Gillikin, D. P., Lorrain, A., Paulet, Y. M., André, L., Dehairs, F., 2008. Synchronous barium peaks in high-resolution profiles of calcite and aragonite marine bivalve shells. Geo-Marine Letters 28, 351–358.

Glynn, D. S., McMahon, K. W., Guilderson, T. P., McCarthy, M. D., 2019. Major shifts in nutrient and phytoplankton dynamics in the North Pacific Subtropical Gyre over the last 5000 years revealed by high-resolution proteinaceous deep-sea coral δ^{15}N and δ^{13}C records. Earth and Planetary Science Letters 515, 145–153.

Gobler, C. J., 2020. Climate change and harmful algal blooms: Insights and perspective. Harmful Algae 91, 101731.

Goodwin, D. H., Gillikin, D. P., Roopnarine, P. D., 2012. Preliminary evaluation of potential stable isotope and trace element productivity proxies in the oyster *Crassostrea gigas*. Palaeogeography, Palaeoclimatology, Palaeoecology 373, 88–97.

Gourault, M., Lavaud, R., Leynaert, A., Pecquerie, L., Paulet, Y. M., Pouvreau, S., 2019. New insights into the reproductive cycle of two great scallop populations in Brittany (France) using a DEB modelling approach. Journal of Sea Research 143, 207–221.

Grall, J., Chauvaud, L., Thouzeau, G., Fifas, S., Glémarec, M., Paulet, Y. M., 1996. Distribution of *Pecten maximus* and its main potential competitors and predators in the Bay of Brest. Comptes Rendus de l'Académie des Sciences - Series III - Sciences de la Vie 319, 931–937.

Grant, H. E., Williams, S. T., 2018. Phylogenetic distribution of shell colour in Bivalvia (Mollusca). Biological Journal of the Linnean Society 125, 377–391.

Grefsrud, E. S., Dauphin, Y., Cuif, J. P., Denis, A., Strand, Ø., 2008. Modifications in microstructure of cultured and wild scallop shells (*Pecten maximus*). Journal of Shellfish Research 27, 633–641.

Guderley, H. E., Tremblay, I., 2016. Swimming in scallops. Developments in Aquaculture and Fisheries Science 40, 535–566.

Guiry, M. D., Guiry, G. M., 2024. *AlgaeBase*. World-wide electronic publication. National University of Ireland, Galway, https://www.algaebase.org, searched on 05 September 2025.

Gutiérrez, D., Sifeddine, A., Field, D. B., Ortlieb, L., Vargas, G., Chávez, F. P., Velazco, F., Ferreira, V., Tapia, P., Salvatteci, R., Boucher, H., Morales, M. C., Valdés, J., Reyss, J. L., Campusano, A., Boussafir, M., Mandeng-Yogo, M., García, M., Baumgartner, T., 2009. Rapid reorganization in ocean biogeochemistry off Peru towards the end of the Little Ice Age. Biogeosciences 6, 835–848.

Gutiérrez, J. L., Jones, C. G., Strayer, D. L., Iribarne, O. O., 2003. Mollusks as ecosystem engineers: the role of shell production in aquatic habitats. Oikos 101, 79–90.

Halfar, J., Steneck, R. S., Joachimski, M., Kronz, A., Wanamaker, A. D., 2008. Coralline red algae as high-resolution climate recorders. Geology 36, 463–466.

Hansen, P. J., 2011. The role of photosynthesis and food uptake for the growth of marine mixotrophic dinoflagellates. Journal of Eukaryotic Microbiology 58, 203–214.

Harley, C. D., Randall Hughes, A., Hultgren, K. M., Miner, B. G., Sorte, C. J. B., Thornber, C. S., Rodriguez, L. F., Tomanek, L., Williams, S. L., 2006. The impacts of climate change in coastal marine systems. Ecology Letters 9, 228–241.

Hartnoll, R. G., 1967. An investigation of the movement of the scallop, *Pecten maximus*. Helgoländer wissenschaftliche Meeresuntersuchungen 15, 523–533.

Hawkins, A. J. S., Pascoe, P. L., Parry, H., Brinsley, M., Cacciatore, F., Black, K. D., Fang, J. G., Jiao, H., McGonigle, C., Moore, H., O'Boyle, N., O'Carroll, T., O'Loan, B., Service, M., Smaal, A. C., Yan, X., Zhang, J. H., Zhang, X. L., Zhu, M. Y., 2013. Comparative feeding on chlorophyll-rich versus remaining organic matter in bivalve shellfish. Journal of Shellfish Research 32, 883–897.

He, Q., Silliman, B. R., 2019. Climate change, human impacts, and coastal ecosystems in the Anthropocene. Current Biology 29, R1021–R1035.

Hedegaard, C., Bardeau, J. F., Chateigner, D., 2006. Molluscan shell pigments: An in situ resonance Raman study. Journal of Molluscan Studies 72, 157–162.

Hillebrand, H., Acevedo-Trejos, E., Moorthi, S. D., Ryabov, A., Striebel, M., Thomas, P. K., Schneider, M. L., 2022. Cell size as driver and sentinel of phytoplankton community structure and functioning. Functional Ecology 36, 276–293.

Höche, N., Walliser, E. O., Schöne, B. R., 2022. Microstructural mapping of *Arctica islandica* shells reveals environmental and physiological controls on biomineral size. Frontiers in Earth Science 9, 781305.

Hodell, D., Lourens, L., Crowhurst, S., Konijnendijk, T., Tjallingii, R., Jiménez-Espejo, F., Skinner, L., Tzedakis, P. C., Abrantes, F., Acton, G. D., Zarikian, C. A. A., Bahr, A., Balestra, B., Barranco, E. L., Carrara, G., Ducassou, E., Flood, R. D., Flores, J. A., Furota, S., Grimalt, J., Grunert, P., Hernández-Molina, J., Kim, J. K., Krissek, L. A., Kuroda, J., Li, B., Lofi, J., Margari, V., Martrat, B., Miller, M. D., Nanayama, F., Nishida, N., Richter, C., Rodrigues, T., Rodríguez-Tovar, F. J., Roque, A. C. F., Goñi, M. F. S., Sánchez, F. J. S., Singh, A. D., Sloss, C. R., Stow, D. A. V., Takashimizu, Y., Tzanova, A., Voelker, A., Xuan, C., Williams, T., 2015. A reference time scale for Site U1385 (Shackleton Site) on the SW Iberian Margin. Global and Planetary Change 133, 49–64.

Husson, B., Hernández-Fariñas, T., Le Gendre, R., Schapira, M., Chapelle, A., 2016. Two decades of *Pseudo-nitzschia* spp. blooms and king scallop (*Pecten maximus*) contamination by domoic acid along the French Atlantic and English Channel coasts: Seasonal dynamics, spatial heterogeneity and interannual variability. Harmful Algae 51, 26–39.

Hutchinson, G. E., 1961. The Paradox of the Plankton. The American Naturalist 95, 137–145.

Iglikowska, A., Bełdowski, J., Chełchowski, M., Chierici, M., Kedra, M., Przytarska, J., Sowa, A., Kukliński, P., 2016. Chemical composition of two mineralogically contrasting Arctic bivalves' shells and their relationships to environmental variables. Marine Pollution Bulletin 114, 903–916.

Immenhauser, A., Schöne, B. R., Hoffmann, R., Niedermayr, A., 2016. Mollusc and brachiopod skeletal hard parts: Intricate archives of their marine environment. Sedimentology 63, 1–59.

Irion, S., Christaki, U., Berthelot, H., L'Helguen, S., Jardillier, L., 2021. Small phytoplankton contribute greatly to CO_2-fixation after the diatom bloom in the Southern Ocean. The ISME Journal 15, 2509–2522.

Jackson, J. B., Kirby, M. X., Berger, W. H., Bjorndal, K. A., Botsford, L. W., Bourque, B. J., Bradbury, R. H., Cooke, R., Erlandson, J., Estes, J. A., Hughes, T. P., Kidwell, S., Lange, C. B., Lenihan, H. S., Pandolfi, J. M., Peterson, C. H., Steneck, R. S., Tegner, M. J., Warner, R. R., 2001. Historical overfishing and the recent collapse of coastal ecosystems. Science 293, 629–637.

Jacob, D. E., Soldati, A. L., Wirth, R., Huth, J., Wehrmeister, U., Hofmeister, W., 2008. Nanostructure, composition and mechanisms of bivalve shell growth. Geochimica et Cosmochimica Acta 72, 5401–5415.

Jakobsen, H. H., Hansen, P. J., 1997. Prey size selection, grazing and growth response of the small heterotrophic dinoflagellate *Gymnodinium* sp. and the ciliate *Balanion comatum* – a comparative study. Marine Ecology Progress Series 158, 75–86.

Jeong, H. J., Yoo, Y. D., Kang, N. S., Rho, J. R., Seong, K. A., Park, J. W., Nam, G. S., Yih, W., 2010. Ecology of *Gymnodinium aureolum*. I. Feeding in western Korean waters. Aquatic Microbial Ecology 59, 239–255.

Jones, D. S., Quitmyer, I. R., 1996. Marking time with bivalve shells: Oxygen isotopes and season of annual increment formation. PALAIOS 11, 340–346.

Jones, D. S., 1980. Annual cycle of shell growth increment formation in two continental shelf bivalves and its paleoecologic significance. Paleobiology 3, 331–340.

Jurgensone, I., Carstensen, J., Ikauniece, A., Kalveka, B., 2011. Long-term changes and controlling factors of phytoplankton community in the Gulf of Riga (Baltic Sea). Estuaries and Coasts 34, 1205–1219.

Kastner, M., 1999. Oceanic minerals: Their origin, nature of their environment, and significance. Proceedings of the National Academy of Sciences 96, 3380–3387.

Kennedy, W. J., Taylor, J. D., Hall, A., 1969. Environmental and biological controls on bivalve shell mineralogy. Biological Reviews 44, 499–530.

Kenny, N. J., McCarthy, S. A., Dudchenko, O., James, K., Betteridge, E., Corton, C., Dolucan, J., Mead, D., Oliver, K., Omer, A. D., Pelan, S., Ryan, Y., Sims, Y., Skelton, J., Smith, M., Torrance, J., Weisz, D., Wipat, A., Aiden, E. L., Howe, K., Williams, S. T., 2020. The gene-rich genome of the scallop *Pecten maximus*. GigaScience 9, giaa037.

Killam, D. E., Clapham, M. E., 2018. Identifying the ticks of bivalve shell clocks: Seasonal growth in relation to temperature and food supply. Palaios 33, 228–236.

Kužat, N., Pfannkuchen, D. M., Tanković, M. S., Baričević, A., Ivančić, I., Vrana, I., Gašparović, B., Pfannkuchen, M., 2022. Morpho-physiological adaptations of *Leptocylindrus aporus* and *L. hargravesii* to phosphate limitation in the northern Adriatic. Scientific Reports 12, 2687.

Labry, C., Delmas, D., Youenou, A., Quere, J., Leynaert, A., Fraisse, S., Raimonet, M., Ragueneau, O., 2016. High alkaline phosphatase activity in phosphate replete waters: The case of two macrotidal estuaries. Limnology and Oceanography 61, 1513–1529.

Larsen, T., Ventura, M., Andersen, N., O'Brien, D. M., Piatkowski, U., McCarthy, M. D., 2013. Tracing carbon sources through aquatic and terrestrial food webs using amino acid stable isotope fingerprinting. PLoS ONE 8, e73441.

Larsen, T., Hansen, T., Dierking, J., 2020. Characterizing niche differentiation among marine consumers with amino acid δ^{13}C fingerprinting. Ecology and Evolution 10, 7768–7782.

Laruelle, G. G., Regnier, P., Ragueneau, O., Kempa, M., Moriceau, B., Ni Longphuirt, S., Leynaert, A., Thouzeau, G., Chauvaud, L., 2009. Benthic-pelagic coupling and the seasonal silic cycle in the Bay of Brest (France): New insights from a coupled physical-biological model. Marine Ecology Progress Series 385, 15–32.

Lavaud, R., Flye-Sainte-Marie, J., Jean, F., Emmery, A., Strand, Ø., Kooijman, S. A., 2014. Feeding and energetics of the great scallop, *Pecten maximus*, through a DEB model. Journal of Sea Research 94, 5–18.

LaVigne, M., Grottoli, A. G., Palardy, J. E., Sherrell, R. M., 2016. Multi-colony calibrations of coral Ba/Ca with a contemporaneous in situ seawater barium record. Geochimica et Cosmochimica Acta 179, 203–216.

Le Pape, O., Menesguen, A., 1997. Hydrodynamic prevention of eutrophication in the Bay of Brest (France), a modelling approach. Journal of Marine Systems 12, 171–186.

Lee, S. D., Joo, H. M., Lee, J. H., 2014. Critical criteria for identification of the genus *Chaetoceros* (Bacillariophyta) based on setae ultrastructure. II. Subgenus *Hyalochaete*. Phycologia 53, 614–638.

Legrand, C., Rengefors, K., Fistarol, G. O., Granéli, E., 2003. Allelopathy in phytoplankton – biochemical, ecological and evolutionary aspects. Phycologia 42, 406–419.

Li, X., Yang, Y., Ishizaka, J., Li, X., 2023. Global estimation of phytoplankton pigment concentrations from satellite data using a deep-learning-based model. Remote Sensing of Environment 294, 113628.

Lisiecki, L. E., Jones, A. M., Rand, D., Lee, T., Lawrence, C. E., 2022. Comparing age model techniques for the last glacial cycle: A case study of ten Iberian Margin sediment cores. Quaternary Science Reviews 287, 107559.

Liu, H., Kelly, M. S., Campbell, D. A., Fang, J., Zhu, J., 2008. Accumulation of domoic acid and its effect on juvenile king scallop *Pecten maximus* (Linnaeus, 1758). Aquaculture 284, 224–230.

Longhurst, A., Sathyendranath, S., Platt, T., Caverhill, C., 1995. An estimate of global primary production in the ocean from satellite radiometer data. Journal of Plankton Research 17, 1245–1271.

Lorenzen, C. J., 1967. Vertical distribution of chlorophyll and phaeo-pigments: Baja California. Deep-Sea Research and Oceanographic Abstracts 14, 735–745.

Lorrain, A., Gillikin, D. P., Paulet, Y. M., Chauvaud, L., Le Mercier, A., Navez, J., André, L., 2005. Strong kinetic effects on Sr/Ca ratios in the calcitic bivalve *Pecten maximus*. Geology 33, 965–968.

Lorrain, A., Paulet, Y. M., Chauvaud, L., Savoye, N., Nézan, E., Guérin, L., 2000. Growth anomalies in *Pecten maximus* from coastal waters (Bay of Brest, France): Relationship with diatom blooms. Journal of the Marine Biological Association of the United Kingdom 80, 667–673.

Louis, V., Besseau, L., Lartaud, F., 2022. Step in time: Biomineralisation of bivalve's shell. Frontiers in Marine Science 9, 906085.

Lu, X., Chen, Z., Hernández-Becerril, D. U., Lundholm, N., Li, Y., 2023. Taxonomy and phylogeny of *Chaetoceros* species of the section *Stenocincta* (Bacillariophyceae), with emendation of *C. affinis* and *C. willei* and description of three new species. Phycologia 62, 462–482.

Marali, S., Schöne, B. R., Mertz-Kraus, R., Griffin, S. M., Wanamaker, A. D., Matras, U., Butler, P. G., 2017. Ba/Ca ratios in shells of *Arctica islandica* – Potential environmental proxy and crossdating tool. Palaeogeography, Palaeoclimatology, Palaeoecology 465, 347–361.

Marañón, E., Lorenzo, M. P., Cermeño, P., Mouriño-Carballido, B., 2018. Nutrient limitation suppresses the temperature dependence of phytoplankton metabolic rates. The ISME Journal 12, 1836–1845.

Marchais, V., Jolivet, A., Hervé, S., Roussel, S., Schöne, B. R., Grall, J., Chauvaud, L., Clavier, J., 2017. New tool to elucidate the diet of the ormer *Haliotis tuberculata* (L.): Digital shell color analysis. Marine Biology 164, 71.

Marchais, V., Richard, J., Jolivet, A., Flye-Sainte-Marie, J., Thébault, J., Jean, F., Richard, P., Paulet, Y. M., Clavier, J., Chauvaud, L., 2015. Coupling experimental and field-based approaches to decipher carbon sources in the shell of the great scallop, *Pecten maximus* (L.) Geochimica et Cosmochimica Acta 168, 58–69.

Marin, F., Le Roy, N., Marie, B., 2012. The formation and mineralization of mollusk shell. Frontiers in Bioscience S4, 1099–1125.

Marin, F., Luquet, G., Marie, B., Medakovic, D., 2007. Molluscan shell proteins: Primary structure, origin, and evolution. Current Topics in Developmental Biology 80, 209–276.

Marino, R., Howarth, R. W., Chan, F., Cole, J. J., Likens, G. E., 2003. Sulfate inhibition of molybdenum-dependent nitrogen fixation by planktonic cyanobacteria under seawater conditions: A non-reversible effect. Hydrobiologia 500, 277–293.

Marriott, C. S., Henderson, G. M., Crompton, R., Staubwasser, M., Shaw, S., 2004. Effect of mineralogy, salinity, and temperature on Li/Ca and Li isotope composition of calcium carbonate. Chemical Geology 212, 5–15.

Martin, J. H., Knauer, G. A., 1973. The elemental composition of plankton. Geochimica et Cosmochimica Acta 37, 1639–1653.

Mathers, N. F., 1976. The effects of tidal currents on the rhythm of feeding and digestion in *Pecten maximus* L. Journal of Experimental Marine Biology and Ecology 24, 271–283.

Matras, U., Salter, I., Larsen, K. M. H., Gaard, E., Steingrund, P., 2022. Relationship between plankton dynamics and growth of the long-lived clam *Arctica islandica* on the Faroe shelf. Frontiers in Marine Science 9, 822343.

McConnaughey, T. A., Gillikin, D. P., 2008. Carbon isotopes in mollusk shell carbonates. Geo-Marine Letters 28, 287–299.

McCulloch, M. T., Gagan, M. K., Mortimer, G. E., Chivas, A. R., Isdale, P. J., 1994. A high-resolution Sr/Ca and δ^{18}O coral record from the Great Barrier Reef, Australia, and the 1982–1983 El Niño. Geochimica et Cosmochimica Acta 58, 2747–2754.

Milano, S., Nehrke, G., Wanamaker, A. D., Ballesta-Artero, I., Brey, T., Schöne, B. R., 2017. The effects of environment on *Arctica islandica* shell formation and architecture. Biogeosciences 14, 1577–1591.

Mook, W. G., Vogel, J. C., 1968. Isotopic equilibrium between shells and their environment. Science 159, 874–875.

Nanjappa, D., Kooistra, W. H. C. F., Zingone, A., 2013. A reappraisal of the genus *Leptocylindrus* (Bacillariophyta), with the addition of three species and the erection of *Tenuicylindrus* gen. nov. Journal of Phycology 49, 917–936.

Nanjappa, D., Sanges, R., Ferrante, M. I., Zingone, A., 2017. Diatom flagellar genes and their expression during sexual reproduction in *Leptocylindrus danicus*. BMC Genomics 18, 813.

Nézan, E., Chomérat, N., Bilien, G., Boulben, S., Duval, A., 2010. *Pseudo-nitzschia australis* on French Atlantic coast – an unusual toxic bloom. Harmful Algae News 41, 1–2.

Nixon, S. W., 1995. Coastal marine eutrophication: A definition, social causes, and future concerns. Ophelia 41, 199–219.

Nowicki, M., DeVries, T., Siegel, D. A., 2022. Quantifying the carbon export and sequestration pathways of the ocean's biological carbon pump. Global Biogeochemical Cycles 26, e2021GB007083.

O'Donnell, T. H., Macko, S. A., Chou, J., Davis-Hartten, K. L., Wehmiller, J. F., 2003. Analysis of δ^{13}C, δ^{15}N, and δ^{34}S in organic matter from the biominerals of modern and fossil *Mercenaria* spp. Organic Geochemistry 34, 165–183.

Okumura, M., Kitano, Y., 1986. Coprecipitation of alkali metal ions with calcium carbonate. Geochimica et Cosmochimica Acta 50, 49–58.

Omta, A. W., Talmy, D., Sher, D., Finkel, Z. V., Irwin, A. J., Follows, M. J., 2017. Extracting phytoplankton physiological traits from batch and chemostat culture data. Limnology and Oceanography: Methods 15, 453–466.

Owen, R., Richardson, C., Kennedy, H., 2002. The influence of shell growth rate on striae deposition in the scallop *Pecten maximus*. Journal of the Marine Biological Association of the United Kingdom 82, 621–623.

Pälike, H., Lyle, M. W., Nishi, H., Raffi, I., Ridgwell, A., Gamage, K., Klaus, A., Acton, G., Anderson, L., Backman, J., Baldauf, J., Beltran, C., Bohaty, S. M., Bown, P., Busch, W., Channell, J. E. T., Chun, C. O. J., Delaney, M., Dewangan, P., Dunkley Jones, T., Edgar, K. M., Evans, H., Fitch, P., Foster, G. L., Gussone, N., Hasegawa, H., Hathorne, E. C., Hayashi, H., Herrle, J. O., Holbourn, A., Hovan, S., Hyeong, K., Iijima, K., Ito, T., Kamikuri, S. I., Kimoto, K., Kuroda, J., Leon-Rodriguez, L., Malinverno, A., Moore, T. C., Murphy, B. H., Murphy, D. P., Nakamura, H., Ogane, K., Ohneiser, C., Richter, C., Robinson, R., Rohling, E. J., Romero, O., Sawada, K., Scher, H., Schneider, L., Sluijs, A., Takata, H., Tian, J., Tsujimoto, A., Wade, B. S., Westerhold, T., Wilkens, R., Williams, T., Wilson, P. A., Yamamoto, Y., Yamamoto, S., Yamazaki, T., Zeebe, R. E., 2012. A Cenozoic record of the equatorial Pacific carbonate compensation depth. Nature 488, 609–614.

Pannella, G., MacClintock, C., 1968. Biological and environmental rhythms reflected in molluscan shell growth. The Paleontological Society 42, 64–80.

Parsons, M. L., Okolodkov, Y. B., Aké-Castillo, J. A., 2012. Diversity and morphology of the species of *Pseudo-nitzschia* (Bacillariophyta) of the national park Sistema Arrecifal Veracruzano, SW Gulf of Mexico. Acta Botanica Mexicana 98, 51–72.

Pedersen, M. W., Overballe-Petersen, S., Ermini, L., Sarkissian, C. D., Haile, J., Hellstrom, M., Spens, J., Thomsen, P. F., Bohmann, K., Cappellini, E., Schnell, I. B., Wales, N. A., Carøe, C., Campos, P. F., Schmidt, A. M., Gilbert, M. T. P., Hansen, A. J., Orlando, L., Willerslev, E., 2015. Ancient and modern environmental DNA. Philosophical Transactions of the Royal Society of London. Series B 370, 20130383.

Peharda, M., Schöne, B. R., Black, B. A., Corrège, T., 2021. Advances of sclerochronology research in the last decade. Palaeogeography, Palaeoclimatology, Palaeoecology 570, 110371.

Peharda, M., Walliser, E. O., Markulin, K., Purroy, A., Uvanović, H., Janeković, I., Župan, I., Vilibić, I., Schöne, B. R., 2019. *Glycymeris pilosa* (Bivalvia) – A high-potential geochemical archive of the environmental variability in the Adriatic Sea. Marine Environmental Research 150, 104759.

Phinney, D. A., Cucci, T. L., 1989. Flow cytometry and phytoplankton. Cytometry 10, 511–521.

Piwoni-Piórewicz, A., Strekopytov, S., Humphreys-Williams, E., Kukliński, P., 2021. The patterns of elemental concentration (Ca, Na, Sr, Mg, Mn, Ba, Cu, Pb, V, Y, U and Cd) in shells of invertebrates representing different $CaCO_3$ polymorphs: A case study from the brackish Gulf of Gdańsk (the Baltic Sea). Biogeosciences 18, 707–728.

Poitevin, P., Roy, V., Galbraith, P. S., Chaillou, G., 2022. Insights into coastal phytoplankton variations from 1979 to 2018 derived from Ba/Ca records in scallop shells (*Chlamys islandica*) from a fishing ground in the northern Gulf of St. Lawrence. Marine Environmental Research 181, 105734.

Poppeschi, C., Charria, G., Daniel, A., Verney, R., Rimmelin-Maury, P., Retho, M., Goberville, E., Grossteffan, E., Plus, M., 2022. Interannual variability of the initiation of the phytoplankton growing period in two French coastal ecosystems. Biogeosciences 19, 5667–5687.

Queguiner, B., Tréguer, P., 1984. Studies on the phytoplankton in the Bay of Brest (Western Europe). Seasonal variations in composition, biomass and production in relation to hydrological and chemical features (1981–1982). Botanica Marina 27, 449–460.

Rabalais, N. N., Turner, R. E., Wiseman, W. J., 2002. Gulf of Mexico Hypoxia, A.K.A. 'The Dead Zone'. Annual Review of Ecology and Systematics 33, 235–263.

Ragueneau, O., Chauvaud, L., Moriceau, B., Leynaert, A., Thouzeau, G., Donval, A., Le Loc'h, F., Jean, F., 2005. Biodeposition by an invasive suspension feeder impacts the biogeochemical cycle of Si in a coastal ecosystem (Bay of Brest, France). Biogeochemistry 75, 19–41.

Ragueneau, O., Chauvaud, L., Leynaert, A., Thouzeau, G., Paulet, Y. M., Bonnet, S., Lorrain, A., Grall, J., Corvaisier, R., Le Hir, M., Jean, F., Clavier, J., 2002. Direct evidence of a biologically active coastal silicate pump: Ecological implications. Limnology and Oceanography 47, 1849–1854.

Ragueneau, O., Raimonet, M., Mazé, C., Coston-Guarini, J., Chauvaud, L., Danto, A., Grall, J., Jean, F., Paulet, Y. M., Thouzeau, G., 2018. The impossible sustainability of the Bay of Brest? Fifty years of ecosystem changes, interdisciplinary knowledge construction and key questions at the science-policy-community interface. Frontiers in Marine Science 5, 124.

Ragueneau, O., Varela, E. D. B., Treguer, P., Queguiner, B., Del Amo, Y., 1994. Phytoplankton dynamics in relation to the biogeochemical cycle of silicon in a coastal ecosystem of Western Europe. Marine Ecology Progress Series 106, 157–172.

Reitan, K. I., 2011. Digestion of lipids and carbohydrates from microalgae (*Chaetoceros muelleri* Lemmermann and *Isochrysis* aff. *galbana* clone T-ISO) in juvenile scallops (*Pecten maximus L.*) Aquaculture Research 42, 1530–1538.

Reynolds, D. J., Hall, I. R., Scourse, J. D., Richardson, C. A., Wanamaker, A. D., Butler, P. G., 2017a. Biological and climate controls on north Atlantic marine carbon dynamics over the last millennium: Insights from an absolutely dated shell-based record from the North Icelandic shelf. Global Biogeochemical Cycles 31, 1718–1735.

Reynolds, D. J., Hall, I. R., Slater, S. M., Scourse, J. D., Halloran, P. R., Sayer, M. D. J., 2017b. Reconstructing past seasonal to multicentennial-scale variability in the NE Atlantic Ocean using the long-lived marine bivalve mollusk *Glycymeris glycymeris*. Paleoceanography 32, 1153–1173.

Reynolds, D. J., Edge, D. C., Black, B. A., 2021. RingdateR: A statistical and graphical tool for crossdating. Dendrochronologia 65, 125797.

Reynolds, D. J., von Biela, V. R., Dunton, K. H., Douglas, D. C., Black, B. A., 2022. Sclerochronological records of environmental variability and bivalve growth in the Pacific Arctic. Progress in Oceanography 206, 102864.

Rhodes, L., Smith, K. F., MacKenzie, L., Wood, S. A., Ponikla, K., Harwood, D. T., Packer, M., Munday, R., 2016. The Cawthron Institute Culture Collection of micro-algae: a significant national collection. New Zealand Journal of Marine and Freshwater Research 50, 291–316.

Richardson, C. A., Crisp, D. J., Runham, N. W., 1980. An endogenous rhythm in shell deposition in *Cerastoderma edule*. Journal of the Marine Biological Association of the United Kingdom 60, 991–1004.

Rines, J. E., Theriot, E. C., 2003. Systematics of Chaetocerotaceae (Bacillariophyceae). I. A phylogenetic analysis of the family. Phycological Research 51, 83–98.

Robson, A. A., Chauvaud, L., Wilson, R. P., Halsey, L. G., 2012. Small actions, big costs: The behavioural energetics of a commercially important invertebrate. Journal of The Royal Society Interface 9, 1486–1498.

Roth, I., Riley, J. P., 1971. The distribution of trace elements in some species of phytoplankton grown in culture. Journal of the Marine Biological Association of the United Kingdom 51, 63–72.

Roux, M., Schein, E., Rio, M., Davanzo, F., Filiy, A., 1990. Environment parameters and growth steps recorded by $^{18}O/^{16}O$ and $^{13}C/^{12}C$ ratios in the shell of *Pecten maximus* (Pectinidae, Bivalvia). Comptes Rendus de l'Académie des Sciences - Series II - Mécanique, Physique, Chimie, Sciences de l'univers, Sciences de la Terre 310, 385–390.

Ryabov, A., Kerimoglu, O., Litchman, E., Olenina, I., Roselli, L., Basset, A., Stanca, E., Blasius, B., 2021. Shape matters: The relationship between cell geometry and diversity in phytoplankton. Ecology Letters 24, 847–861.

Saha, N., Webb, G. E., Zhao, J. X., Leonard, N. D., Nguyen, A. D., 2018. Influence of marine biochemical cycles on seasonal variation of Ba/Ca in the near-shore coral Cyphastrea, Rat Island, southern Great Barrier Reef. Chemical Geology 499, 71–83.

Sauvey, A., Denis, F., Hégaret, H., Le Roy, B., Lelong, C., Jolly, O., Pavie, M., Fauchot, J., 2021. Interactions between filter-feeding bivalves and toxic diatoms: Influence on the feeding behavior of *Crassostrea gigas* and *Pecten maximus* and on toxin production by *Pseudo-nitzschia*. Toxins 13, 577.

Schein, E., Roux, M., Barbin, V., Chiesi, F., Renard, M., Rio, M., 1991. Ecological parameters recorded by bivalve shell – pluridisciplinary approach. Bulletin de la Société Géologique de France 162, 687–698.

Schöne, B. R., Radermacher, P., Zhang, Z., Jacob, D. E., 2013. Crystal fabrics and element impurities (Sr/Ca, Mg/Ca, and Ba/Ca) in shells of *Arctica islandica* – Implications for paleoclimate reconstructions. Palaeogeography, Palaeoclimatology, Palaeoecology 373, 50–59.

Schöne, B. R., Kröncke, I., Houk, S. D., Freyre Castro, A. D., Oschmann, W., 2003. The cornucopia of chilly winters: Ocean quahog (*Arctica islandica* L., Mollusca) master chronology reveals bottom water nutrient enrichment during colder winters (North Sea). Senckenbergiana Maritima 32, 165–175.

Schöne, B. R., Zhang, Z., Jacob, D., Gillikin, D. P., Tütken, T., Garbe-Schönberg, D., Mcconnaughey, T., Soldati, A., 2010. Effect of organic matrices on the determination of the trace element chemistry (Mg, Sr, Mg/Ca, Sr/Ca) of aragonitic bivalve shells (*Arctica is-*

landica) – Comparison of ICP-OES and LA-ICP-MS data. Geochemical Journal 44, 23–37.

Schöne, B. R., 2008. The curse of physiology – Challenges and opportunities in the interpretation of geochemical data from mollusk shells. Geo-Marine Letters 28, 269–285.

Schöne, B. R., 2013. *Arctica islandica* (Bivalvia): A unique paleoenvironmental archive of the northern North Atlantic Ocean. Global and Planetary Change 111, 199–225.

Schöne, B. R., Fiebig, J., Pfeiffer, M., Gleß, R., Hickson, J., Johnson, A. L., Dreyer, W., Oschmann, W., 2005a. Climate records from a bivalved Methuselah (*Arctica islandica*, Mollusca; Iceland). Palaeogeography, Palaeoclimatology, Palaeoecology 228, 130–148.

Schöne, B. R., Houk, S. D., Freyre Castro, A. D., Fiebig, J., Oschmann, W., Kröncke, I., Dreyer, W., Gosselck, F., 2005b. Daily growth rates in shells of *Arctica islandica*: Assessing sub-seasonal environmental controls on a long-lived bivalve mollusk. Palaios 20, 78–92.

Schöne, B. R., Marali, S., Jantschke, A., Mertz-Kraus, R., Butler, P. G., Fröhlich, L., 2023. Can element chemical impurities in aragonitic shells of marine bivalves serve as proxies for environmental variability? Chemical Geology 616, 121215.

Shikata, T., Nagasoe, S., Matsubara, T., Yoshikawa, S., Yamasaki, Y., Shimasaki, Y., Oshima, Y., Jenkinson, I. R., Honjo, T., 2008. Factors influencing the initiation of blooms of the raphidophyte *Heterosigma akashiwo* and the diatom *Skeletonema costatum* in a port in Japan. Limnology and Oceanography 53, 2503–2518.

Siebert, V., Fröhlich, L., Thébault, J., Schöne, B. R., Delebecq, G., Picheral, M., Waeles, M., Moriceau, B., 2024. Dynamics of molybdenum and barium in the Bay of Brest (France) explained by phytoplankton community structure and aggregation events. Estuarine, Coastal and Shelf Science 303, 108783.

Siebert, V., Moriceau, B., Fröhlich, L., Schöne, B. R., Amice, E., Beker, B., Bihannic, K., Bihannic, I., Delebecq, G., Devesa, J., Gallinari, M., Germain, Y., Grossteffan, É., Jochum, K. P., Le Bec, T., Le Goff, M., Liorzou, C., Leynaert, A., Marec, C., Picheral, M., Rimmelin-Maury, P., Rouget, M. L., Waeles, M., Thébault, J., 2023. HIPPO environmental monitoring: impact of phytoplankton dynamics on water column chemistry and

the sclerochronology of the king scallop (*Pecten maximus*) as a biogenic archive for past primary production reconstructions. Earth System Science Data 15, 3263–3281.

Simon, N., Cras, A. L., Foulon, E., Lemée, R., 2009. Diversity and evolution of marine phytoplankton. Comptes Rendus Biologies 332, 159–170.

Sinniger, F., Pawlowski, J., Harii, S., Gooday, A. J., Yamamoto, H., Chevaldonné, P., Cedhagen, T., Carvalho, G., Creer, S., 2016. Worldwide analysis of sedimentary DNA reveals major gaps in taxonomic knowledge of deep-sea benthos. Frontiers in Marine Science 3, 92.

Soldati, A. L., Jacob, D. E., Glatzel, P., Swarbrick, J. C., Geck, J., 2016. Element substitution by living organisms: The case of manganese in mollusc shell aragonite. Scientific Reports 6, 22514.

Sonnet, V., Mouw, C. B., Ciochetto, A. B., Carney-Almeida, J., 2024. Hit or miss? Impact of time series resolution on resolving phytoplankton dynamics at hourly, weekly, and satellite remote sensing frequencies. Limnology and Oceanography: Methods 22, 254–267.

Sournia, A., Chrétiennot-Dinet, M. J., Ricard, M., 1991. Marine phytoplankton: How many species in the world ocean? Journal of Plankton Research 13, 1093–1099.

Stahl, A. R., Rynearson, T. A., McMahon, K. W., 2023. Amino acid carbon isotope fingerprints are unique among eukaryotic microalgal taxonomic groups. Limnology and Oceanography 68, 1331–1345.

Stecher, H. A., Krantz, D. E., Lord, C. J., Luther, G. W., Bock, K. W., 1996. Profiles of strontium and barium in *Mercenaria mercenaria* and *Spisula solidissima* shells. Geochimica et Cosmochimica Acta 60, 3445–3456.

Stecher, H. A., Kogut, M. B., 1999. Rapid barium removal in the Delaware estuary. Geochimica et Cosmochimica Acta 63, 1003–1012.

Sternberg, E., Tang, D., Ho, T. Y., Jeandel, C., Morel, F. M. M., 2005. Barium uptake and adsorption in diatoms. Geochimica et Cosmochimica Acta 69, 2745–2752.

Takesue, R. K., Bacon, C. R., Thompson, J. K., 2008. Influences of organic matter and calcification rate on trace elements in aragonitic estuarine bivalve shells. Geochimica et Cosmochimica Acta 72, 5431–5445.

Tett, P., Barton, E. D., 1995. Why are there about 5000 species of phytoplankton in the sea? Journal of Plankton Research 17, 1693–1704.

Thébault, J., Chauvaud, L., 2013. Li/Ca enrichments in great scallop shells (*Pecten maximus*) and their relationship with phytoplankton blooms. Palaeogeography, Palaeoclimatology, Palaeoecology 373, 108–122.

Thébault, J., Chauvaud, L., L'Helguen, S., Clavier, J., Barats, A., Jacquet, S., Pécheyran, C., Amouroux, D., 2009a. Barium and molybdenum records in bivalve shells: Geochemical proxies for phytoplankton dynamics in coastal environments? Limnology and Oceanography 54, 1002–1014.

Thébault, J., Jolivet, A., Waeles, M., Tabouret, H., Sabarot, S., Pécheyran, C., Leynaert, A., Jochum, K. P., Schöne, B. R., Fröhlich, L., Siebert, V., Amice, E., Chauvaud, L., 2022. Scallop shells as geochemical archives of phytoplankton-related ecological processes in a temperate coastal ecosystem. Limnology and Oceanography 67, 187–202.

Thébault, J., Schöne, B. R., Hallmann, N., Barth, M., Nunn, E. V., 2009b. Investigation of Li/Ca variations in aragonitic shells of the ocean quahog *Arctica islandica*, northeast Iceland. Geochemistry, Geophysics, Geosystems 10, Q12008.

Thessen, A. E., Patterson, D. J., Murray, S. A., 2012. The taxonomic significance of species that have only been observed once: The genus *Gymnodinium* (Dinoflagellata) as an example. PLoS ONE 7, e44015.

Thomas, G. E., Gruffydd, L. D., 1971. The types of escape reactions elicited in the scallop *Pecten maximus* by selected sea-star species. Marine Biology 10, 87–93.

Thompson, I., Jones, D. S., Dreibelbis, D., 1980. Annual internal growth banding and life history of the ocean quahog *Arctica islandica* (Mollusca: Bivalvia). Marine Biology 57, 25–34.

Thornton, D. C. O., 2002. Diatom aggregation in the sea: Mechanisms and ecological implications. European Journal of Phycology 37, 149–161.

Trainer, V. L., Bates, S. S., Lundholm, N., Thessen, A. E., Cochlan, W. P., Adams, N. G., Trick, C. G., 2012. *Pseudo-nitzschia* physiological ecology, phylogeny, toxicity, monitoring and impacts on ecosystem health. Harmful Algae 14, 271–300.

Trauth, M. H., Sarnthein, M., Arnold, M., 1997. Bioturbational mixing depth and carbon flux at the seafloor. Paleoceanography 12, 517–526.

Trofimova, T., Alexandroff, S. J., Mette, M. J., Tray, E., Butler, P. G., Campana, S. E., Harper, E. M., Johnson, A. L. A., Morrongiello, J. R., Peharda, M., Schöne, B. R., Andersson, C., Andrus, C. F. T., Black, B. A., Burchell, M., Carroll, M. L., DeLong, K. L., Gillanders, B. M., Grønkjær, P., Killam, D., Prendergast, A. L., Reynolds, D. J., Scourse, J. D., Shirai, K., Thébault, J., Trueman, C., de Winter, N., 2020. Fundamental questions and applications of sclerochronology: Community-defined research priorities. Estuarine, Coastal and Shelf Science 245, 106977.

Trofimova, T., Milano, S., Andersson, C., Bonitz, F. G. W., Schöne, B. R., 2018. Oxygen isotope composition of *Arctica islandica* aragonite in the context of shell architectural organization: Implications for paleoclimate reconstructions. Geochemistry, Geophysics, Geosystems 19, 453–470.

Vander Putten, E., Dehairs, F., Keppens, E., Baeyens, W., 2000. High resolution distribution of trace elements in the calcite shell layer of modern *Mytilus edulis*: Environmental and biological controls. Geochimica et Cosmochimica Acta 64, 997–1011.

Vane, K., Cobain, M. R. D., Larsen, T., 2025. The power and pitfalls of amino acid carbon stable isotopes for tracing origin and use of basal resources in food webs. Ecological Monographs 95, e1647.

Vihtakari, M., Ambrose, W. G., Renaud, P. E., Locke, W. L., Carroll, M. L., Berge, J., Clarke, L. J., Cottier, F., Hop, H., 2017. A key to the past? Element ratios as environmental proxies in two Arctic bivalves. Palaeogeography, Palaeoclimatology, Palaeoecology 465, 316–332.

Violle, C., Navas, M. L., Vile, D., Kazakou, E., Fortunel, C., Hummel, I., Garnier, E., 2007. Let the concept of trait be functional! Oikos 116, 882–892.

Waeles, M., Dulaquais, G., Jolivet, A., Thébault, J., Riso, R., 2013. Systematic non-conservative behavior of molybdenum in a macrotidal estuarine system (Aulne-Bay of Brest, France). Estuarine, Coastal and Shelf Science 131, 310–318.

Wanamaker, A. D., Heinemeier, J., Scourse, J. D., Richardson, C. A., Butler, P. G., Eiríksson, J., Knudsen, K. L., 2008. Very long-lived mollusk confirm 17th century AD tephra-based radiocarbon reservoir ages for north Icelandic shelf waters. Radiocarbon 50, 399–412.

Wanamaker, A. D., Kreutz, K. J., Schöne, B. R., Maasch, K. A., Pershing, A. J., Borns, H. W., Introne, D. S., Feindel, S., 2009. A late Holocene paleo-productivity record in the western Gulf of Maine, USA, inferred from growth histories of the long-lived ocean quahog (*Arctica islandica*). International Journal of Earth Sciences 98, 19–29.

Wang, D.-Z., 2008. Neurotoxins from marine dinoflagellates: A brief review. Marine Drugs 6, 349–371.

Ward, J. E., Shumway, S. E., 2004. Separating the grain from the chaff: Particle selection in suspension- and deposit-feeding bivalves. Journal of Experimental Marine Biology and Ecology 300, 83–130.

Williams, S. T., 2017. Molluscan shell colour. Biological Reviews 92, 1039–1058.

Wiltshire, K. H., Manly, B. F., 2004. The warming trend at Helgoland Roads, North Sea: Phytoplankton response. Helgoland Marine Research 58, 269–273.

Witbaard, R., Duineveld, G. C. A., De Wilde, P. A. W. J., 1999. Geographical differences in growth rates of *Arctica islandica* (Mollusca: Bivalvia) from the North Sea and adjacent waters. Journal of the Marine Biological Association of the United Kingdom 79, 907–915.

Witkowski, J., Bohaty, S. M., Edgar, K. M., Harwood, D. M., 2014. Rapid fluctuations in mid-latitude siliceous plankton production during the Middle Eocene Climatic Optimum (ODP Site 1051, western North Atlantic). Marine Micropaleontology 106, 110–129.

Wörmer, L., Elvert, M., Fuchser, J., Lipp, J. S., Buttigieg, P. L., Zabel, M., Hinrichs, K. U., 2014. Ultra-high-resolution paleoenvironmental records via direct laser-based analysis of lipid biomarkers in sediment core samples. Proceedings of the National Academy of Sciences 111, 15669–15674.

You, J. H., Jeong, H. J., Lim, A. S., Ok, J. H., Kang, H. C., 2020. Effects of irradiance and temperature on the growth and feeding of the obligate mixotrophic dinoflagellate *Gymnodinium smaydae*. Marine Biology 167, 64.

Zielinski, U., Gersonde, R., 1997. Diatom distribution in Southern Ocean surface sediments (Atlantic sector): Implications for paleoenvironmental reconstructions. Palaeogeography, Palaeoclimatology, Palaeoecology 129, 213–250.

Zonneveld, K. A. F., Versteegh, G. J. M., de Lange, G. J., 1997. Preservation of organic-walled dinoflagellate cysts in different oxygen regimes: A 10,000 year natural experiment. Marine Micropaleontology 29, 393–405.

Zonneveld, K. A. F., Versteegh, G. J. M., de Lange, G. J., 2001. Palaeoproductivity and post-depositional aerobic organic matter decay reflected by dinoflagellate cyst assemblages of the Eastern Mediterranean S1 sapropel. Marine Geology 172, 181–195.

2 Ba/Ca profiles in shells of *Pecten maximus* – A proxy for specific primary producers rather than bulk phytoplankton

---

Lukas Fröhlich[1], Valentin Siebert[2], Eric O. Walliser[1,3], Julien Thébault[2], Klaus Peter Jochum[4], Laurent Chauvaud[2], Bernd R. Schöne[1],

[1] *Johannes Gutenberg University, Mainz, Germany*

[2] *Univ Brest, CNRS, IRD, Plouzané, France*

[3] *Museum Wiesbaden, Hessisches Landesmuseum für Kunst und Natur, Wiesbaden, Germany*

[4] *Climate Geochemistry Department, Max Planck Institute for Chemistry, Mainz, Germany*

Reference:

Fröhlich, L., Siebert, V., Walliser, E. O., Thébault, J., Jochum, K. P., Chauvaud, L., Schöne, B. R., 2022. Ba/Ca profiles in shells of *Pecten maximus* – A proxy for specific primary producers rather than bulk phytoplankton. Chemical Geology 593, 120743.

In this chapter, daily resolved Ba/Ca_{shell} ratios were extracted from live-collected shells of *P. maximus* that grew during 2011 and 2012 in the Bay of Brest, France. Together with detailed data about the prevailing primary producers, i.e., the timing and magnitude of specific phytoplankton taxa and bulk phytoplankton, potential links with the shell geochemistry were determined. It could be demonstrated that peaks in the profiles of Ba/Ca_{shell} were potentially induced by the blooms of specific phytoplankton taxa and that a time lag exists between such blooms and the incorporation of Ba into the shell matrix. Furthermore, the outcomes suggested that a species-specific amount of Ba is associated with the different phytoplankton taxa. This chapter was published as a manuscript in the journal 'Chemical Geology'. My contributions to this manuscript were the conceptualization, formal analysis, investigation, methodology, visualization and writing of the original draft. Financial funding for this work were received from the German Research Foundation (DFG) with a grant to BRS (SCHO 793/21) within the framework of the French-German collaborative research project HIPPO funded jointly by the DFG and ANR (Agence Nationale de la Recherche).

Author contributions:

LF – Conceptualization, Formal analysis, Investigation, Methodology, Visualization, Writing - original draft, Writing - review and editing

VS – Investigation, Formal analysis, Writing - review and editing

EOW – Conceptualization, Methodology, Formal analysis, Supervision, Writing - review and editing

JT – Project administration, Resources, Validation, Writing - review and editing

KPJ – Resources, Validation, Writing - review and editing

LC – Resources, Data curation

BRS – Resources, Conceptualization, Formal analysis, Funding Acquisition, Supervision, Validation, Writing - original draft, Writing - review and editing

Abstract

Molar barium-to-calcium ratios in bivalve shells (Ba/Ca_{shell}) have been proposed in a variety of studies to serve as a potential proxy for the reconstruction of phytoplankton dynamics. However, the link between phytoplankton and Ba/Ca_{shell} profiles remains unclear and needs to be deciphered more accurately. In this study, we analyzed the relationship between Ba/Ca_{shell} peaks and specific phytoplankton species, and assessed the applicability of Ba/Ca_{shell} ratios as a species-specific phytoplankton proxy. The timing of peaks in highly resolved Ba/Ca_{shell} time-series in *Pecten maximus* shells (Bay of Brest, France) from two years (2011, 2012) were compared to the chlorophyll *a* concentration and the occurrence of individual diatom and dinoflagellate species. In addition, Monte Carlo simulations were used to approximate a species-specific contribution to the measured Ba/Ca_{shell} peaks. The results clearly demonstrated that the Ba/Ca_{shell} profiles cannot be explained either by the chlorophyll *a* concentration nor by the total diatom or dinoflagellate abundance. Instead, time-series of specific phytoplankton, especially diatoms, revealed a high degree of synchronicity with Ba/Ca_{shell} peaks when temporally lagged by 8 to 13 days (depending on species). The Monte Carlo simulations suggested that the Ba/Ca_{shell} peak heights cannot be fully explained by the observed phytoplankton cell concentration, but rather by individually weighted phytoplankton time-series, most likely caused by inter-specific differences such as cell size and chemical ability to adsorb Ba. Moreover, the approximated species-specific weighting factors agreed well between the studied years. According to our findings, Ba/Ca_{shell} peaks are likely associated with blooms of specific phytoplankton taxa, with a time lag of ca. one to two weeks, and the amount of cell-associated Ba varies between phytoplankton species. These conclusions provide further insights into the formation of Ba enrichments in bivalve shells and improves the applicability of Ba/Ca_{shell} profiles as a species-specific proxy of past phytoplankton dynamics.

2.1 Introduction

Marine phytoplankton plays a crucial role in the global net primary production (Field et al., 1998; Westberry et al., 2008). It also contributes significantly to the photosynthetic fixation and regulation of atmospheric CO_2 (Shuter, 1979; Sigman and Boyle, 2000; Iglesias-Rodriguez et al., 2008) and oxygen production (Field et al., 1998), and serves as the basis of the marine food web. Changing environmental conditions such as climate warming (Winder and Sommer, 2012; Barton et al., 2020), ocean acidification (Iglesias-Rodriguez et al., 2008) or nutrient input by artificial fertilizers (Del Amo et al., 1997; Beman et al., 2005) can lead to a shift in the phytoplankton community composition (Behl et al., 2011). Shifting community structures in turn can have important consequences for climate and ecosystems (Cardinale et al., 2006; Worm et al., 2006) and impact commercial fisheries because of eutrophication and harmful algae blooms (Shumway and Cembella, 1993; Ragueneau et al., 2002; Smith, 2003; Liu et al., 2008). To better understand long-term repercussions of changes in phytoplankton species composition it is necessary to gain a better comprehension of past phytoplankton dynamics. This includes insights into changes of the primary producer community structures through time and space.

Continuous and highly resolved primary production records are only available since a few decades and for a few localities (e.g., Lindahl et al., 1988; Richardson and Heilmann, 1995; Chauvaud et al., 2000; Cadée and Hegeman, 2002). However, this time interval is too short to reliably identify long-term changes in global phytoplankton dynamics and evaluate the anthropogenic impact (Henson et al., 2010). Therefore, different past marine primary production data were reconstructed from various proxies (Averyt and Paytan, 2004; Anderson and Winckler, 2005) such as the amount of barite in marine sediments that is linked to the decay of phytoplankton cells (Dehairs et al., 1980; Bishop, 1988; Ganeshram et al., 2003), foraminiferal assemblages (Herguera and Berger, 1991; Herguera, 2000) as well as Ba/Ti and Al/Ti ratios of bulk sediments (Dymond et al., 1997). Although marine sediment cores provide long-term archives, covering several thousands of years (e.g., Cheshire et al., 2005), the low accumulation rates prevent gaining a high temporal resolution. This prohibits a detailed reconstruction of short-term events, on a daily to weekly scale, of past phytoplankton dynamics. Instead, shells of bivalves potentially serve as an alternative high-resolution, temporally well-constrained archive of primary production. Bivalve mollusks precipitate their shell periodically (Richardson et al., 1980; Hallmann et al., 2008; Schöne, 2008) resulting in

distinct growth patterns, i.e., daily, fortnightly and annual growth lines. These growth increments (periods of slow and fast growth, respectively) can be used to place the shell record into a precise temporal context. During growth, bivalves record environmental changes in the form of variable increment widths and chemical properties. According to previous studies of different bivalve species, barium-to-calcium ratios of the shell (Ba/Ca_{shell}) potentially serve as a proxy for primary production in marine settings (Stecher et al., 1996; Vander Putten et al., 2000; Lazareth et al., 2003; Gillikin et al., 2006; Barats et al., 2009; Thébault et al., 2009; Marali et al., 2017a; Marali et al., 2017b; Doré et al., 2020). A common pattern of Ba/Ca_{shell} ratios in bivalves includes a relatively stable and low background signal interrupted by sharp Ba/Ca_{shell} peaks (Gillikin et al., 2008; Barats et al., 2009; Thébault et al., 2009; Hatch et al., 2013; Marali et al., 2017a). Since the Ba/Ca_{shell} profiles of contemporaneous shells from the same population are highly synchronous (Gillikin et al., 2008; Barats et al., 2009; Thébault et al., 2009; Marali et al., 2017a; Marali et al., 2017b; Doré et al., 2020), a common environmental forcing is likely (Vander Putten et al., 2000; Carré et al., 2006; Gillikin et al., 2008; Hatch et al., 2013). Although a general consensus exists regarding the cause of the stable background signal, it most likely reflects the Ba/Ca ratio of the seawater (Gillikin et al., 2006; Gillikin et al., 2008; Barats et al., 2009), different hypotheses emerged concerning the sharp Ba/Ca_{shell} peaks, which cannot be adequately explained by variations in the dissolved barium concentration of the surrounding medium (Gillikin et al., 2008; Barats et al., 2009). It is possible that bivalves ingest barite crystals induced by the decomposition of large amounts of phytoplankton cells following blooms (Bishop, 1988; Stecher et al., 1996; Stecher and Kogut, 1999; Ganeshram et al., 2003), leading to the desorption of barium in their gut and followed by the incorporation of barium into the shell carbonate (Takesue et al., 2008). However, it appears more likely that the direct ingestion of phytoplankton cells enriched in barium lead to the formation of Ba/Ca_{shell} peaks, because the ingestion of barite particles insufficiently explains the Ba/Ca_{shell} time-series in pectinids (Thébault et al., 2009). Previous studies demonstrated a large variability in the barium concentration between various marine phytoplankton species (Roth and Riley, 1971; Martin and Knauer, 1973; Fisher et al., 1991). Furthermore, according to Sternberg et al. (2005), barium is precipitated onto diatom frustules via the adsorption onto iron oxyhydroxides. Since a direct link between Ba/Ca_{shell} profiles and phytoplankton biomass could not be established in previous studies (Gillikin et al., 2008; Barats et al., 2009; Thébault et al., 2009), detailed analyses are required to decipher a potential relation between Ba/Ca_{shell} peaks and

phytoplankton dynamics on a species level.

The goal of this study is to refine knowledge about Ba/Ca_{shell} profiles from bivalve shells and the interconnection with phytoplankton in coastal ecosystems. To evaluate this relationship, shells of the short-lived bivalve, *Pecten maximus*, serve as an ideal geochemical archive as they provide growth increments that are formed on a daily basis (Chauvaud et al., 1998) which in turn allows to extract daily resolved Ba/Ca_{shell} time-series. This high temporal resolution is necessary in order to reconstruct primary producers dynamics, such as efflorescence, which is ephemeral and occurs over a short period of time. This study compares highly resolved phytoplankton observations with temporally contextualized Ba/Ca_{shell} profiles. The following questions will be addressed herein: (1) Does a direct relationship exist between the bulk phytoplankton in the water column and Ba/Ca_{shell} profiles? (2) Can the timing and magnitude of Ba/Ca_{shell} peaks be used to interpret past phytoplankton dynamics? (3) Is there a species-specific contribution of phytoplankton to the Ba/Ca_{shell} profile? Diatoms and dinoflagellates constitute the main phytoplankton groups in the studied coastal area and were used together with the chlorophyll *a* concentration (a rough gauge of the bulk phytoplankton biomass) to address these questions. To substantiate possible relationships between phytoplankton and shell chemistry, a special focus was placed on the timing and magnitude of Ba/Ca_{shell} enrichments and phytoplankton blooms. Deciphering this linkage will promote the applicability of Ba/Ca_{shell} profiles as a valuable proxy for past phytoplankton dynamics.

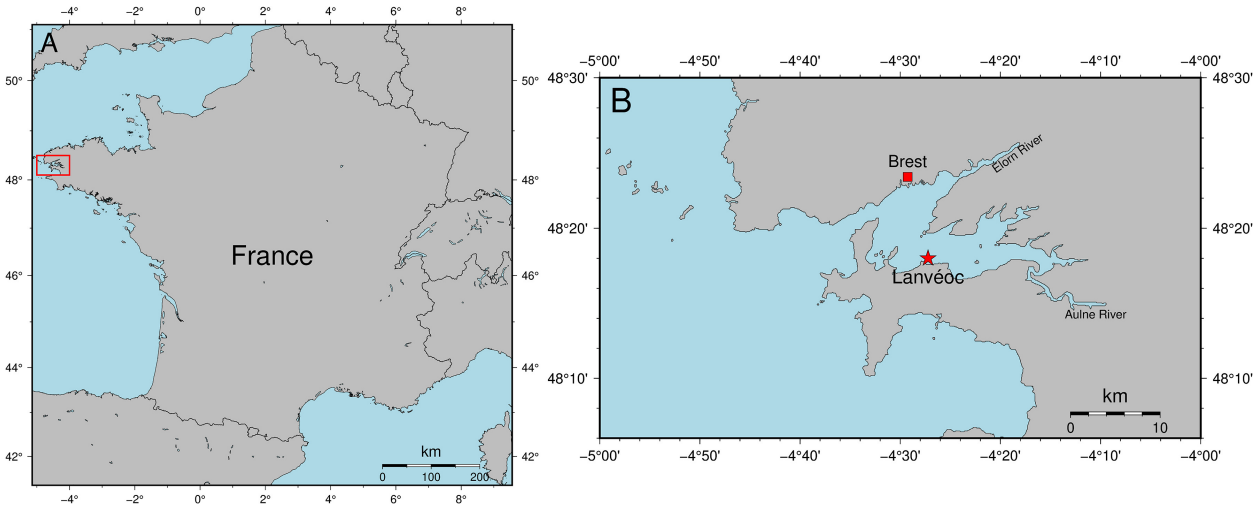

Figure 2.1 **A**) Map of France and the study site (Bay of Brest) marked with a red rectangle. **B**) Magnification of the Bay of Brest showing the sampling locality (Lanvéoc, red star).

2.2 Material and methods

2.2.1 Study site and sample preparation

A total of six specimens of *P. maximus* were collected alive at a depth of about 8 m by SCUBA diving at Lanvéoc (48°17′N 4°30′W), Bay of Brest, Brittany, northwest France (Fig. 2.1). The Bay of Brest is a semi-enclosed coastal ecosystem (180 km^2) with an average depth of 8 m. The sampling site, Lanvéoc, is located in the southern part of the bay. Three specimens were obtained on 30 August 2011 and another three on 23 October 2012 (Table 2.1). Shells of all studied specimens showed one winter growth line and are therefore referred to as age-class 1 shells. Immediately after collection, the specimens were stored in the freezer at -20 °C. Prior to sclerochronological analysis, the bivalves were eviscerated and epibionts were removed. Following previous studies (e.g., Chauvaud et al., 1998; Chauvaud et al., 2011; Jolivet et al., 2015; Marchais et al., 2015), the left (flat) valves were used for element chemical and growth pattern analyses (Fig. 2.2). In order to clean the surface of the shells (outer shell layer made of calcite), remove the periostracum and adhering sediment that was trapped between adjacent striae, the valves were gently cleaned using a plastic brush, followed by 3 min ultrasonication in deionized water. In advance of chemical analyses, further cleaning steps were applied (see section 2.2.3).

2.2.2 Growth pattern analysis and temporal alignment

For growth pattern analysis, photographs (e.g., see Supplementary Fig. S2.1) were taken on the outer surface of the shells within the depression between radiating ribs along the axis of maximum growth (Fig. 2.2), more specifically, the portion between the firs winter line and the ventral margin. For this purpose, a Canon EOS 600 DSLR camera was coupled to a Wild Heerbrugg binocular microscope equipped with a Schott VisiLED MC 1000 light source (sectoral dark field). Overlapping images were stitched together using the Image Composite Editor software (version 2.0.3.0) provided as freeware by the Microsoft Research Computational Photography Group.

The daily formed microgrowth increments and lines (called striae) of *P. maximus* can be used to place the shell growth record including geochemical data into a precise temporal context. If the date of collection is known, exact calendar days can be assigned to each microgrowth increment (e.g., Chauvaud et al., 1998; Lorrain et al., 2004; Gillikin et al.,

Table 2.1 Overview of specimens analyzed in this study for barium content by means of LA-ICP-MS. LOD = Limit of detection. Relative standard deviations (RSD) were calculated from repeated measurements of the external standard material NIST SRM 612. For quality control, the average concentrations and standard deviations ($\pm 1\sigma$) for blind measurements of the synthetic carbonate reference material USGS MACS-3 are given and compared with a reference value ($59.6 \pm 1.4\,\mu g\,g^{-1}$) provided by the GeoReM database (http://georem.mpch-mainz.gwdg.de/). Differences between measured MACS-3 values and literature value vary between 1.4% to 12.2%.

Sample ID	Date of collection	LOD (mmol mol^{-1})	RSD (%)	Concurrently analyzed MACS-3 values ($\mu g\,g^{-1}$)
Shell A	30 August 2011	9×10^{-6}	2.0	56.6 ± 4.8
Shell B	30 August 2011	1×10^{-5}	1.7	65.6 ± 4.3
Shell C	30 August 2011	8×10^{-6}	2.6	54.8 ± 4.6
Shell D	23 October 2012	9×10^{-6}	5.5	66.9 ± 4.0
Shell E	23 October 2012	5×10^{-6}	3.1	58.8 ± 2.5
Shell F	23 October 2012	1×10^{-5}	2.5	66.2 ± 5.8

2008). This is accomplished by counting the striae from the ventral margin (most recently formed shell portion) toward the umbo. Increment widths were determined by measuring the distance between adjacent striae following the method described by Chauvaud et al. (1998). Shell growth rates are given in $\mu m\,day^{-1}$. Growth curves of different contemporaneous specimens were then crossdated by wiggle-matching and minimizing the sum of least squares. As previously demonstrated by Thébault et al. (2006; 2009) for the pectinid shells, *C. radula*, the visual determination of successive striae is not always unambiguous (i.e., because of slightly fractured shell portions, overlapping striae or barely visible striae) leading to a subjective, inter-reader difference. The inter-reader discrepancies in striae determination in *P. maximus* shells were calculated from differences in repeated counts and measurements of daily formed striae performed by different readers ($n = 3$) and expressed as the relative standard deviation (RSD%). In this study, the inter-reader differences remain low (RSD% of 0.67%), i.e., solely a small uncertainty ($\pm$ 2 days) in the growth reading process and thus, in the temporal assignment of the geochemical data, has to be considered.

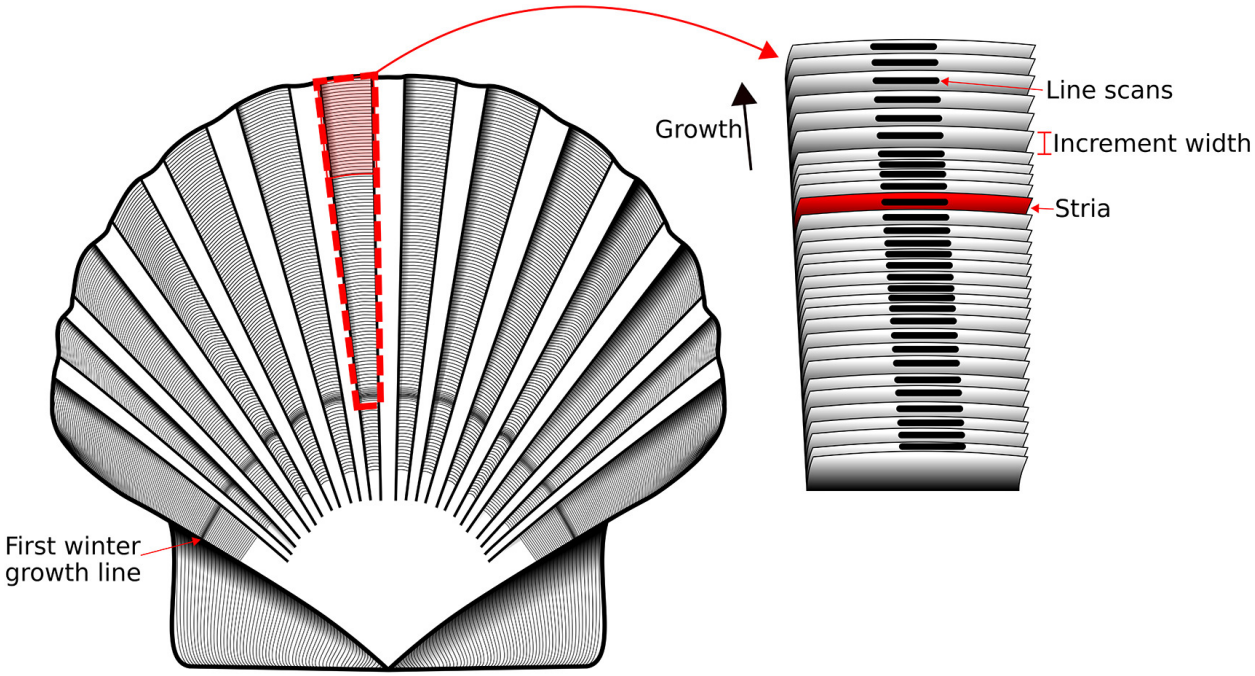

Figure 2.2 Schematic illustration of the left valve of an age class 1 specimen (*P. maximus*) showing one annual growth line. Dashed red line represents the extracted shell portion of an indented valley that is located between radial ribs. LA-ICP-MS measurements were performed on this shell portion. The magnification (right panel) displays daily formed increments (distance between two successively formed striae) on the external shell surface. The distance between successive growth striae was used to determine the growth rate of the shell. The thick black markers indicate the LA-ICP-MS sampling, i.e., line scans that were conducted on each growth increment. The direction of growth is indicated as a black arrow.

2.2.3 LA-ICP-MS analysis

In preparation for chemical analysis, the portion used for growth pattern analysis was cut from each shell (Fig. 2.2) using a 150 µm-thin diamond disk (disk with galvanically bonded diamonds; Komet–Dental Gebr. Brasseler GmbH & Co. KG; Art.-No.: 6911H.-104.220) mounted to a handheld drill. To remove potential surface contaminants, the shell slab was soaked in acetic acid (10 vol%) for ca. 1 min. Followed by rinsing in deionized water. Since the studied species attains its maximum annual increment width between the 1st and the 2nd winter growth stops in scallop populations from the Bay of Brest, chemical analyses provided a nearly daily resolution.

Geochemical anylses were performed with a Laser Ablation – Inductively Coupled Plasma –

Mass Spectrometer (LA-ICP-MS) system at the Max Planck Institute for Chemistry (Mainz, Germany). In total, six shell slabs (three from 2011 and three from 2012) were analyzed for their barium (using ^{137}Ba as analyte) content. Laser scans were completed on the striae, by running the laser in line scan mode on the outer shell surface perpendicular to the growth direction and parallel to the striae (Fig. 2.2). Within each stria, measurements were completed with a laser spot diameter of 80 µm at a constant speed of 5 µm s^{-1}. Each scan was 600 µm long. Where possible, every daily stria was sampled (Fig. 2.2), unless the stria width was narrower than 80 µm (smaller than the laser spot size). Prior to sample ablation and measurement, each sample was pre-ablated (100 µm spot size, 80 µm s^{-1}) to remove potential contaminants. According to previous in-situ chemical analyses (Barats et al., 2007), trace elements are homogeneously distributed within single striae of *P. maximus*. Thus, measured signal intensities were averaged for each line scan. For consistency, reference materials used for calibration and quality control were ablated in the same manner. The ablation was performed with a NewWave Research UP-213 Nd:YAG laser ablation system (New Wave Research, Fremont, CA, USA) at a repetition rate of 10 Hz and a laser energy density of 15.8 J cm^{-2} with helium as an initial carrier gas (quality 5.0, flow rate 0.57 L min^{-1}). The reference material NIST SRM 612, a synthetic silicate glass, was used as an external standard (values obtained from the GeoReM database; http://georem.mpch-mainz.gwdg.de/; last access: 18 March 2021; Jochum et al., 2011) and ^{43}Ca was used as an internal standard to normalize obtained barium signal intensities.

A Microsoft Excel spreadsheet was used for data reduction, following the calculations provided by Longerich et al. (1996) and Jochum et al. (2007; 2011). Blanks were determined 15 s prior to ablation. Detection limits were calculated based on the 3σ criterion. All detection limits (Table 2.1) were significantly lower than the Ba/Ca_{shell} signal, with an average limit of detection of 9×10^{-6} mmol mol^{-1}. To account for uncertainties of reproducibility, the relative standard deviation in percent (RSD%) was calculated from repeated measurements of the NIST SRM 612 reference material. For Ba, an average RSD% value of 2.9% was obtained (Table 2.1). The synthetic carbonate USGS MACS-3, a pressed powder pellet, was used for quality control. Measured Ba concentrations of USGS MACS-3 differed by 1.4 to 12.2% from the published reference value (GeoReM database; Table 2.1). High deviations from the reference value might be induced by changing ablation behavior due to varying particle sizes of the MACS-3 carbonate pellet leading to differences in ionization and uncertainties of the non-certified MACS-3 reference material (Jochum et al., 2019).

2.2.4 Environmental parameters

To determine the species composition of phytoplankton and chlorophyll *a* concentration at Lanvéoc (Fig. 2.1; similar sampling size as shell collection), seawater was collected during daytime (within a 3-h window before or after high tide) using a 5 L Niskin bottle that was positioned vertically in the water column approx. 1.5 m below the water surface. In 2011, seawater was sampled once a week between January – March and July – October and twice per week from April until June. In 2012, samples were taken once a week between March and May, and biweekly between June and December. This resulted in 52 water samples collected during 2011 and 26 samples in 2012 (Supplementary Table S2.1). Each water sample (250 mL) was filled in a vial using a silicone tube that was in contact with the bottom of the bottle to avoid turbulence within the sample and to prevent the phytoplankton cells from disintegration. The phytoplankton cells were fixed with 2.5 mL of Lugol's solution and transported to the laboratory within one hour after sampling. Until further analyses, the samples were stored in a dark place to prevent the alteration of the cells by UV radiation. To determine the phytoplankton species and abundance, 50 mL of the sample was filled into a sedimentation column and left for 24 h to let the phytoplankton cells settle down onto a microscope glass slide. The species determination and the cell counting were performed by observing the recovered glass slide with an inverted microscope (Axio Observer.A1-ZEISS, Carl Zeiss MicroImaging GmbH, Göttingen, Germany). Phytoplankton cell abundances are given in cells L^{-1}. Hereafter, the short-term increase in cell concentration of a specific phytoplankton species is referred to as a phytoplankton peak or bloom, i.e., clearly observable maxima in the cell concentration time-series (see Supplementary Fig. S2.2 and S2.3). Water samples were analyzed for their chlorophyll *a* concentration by filtering the water with glass fiber filters (GF/F Whatman). Chlorophyll *a* pigments were then extracted using 6 mL of 90% acetone and stored in the dark for 12 h at 4 °C, followed by two episodes of centrifugation (for 5 and 10 min at 3000 rpm) and fluorescence measurements with a Turner Design fluorometer. The chlorophyll *a* concentration was then calculated based on the equation of Lorenzen (1966).

2.2.5 Timing of phytoplankton blooms and Ba/Ca_{shell} peaks

To evaluate the possible relationship between phytoplankton cells in the water column and exceptionally high Ba/Ca_{shell} values in *P. maximus*, the timing of blooms of different phy-

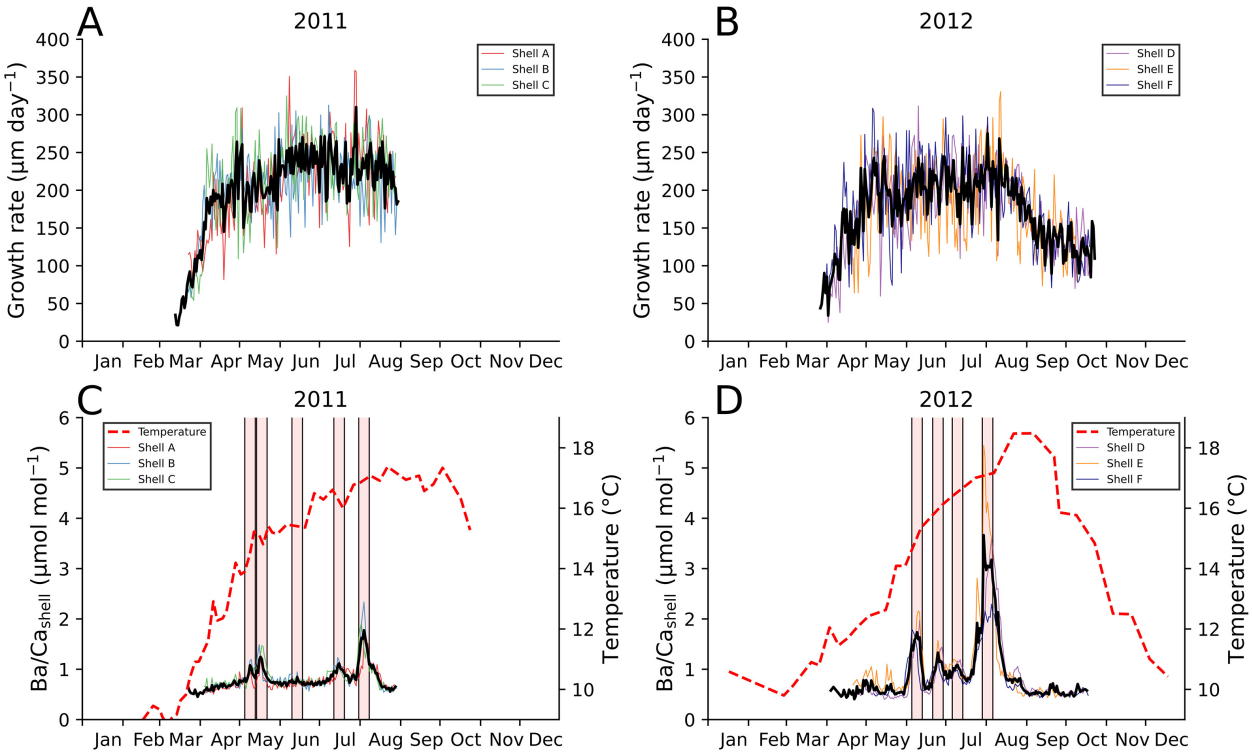

Figure 2.3 Growth rates of three age class 1 specimens from 2011 (**A**) and 2012 (**B**). The Ba/Ca_{shell} data of each specimen (**C**, **D**) were temporally aligned by counting daily growth increments from the date of collection. Black lines represent arithmetic means of shell growth rates and Ba/Ca_{shell} values for the three studied specimens in the respective year. Ba/Ca_{shell} peaks (see Table 2.2 for the exact peak position) are highlighted in red for better visual detection (peak position ±4 days). In addition, the water surface temperature measured at the site of shell collection is shown (**C**, **D**).

toplankton species was compared to the timing of Ba/Ca_{shell} peaks. Since previous studies observed a temporal lag between environmental changes, such as chlorophyll *a* peaks or phytoplankton blooms, and the occurrence of transient Ba/Ca_{shell} peaks (e.g., Barats et al., 2009; Thébault et al., 2009), the following method was used to account for this eventual temporal offset. The temporal alignment of the barium peaks was accomplished by growth pattern analysis (see section 2.2). To define a narrow temporal time frame for each distinct Ba/Ca_{shell} peak, a time interval of ±4 days was assigned for each peak (see Fig. 2.3; red areas). This time interval was determined in order to fulfill the following purposes: (1) Since small inter-shell variations in the absolute timing of Ba/Ca_{shell} peaks of contemporaneous specimens exist (e.g., the temporal occurrence of last Ba/Ca_{shell} peaks in shell E and

shell D differ about 7 days), this time interval ensures to enclose all simultaneously occurring Ba/Ca_{shell} peaks. (2) The time interval considers a small uncertainty yielded by the temporal alignment of the geochemical data (see section 2.2). (3) For the comparison between timing of Ba/Ca_{shell} peaks and species-specific phytoplankton cell concentration time-series, the assigned time intervals serve as clearly defined time frame that allows to explicitly identify time lags between a phytoplankton bloom and the occurrence of a Ba/Ca_{shell} peak.

To determine the time lag between the occurrence of blooms of specific phytoplankton cells and Ba/Ca_{shell} peaks, each phytoplankton time-series was shifted manually relative to the Ba/Ca_{shell} time-series until peaks overlapped, i.e., peaks in the phytoplankton time-series fell in the Ba/Ca_{shell} time interval (see Supplementary Fig. S2.2, S2.3). For the ease of analyzing the various phytoplankton time-series, studied phytoplankton species were classified into four categories, based on their agreement with Ba/Ca_{shell} peaks (without considering physiological characteristics). Phytoplankton time-series that were assigned to category 1 provided a distinct time lag so that all cell concentration peaks coincided to a Ba/Ca_{shell} peak. Time-series of category 2 denoted species that cell concentration peaked multiple time throughout the year, but not all phytoplankton peaks (or just minor peaks) matched with Ba/Ca_{shell} excursions after shifting the time-series with a certain temporal lag. Phytoplankton time-series were assigned to category 3 if the peaks occurred more than 30 days before the Ba/Ca_{shell} peaks, or after the last Ba/Ca_{shell} peak. All remaining species correspond to category 4 indicating that no running similarity exists between the chronologies. Consequently, species-specific time lags could only be determined for phytoplankton time-series of category 1 and 2.

Table 2.2 Determined Ba/Ca_{shell} maxima in *P. maximus* shells from 2011 and 2012 and their respective temporal occurrence within the shell chronology.

	2011		2012	
Peak#	Date	Ba/Ca_{shell} ($\mu mol\,mol^{-1}$)	Date	Ba/Ca_{shell} ($\mu mol\,mol^{-1}$)
Peak 1	05 May to 13 May	1.08	05 June to 13 June	1.73
Peak 2	14 May to 22 May	1.24	21 June to 29 June	1.33
Peak 3	10 June to 18 June	0.84	06 July to 14 July	1.08
Peak 4	12 July to 20 July	1.11	29 July to 06 August	3.66
Peak 5	31 July to 08 August	1.77	–	–

2.2.6 Evaluation of the relationship between individual phytoplankton species and Ba/Ca_{shell} using pseudo-random sampling simulations

Since it was impractical to measure the barium content of individual phytoplankton cells in the studied years, the Ba/Ca_{shell} peaks were approximated by applying a specific weighting factor to individual diatom and dinoflagellate cell concentration time-series generated by Monte Carlo simulations. The aim of this approach is to numerically analyze complex systems such as the potential relationship between Ba-associated phytoplankton cells of various species and the formation of Ba/Ca_{shell} peaks. The immense number of possibilities makes it nearly impossible to determine a theoretical factor that optimally describes the relative amount of cell-associated Ba for each phytoplankton taxon and how it contributes to the measured Ba/Ca_{shell} chronologies. The Monte Carlo method iteratively tests billions of possible scenarios by using randomly generated parameters (i.e., differently weighted phytoplankton time-series). Within each simulation, a randomly selected weighting factor (between 0 and 100) was assigned to each phytoplankton time-series that was included in the respective simulation. All time-series were temporally shifted by a previously determined time lag (see section 2.2.5). In addition, the randomly obtained values were used to assign a weight to the individual time-series by multiplying the cell concentration data with the respective weighting factor (Supplementary Fig. S2.4). For each simulation, the weighted cell concentration data of the different phytoplankton taxa were then combined to a new time-series and compared to the Ba/Ca_{shell} profile of the respective year by calculating the Pearson correlation coefficient. Each run consisted of 10^8 simulations, where the simulation with the largest Pearson correlation coefficient constituted the result of the run (see Appendix A). Sixteen different phytoplankton species were included in the simulation for 2011, and fifteen for 2012. In total, 50 runs with 5 billion tested combinations were performed for each year. Based on this large number of repetitions, a pattern could be derived that provided information about the potential species-specific contribution to the Ba/Ca_{shell} profile. The underlying assumptions for this random sampling approach were: (1) All included phytoplankton species can potentially be ingested and digested by the bivalves. (2) There is no pre-digestive selection preference of individual phytoplankton species by the scallops, i.e., all phytoplankton cells were ingested and digested proportionally to the number of cells in the water column. (3) Cells of different phytoplankton species can contain different amounts

of Ba that will end up in the shell.

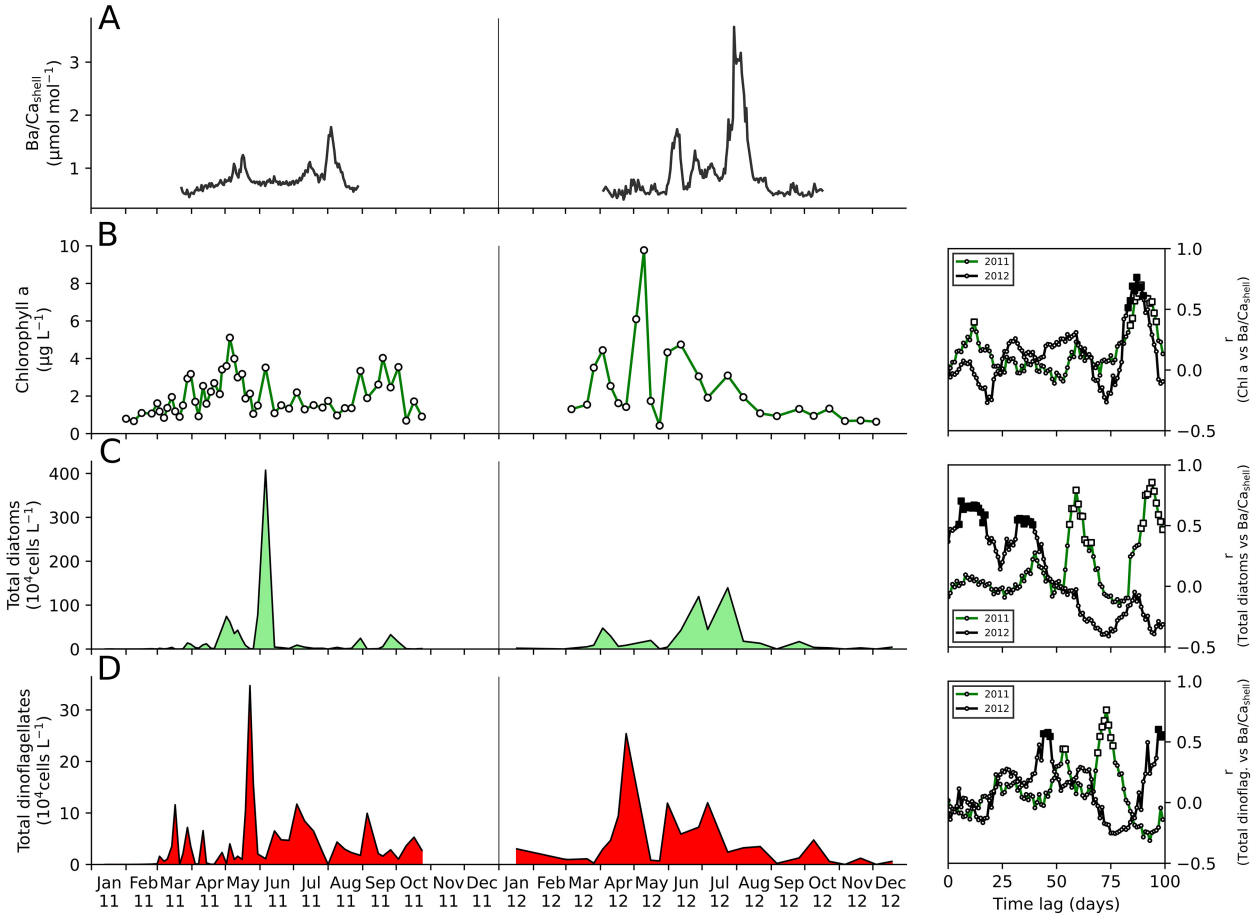

Figure 2.4 Variations in Ba/Ca_{shell} in shells from *P. maximus* (**A**), in chlorophyll *a* (**B**), total diatoms cell counts (**C**) and total dinoflagellate cell counts (**D**) at Lanvéoc during 2011 and 2012. Diagrams to the right display the Pearson correlation coefficients (r) calculated between the respective environmental parameter and the measured Ba/Ca_{shell} profiles for lags of 0 to 100 days. Statistically significant correlations (with $p < 0.05$) are depicted as solid squares.

2.3 Results

2.3.1 Shell growth patterns and Ba/Ca_{shell} profiles of *P. maximus*

Within the same calendar year, daily increment width chronologies of the studied specimens showed a high degree of synchronicity (Fig. 2.3). The general pattern of seasonal growth

during the two studied years also compared well to each other (Fig. 2.3). Annual growth lines were formed between November and March. Daily growth rates increased gradually from late March (20 to 60 µm day^{-1}) to the beginning of May. As revealed by daily growth pattern analysis, the period of maximum growth (between May and late August) of the studied *P. maximus* specimens comprised ca. 121 ± 2 days, with growth rates between 130 and 150 µm day^{-1} in 2011 and 130 and 80 µm day^{-1} in 2012 (Fig. 2.3A, B). After the end of August, growth rates declined until the date of collection (Fig. 2.3A, B).

Similar to the daily growth curves, Ba/Ca_{shell} chronologies of contemporaneous specimens agreed well with each other and exhibited a strong reproducibility (Fig. 2.3C, D). Pearson correlation coefficients ($p < 0.05$) ranged between 0.58 (shell A vs shell C) and 0.78 (shell B vs shell C) for 2011 and between 0.82 (shell D vs shell E) and 0.89 (shell D vs shell F) for 2012. In general, the Ba/Ca_{shell} profiles were characterized by a constant background level (2011: 0.63 ± 0.06 µmol mol^{-1}; 2012: 0.56 ± 0.06 µmol mol^{-1}) that was occasionally interrupted by sharp Ba/Ca_{shell} peaks (Fig. 2.3C, D, 2.4A). Despite the high Ba/Ca_{shell} reproducibility within the same calendar year, Ba/Ca_{shell} trajectories of the three shells from 2011 differed strongly from those of 2012. Five Ba/Ca_{shell} peaks were identified in the specimens from 2011 (Fig. 2.3C; Table 2.2) with average Ba/Ca_{shell} peak heights varying between 0.84 and 1.77 µmol mol^{-1}. The Ba/Ca_{shell} profiles from 2012 revealed four distinct maxima (Fig. 2.3D; Table 2.2), with peak heights ranging between 1.08 and 3.66 µmol mol^{-1}. Notably, in both studied years, strong Ba/Ca_{shell} excursions were missing at the beginning of the growing season, i.e., between March and May (Fig. 2.3C, D; Table 2.2).

2.3.2 Phytoplankton dynamics and seawater temperature

In 2011, the chlorophyll *a* concentration varied between 0.67 µg L^{-1} in February and 5.11 µg L^{-1} in May (Fig. 2.4B), with an average of 1.99 ± 1.04 µg L^{-1}. The highest chlorophyll *a* values corresponded to a diatom peak (approx. 742,500 cells L^{-1}) recorded on 2 May 2011 (referred here to as 'spring diatom bloom'). However, a much larger diatom bloom (maximum approx. 4,072,860 cells L^{-1}) that occurred on 6 June and lasted 19 days ('summer diatom bloom') was only associated with a smaller peak in chlorophyll *a* (Fig. 2.4B, C). Two smaller diatom blooms evolved during the end of August and the end of September 2011 with 244,640 and 327,300 cells L^{-1}, respectively. The largest number of dinoflagellates (approx. 347,080 cells L^{-1}) was recorded on 23 May, i.e., after the diatom spring bloom and

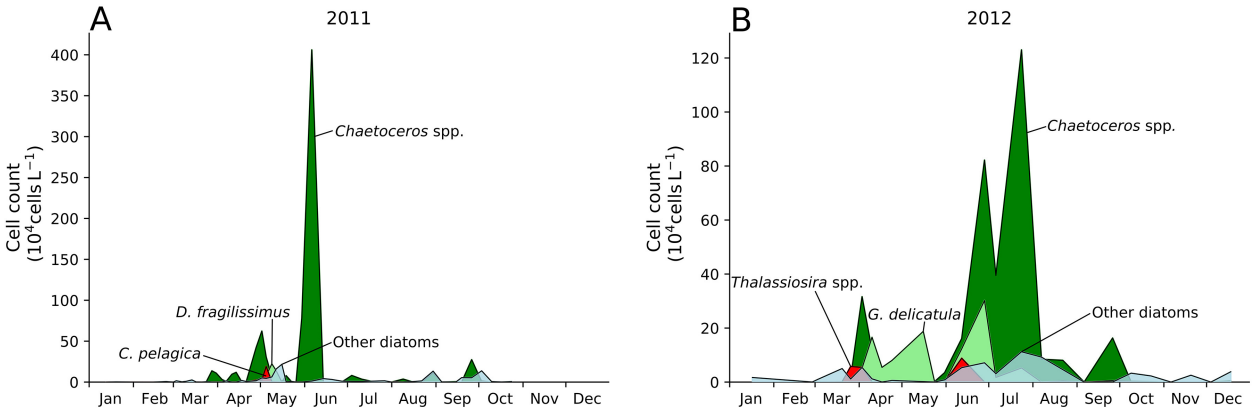

Figure 2.5 Temporal distribution and cell concentration of the three most abundant diatom species (*Chaetoceros* spp., *Dactyliosolen fragilissimus* and *Cerataulina pelagica*) and the sum of 23 minor diatoms at Lanvéoc during 2011 (**A**). The temporal variations in cell counts of *Chaetoceros* spp., *Thalassiosira* spp., *Guinardia delicatula* and the sum of 20 minor diatoms in 2012 (**B**). Species names of minor diatoms are given in Table S2.3 (Supplementary) for 2011 and Table S2.5 (Supplementary) for 2012. Note different scaling of y-axes in **A** and **B**.

prior to the summer diatom bloom (Fig. 2.4D). This dinoflagellate bloom was the largest of both studied calendar years. In addition, 11 smaller dinoflagellate peaks (on average 65,714 cells L^{-1}) occurred throughout 2011. During 2011, 25 different types of diatoms, with blooms containing more than 1000 cells L^{-1}, were identified in the surface water (Supplementary Table S2.3). By far, the most abundant diatom taxon (79.10% of total diatom cells) belonged to single, isolated cells of the genus *Chaetoceros* (Supplementary Table S2.3) and made up nearly 30% of the total phytoplankton cells at Lanvéoc. The largest bloom of *Chaetoceros* spp. emerged between 26 May and 13 June (Fig. 2.5A). During the decline of the *Chaetoceros* spp. cells around 8 May, two other diatom species started to grow, which made up the second and third most abundant diatoms in 2011, i.e., *Dactyliosolen fragilissimus* and *Cerataulina pelagica* (Supplementary Table S2.3; Fig. 2.5A). The lower abundances of *D. fragilissimus* around 12 May potentially promoted the formation of blooms composed of minor diatom species (Supplementary Table S2.3; Fig. 2.5A). After the large summer bloom, only smaller diatom blooms occurred until the end of September. Then, *Chaetoceros* spp. growth restarted concomitantly with blooms of other, less abundant diatom species. The most abundant dinoflagellates belonged to the species *Heterocapsa minima* and *Gymnodinium* sp. (with cell size >20 µm), which presented 80% of the total dinoflagellate cells

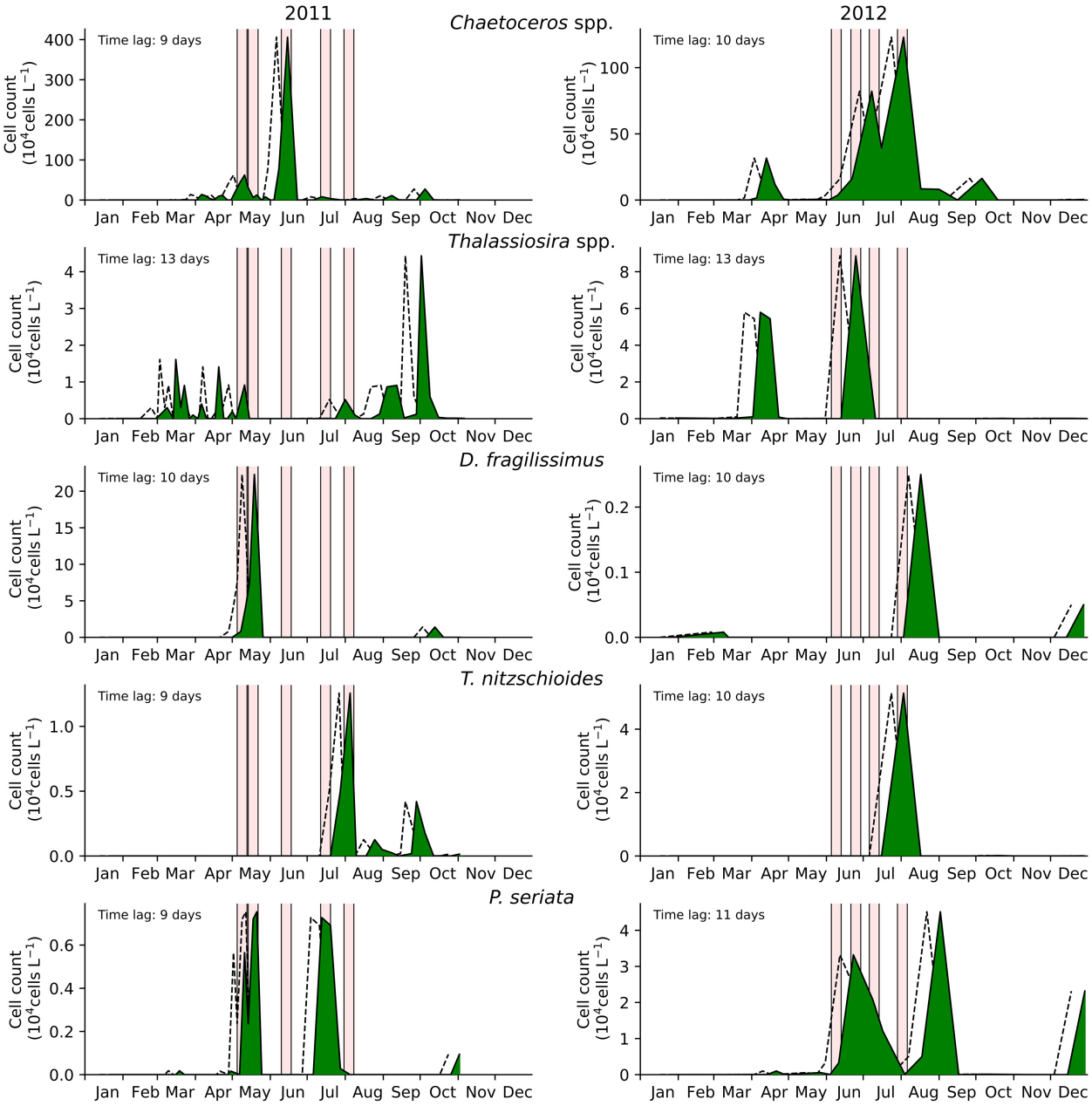

Figure 2.6 Cell counts of five different diatom species at Lanvéoc during 2011 and 2012. The dashed line represents the original time of occurrence of each species, and the green area denotes the time-shifted diatom cell counts. To compare diatom cell peaks with Ba/Ca_{shell} peaks (red, vertical areas), a species-specific time lag (in days) was applied until the peaks agreed with each other.

Table 2.3 Diatom and dinoflagellate species observed in 2011 and 2012 and their time lag between corresponding Ba/Ca_{shell} peaks.

Phytoplankton species	Taxon	2011 Time lag (days)	2012 Time lag (days)
Chaetoceros didymus	Diatom	5	13
Chaetoceros spp.	Diatom	9	10
Dinophysis acuminata	Dinoflag.	26	10
Guinardia delicatula	Diatom	25	11
Guinardia flaccida	Diatom	8	11
Haslea wawrickae	Diatom	10	12
Lepidodinium chlorophorum	Dinoflag.	12	12
Pseudo-nitzschia pungens	Diatom	10	10
Pseudo-nitzschia seriata	Diatom	9	11
Rhizosolenia imbricata	Diatom	8	10
Thalassionema nitzschioides	Diatom	9	10
Thalassiosira spp.	Diatom	13	13
Tripos kofoidii	Dinoflag.	16	12

(Supplementary Table S2.4). However, these dinoflagellates contributed only to a small extent (6.13%) to the total phytoplankton cells that were observed in 2011. The largest bloom of *H. minima* occurred around 23 May, i.e., between the largest diatom blooms (Fig. 2.4C, D). In general, blooms of dinoflagellate species emerged more frequently throughout the year (e.g., cell counts of *Gymnodinium* sp. peaked 13 times in 2011) in comparison to diatom species, though to a smaller extent.

In 2012, the chlorophyll *a* concentration fluctuated between 0.43 in late May and 9.77 $\mu g\,L^{-1}$ in early May with a mean concentration of $2.44 \pm 2.13\,\mu g\,L^{-1}$ (Fig. 2.4B). Two diatom peaks occurred on 28 June (821,830 cells L^{-1}) and 24 July (1,230,000 cells L^{-1}) that corresponded to contemporaneous elevations in chlorophyll *a* (Fig. 2.4C). However, the largest chlorophyll *a* concentration of 10 May did not coincide with seasonal diatom growth peak. Three main dinoflagellate blooms (up to 253,960 cells L^{-1}) occurred on 24 April, 3 May and 6 July (Fig. 2.4D), i.e., during time intervals of relative low diatom abundance. Similar to 2011, diatoms were dominated by *Chaetoceros* spp. (Fig. 2.5B; Supplementary Table S2.5), which contributed 63.65% to the total amount of diatom cells in 2012. Three *Chaetoceros*

spp. blooms emerged on 24 July, 28 June and 3 April. *Guinardia delicatula* and cells of the genus *Thalassiosira* made up the second and third most abundant diatoms that were present during 2012 and peaked concomitantly with the second *Chaetoceros* spp. bloom. Between mid-April and June, the diatom *G. delicatula* clearly dominated the phytoplankton community and reached a maximum on 16 May (187,770 cells L^{-1}; Fig. 2.5B). In addition, 20 minor diatom species were identified with peaks containing more than 1000 cells L^{-1} (Supplementary Table S2.5). Dinoflagellates were mostly represented by *Gymnodinium* sp. (with cell size <20 µm) and *H. minima*, which made up 78.41% of the total dinoflagellate cells but only 3.18% of the total phytoplankton cells in 2012 (Supplementary Table S2.6). These dinoflagellates emerged after the diatom spring bloom around 24 April and after the second *G. delicatula* bloom.

The diatom and dinoflagellate taxa observed in the studied period belong to phytoplankton groups typically found in the Bay of Brest (e.g., Queguiner and Tréguer, 1984). Between 2011 and 2017, approx. 46% of the total diatom cells belonged to the genus *Chaetoceros* and nearly half of the recorded dinoflagellate cells to the genus *Gymnodinium* (49%). The predominance of either diatoms or dinoflagellates was largely influenced by the availability of nutrients in the water column, e.g., the concentration of silicic acid (Ragueneau et al., 2002). In both years, the formation of large diatom blooms, which likely altered silicic acid stocks, was followed by the growth of non-siliceous dinoflagellates (Fig. 2.4C, D). The observed sea surface temperature (SST) varied between 8.7°C (February) and 17.4°C (September) in 2011 and between 9.8°C (February) and 18.5°C (August) in 2012 (Fig. 2.3C, D). In both years, the temperature stayed mostly below 12.5°C prior to the first observed Ba/Ca_{shell} peak (Table 2.2), whereas the maximum temperature occurred after the last Ba/Ca_{shell} peak.

2.3.3 Time lag between phytoplankton blooms and Ba/Ca_{shell} peaks

Fourteen phytoplankton species of 2011 were assigned to category 1 (Supplementary Table S2.2). For another 13 phytoplankton species of 2011, a temporal shift of the chronology resulted in a good agreement with the barium data, but not all phytoplankton peaks coincided perfectly with Ba/Ca_{shell} peaks (assigned to category 2; Supplementary Table S2.2). Eight phytoplankton species showed strongly elevated abundances more than 30 days before the first Ba/Ca_{shell} peak or after the last Ba/Ca_{shell} peak (category 3; Supplementary Ta-

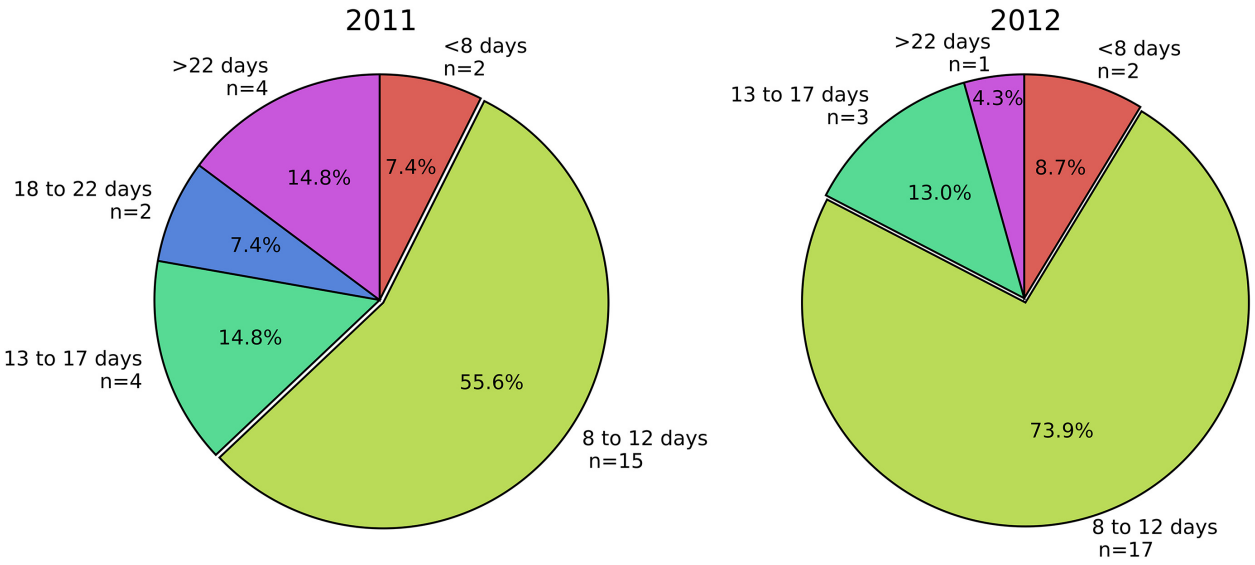

Figure 2.7 The distribution of potential time lags (in days) that were determined for different diatom and dinoflagellate genera in 2011 ($n = 27$) and 2012 ($n = 23$).

ble S2.2) and were thus not recorded in the Ba/Ca_{shell} profile. The remaining six species of 2011 did not show any running similarity with the barium data, even when different time shifts were tested (category 4; Supplementary Table S2.2). Similar results were achieved for 2012. Thirteen species fell into category 1 and ten species into category 2 (Supplementary Table S2.2). Blooms of 14 species occurred either one month before the first Ba/Ca_{shell} peak or after the last Ba/Ca_{shell} excursion (category 3; Supplementary Table S2.2). The remaining three species belonged to category 4 (Supplementary Table S2.2).

In both years, the lead time of two species relative to Ba/Ca_{shell} peaks was less than eight days (*C. didymus*, *Protoperidinium depressum* in 2011 and *Alexandrium* spp., *Chaetoceros danicus* in 2012; Fig. 2.7). For another fifteen (2011) and seventeen (2012) species, a lag by eight to twelve days (Fig. 2.7) was required to manually crossdate the phytoplankton time-series with Ba/Ca_{shell} curves. Time lags larger than twelve days were determined for ten species in 2011, with a maximum of 30 days, and four species in 2012, with a maximum of 26 days (Fig. 2.7). The manual determination of a temporal lag was ambiguous for some phytoplankton species, e.g., in 2011, the temporally non-shifted bloom of *D. fragilissimus* occurred contemporaneously with the first Ba/Ca_{shell} peak as well as with the second Ba/Ca_{shell} peak after shifting the time-series about ten days.

For ten diatoms and three dinoflagellate genera, a temporal shift could be determined that

allowed an inter-annual comparison between 2011 and 2012 (Table 2.3). Nine phytoplankton species show similar temporal offsets (with an error of ±3 days) ranging from eight to thirteen days (i.e., *Chaetoceros* spp., *Guinardia flaccida*, *Haslea wawrickae*, *Lepidodinium* cf. *chlorophorum*, *Pseudo-nitzschia pungens*, *P. seriata*, *Rhizosolenia imbricata*, *Thalassionema nitzschioides*, *Thalassiosira* spp.). Offsets of three genera differed more than eight days (Table 2.3).

2.3.4 Random sampling simulation

The Monte Carlo simulations revealed distinct, randomly approximated weighting factors for the various tested phytoplankton species (Fig. 2.8). In general, the obtained confidence intervals (95% confidence level) varied between 0.24% (*Chaetoceros* spp.) and 18.04% (*Haslea wawrickae*) in 2011, and 0.57% (*Thalassiosira* spp.) and 18.69% (*Haslea wawrickae*) in 2012. For both studied years, the highest weighting factor was determined for the diatom species *T. nitzschioides* and the lowest for the diatom genus *Chaetoceros* spp. The calculated confidence intervals decreased with decreasing weighting factors, whereas the largest ranges occurred at weighting factors around 0.5 (Fig. 2.8).

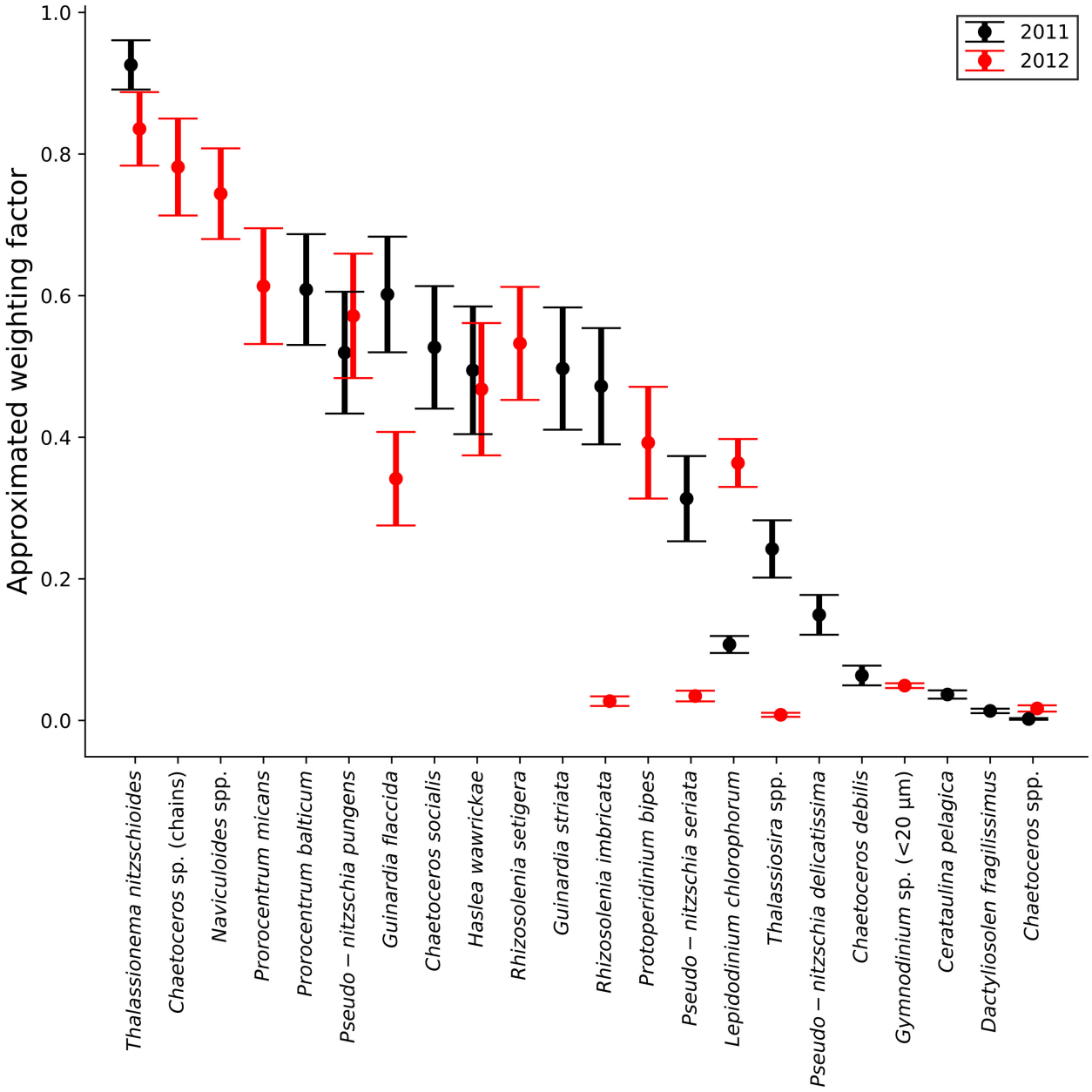

Figure 2.8 95% confidence intervals (circles indicate the corresponding mean) for different phytoplankton species calculated from 50 Monte Carlo experiments, including five billion simulations (see section 2.2.6), for 2011 and 2012. With a high probability, a certain weighting factor that describes the potential contribution of a phytoplankton species to the overall Ba/Ca_{shell} profile the best lies within the approximated weighting factor range that is determined for each species.

2.4 Discussion

In agreement with previous findings (Barats et al., 2009), sharp Ba/Ca_{shell} peaks were largely uncorrelated to chlorophyll *a* values, as well as to the total diatom and dinoflagellate abundance. However, Ba/Ca_{shell} peaks showed a strong agreement with the occurrence of certain diatom and dinoflagellate species when a short time lag of 8 to 13 days was applied. Besides this temporal accordance, Monte Carlo simulations suggested that cells of the various diatom and dinoflagellates species are likely to be associated with different amounts of Ba that can be incorporated into the shell.

2.4.1 Relationship between shell barium enrichments, chlorophyll *a* and the diatom and dinoflagellate abundance

As demonstrated by the highly resolved data, no direct link exists between Ba/Ca_{shell} profile and chlorophyll *a* pigment concentration (Fig. 2.4B). In both studied years, Ba/Ca_{shell} patterns differed significantly from the chlorophyll *a* time-series. For example, the double peak in Ba/Ca_{shell} in May 2011 (Fig. 2.4A) was not associated with a similar pattern in the chlorophyll *a* data. Although three gradually decreasing peaks occurred in the chlorophyll *a* data as well as in the Ba/Ca_{shell} profile in 2012, no temporal coincidence existed among both time-series, even when leads and lags were considered. In 2011, the highest chlorophyll *a* concentration occurred ca. 90 days before the Ba/Ca_{shell} maximum (Fig. 2.4A, B). In contrast, in May 2012, the chlorophyll *a* concentration attained a high-stand ca. 80 days before the strongest shell Ba enrichment (Fig. 2.4A, B). The strongest correlation between the two time-series was obtained when the chlorophyll *a* time-series were shifted by 86 days and thus assuming that the signal transfer from the environment into the shell took ca. three months (Fig. 2.4B; right panel). However, this deduction seems unlikely. While the largest chlorophyll *a* and barium peaks agreed with each other, many smaller Ba/Ca_{shell} peaks could not be associated with chlorophyll *a* excursions, suggesting the larger correlation coefficient results from a bias. Due to the three-month offset between the two time-series, a much lower number of data points – specifically such of the few coinciding peaks – is used to compute the Pearson correlation coefficient. Furthermore, in previously published works different lags were observed between chlorophyll *a* and Ba/Ca_{shell} profiles of scallop shells. For example, in the study by Barats et al. (2009), the temporal offset between the timing of the chlorophyll *a*

maximum and the largest Ba/Ca_{shell} peak varied strongly from year to year (ca. seven to 83 days). Gillikin et al. (2008) described a similarity between the overall chlorophyll *a* pattern and the Ba/Ca_{shell} peaks with an offset of 40 days, whereas Thébault et al. (2009) observed an offset of about one week in juvenile scallops of *Comptopallium radula*. It appears that the chlorophyll *a* maximum, which is usually associated with the phytoplankton spring bloom in the Bay of Brest, always occurs prior to the Ba/Ca_{shell} maximum, but with variable temporal offsets. Together with these findings, the data presented in the current study suggest no direct link between the chlorophyll *a* pigment concentration and the formation of Ba/Ca_{shell} maxima. However, it should be mentioned that the chlorophyll *a* concentration is not an ideal indicator for the total phytoplankton biomass (Desortová, 1981; Kruskopf and Flynn, 2006) as the chlorophyll *a* concentration is also affected by light and nutrient availability, algal composition and the physiological condition of the phytoplankton cells (Behrenfeld et al., 2005; Behrenfeld and Boss, 2006; Lee et al., 2020).

Time-series of the total amount of diatom cells in the water column differed between the studied sampling years (Fig. 2.4C). At first sight, a relationship between blooms of diatoms and the Ba/Ca_{shell} peaks cannot be determined. However, some similarities are evident: Firstly, the double peak associated with the spring bloom in 2011 also occurred in the Ba/Ca_{shell} time-series, but with an offset of about nine days. In addition, after a similar temporal lag of nine days, the largest diatom cell concentration that was observed in both years coincided with the smallest Ba/Ca_{shell} peak (Fig. 2.4A, C). In 2012, only a smaller diatom spring bloom was observed followed by two larger summer blooms that were synchronized with the third and fourth Ba/Ca_{shell} peak with an offset of about ten days (Fig. 2.4A, C). Despite these overlapping patterns, not all Ba/Ca_{shell} peaks can be adequately explained as a response to the total diatom cell counts, i.e., the fourth peak in 2011 and the first and second peaks in 2012. Moreover, the Ba/Ca_{shell} peaks appear to be unrelated to the magnitude of the diatom cell concentration. For example, the largest diatom bloom in 2011 was associated with the lowest Ba enrichment, whereas the largest Ba peak (in 2012) can solely be attributed to a smaller diatom bloom. These observations were supported by the correlation coefficient plots (Fig. 2.4C; right panel) suggesting no statistical relationship exists between the total amount of diatom cells in the water column and the formation of Ba/Ca_{shell} peaks.

In both years, the concentration of dinoflagellate cells is significantly smaller than that of diatoms (Fig. 2.4D), which is a common observation in the Bay of Brest (Del Amo et al.,

1997). The dinoflagellate time-series revealed several cell count maxima throughout both years. This impedes the comparison between Ba/Ca_{shell} peaks and dinoflagellate blooms because an unambiguous bloom-to-Ba/Ca_{shell} peak assignment was difficult to obtain. The correlation coefficients (Fig. 2.4D) indicated that no significant correlation existed in both years when a similar time lag was applied. Thus, a causal relationship between the total cell concentration of dinoflagellates and Ba/Ca_{shell} peaks could not be verified.

The lack of similarity between the observed bulk phytoplankton dynamics and the Ba/Ca_{shell} peaks can likely be attributed to differences in the species composition of different chlorophyll *a*, diatoms, and dinoflagellate peaks (e.g., compare Fig. 2.4C and Fig. 2.5; each diatom peak differs in species composition). It was demonstrated that particle retention and subsequent ingestion in heterorhabdic bivalves (i.e., bivalves with gills containing two types of filaments), such as *P. maximus*, is not solely influenced by particle size (i.e., phytoplankton cell size) but is also affected by the nutritional value of the particles (Shumway et al., 1997; Chauvaud et al., 2001; Beninger et al., 2004; Ward and Shumway, 2004). This selective filter behavior supports the assumption that not all of the observed phytoplankton species, summarized in the bulk phytoplankton time-series, were consumed by the bivalves because the various taxa differed in cell size and nutritional value. In addition, different diatom species were shown to adsorb different amounts of barium leading to a variable vertical flux of this element toward the sediment water interface (SWI) (Dehairs et al., 1980; Fisher et al., 1991). In addition, environmental variables such as pH, iron supply and the dissolved Ba concentration in the water column affect the amount of phytoplankton cell-associated Ba that reaches the SWI (Sternberg et al., 2005). Accordingly, a species-specific comparison of individual phytoplankton genera and the timing of Ba/Ca_{shell} peaks is necessary to further disentangle a potential link between phytoplankton and barium peaks in the shell.

2.4.2 Ba/Ca_{shell} peaks and the timing of individual phytoplankton genera

In both studied years, most diatom blooms coincided with a subsequent formation of Ba/Ca_{shell} enrichments after a time lag of eight to twelve days, and only a few genera required larger or smaller theoretical temporal shifts to synchronize the peak patterns (Fig. 2.7, Supplementary Table S2.2). This observation is in accordance with the temporal offset determined for the total amount of diatom cells and the Ba/Ca_{shell} maxima (nine to ten

days; section 2.4.1), as the total diatom cell concentration is largely influenced by a single diatom genus (Fig. 2.6; *Chaetoceros* spp.; this diatom group accounted for nearly 80% and 65% of the total diatom cells in 2011 and 2012, respectively). If the underlying hypothesis holds, i.e., that Ba/Ca_{shell} peaks are related to specific Ba-rich phytoplankton cells, Ba/Ca_{shell} peaks may not only be explained by blooms of the main diatom genus *Chaetoceros* spp., but also by blooms of less abundant diatom species (when a time lag of a few days was applied). However, most of the dinoflagellate species do not provide an observable relationship between the cell concentration time-series and Ba/Ca_{shell} peaks (Supplementary Table S2.2).

The comparison between species-specific temporal lags obtained for both years (Table 2.3; Supplementary Table S2.2) allows to evaluate inter-annual similarities of individual phytoplankton species with the timing of Ba/Ca_{shell} peaks. Unfortunately, not all phytoplankton species present in 2011 also occurred in 2012, and vice versa (Supplementary Table S2.2). From the genera identified in both years, the blooms of nearly all species (except four) fitted best with Ba/Ca_{shell} peaks when a lag of 8 to 13 days was applied, with a small species-specific year-to-year difference of less than three days (Table 2.3). The heterogeneous patterns in the timing of Ba/Ca_{shell} peaks between 2011 and 2012, on the one hand, and the similarity of theoretically determined time lags, on the other hand, supports the assumption that a potential link exists between blooms of specific phytoplankton species (i.e., especially diatoms) and the incorporation of Ba into the shell. In other words, if there were no causal relationship between the timing of phytoplankton blooms and the occurrence of Ba/Ca_{shell} peaks it would be highly unlikely to expect similarities in the temporal lags between the two studied years (see Fig. 2.7).

2.4.3 Time lag

Although the Bay of Brest is a well-mixed ecosystem, the distribution of phytoplankton species varied between different sites (see Thébault and Chauvaud, 2013) and between bottom and surface waters. For instance, the main bloom of the diatom genus *Chaetoceros* near the sea surface was only recorded contemporaneously to a small extent at the SWI (see Supplementary Fig. S2.5). This vertically heterogenous phytoplankton distribution indicates that observed blooms in the upper water column do not occur simultaneously at the SWI. Consequently, a temporal offset has to be considered between the formation of a phytoplankton bloom at the surface and the time the cells require to reach the SWI where they

are potentially ingested by filter feeders. Therefore, the time lag between a phytoplankton bloom and the subsequent formation of Ba/Ca_{shell} peaks is influenced by the sedimentation rate of the phytoplankton cells as well as the time it takes for Ba to be incorporated into the shell calcite after ingestion.

As shown in section 2.4.2, the shell Ba content lagged behind the majority of phytoplankton blooms by about 8 to 13 days (Fig. 2.7). The phytoplankton cell identifications were performed on water samples from 2 m below sea surface and the water depth at Lanvéoc is approx. 8 m. To reach the SWI within less than 8 to 13 days, phytoplankton cells have to sink, on average, 0.46 to 0.75 $m\,d^{-1}$. This sinking velocity is in the range observed for various phytoplankton species (Peperzak et al., 2003). However, it is shown that the sinking rate of phytoplankton cells does not correlate with the biovolume of the cells, but is rather influenced by the nutrient availability in the medium and by the colony density (Bienfang et al., 1982). Furthermore, aggregate forming diatoms exhibit a sinking velocity two orders of magnitude higher than that of unicellular diatoms (Alldredge and Gotschalk, 1989) leading to a rapid vertical flux of particles toward the SWI. In addition, the water depth strongly varies with the tide leading to a rapidly changing height of the water column throughout the year. These characteristics impede a theoretical approximation of a temporal lag solely based on constantly sinking particles from the upper part of the water column to the SWI.

Following Tabouret et al. (2012), Ba was enriched in the shell of *P. maximus* 6 to 8 days after an elevated level of dissolved Ba was measured in the ambient water. However, the sharp peaks in Ba/Ca_{shell} are potentially induced by the ingestion of phytoplankton cells containing Ba (Thébault et al., 2009) rather than dissolved Ba in the water column (Gillikin et al., 2008; Barats et al., 2009; Poitevin et al., 2020). The ingestion of Ba-rich phytoplankton cells is followed by a subsequent desorption of Ba in the digestive tract induced by the low gut pH. This results in larger amounts of Ba^{2+} reaching the site of shell formation (extrapallial space). Based on the high filtration rate of scallops (5 $L\,h^{-1}\,g^{-1}$ dry weight) (Palmer, 1980; Laing, 2004), and the high biomineralization rates of *P. maximus* (Fig. 2.3A, B), especially after the first winter growth cessation, scallops could incorporate Ba into their shells rapidly. Therefore, it is reasonable to consider the observed temporal offset of 8 to 13 days in *P. maximus* as a potential time lag, although future studies about the species-specific sinking, digestion and incorporation rates of barium rich particles are needed to further prove such a lag. It should be mentioned that there is a small uncertainty (±2 days) given in the dating of the Ba/Ca_{shell} profiles and in the exact timing of phytoplankton

cell peaks. Here, the measured maximum cell concentration of a respective bloom was used to determine the initial timing of the bloom. However, the actual bloom eventually arose shortly before or after the sampling (this can be concluded from the slight asymmetrical shape of the phytoplankton abundance peaks; see Fig. 2.6).

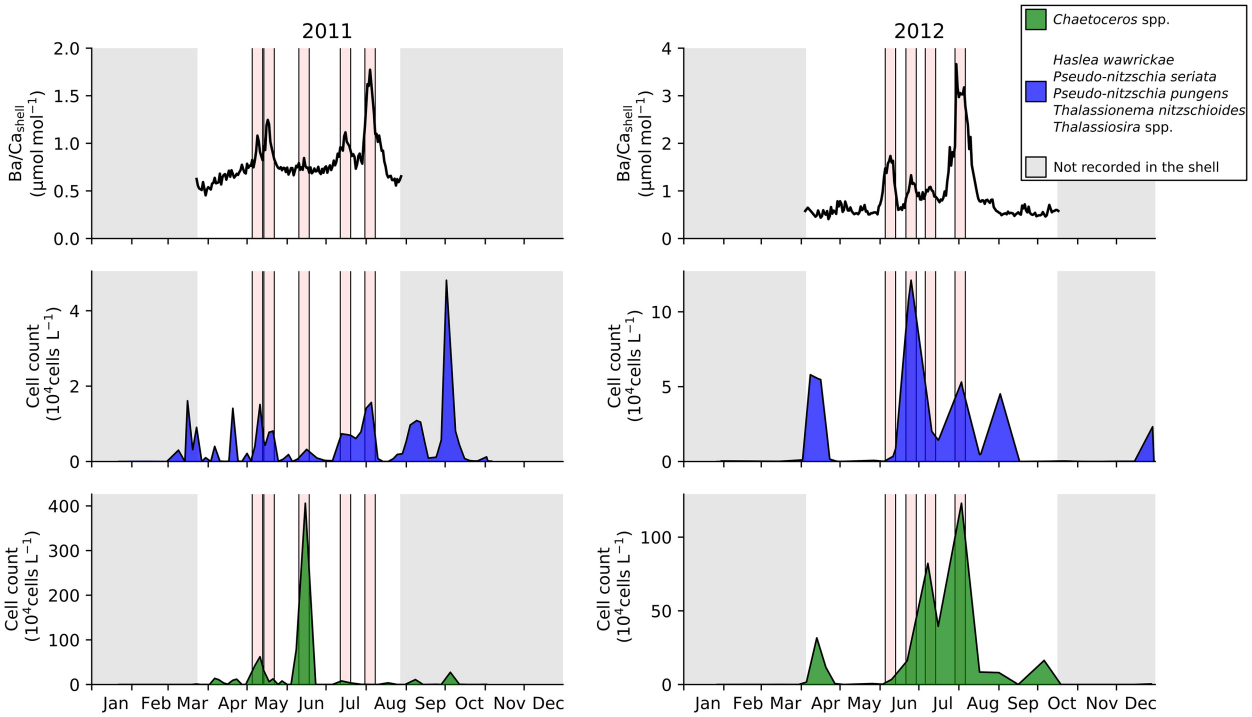

Figure 2.9 Synchronicity of Ba/Ca_{shell} peaks (1st subplot) and six diatom species after applying a species-specific time lag of 8 to 13 days. The blue area (2nd subplot) indicates the sum of five diatoms referenced in the legend. To account for the exceedingly large abundance of *Chaetoceros* spp. cells in the studied years this species is displayed in an additional subplot (3rd subplot).

2.4.4 Magnitude of Ba/Ca_{shell} peaks as a response to blooms of specific phytoplankton species

As previously shown, the timing of most phytoplankton blooms that were observed in both years coincided with Ba/Ca_{shell} peaks considering a small temporal lag (see Table 2.3). However, if a direct link exists between the mass occurrence of certain phytoplankton species and the subsequent formation of Ba enrichments in the shell, the monitored cell concentrations did not serve as a suitable estimate for the amount of Ba that reached the site of shell

formation, because the sum of cells of different phytoplankton time-series did not correlate well with the Ba/Ca_{shell} peak heights (Fig. 2.9). For example, the large abundance of the main diatom *Chaetoceros* spp. in 2011 coincided with the smallest Ba enrichment (Fig. 2.9; lower panel). Although peaks were temporally overlapping, the Ba/Ca_{shell} magnitude is not correlated with relative variations in the cell concentration. In addition, some blooms were not coinciding with Ba enrichments, in particular at the start of the growing season (see Fig. 2.6; blooms of *Thalassiosira* spp.). Therefore, even when considering a reasonable time lag, Ba/Ca_{shell} profiles cannot be reconstructed from the phytoplankton cell concentration time-series.

Three potential explanations for the observed discrepancies between the magnitude of Ba/Ca_{shell} peaks and cell concentrations are described as follows. (1) Temperature may affect the filtration activity of the bivalve (Laing, 2000; Laing, 2004). A gradual reduction in the filtration rate was determined for temperatures below 11°C (Laing, 2004) which potentially hampers the formation of excessive Ba/Ca_{shell} peaks due to a reduced ingestion of Ba-rich particles. Although seawater temperature appears to have occasionally influenced the formation of Ba/Ca_{shell} peaks at the beginning of the growing season, when temperatures dropped below 12.5°C (Fig. 2.3C, D), Barats et al. (2009) demonstrated that no significant correlation exists between Ba/Ca_{shell} ratios and SST. (2) The ability of the scallop gills to selectively filter particles out of the water column based on the particle size as well as the nutritional value (e.g., Beninger et al., 1992; Shumway et al., 1997; Beninger et al., 2004) is likely to account for the observation that not all blooms of certain phytoplankton taxa could be assigned to Ba enrichments in the shell. Although this assumption does not apply for the discrepancies between blooms of the two diatom genera *Chaetoceros* and *Thalassiosira* and Ba/Ca_{shell} peaks (see Fig. 2.6), as these diatoms were known to be consumed by *P. maximus* (Paulet et al., 1988; Lorrain et al., 2000; Laing, 2004), it may account for other phytoplankton species. (3) Environmental influences alter the phytoplankton cell-associated amount of Ba and/or species-specific differences in the ability to adsorb Ba. Following Sternberg et al. (2005), Ba is adsorbed onto iron oxyhydroxides on phytoplankton cell walls indicating that the ingestion and digestion of these Ba-rich cell walls account for the formation of Ba/Ca_{shell} peaks (Thébault et al., 2009). As environmental conditions such as pH, iron and dissolved Ba concentration of the ambient seawater influence the amount of Ba linked to the cell walls (Fisher et al., 1991; Sternberg et al., 2005), these parameters should be taken into account when approximating the amount of Ba potentially reaching the site of

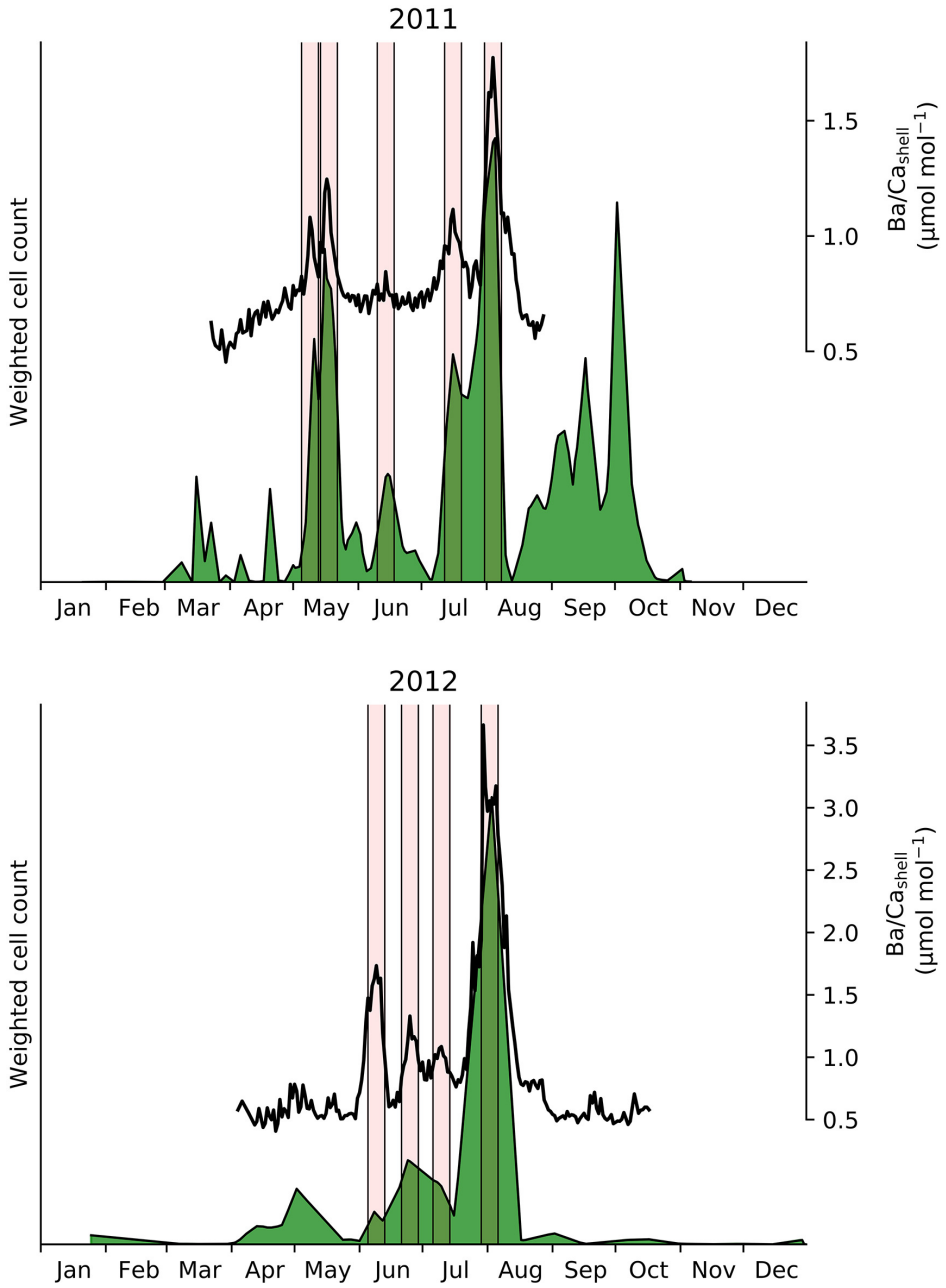

Figure 2.10 The sum of cells of differently weighted phytoplankton species (green area), after a time lag of 8 to 13 days, for 2011 (16 species) and 2012 (15 species) and the respective Ba/Ca_{shell} profiles. The species-specific factors were approximated by several Monte Carlo simulations (see section 2.2.6). The weighted cell counts are given in arbitrary units.

biomineralization. Water pH did not vary strongly throughout 2011 and 2012 (average pH: 8.0 ± 0.1 in 2011 and 8.1 ± 0.1 in 2012) and was in the range described by Sternberg et al. (2005) to favor Ba adsorption onto phytoplankton cells. Unfortunately, iron and dissolved Ba concentration were not recorded in the studied years, but Barats et al. (2009) demonstrated that the dissolved Ba concentration is not correlated to the formation of transient Ba/Ca_{shell} peaks. However, detailed environmental records are needed to better assess the relationship of plankton-associated Ba and Ba enrichments in scallop shells.

To further address the observed discrepancies in cell concentration and the magnitude of Ba/Ca_{shell} peaks, a species-specific Ba enrichment factor was introduced, as previous studies reported a large variability in cell-associated Ba among various phytoplankton species (Roth and Riley, 1971; Dehairs et al., 1980; Fisher et al., 1991). First, it is hypothesized here that the cell surface area of the individual phytoplankton cells potentially serves as a rough estimator for the amount of Ba that can be attributed to a single cell, as demonstrated by Sternberg et al. (2005), Ba is adsorbed onto phytoplankton cell walls. However, testing this assumption did not provide adequate results, indicating that the surface area of individual phytoplankton species alone could not satisfactorily describe the relationship between the cell concentration and the magnitude of Ba/Ca_{shell} peaks (see Supplementary Fig. S2.6). Therefore, another approach was considered to assess and quantify the contribution of specific phytoplankton species to the observed Ba/Ca_{shell} profile, i.e., Monte Carlo simulations that randomly tested a huge number (five billion simulations per year) of different species-specific weighting combinations. This random sampling approach allowed to (1) weight each phytoplankton species individually, (2) calculate probability ranges that likely contain a deterministic best-fit weighting factor, (3) to draw species-specific conclusion and (4) to conduct an inter-annual comparison. The weights determined from these simulations (Fig. 2.8) represent species-specific approximations comprising and quantifying potential physiological and morphological variables (e.g., cell surface area, cell ornamentation, Si-content of the cell wall, microstructure of the cell wall, hydrous ferric oxide concentration of the cell surface) affecting the amount of Ba associated with a single cell.

The results (Fig. 2.8) demonstrate a clear pattern: Different phytoplankton species likely contribute differently to the Ba/Ca_{shell} profiles, e.g., the largest weight was assigned to the diatom *T. nitzschioides* (Fig. 2.8). Individual cells of this species contribute more to the Ba content of the shell than cells of other species. Interestingly, this conclusion can be drawn from simulations independently performed for both studied years, which in turn, pro-

motes the reliability of this random sampling approach. Since similar weights for both years were also obtained for other species, i.e., *P. pungens*, *Haslea wawrickae*, *Chaetoceros* spp. (Fig. 2.8), it is rather inappropriate to consider these results as simply random outcomes, although the approximations are based on random sampling. However, for some species larger inter-annual differences in weighting factors were obtained, i.e., *G. flaccida*, *R. imbricata*, *Pseudo-nitzschia seriata*, *Lepidodinium chlorophorum* and *Thalassiosira* spp. (Fig. 2.8; maximum difference of 45% between the mean weighting factors for *R. imbricata*). Accordingly, the influence of these species to the total Ba/Ca_{shell} profile likely differed between the studied years. Since the approximation of the species-specific weights were based on simple assumptions (section 2.2.6), variable environmental factors likely affected the amount of cell-associated Ba, and potential differences in Ba assimilation rates contributed to the observed deviations among years. In addition, the simulations theoretically estimated the weighting factors while discarding a potential feeding preference of the scallops which could also account for inter-annual discrepancies observed for some phytoplankton taxa.

Many diatom species form large aggregates (Alldredge and Gotschalk, 1989), reaching several millimeters to centimeters in size, when the cells are physiologically stressed. These aggregates form at the end of an efflorescence and could cause gill clogging and a reduction in growth and filtration rates in scallops (e.g., Chauvaud et al., 1998; Lorrain et al., 2000). Likely, an increased amount of Ba is linked to polysaccharides exudated by flocculated diatoms (e.g., Alldredge et al., 1993; Stecher and Kogut, 1999; Martinez-Ruiz et al., 2018) which can support the formation of Ba/Ca_{shell} peaks in scallop shells after ingestion of such aggregates. Accordingly, it should be hypothesized that aggregated diatoms can accumulate Ba to different amounts than single diatom cells.

Taking the species-specific weights and temporal lags (between 8 and 13 days) into account results in the time-series depicted in Fig. 2.10. These time-series compare well to the Ba/Ca_{shell} profiles of the respective year and reveal relationships between different phytoplankton species and the Ba/Ca_{shell} profile. Using this configuration, all Ba/Ca_{shell} peaks can be explained with temporally lagged blooms of different phytoplankton species. Moreover, the magnitude of the shell Ba enrichments is approximated by weighting each bloom individually. Except for the first Ba/Ca_{shell} peak in 2012 (Fig. 2.10), the relative magnitude of the Ba enrichments was well approximated. This can potentially be attributed to the fact that only diatoms and dinoflagellate species with cell concentrations larger than 1000 cells L^{-1} were included in this study. Furthermore, minor blooms or the overall sum of minor blooms

could have also contributed to the Ba/Ca_{shell} peak.

The proposed species-specific contribution to the Ba/Ca_{shell} profile should be evaluated by actual measurements and quantified in future studies. Since blooms of diatoms are likely to induce shell Ba enrichments, a special focus of subsequent experiments should be placed on phytoplankton species and their potential to adsorb Ba onto their cells. Furthermore, potential differences in the Ba content between unicellular and aggregate forming species have to be evaluated. To refine the determination of digestible phytoplankton species and their barium load, the feeding behavior of scallops should also be further assessed. Since this study solely focused on diatom and dinoflagellate species, it will be inevitable to consider other taxonomic groups that can also affect the formation of Ba/Ca_{shell} peaks. Concerning the methodology, to the best of our knowledge, this study constitutes the first attempt to include random sampling simulations to reconstruct geochemical information from bivalve shells from complex environmental records, such as phytoplankton time-series, providing a promising tool for future studies to detect potential patterns between environment and geochemistry.

2.5 Summary and conclusions

According to the findings presented herein, Ba/Ca_{shell} peaks of *P. maximus* were most likely induced by blooms of specific phytoplankton taxa, especially diatoms. This assumption is based upon the following findings: (1) Neither the amount of chlorophyll *a* pigment concentration nor the total cell concentration of dinoflagellates can explain the Ba/Ca_{shell} patterns. The total cell concentration of diatoms agreed only weakly with the barium signals, even when a temporal offset of nine to ten days was assumed. (2) Time lags between the occurrence of blooms of certain phytoplankton species and the timing of Ba/Ca_{shell} peaks indicate that the shell Ba enrichments are related to the mass production of certain phytoplankton species. Actually, many species appeared eight to thirteen days prior to the formation of a Ba/Ca_{shell} peak. (3) Not all phytoplankton species could be linked with Ba/Ca_{shell} peaks, suggesting a capability of scallops to select which particles can be ingested. It is shown that the magnitude of the Ba/Ca_{shell} peaks does not correlate with the concentration of identified cells in the water column. However, applying species-specific weighting factors results in a high degree of running similarity between the Ba/Ca_{shell} and the weighted cell concentration time-series. Thus, a species-specific amount of frustule-associated Ba is likely.

Ba/Ca_{shell} profiles were associated with specific phytoplankton taxa. Therefore, the timing and magnitude of Ba/Ca_{shell} peaks can potentially serve as a proxy for the dynamics of specific phytoplankton taxa. The species-specificity of Ba/Ca_{shell} peaks limits the usability of Ba/Ca_{shell} profiles as an indicator for the overall phytoplankton dynamics that prevailed in the water column. However, understanding this connection between edible phytoplankton species and Ba in shells could help to evaluate past phytoplankton community structures on a species level. Findings of the present study are important to further constrain the applicability of Ba/Ca_{shell} of *P. maximus* and can potentially be extrapolated to other bivalve species.

2.6 Supplementary material

2.6.1 Appendix A – Description of the Monte Carlo simulation

In this study, 10 billion individual pseudo-random sampling simulations were computed. For performance reasons, the simulations were conducted using the scripting language C++ (version C++14). In general, the algorithm contains the following steps: (1) Reading time-series data (Ba/Ca_{shell} and phytoplankton cell concentration time-series (n)) and storing into computer memory. (2) Initialize a random number generator and define its seed value (read below). (3) Performing 10^8 iterations. (4) Within each iteration, generate n pseudo-random integer values ($0 \geq x \leq 100$) and (5) multiply each phytoplankton time-series data with its respectively generated value. (6) Calculating the sum of all randomly weighted phytoplankton time-series. (7) Computing the Pearson correlation between the Ba/Ca_{shell} and the randomly generated phytoplankton sum time-series. (8) If the Pearson correlation coefficient of an iteration is higher than a previously calculated one, store the correlation coefficient as well as the randomly generated integer values. (9) After all iterations, return the largest correlation coefficient and the random weighting factors, as well as the initial seed value.

Since computer-based calculations are purely deterministic, generating 'real' random numbers is not possible. However, different algorithms allow to determine equidistributed and reproducible pseudo-random numbers that were calculated based on an initial seed value, i.e., a value that should be different for each run. In this study, the pseudo-random numbers were generated based on the Mersenne Twister algorithm (Matsumoto and Nishimura, 1998) using an initial seed value that is given by the number of seconds that have passed since 00:00:00 GMT, 01 January, 1970.

Table S2.1 Date of collection of each water sample at Lanvéoc during the observation period in 2011 and 2012.

Sample #	2011	2012
1	13 January 2011	17 January 2012
2	20 January 2011	28 February 2012
3	01 February 2011	03 March 2012
4	15 February 2011	20 March 2012
5	24 February 2011	26 March 2012
6	01 March 2011	03 April 2012
7	03 March 2011	10 April 2012
8	07 March 2011	17 April 2012
9	10 March 2011	24 April 2012
10	14 March 2011	16 May 2012
11	17 March 2011	24 May 2012
12	21 March 2011	31 May 2012
13	24 March 2011	12 June 2012
14	28 March 2011	28 June 2012
15	31 March 2011	06 July 2012
16	04 April 2011	24 July 2012
17	07 April 2011	07 August 2012
18	11 April 2011	22 August 2012
19	14 April 2011	06 September 2012
20	18 April 2011	26 September 2012
21	21 April 2011	09 October 2012
22	28 April 2011	23 October 2012
23	02 May 2011	06 November 2012
24	05 May 2011	20 November 2012
25	09 May 2011	04 December 2012
26	12 May 2011	18 December 2012
27	16 May 2011	–
28	19 May 2011	–
29	23 May 2011	–

30	26 May 2011	–
31	30 May 2011	–
32	06 June 2011	–
33	14 June 2011	–
34	20 June 2011	–
35	27 June 2011	–
36	04 July 2011	–
37	11 July 2011	–
38	19 July 2011	–
39	27 July 2011	–
40	01 August 2011	–
41	09 August 2011	–
42	16 August 2011	–
43	22 August 2011	–
44	30 August 2011	–
45	05 September 2011	–
46	15 September 2011	–
47	19 September 2011	–
48	26 September 2011	–
49	03 October 2011	–
50	10 October 2011	–
51	17 October 2011	–
52	24 October 2011	–

Table S2.2 Estimated time lag for each diatom and dinoflagellate species observed in 2011 and 2012, with cell counts ≥ 1000 cells L^{-1}. Each species was assigned to one out of four categories (category 1: all or the majority of peaks coincided with Ba/Ca_{shell} maxima; category 2: not all peaks coincided with Ba/Ca_{shell} maxima; category 3: phytoplankton peaks too early or too late; category 4: phytoplankton peaks do not fit to Ba/Ca_{shell} maxima). If no category was assigned, the phytoplankton species was not observed during the respective year.

Phytoplankton species	Taxon	2011		2012	
		Category	Time lag (days)	Category	Time lag (days)
Alexandrium spp.	Dinoflag.			2	6
Cerataulina pelagica	Diatom	1	11		
Chaetoceros curvisetus	Diatom	2	16		
Chaetoceros danicus	Diatom			1	7
Chaetoceros debilis	Diatom	1	9	3	
Chaetoceros didymus	Diatom	2	5	2	13
Chaetoceros pseudobrevis	Diatom	1	20		
Chaetoceros socialis	Diatom	1	8		
Chaetoceros sp. (chains)	Diatom			1	10
Chaetoceros spp.	Diatom	1	9	1	10
Coscinodiscus wailesii	Diatom	2	30	3	
Cyclotella sp.	Diatom	3		3	
Cylindrotheca closterium	Diatom	3		3	
Dactyliosolen fragilissimus	Diatom	1	10	3	
Diatoma vulgare	Diatom			3	
Dinophysis acuminata	Dinoflag.	2	26	2	10
Guinardia delicatula	Diatom	1	25	1	11
Guinardia flaccida	Diatom	2	8	2	11
Guinardia striata	Diatom	2	11	3	
Gymnodinium sp. ($<20\,\mu m$)	Dinoflag.			2	8
Gymnodinium sp. ($>20\,\mu m$)	Dinoflag.	4		4	
Gyrodinium flagellare	Dinoflag.	3		1	26
Gyrodinium spp.	Dinoflag.	4		3	

Haslea wawrickae	Diatom	2	10	1	12
Heterocapsa minima	Dinoflag.	2	22	4	
Heterocapsa triquetra	Dinoflag.	4			
Lauderia annulata	Diatom			3	
Lepidodinium chlorophorum	Dinoflag.	2	12	1	12
Leptocylindrus danicus	Diatom	1	30		
Minidiscus sp.	Diatom	3		3	
Navicula sp. (8–10 µm)	Diatom	3		3	
Naviculoides spp.	Diatom	3		2	8
Nitzschia longissima	Diatom	2	16		
Prorocentrum balticum	Dinoflag.	1	10	3	
Prorocentrum micans	Dinoflag.	4		2	12
Prorocentrum triestinum	Dinoflag.	3		1	15
Protoperidinium bipes	Dinoflag.	4		1	12
Protoperidinium depressum	Dinoflag.	1	6		
Pseudo-nitzschia delicatissima	Diatom	1	8	3	
Pseudo-nitzschia pungens	Diatom	2	10	1	10
Pseudo-nitzschia seriata	Diatom	1	9	2	11
Rhizosolenia imbricata	Diatom	2	8	2	10
Rhizosolenia setigera	Diatom	3		2	12
Scrippsiella sp.	Dinoflag.	4		4	
Skeletonema marinoi	Diatom	3		3	
Thalassionema nitzschioides	Diatom	1	9	1	10
Thalassiosira spp.	Diatom	1	13	1	13
Tripos kofoidii	Dinoflag.	2	16	1	12

Table S2.3 Overview of the most abundant diatoms (cell concentration ≥ 1000 cells L^{-1}) observed in surface waters at Lanvéoc in 2011 and the corresponding date of the maximum bloom.

Diatom	Max. abundance (cells L^{-1})	Date of max. peak	% of total diatom cells	% of total phytoplankton cells	Cell surface (μm^2)
Chaetoceros spp.	4,060,000	06 June	79.10	29.03	627
Dactyliosolen fragilissimus	222,880	09 May	5.29	1.94	1,263
Cerataulina pelagica	190,900	05 May	2.59	0.95	9,186
Leptocylindrus danicus	144,720	16 May	3.04	1.12	4,532
Guinardia delicatula	129,900	03 October	3.38	1.24	4,213
Chaetoceros didymus	70,350	16 May	2.02	0.74	849
Thalassiosira spp.	44,310	19 September	1.47	0.54	1,624
Chaetoceros debilis	37,170	02 May	0.63	0.23	1,205
Cyclotella sp.	26,180	14 March	0.28	0.10	249
Pseudo-nitzschia delicatissima	22,610	12 May	0.41	0.15	952
Chaetoceros pseudobrevis	17,110	18 April	0.32	0.12	1,133
Thalassionema nitzschioides	12,560	27 July	0.27	0.10	338
Chaetoceros curvisetus	8,760	26 September	0.10	0.04	
Pseudo-nitzschia seriata	7,540	12 May	0.40	0.15	1,063

Guinardia flaccida	3,000	06 June	0.09	0.03	14,184
Rhizosolenia imbricata	2,800	19 May	0.16	0.06	24,083
Skeletonema marinoi	2,400	24 February	0.03	0.01	
Minidiscus sp.	2,400	20 January	0.02	0.01	141
Pseudo-nitzschia pungens	1,960	06 June	0.10	0.04	1,610
Haslea wawrickae	1,750	23 May	0.06	0.02	1,001
Rhizosolenia setigera	1,750	14 October	0.02	0.01	6,644
Nitzschia longissima	1,630	23 May	0.02	0.01	139
Cylindrotheca closterium	1,500	19 September	0.04	0.01	179
Guinardia striata	1,250	26 September	0.03	0.01	6,642
Chaetoceros socialis	1,080	02 May	0.01	0.00	19

Table S2.4 Overview of the most abundant dinoflagellates (cell concentration $\geq$ 1000 cells L^{-1}) observed in surface waters at Lanvéoc in 2011 and the corresponding date of the maximum bloom.

Dinoflagellate	Max. abundance (cells L^{-1})	Date of max. peak	% of total dinoflag. cells	% of total phytoplankton cells	Cell surface (μm^2)
Heterocapsa minima	292,000	23 May	41.14	3.14	65
Gymnodinium sp. (<20 µm)	110,770	17 March	39.11	2.99	
Lepidodinium chlorophorum	69,480	05 Sep.	13.20	1.01	
Scrippsiella sp.	20,270	11 April	2.49	0.19	2,057
Gyrodinium flagellare	8,060	19 Sep.	0.96	0.07	97
Prorocentrum triestinum	5,880	22 Aug.	0.58	0.04	713
Heterocapsa triquetra	3,250	17 March	0.28	0.02	501
Prorocentrum micans	2,500	19 May	0.58	0.04	3,770
Dinophysis acuminata	1,500	19 May	0.27	0.02	9,325
Protoperidinium depressum	1,350	12 May	0.08	0.01	7,078
Gyrodinium spp.	1,200	27 June	0.19	0.01	2,412
Prorocentrum balticum	1,200	27 July	0.06	0.00	389
Tripos kofoidii	1,120	30 May	0.23	0.02	
Protoperidinium bipes	1,000	09 Aug.	0.14	0.01	1,597

Table S2.5 Overview of the most abundant diatoms (cell concentration $\geq$ 1000 cells L^{-1}) observed in surface waters at Lanvéoc in 2012 and the corresponding date of the maximum bloom.

Diatom	Max. abundance (cells L^{-1})	Date of max. peak	% of total diatom cells	% of total phytoplankton cells	Cell surface (μm^2)
Chaetoceros spp.	1,230,000	24 July	63.65	18.71	627
Guinardia delicatula	302,100	28 June	19.45	5.72	4,213
Thalassiosira spp.	88,620	12 June	3.78	1.11	1,624
Chaetoceros didymus	85,100	07 August	3.32	0.98	849
Thalassionema nitzschioides	51,350	24 July	0.95	0.28	338
Chaetoceros sp. (chains)	46,310	24 July	0.86	0.25	
Pseudo-nitzschia seriata	45,130	22 August	2.68	0.79	1,063
Coscinodiscus wailesii	44,310	20 March	0.82	0.24	1,630,253
Rhizosolenia imbricata	32,530	03 April	0.98	0.29	24,083
Minidiscus sp.	30,210	09 October	1.10	0.32	141
Lauderia annulata	21,650	03 April	0.45	0.13	
Skeletonema marinoi	12,100	20 November	0.63	0.18	
Cyclotella sp.	10,100	03 March	0.37	0.11	249
Pseudo-nitzschia delicatissima	5,750	24 April	0.21	0.06	952

Chaetoceros danicus	4,000	06 July	0.07	0.02	
Navicula sp. (8–10 µm)	4,000	18 December	0.07	0.02	86
Dactyliosolen fragilissimus	3,100	07 August	0.06	0.02	1,263
Guinardia flaccida	2,300	28 June	0.10	0.03	14,184
Naviculoides spp.	2,250	17 January	0.05	0.02	1,954
Haslea warwickae	1,760	28 June	0.07	0.02	1,001
Diatoma vulgare	1,510	18 December	0.03	0.01	
Cylindrotheca closterium	1,500	17 January	0.05	0.02	179
Rhizosolenia setigera	1,380	12 June	0.06	0.02	6,644

Table S2.6 Overview of the most abundant dinoflagellates (cell concentration ≥ 1000 cells L^{-1}) observed in surface waters at Lanvéoc in 2012 and the corresponding date of the maximum bloom.

Dinoflagellate	Max. abundance (cells L^{-1})	Date of max. peak	% of total dinoflag. cells	% of total phytoplankton cells	Cell surface (µm²)
Gymnodinium sp. (<20 µm)	207,440	24 April	50.84	2.06	
Heterocapsa minima	47,330	28 June	27.57	1.12	65
Alexandrium spp.	46,310	06 July	5.04	0.20	
Lepidodinium chlorophorum	28,190	12 June	4.02	0.16	
Gyrodinium spp.	26,180	17 January	2.66	0.11	2,412
Gyrodinium flagellare	13,250	06 July	1.45	0.06	97
Gymnodinium sp. (>20 µm)	11,070	06 July	3.90	0.16	
Prorocentrum balticum	8,060	17 April	0.81	0.03	389
Tripos kofoidii	7,510	28 June	1.19	0.05	
Protoperidinium bipes	5,000	12 June	0.48	0.02	1,597
Scrippsiella sp.	2,300	20 March	0.86	0.03	2,057
Prorocentrum micans	2,250	28 June	0.45	0.02	3,770

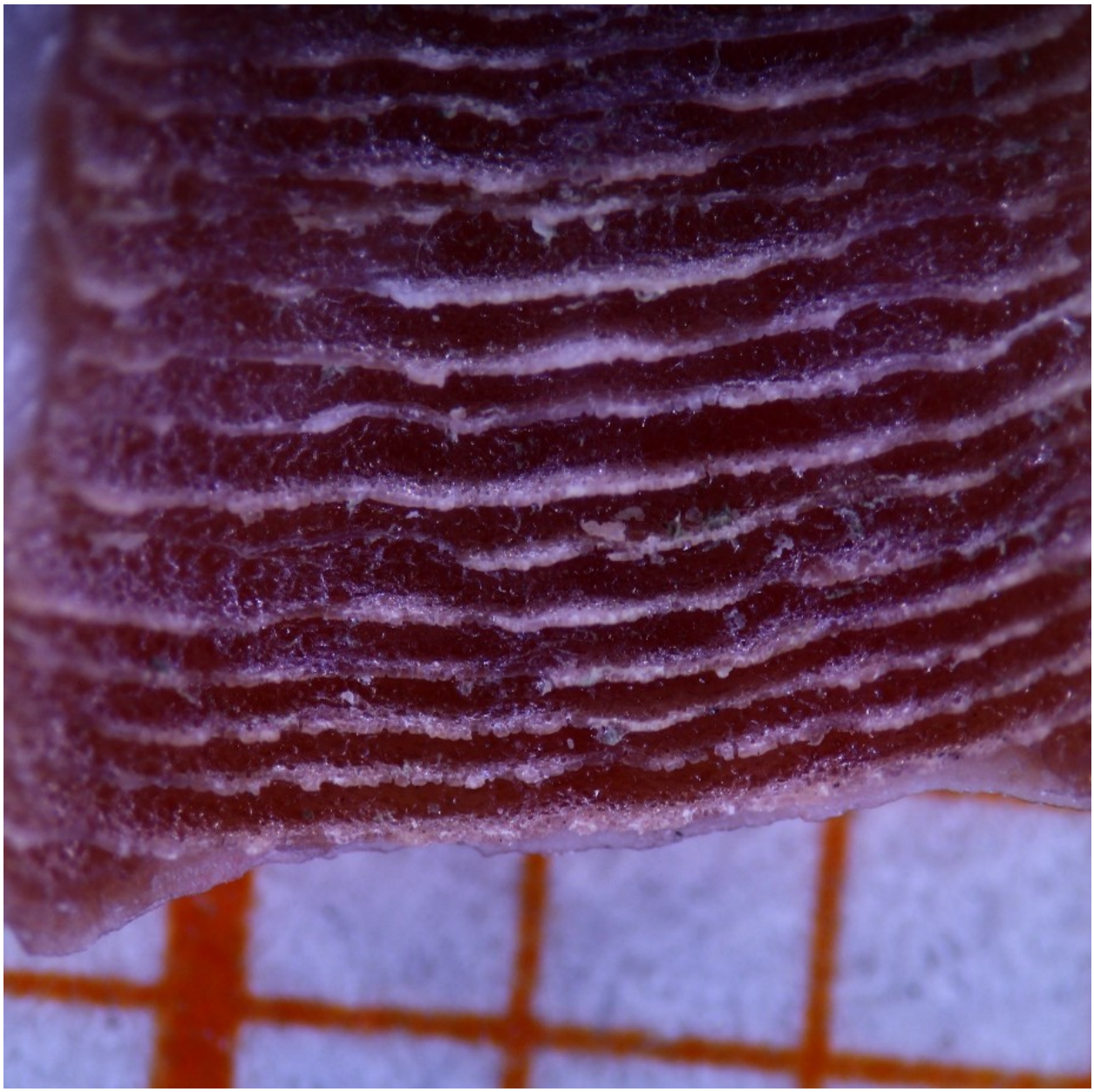

Figure S2.1 Microscope image taken from the ventral margin of a *P. maximus* specimen with visible daily formed growth increments (growth direction: top to bottom). For scale, orange grid width equals 1 mm.

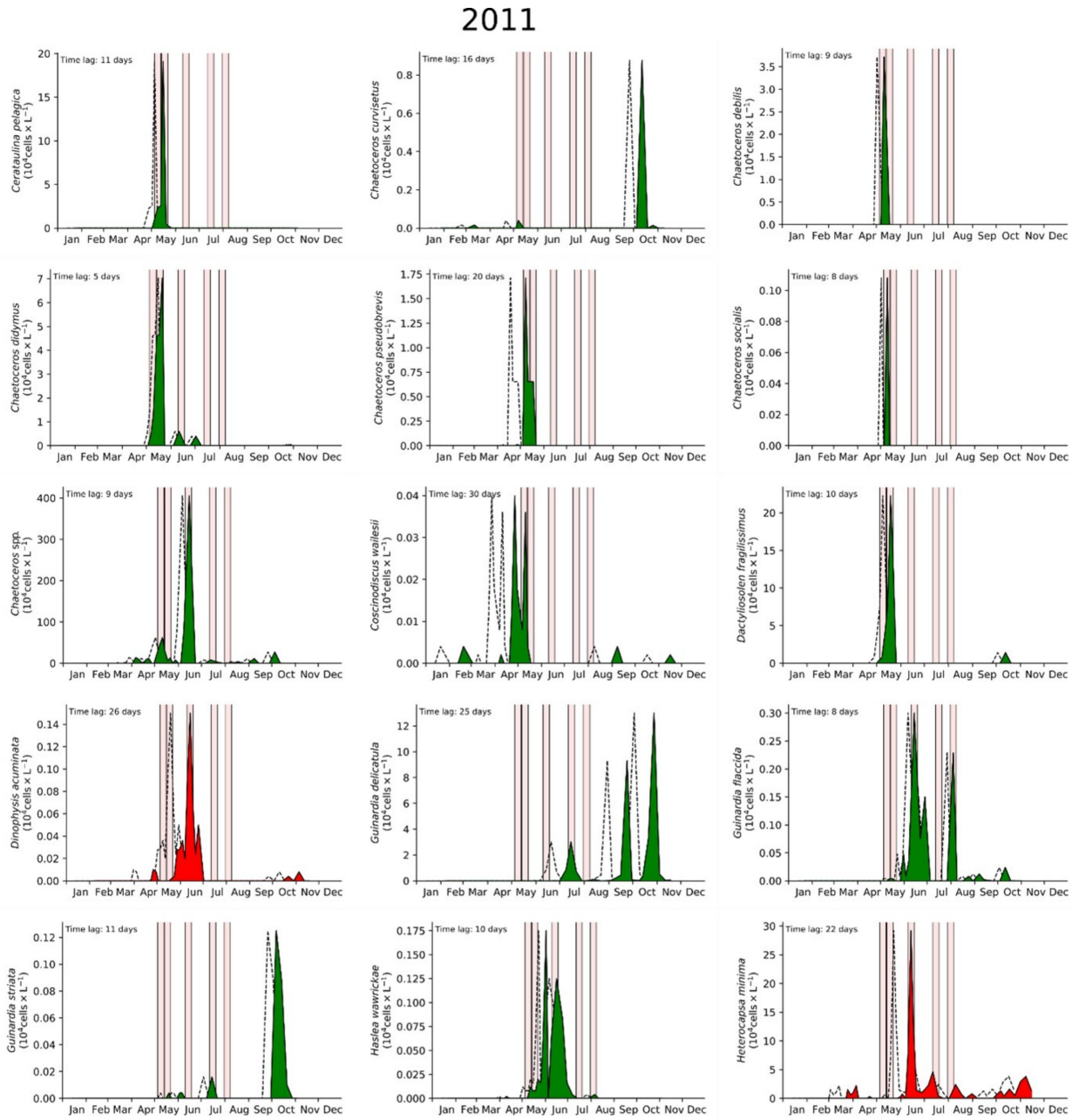

Figure S2.2 Temporally shifted diatom (green) and dinoflagellate (red) cell concentration time-series that were observed at Lanvéoc in 2011. Dashed line represents the initial temporal occurrence of the respective cell concentration. Time lags were determined manually for each species according to the best fit of phytoplankton cell concentration maxima and the Ba/Ca_{shell} profiles. (1/2)

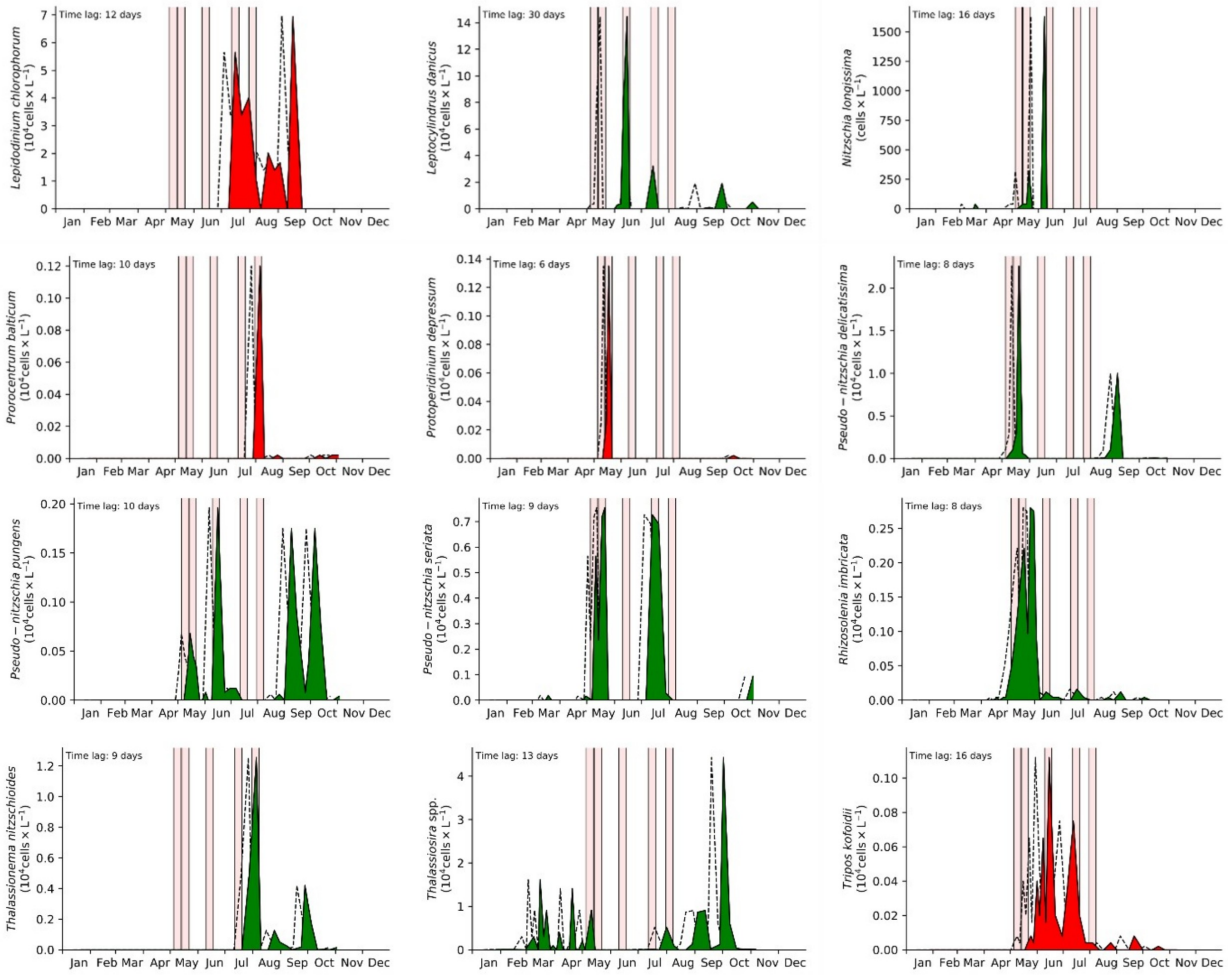

Figure S2.2 (continued) (2/2)

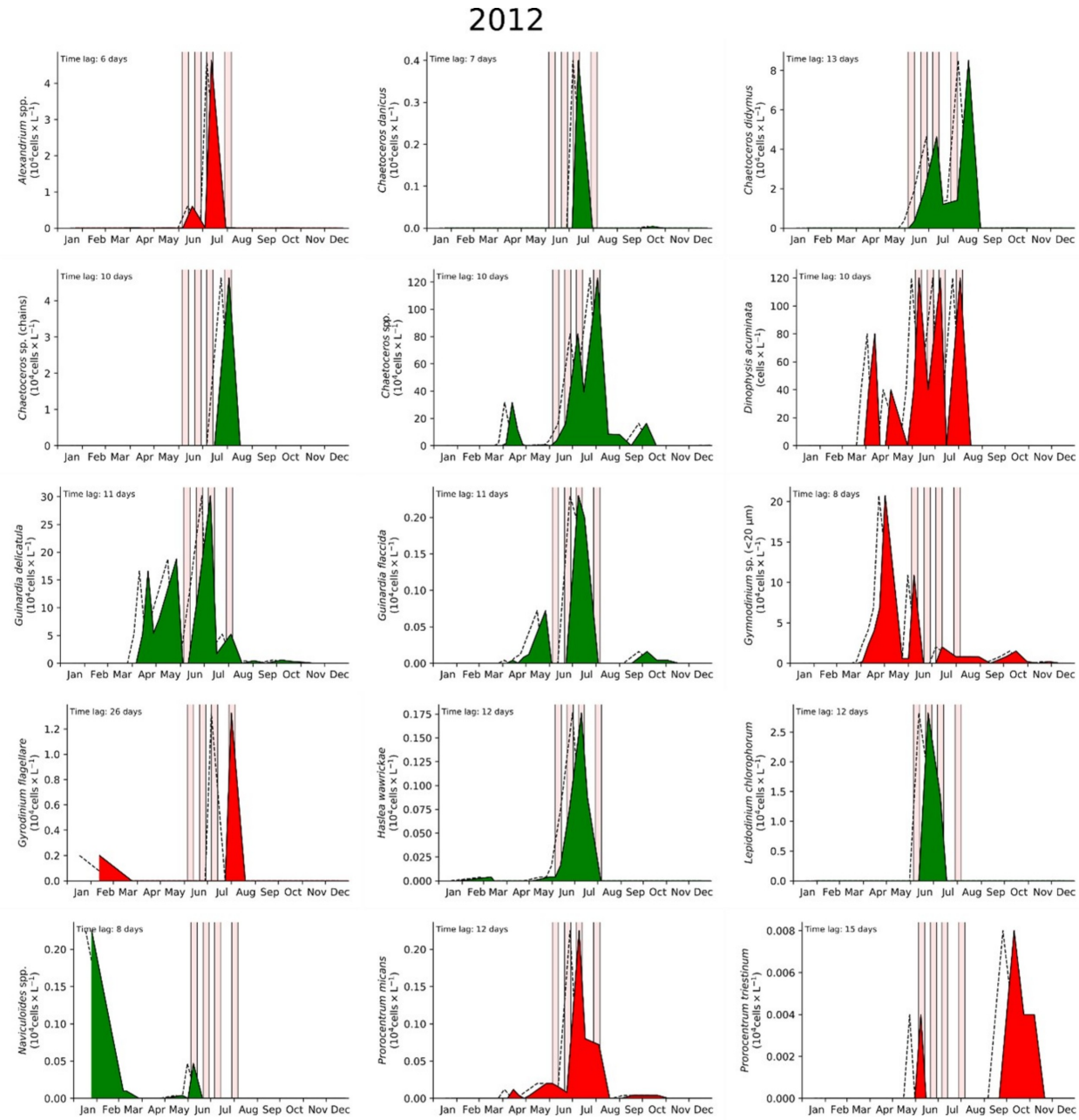

Figure S2.3 Temporally shifted diatom (green) and dinoflagellate (red) cell concentration time-series that were observed at Lanvéoc in 2012. Dashed line represents the initial temporal occurrence of the respective cell concentration. Time lags were determined manually for each species according to the best fit of phytoplankton cell concentration maxima and the Ba/Ca_{shell} profiles. (1/2)

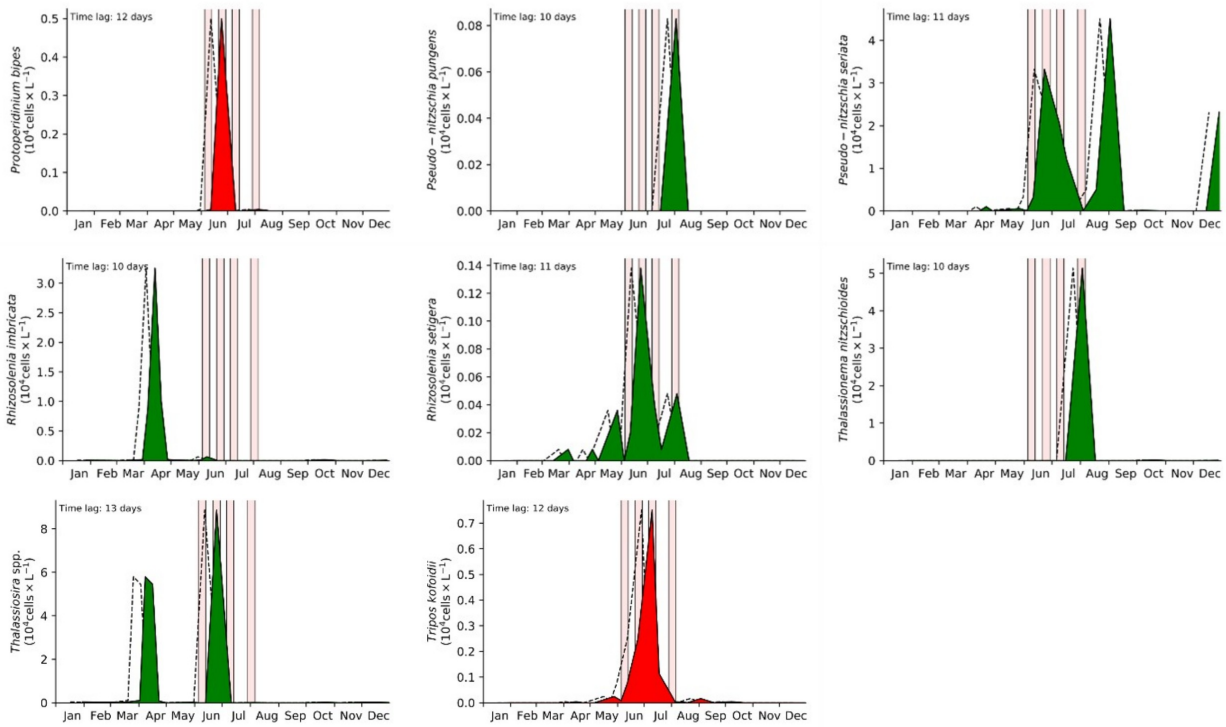

Figure S2.3 (continued) (2/2)

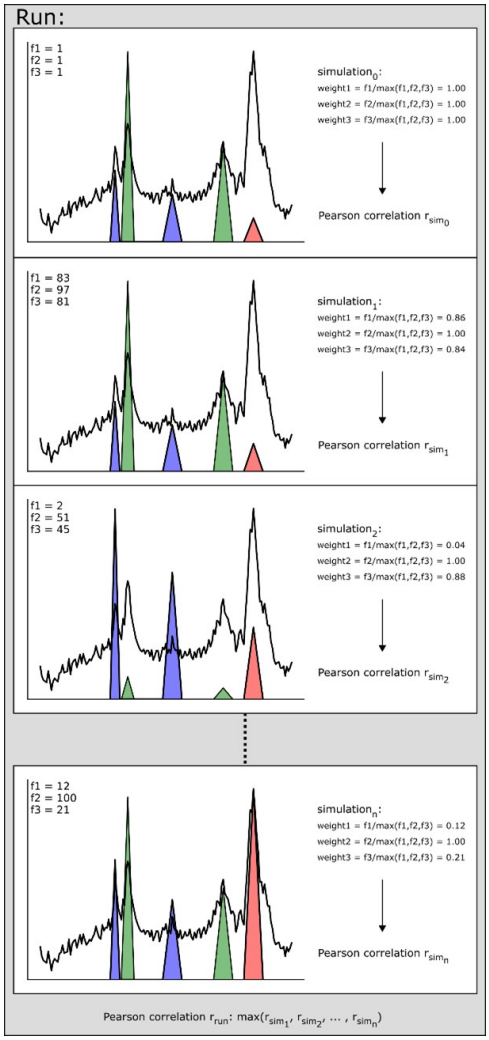

Figure S2.4 Simplified depiction of the random sampling simulations performed in this study. As an example, three arbitrary phytoplankton time-series were generated that are indicated as green (species 1), red (species 2) and blue (specie 3) areas. A single run consists of $n = 10^8$ independently executed simulations. For each simulation a pseudo-randomly generated factor ($[0, 100] = \{x \in R : 0 \leq x \leq 100\}$) was determined for each time-series, i.e., factor 1 (f1) was generated for species 1, factor 2 (f2) for species 2 and factor 3 (f3) for species 3. After the random sampling, each time-series was multiplied with the respective factor, leading to differently weighted phytoplankton blooms. As an indicator for the quality of the simulation, the Pearson correlation was calculated using the Ba/Ca_{shell} data and the sum of the weighted phytoplankton blooms. The result of a run was determined by the simulation that provided the maximum correlation coefficient. In order to ensure an inter-run comparison of the randomly generated factors, each species-specific factor was divided by the maximum factor (if max(f1, f2, f3) $\neq 0$), leading to comparable weighting-values between 0 and 1.

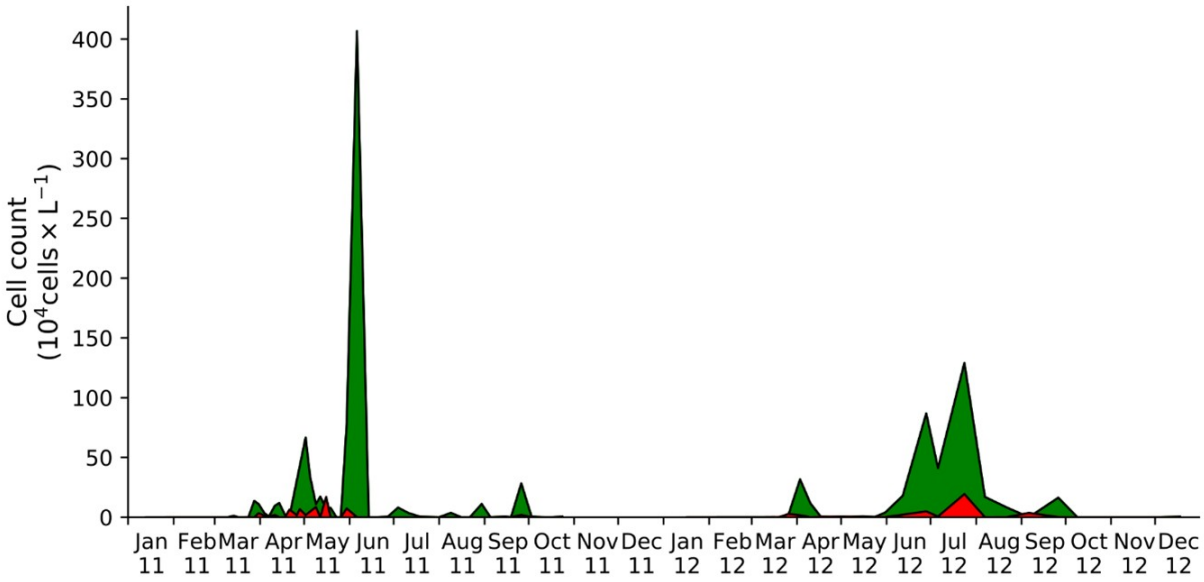

Figure S2.5 Observed cell concentration of *Chaetoceros* spp. in surface waters (green area) and at the SWI (red area; at approx. 8 m depth).

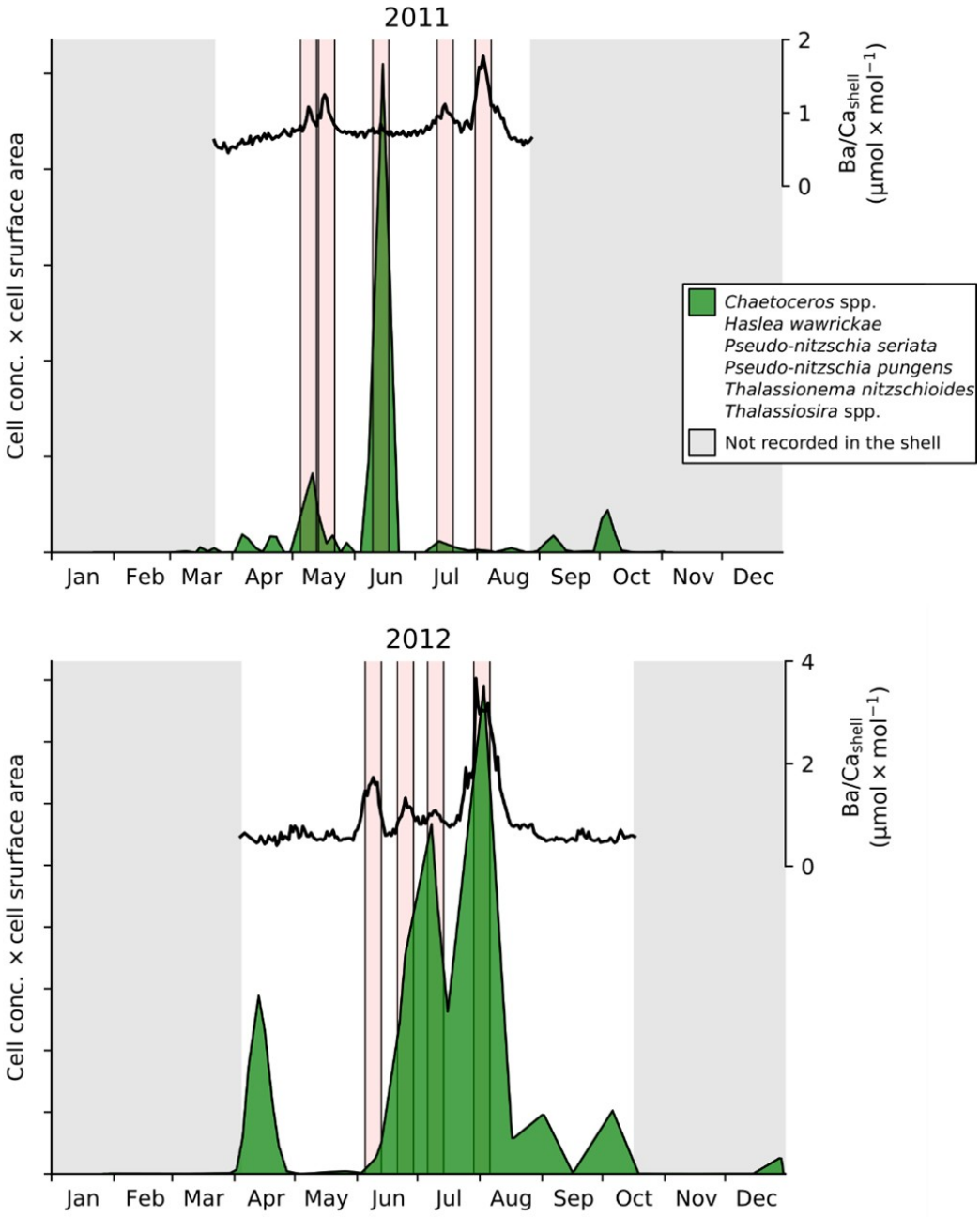

Figure S2.6 Ba/Ca$_{shell}$ profiles and the sum of six diatom species (see legend) after applying a species-specific time lag of 8 to 13 days. Each cell concentration time-series was multiplied with its respective cell surface area, that serves as a potential estimator for the amount of Ba that can be associated to a single phytoplankton cell.

References

Alldredge, A. L., Gotschalk, C. C., 1989. Direct observations of the mass flocculation of diatom blooms: Characteristics, settling velocities and formation of diatom aggregates. Deep Sea Research Part A, Oceanographic Research Papers 36, 159–171.

Alldredge, A. L., Passow, U., Logan, B. E., 1993. The abundance and significance of a class of large, transparent organic particles in the ocean. Deep Sea Research Part I: Oceanographic Research Papers 40, 1131–1140.

Anderson, R. F., Winckler, G., 2005. Problems with paleoproductivity proxies. Paleoceanography 20, PA3012.

Averyt, K. B., Paytan, A., 2004. A comparison of multiple proxies for export production in the equatorial Pacific. Paleoceanography 19, PA4003.

Barats, A., Amouroux, D., Chauvaud, L., Pécheyran, C., Lorrain, A., Thébault, J., Church, T. M., Donard, O. F., 2009. High frequency barium profiles in shells of the great scallop *Pecten maximus*: A methodical long-term and multi-site survey in Western Europe. Biogeosciences 6, 157–170.

Barats, A., Pécheyran, C., Amouroux, D., Dubascoux, S., Chauvaud, L., Donard, O. F. X., 2007. Matrix-matched quantitative analysis of trace-elements in calcium carbonate shells by laser-ablation ICP-MS: Application to the determination of daily scale profiles in scallop shell (*Pecten maximus*). Analytical and Bioanalytical Chemistry 387, 1131–1140.

Barton, S., Jenkins, J., Buckling, A., Schaum, C. E., Smirnoff, N., Raven, J. A., Yvon-Durocher, G., 2020. Evolutionary temperature compensation of carbon fixation in marine phytoplankton. Ecology Letters 23, 722–733.

Behl, S., Donval, A., Stiborb, H., 2011. The relative importance of species diversity and functional group diversity on carbon uptake in phytoplankton communities. Limnology and Oceanography 56, 683–694.

Behrenfeld, M. J., Boss, E., 2006. Beam attenuation and chlorophyll concentration as alternative optical indices of phytoplankton biomass. Journal of Marine Research 64, 431–451.

Behrenfeld, M. J., Boss, E., Siegel, D. A., Shea, D. M., 2005. Carbon-based ocean productivity and phytoplankton physiology from space. Global Biogeochemical Cycles 19, GB1006.

Beman, J. M., Arrigo, K. R., Matson, P. A., 2005. Agricultural runoff fuels large phytoplankton blooms in vulnerable areas of the ocean. Nature 434, 211–214.

Beninger, P. G., Decottignies, P., Rincé, Y., 2004. Localization of qualitative particle selection sites in the heterorhabdic filibranch *Pecten maximus* (Bivalvia: Pectinidae). Marine Ecology Progress Series 275, 163–173.

Beninger, P. G., Ward, J. E., MacDonald, B. A., Thompson, R. J., 1992. Gill function and particle transport in *Placopecten magellanicus* (Mollusca: Bivalvia) as revealed using video endoscopy. Marine Biology 114, 281–288.

Bienfang, P. K., Harrison, P. J., Quarmby, L. M., 1982. Sinking rate response to depletion of nitrate, phosphate and silicate in four marine diatoms. Marine Biology 67, 295–302.

Bishop, J. K. B., 1988. The barite-opal-organic carbon association in oceanic particulate matter. Nature 332, 341–343.

Cadée, G. C., Hegeman, J., 2002. Phytoplankton in the Marsdiep at the end of the 20th century; 30 years monitoring biomass, primary production, and *Phaeocystis* blooms. Journal of Sea Research 48, 97–110.

Cardinale, B. J., Srivastava, D. S., Duffy, J. E., Wright, J. P., Downing, A. L., Sankaran, M., Jouseau, C., 2006. Effects of biodiversity on the functioning of trophic groups and ecosystems. Nature 443, 989–992.

Carré, M., Bentaleb, I., Bruguier, O., Ordinola, E., Barrett, N. T., Fontugne, M., 2006. Calcification rate influence on trace element concentrations in aragonitic bivalve shells: Evidences and mechanisms. Geochimica et Cosmochimica Acta 70, 4906–4920.

Chauvaud, L., Donval, A., Thouzeau, G., Paulet, Y. M., Nézan, E., 2001. Variations in food intake of *Pecten maximus* (L.) from the Bay of Brest (France): Influence of environmental factors and phytoplankton species composition. Comptes Rendus de l'Académie des Sciences - Series III - Sciences de la Vie 324, 743–755.

Chauvaud, L., Jean, F., Ragueneau, O., Thouzeau, G., 2000. Long-term variation of the Bay of Brest ecosystem: Benthic-pelagic coupling revisited. Marine Ecology Progress Series 200, 35–48.

Chauvaud, L., Thébault, J., Clavier, J., Lorrain, A., Strand, Ø., 2011. What's hiding behind ontogenetic δ^{13}C variations in mollusk shells? New insights from the great scallop (*Pecten maximus*). Estuaries and Coasts 34, 211–220.

Chauvaud, L., Thouzeau, G., Paulet, Y. M., 1998. Effects of environmental factors on the daily growth rate of *Pecten maximus* juveniles in the Bay of Brest (France). Journal of Experimental Marine Biology and Ecology 227, 83–111.

Cheshire, H., Thurow, J., Nederbragt, A. J., 2005. Late Quaternary climate change record from two long sediment cores from Guaymas Basin, Gulf of California. Journal of Quaternary Science 20, 457–469.

Dehairs, F., Chesselet, R., Jedwab, J., 1980. Discrete suspended particles of barite and the barium cycle in the open ocean. Earth and Planetary Science Letters 49, 528–550.

Del Amo, Y., Quéguiner, B., Tréguer, P., Breton, H., Lampert, L., 1997. Impacts of high-nitrate freshwater inputs on macrotidal ecosystems. II. Specific role of the silicic acid pump in the year-round dominance of diatoms in the Bay of Brest (France). Marine Ecology Progress Series 161, 225–237.

Desortová, B., 1981. Relationship between chlorophyll-*a* concentration and phytoplankton biomass in several reservoirs in Czechoslovakia. Internationale Revue der gesamten Hydrobiologie und Hydrographie 66, 153–169.

Doré, J., Chaillou, G., Poitevin, P., Lazure, P., Poirier, A., Chauvaud, L., Archambault, P., Thébault, J., 2020. Assessment of Ba/Ca in *Arctica islandica* shells as a proxy for phytoplankton dynamics in the Northwestern Atlantic Ocean. Estuarine, Coastal and Shelf Science 237, 106628.

Dymond, J., Collier, R., McManus, J., Honjo, S., Manganini, S., 1997. Can the aluminum and titanium contents of ocean sediments be used to determine the paleoproductivity of the oceans? Paleoceanography 12, 586–593.

Field, C. B., Behrenfeld, M. J., Randerson, J. T., Falkowski, P., 1998. Primary production of the biosphere: Integrating terrestrial and oceanic components. Science 281, 237–240.

Fisher, N. S., Guillard, R. R. L., Bankston, D. C., 1991. The accumulation of barium by marine phytoplankton grown in culture. Journal of Marine Research 49, 339–354.

Ganeshram, R. S., François, R., Commeau, J., Brown-Leger, S. L., 2003. An experimental investigation of barite formation in seawater. Geochimica et Cosmochimica Acta 67, 2599–2605.

Gillikin, D. P., Dehairs, F., Lorrain, A., Steenmans, D., Baeyens, W., André, L., 2006. Barium uptake into the shells of the common mussel (*Mytilus edulis*) and the potential for estuarine paleo-chemistry reconstruction. Geochimica et Cosmochimica Acta 70, 395–407.

Gillikin, D. P., Lorrain, A., Paulet, Y. M., André, L., Dehairs, F., 2008. Synchronous barium peaks in high-resolution profiles of calcite and aragonite marine bivalve shells. Geo-Marine Letters 28, 351–358.

Hallmann, N., Schöne, B. R., Strom, A., Fiebig, J., 2008. An intractable climate archive – Sclerochronological and shell oxygen isotope analyses of the Pacific geoduck, *Panopea abrupta* (bivalve mollusk) from Protection Island (Washington State, USA). Palaeogeography, Palaeoclimatology, Palaeoecology 269, 115–126.

Hatch, M. B. A., Schellenberg, S. A., Carter, M. L., 2013. Ba/Ca variations in the modern intertidal bean clam *Donax gouldii*: An upwelling proxy? Palaeogeography, Palaeoclimatology, Palaeoecology 373, 98–107.

Henson, S. A., Sarmiento, J. L., Dunne, J. P., Bopp, L., Lima, I., Doney, S. C., John, J., Beaulieu, C., 2010. Detection of anthropogenic climate change in satellite records of ocean chlorophyll and productivity. Biogeosciences 7, 621–640.

Herguera, J. C., 2000. Last glacial paleoproductivity patterns in the eastern equatorial Pacific: Benthic foraminifera records. Marine Micropaleontology 40, 259–275.

Herguera, J. C., Berger, W. H., 1991. Paleoproductivity from benthic foraminifera abundance: Glacial to postglacial change in the West-Equatorial Pacific. Geology 19, 1173–1176.

Iglesias-Rodriguez, M. D., Halloran, P. R., Rickaby, R. E. M., Hall, I. R., Colmenero-Hidalgo, E., Gittins, J. R., Green, D. R. H., Tyrrell, T., Gibbs, S. J., von Dassow, P., Rehm, E., Armbrust, E. V., Boessenkool, K. P., 2008. Phytoplankton calcification in a high-CO_2 world. Science 320, 336–340.

Jochum, K. P., Garbe-Schönberg, D., Veter, M., Stoll, B., Weis, U., Weber, M., Lugli, F., Jentzen, A., Schiebel, R., Wassenburg, J. A., Jacob, D. E., Haug, G. H., 2019. Nano-powdered calcium carbonate reference materials: Significant progress for microanalysis? Geostandards and Geoanalytical Research 43, 595–609.

Jochum, K. P., Stoll, B., Herwig, K., Willbold, M., 2007. Validation of LA-ICP-MS trace element analysis of geological glasses using a new solid-state 193 nm Nd:YAG laser and matrix-matched calibration. Journal of Analytical Atomic Spectrometry 22, 112–121.

Jochum, K. P., Weis, U., Stoll, B., Kuzmin, D., Yang, Q., Raczek, I., Jacob, D. E., Stracke, A., Birbaum, K., Frick, D. A., Günther, D., Enzweiler, J., 2011. Determination of reference values for NIST SRM 610-617 glasses following ISO guidelines. Geostandards and Geoanalytical Research 35, 397–429.

Jolivet, A., Asplin, L., Strand, Ø., Thébault, J., Chauvaud, L., 2015. Coastal upwelling in Norway recorded in great scallop shells. Limnology and Oceanography 60, 1265–1275.

Kruskopf, M., Flynn, K. J., 2006. Chlorophyll content and fluorescence responses cannot be used to gauge reliably phytoplankton biomass, nutrient status or growth rate. New Phytologist 169, 525–536.

Laing, I., 2000. Effect of temperature and ration on growth and condition of king scallop (*Pecten maximus*) spat. Aquaculture 183, 325–334.

Laing, I., 2004. Filtration of king scallops (*Pecten maximus*). Aquaculture 240, 369–384.

Lazareth, C. E., Vander Putten, E., André, L., Dehairs, F., 2003. High-resolution trace element profiles in shells of the mangrove bivalve *Isognomon ephippium*: A record of environmental spatio-temporal variations? Estuarine, Coastal and Shelf Science 57, 1103–1114.

Lee, J. H., Lee, W. C., Kim, H. C., Jo, N., Kim, K., Lee, D., Kang, J. J., Sim, B. R., Kwon, J. I., Lee, S. H., 2020. Temporal and spatial variations of the biochemical composition of phytoplankton and potential food material (FM) in Jaran Bay, South Korea. Water 12, 3093.

Lindahl, O., Belgrano, A., Davidsson, L., Hernroth, B., 1988. Primary production, climatic oscillations, and physico-chemical processes: The Gullmar Fjord time-series data set (1985-1996). ICES Journal of Marine Science 55, 723–729.

Liu, H., Kelly, M. S., Campbell, D. A., Fang, J., Zhu, J., 2008. Accumulation of domoic acid and its effect on juvenile king scallop *Pecten maximus* (Linnaeus, 1758). Aquaculture 284, 224–230.

Longerich, H. P., Jackson, S. E., Günther, D., 1996. Laser ablation inductively coupled plasma mass spectrometric transient signal data acquisition and analyte concentration calculation. Journal of Analytical Atomic Spectrometry 11, 899–904.

Lorenzen, C. J., 1966. A method for the continuous measurement of *in vivo* chlorophyll concentration. Deep-Sea Research and Oceanographic Abstracts 13, 223–227.

Lorrain, A., Paulet, Y. M., Chauvaud, L., Dunbar, R. B., Mucciarone, D., Fontugne, M., 2004. δ^{13}C variation in scallop shells: Increasing metabolic carbon contribution with body size? Geochimica et Cosmochimica Acta 68, 3509–3519.

Lorrain, A., Paulet, Y. M., Chauvaud, L., Savoye, N., Nézan, E., Guérin, L., 2000. Growth anomalies in *Pecten maximus* from coastal waters (Bay of Brest, France): Relationship with diatom blooms. Journal of the Marine Biological Association of the United Kingdom 80, 667–673.

Marali, S., Schöne, B. R., Mertz-Kraus, R., Griffin, S. M., Wanamaker, A. D., Butler, P. G., Holland, H. A., Jochum, K. P., 2017a. Reproducibility of trace element time-series (Na/Ca, Mg/Ca, Mn/Ca, Sr/Ca, and Ba/Ca) within and between specimens of the bivalve *Arctica islandica* – a LA-ICP-MS line scan study. Palaeogeography, Palaeoclimatology, Palaeoecology 484, 109–128.

Marali, S., Schöne, B. R., Mertz-Kraus, R., Griffin, S. M., Wanamaker, A. D., Matras, U., Butler, P. G., 2017b. Ba/Ca ratios in shells of *Arctica islandica* – Potential environmental proxy and crossdating tool. Palaeogeography, Palaeoclimatology, Palaeoecology 465, 347–361.

Marchais, V., Richard, J., Jolivet, A., Flye-Sainte-Marie, J., Thébault, J., Jean, F., Richard, P., Paulet, Y. M., Clavier, J., Chauvaud, L., 2015. Coupling experimental and field-based approaches to decipher carbon sources in the shell of the great scallop, *Pecten maximus* (L.) Geochimica et Cosmochimica Acta 168, 58–69.

Martin, J. H., Knauer, G. A., 1973. The elemental composition of plankton. Geochimica et Cosmochimica Acta 37, 1639–1653.

Martinez-Ruiz, F., Jroundi, F., Paytan, A., Guerra-Tschuschke, I., Abad, M. D. M., González-Muñoz, M. T., 2018. Barium bioaccumulation by bacterial biofilms and implications for Ba cycling and use of Ba proxies. Nature Communications 9, 1619.

Matsumoto, M., Nishimura, T., 1998. Mersenne Twister: A 623-Dimensionally equidistributed uniform pseudo-random number generator. ACM Transactions on Modeling and Computer Simulation 8, 3–30.

Palmer, R. E., 1980. Behavioral and rhythmic aspects of filtration in the bay scallop, *Argopecten irradians concentricus* (Say), and the oyster, *Crassostrea virginica* (Gmelin). Journal of Experimental Marine Biology and Ecology 45, 273–295.

Paulet, Y. M., Lucas, A., Gerard, A., 1988. Reproduction and larval development in two *Pecten maximus* (L.) populations from Brittany. Journal of Experimental Marine Biology and Ecology 119, 145–156.

Peperzak, L., Colijn, F., Koeman, R., Gieskes, W. W. C., Joordens, J. C. A., 2003. Phytoplankton sinking rates in the Rhine region of freshwater influence. Journal of Plankton Research 25, 365–383.

Poitevin, P., Chauvaud, L., Pécheyran, C., Lazure, P., Jolivet, A., Thébault, J., 2020. Does trace element composition of bivalve shells record utra-high frequency environmental variations? Marine Environmental Research 158, 104943.

Queguiner, B., Tréguer, P., 1984. Studies on the phytoplankton in the Bay of Brest (Western Europe). Seasonal variations in composition, biomass and production in relation to hydrological and chemical features (1981–1982). Botanica Marina 27, 449–460.

Ragueneau, O., Chauvaud, L., Leynaert, A., Thouzeau, G., Paulet, Y. M., Bonnet, S., Lorrain, A., Grall, J., Corvaisier, R., Le Hir, M., Jean, F., Clavier, J., 2002. Direct evidence of a biologically active coastal silicate pump: Ecological implications. Limnology and Oceanography 47, 1849–1854.

Richardson, C. A., Crisp, D. J., Runham, N. W., 1980. An endogenous rhythm in shell deposition in *Cerastoderma edule*. Journal of the Marine Biological Association of the United Kingdom 60, 991–1004.

Richardson, K., Heilmann, J. P., 1995. Primary production in the Kattegat: Past and present. Ophelia 41, 317–328.

Roth, I., Riley, J. P., 1971. The distribution of trace elements in some species of phytoplankton grown in culture. Journal of the Marine Biological Association of the United Kingdom 51, 63–72.

Schöne, B. R., 2008. The curse of physiology – Challenges and opportunities in the interpretation of geochemical data from mollusk shells. Geo-Marine Letters 28, 269–285.

Shumway, S. E., Cucci, T. L., Lesser, M. P., Bourne, N., Bunting, B., 1997. Particle clearance and selection in three species of juvenile scallops. Aquaculture International 5, 89–99.

Shumway, S. E., Cembella, A. D., 1993. The impact of toxic algae on scallop culture and fisheries. Reviews in Fisheries Science 1, 121–150.

Shuter, B., 1979. A model of physiological adaptation in unicellular algae. Journal of Theoretical Biology 78, 519–552.

Sigman, D. M., Boyle, E. A., 2000. Glacial/interglacial variations in atmospheric carbon dioxide. Nature 407, 859–869.

Smith, V. H., 2003. Eutrophication of freshwater and coastal marine ecosystems: A global problem. Environmental Science and Pollution Research 10, 126–139.

Stecher, H. A., Krantz, D. E., Lord, C. J., Luther, G. W., Bock, K. W., 1996. Profiles of strontium and barium in *Mercenaria mercenaria* and *Spisula solidissima* shells. Geochimica et Cosmochimica Acta 60, 3445–3456.

Stecher, H. A., Kogut, M. B., 1999. Rapid barium removal in the Delaware estuary. Geochimica et Cosmochimica Acta 63, 1003–1012.

Sternberg, E., Tang, D., Ho, T. Y., Jeandel, C., Morel, F. M. M., 2005. Barium uptake and adsorption in diatoms. Geochimica et Cosmochimica Acta 69, 2745–2752.

Tabouret, H., Pomerleau, S., Jolivet, A., Pécheyran, C., Riso, R., Thébault, J., Chauvaud, L., Amouroux, D., 2012. Specific pathways for the incorporation of dissolved barium and molybdenum into the bivalve shell: An isotopic tracer approach in the juvenile great scallop (*Pecten maximus*). Marine Environmental Research 78, 15–25.

Takesue, R. K., Bacon, C. R., Thompson, J. K., 2008. Influences of organic matter and calcification rate on trace elements in aragonitic estuarine bivalve shells. Geochimica et Cosmochimica Acta 72, 5431–5445.

Thébault, J., Chauvaud, L., 2013. Li/Ca enrichments in great scallop shells (*Pecten maximus*) and their relationship with phytoplankton blooms. Palaeogeography, Palaeoclimatology, Palaeoecology 373, 108–122.

Thébault, J., Chauvaud, L., Clavier, J., Fichez, R., Morize, E., 2006. Evidence of a 2-day periodicity of striae formation in the tropical scallop *Comptopallium radula* using calcein marking. Marine Biology 149, 257–267.

Thébault, J., Chauvaud, L., L'Helguen, S., Clavier, J., Barats, A., Jacquet, S., Pécheyran, C., Amouroux, D., 2009. Barium and molybdenum records in bivalve shells: Geochemical proxies for phytoplankton dynamics in coastal environments? Limnology and Oceanography 54, 1002–1014.

Vander Putten, E., Dehairs, F., Keppens, E., Baeyens, W., 2000. High resolution distribution of trace elements in the calcite shell layer of modern *Mytilus edulis*: Environmental and biological controls. Geochimica et Cosmochimica Acta 64, 997–1011.

Ward, J. E., Shumway, S. E., 2004. Separating the grain from the chaff: Particle selection in suspension- and deposit-feeding bivalves. Journal of Experimental Marine Biology and Ecology 300, 83–130.

Westberry, T., Behrenfeld, M. J., Siegel, D. A., Boss, E., 2008. Carbon-based primary productivity modeling with vertically resolved photoacclimation. Global Biogeochemical Cycles 22, 1–18.

Winder, M., Sommer, U., 2012. Phytoplankton response to a changing climate. Hydrobiologia 698, 5–16.

Worm, B., Barbier, E. B., Beaumont, N., Duffy, J. E., Folke, C., Halpern, B. S., Jackson, J. B. C., Lotze, H. K., Micheli, F., Palumbi, S. R., Sala, E., Selkoe, K. A., Stachowicz, J. J., Watson, R., 2006. Impacts of biodiversity loss on ocean ecosystem services. Science 314, 787–790.

3 Deciphering the potential of Ba/Ca, Mo/Ca and Li/Ca profiles in the bivalve shell *Pecten maximus* as proxies for the reconstruction of phytoplankton dynamics

---

Lukas Fröhlich[1], Valentin Siebert[2], Qian Huang[1], Julien Thébault[2], Klaus Peter Jochum[3], Bernd R. Schöne[1],

[1] *Johannes Gutenberg University, Mainz, Germany*
[2] *Univ Brest, CNRS, IRD, Plouzané, France*
[3] *Climate Geochemistry Department, Max Planck Institute for Chemistry, Mainz, Germany*

Reference:

Fröhlich, L., Siebert, V., Huang, Q., Thébault, J., Jochum, K. P., Schöne, B. R., 2022. Deciphering the potential of Ba/Ca, Mo/Ca and Li/Ca profiles in the bivalve shell *Pecten maximus* as proxies for the reconstruction of phytoplankton dynamics. Ecological Indicators 141, 109121.

In this chapter, high-resolution geochemical profiles of Ba/Ca_{shell}, Mo/Ca_{shell} and Li/Ca_{shell} from *P. maximus* shells from three different years were contextualized with the complex primary producer dynamics monitored at the study site. Based on the findings of the preceding chapter, a pseudo-random sampling method is introduced that identify potential links between trace element chronologies and phytoplankton dynamics. The results indicate that the magnitude and occurrence of Ba/Ca_{shell}, Mo/Ca_{shell} and Li/Ca_{shell} peaks is linked to phytoplankton blooms that developed about two weeks prior. Ba/Ca_{shell} peaks were related with the abundance of ingestible phytoplankton species. Peaks in Mo/Ca_{shell} records exhibit patterns that match those of the dominant dinoflagellate genus *Gymnodinium* spp. as well as to phytoplankton aggregation events. Li/Ca_{shell} profiles are potentially affected by blooms of the dominant diatom *Chaetoceros* spp. or the abundance of neuro-toxin producing diatoms. This work was published as a manuscript in the journal 'Ecological Indicators'. I contributed to the conceptualization, the formal analysis, the investigation, methodology, visualization and writing of the original draft. This study was funded by by the German Research Foundation (DFG) with a grant to BRS (SCHO 793/21) and a French National Research Agency (ANR) grant to JT within the framework of the French-German collaborative project HIPPO.

Author contributions:

LF – Conceptualization, Formal analysis, Investigation, Methodology, Visualization, Writing - original draft, Writing - review and editing

VS – Investigation, Formal analysis, Writing - review and editing

QH – Conceptualization, Methodology, Formal analysis, Supervision, Writing - review and editing

JT – Project administration, Investigation, Resources, Validation, Supervision, Writing - review and editing

KPJ – Resources, Validation, Writing - review and editing

BRS – Resources, Conceptualization, Formal analysis, Funding Acquisition, Supervision, Validation, Writing - original draft, Writing - review and editing

Abstract

Shells of the fast-growing bivalve *P. maximus* serve as a geochemical archive for the reconstruction of past phytoplankton dynamics. Specifically, high-resolution, temporally accurately aligned molar barium-to-calcium (Ba/Ca_{shell}), molybdenum-to-calcium (Mo/Ca_{shell}) and lithium-to-calcium ratios (Li/Ca_{shell}) of the shell calcite revealed distinct peaks which are closely linked to phytoplankton dynamics. Yet, the development and applicability of these geochemical proxies is still at an early stage and needs further calibration. In this study, we examined the relationship between the timing and magnitude of Ba/Ca_{shell}, Mo/Ca_{shell} and Li/Ca_{shell} peaks of *P. maximus* and the occurrence of various phytoplankton species (diatoms and dinoflagellates) from a statistical perspective. Studied shell samples (three specimens per calendar year) as well as detailed phytoplankton observation data were derived from the well-studied coastal ecosystem of the Bay of Brest (France) over three years (2011, 2012 and 2019). An algorithm-based pseudo-random sampling simulation technique was established that analyzed the complex phytoplankton datasets with respect to the profiles of Ba/Ca_{shell}, Mo/Ca_{shell} and Li/Ca_{shell} to identify potential patterns between phytoplankton and trace element time-series. The simulation results indicate that the timing and magnitude of Ba/Ca_{shell}, Mo/Ca_{shell} and Li/Ca_{shell} peaks agreed best with the occurrence of specific phytoplankton blooms that developed ca. one to two weeks earlier. The data suggest that the formation of transient Ba/Ca_{shell} peaks had a pluripspecific origin, i.e., potentially linked to blooms of ingestible diatom, dinoflagellate and flagellate species enriched in Ba that occurred 8 to 12 days earlier. Observed peaks in Mo/Ca_{shell} profiles demonstrably followed the timing and intensity of blooms of the dominant dinoflagellate genus *Gymnodinium* spp. after a short time lag of around 8 days, potentially linked to an enhanced enzyme activity of nitrate reductase that requires the presence of Mo in the dinoflagellate cells. In addition, Mo/Ca_{shell} peaks agreed with periods of diatom aggregate formation which were hypothesized to induce the formation of Mo/Ca_{shell} peaks in scallop shells. Li/Ca_{shell} profiles revealed similar patterns as large blooms of the diatom *Chaetoceros* spp. as well as to neurotoxin producing diatoms of the genus *Pseudo-nitzschia* when considering a short time lag of 8 to 12 days. These findings highlight the great potential of using Ba/Ca_{shell}, Mo/Ca_{shell} and Li/Ca_{shell} chronologies in *P. maximus* shells as proxies of past phytoplankton dynamics.

3.1 Introduction

Marine phytoplankton form the foundation of marine food webs and contribute considerably to global photosynthetic CO_2 fixation and oxygen production (e.g., Shuter, 1979; Sigman and Boyle, 2000; Iglesias-Rodriguez et al., 2008; Westberry et al., 2008). Despite accounting for <1% of the total photosynthetic biomass, marine phytoplankton contribute to nearly half of the global net primary production (Field et al., 1998). Coastal habitats are among the most precious ecosystems (Barbier et al., 2011) that provide food for millions of people. However, these systems are increasingly threatened by climate change (e.g., ocean warming and acidification; Wiltshire and Manly, 2004; Winder and Sommer, 2012) and other anthropogenic influences (e.g., over-exploitation, increased nutrient inputs from artificial fertilizers and pollutants; Nixon, 1995; Del Amo et al., 1997; Smith, 2003; Beman et al., 2005), leading to changes in phytoplankton community structures and dynamics (Hare et al., 2007; Marinov et al., 2010) as well as a loss in biodiversity (Cardinale et al., 2006; Worm et al., 2006). One consequence is the shift from a diatom-dominated ecosystem to one dominated by non-siliceous phytoplankton groups such as dinoflagellates (Radach et al., 1990; Ragueneau et al., 1994; Cloern, 2001), which can have negative impacts on fisheries and food webs due to toxic algal blooms. Accounting for these changes in phytoplankton dynamics over time is essential for the reliable modeling of potential future trends of marine ecosystems.

Detailed and long-term records of phytoplankton dynamics are sparse and limited to a few localities (e.g., Warner and Hays, 1994; Richardson and Heilmann, 1995; Chauvaud et al., 2000). Remotely sensed observations (e.g., Gordon et al., 1980; Hovis et al., 1980) provide a large spatial coverage but cannot be used to assess phytoplankton community structures on a higher taxonomic level (e.g., species) and are only available since a few decades. Traditional microscopic in-situ analyses as well as high-performance liquid chromatography of biochemical markers (e.g., carotenoid pigments) allow to evaluate phytoplankton community compositions on a fine temporal scale (e.g., Lionard et al., 2008; Wright et al., 2010; Wang et al., 2021), but are less useful to reconstruct past phytoplankton dynamics. A variety of tools are used to assess pre-industrial primary production, e.g., the biogeochemical analysis of marine sediments including barite precipitation rates, aluminum-to-titanium and barium-to-titanium ratios (e.g., Dehairs et al., 1980; Bishop, 1988; Dymond et al., 1997). However, these data only provide a limited temporal resolution that is insufficient to identify short-term phytoplankton events (days to weeks). Mollusk shells potentially provide a

more suitable archive for this purpose as they record prevailing environmental conditions in the form of geochemical properties over seasons, years, decades or even centuries. These geochemical data can be temporally constrained by growth pattern analysis (Richardson et al., 1980; Hallmann et al., 2008; Schöne, 2008). To reconstruct phytoplankton dynamics, several studies used shells of the short-lived (up to ca. 12 years) bivalve, *Pecten maximus* (e.g., Gillikin et al., 2008; Barats et al., 2010; Chauvaud et al., 2011; Tabouret et al., 2012; Thébault et al., 2022). Especially during their second year of life (after the first winter growth cessation), these bivalves form distinct daily increments allowing to retrieve high resolved time-series (e.g., Chauvaud et al., 2005) that provide an ideal temporal resolution for assessing short-term phytoplankton events. Transient peaks in trace element profiles of barium (Ba), molybdenum (Mo) and lithium (Li) occurring synchronously among contemporaneous *P. maximus* shells were proposed to originate from food sources (e.g., Gillikin et al., 2008; Barats et al., 2009; Thébault et al., 2009; Barats et al., 2010; Thébault and Chauvaud, 2013). The formation of molar barium-to-calcium (Ba/Ca_{shell}) peaks are induced by the ingestion of Ba-rich diatom frustules rather than by an increase in the dissolved Ba concentration of the ambient water (Gillikin et al., 2006; Gillikin et al., 2008; Barats et al., 2009) or by enhanced riverine inputs (Thébault et al., 2009). While Ba/Ca_{shell} profiles do not correlate strongly with bulk phytoplankton variations, Ba/Ca_{shell} peaks correspond to the timing of blooms of individual phytoplankton species when applying a short time lag of several days (Fröhlich et al., 2022). Given the large inter-taxa variability in phytoplankton cell-associated Ba (Roth and Riley, 1971; Martin and Knauer, 1973; Fisher et al., 1991), it is hypothesized that various taxa contribute differently to the measured Ba/Ca_{shell} peaks (Thébault et al., 2009; Fröhlich et al., 2022). Yet, further studies are needed to test this hypothesis. Similar to Ba enrichments in shells, molar molybdenum-to-calcium (Mo/Ca_{shell}) peaks are considered to have a dietary origin (Tabouret et al., 2012). According to Thébault et al. (2022), the formation of Mo/Ca_{shell} peaks in scallop shells could be induced by the ingestion of Mo-rich diatom aggregates forming during periods of nutrient limitation. Molar lithium-to-calcium (Li/Ca_{shell}) peaks have been associated with blooms of diatoms that adsorb dissolved Li from the water column onto their frustules and as such transport large quantities of Li to the site of calcification when digested by the bivalves (Thébault and Chauvaud, 2013; Thébault et al., 2022). Thus, peaks of Ba/Ca_{shell}, Mo/Ca_{shell} and Li/Ca_{shell} in scallop shells were demonstrably linked to phytoplankton dynamics, but the mechanisms controlling the formation of trace element peaks are still poorly understood. To improve the

applicability of Ba/Ca_{shell}, Mo/Ca_{shell} and Li/Ca_{shell} as reliable indicators for past phytoplankton dynamics using fossil or subfossil shells, it is necessary to further disentangle the relationship between phytoplankton on a species level and the formation of trace element peaks in *P. maximus* shells.

This study analyzed the direct relationship between three years of highly resolved Ba/Ca_{shell}, Mo/Ca_{shell} and Li/Ca_{shell} profiles and the contemporaneous phytoplankton dynamics in the Bay of Brest, France. Diatoms and dinoflagellate species were shown to be the dominant phytoplankton taxa in the studied coastal ecosystem and are the main food source for the studied bivalve. Therefore, the analyses conducted herein focused primarily on the dynamics of diatom and dinoflagellate species. The objective of this work was to examine whether the formation of transient trace element peaks could be related to the occurrence of short-term phytoplankton events and whether a monospecific or a plurispecific connection exists. To identify patterns within the largely unknown relationship between phytoplankton dynamics and trace element profiles in scallop shells, a pseudo-random sampling method was used that calculated millions of possible phytoplankton combinations at various hypothetical time lags. This computational approach allowed to evaluate a complex ecosystem and its potential responses in shell geochemistry from a statistical perspective and adds information required for the interpretation of Ba/Ca_{shell}, Mo/Ca_{shell} and Li/Ca_{shell} profiles as proxies for past phytoplankton dynamics. Deciphering this link will help to further improve the applicability of shells of *P. maximus* as powerful and highly resolved geochemical archives.

3.2 Material and methods

3.2.1 Sampling locality, shell collection and preparation

Nine living specimens of *P. maximus* were collected by SCUBA divers at Lanvéoc (48°17′N 4°30′W), Bay of Brest, Brittany, northwest France (Fig. 3.1). The bay (ca. 180 km^2), a semi-enclosed ecosystem, is characterized as a macrotidal regime and an average water depth of 8 m. The sampling locality, Lanvéoc, is situated in the southern area, close to the Aulne river (Fig. 3.1). Three scallop shells were collected on 30 August 2011, three on 23 October 2012 and three specimens on 15 November 2019 (Table 3.1) and stored at -20 °C. All shells experienced one winter growth cessation. In order to prepare the shells for elemental analyses, all specimens were gently cleaned with tap water using a plastic brush,

and epibionts were removed after dissecting each specimen. In this study, sclerochronological analyses were performed on the surface of the left (flat) valves (Fig. 3.2) that were rinsed ultrasonically for 3 min with deionized water to remove sediment trapped between adjacent striae.

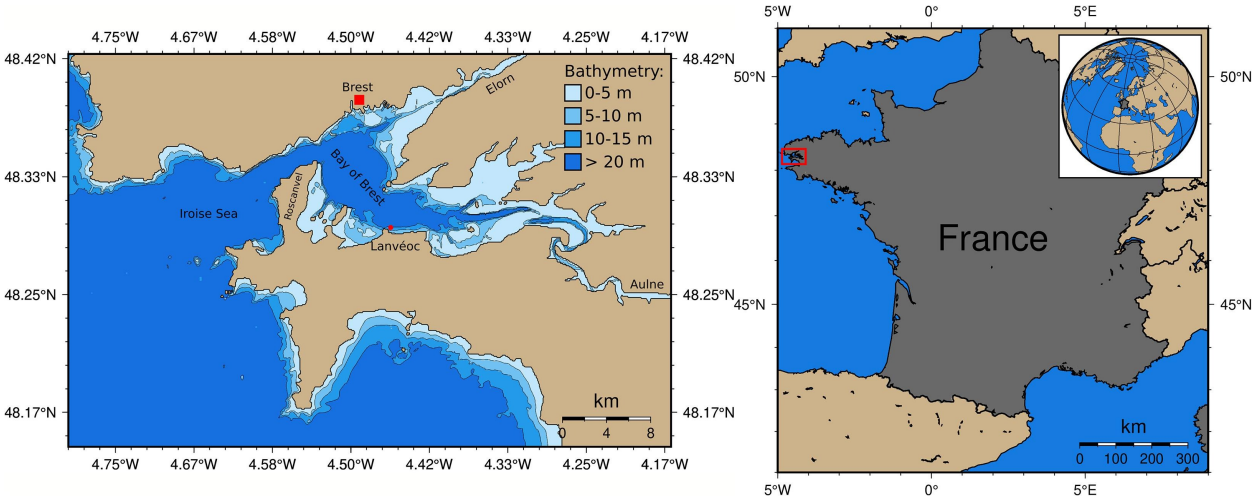

Figure 3.1 Map of the Bay of Brest (left panel) with the sampling locality, Lanvéoc (red circle), near to the city of Brest (red square) in northwest France (right panel).

3.2.2 LA-ICP-MS analysis

In-situ chemical analyses were performed on the surface of the shell sections that were cut along the axis of maximum growth (Fig. 3.2) using a handheld drill equipped with a 150 µm-thin disk (disk with galvanically bonded diamonds; Komet – Dental Gebr. Brasseler GmbH & Co. KG; Art.–No.: 6911H.-104.220). After cutting, the shell slabs were immersed in acetic acid (10 vol%) for ca. 1 min and thoroughly rinsed using deionized water to remove potential surface contamination. All shell samples were analyzed for their Ba (measured as ^{137}Ba), Mo (^{97}Mo) and Li (^{7}Li) content using a Laser Ablation-Inductively Coupled Plasma-Mass Spectrometer (LA-ICP-MS) system at the Max Planck Institute for Chemistry (Mainz, Germany). The laser operated in a line scan mode by ablating shell material on the outer shell surface perpendicular to the growth direction and parallel to the striae (Fig. 3.2). To avoid sample contamination, each scan was pre-ablated with a laser spot size of 100 µm at a constant speed of 80 µm s^{-1}. Then, sample ablation was performed using a laser spot size of 80 µm at a speed of 5 µm s^{-1}. Each line scan attained a total length of 600 µm.

Table 3.1 Limit of detection (LOD) and relative standard deviation (RSD) calculated from repeated measurements of the external standard material (NIST SRM 612) for their lithium, molybdenum and barium content via LA-ICP-MS. The USGS MACS-3 reference material served as quality control samples in which the measured values ($\pm 1\sigma$) were compared to known reference values (59.6, 1.21 and 62.9 $\mu g\,g^{-1}$ for Ba, Mo and Li, respectively) obtained from the GeoReM database (http://georem.mpch-mainz.gwdg.de/).

		Ba/Ca_{shell}			Mo/Ca_{shell}			Li/Ca_{shell}		
Sample ID	Date of collection	LOD ($mmol\,mol^{-1}$)	RSD (%)	MACS-3 values ($\mu g\,g^{-1}$)	LOD ($mmol\,mol^{-1}$)	RSD (%)	MACS-3 values ($\mu g\,g^{-1}$)	LOD ($mmol\,mol^{-1}$)	RSD (%)	MACS-3 values ($\mu g\,g^{-1}$)
Shell A	30. Aug 11	9×10^{-6}	2	56.6 ± 4.8	2×10^{-5}	4.7	1.5 ± 0.2	3×10^{-3}	3.2	49.9 ± 1.9
Shell B	30. Aug 11	1×10^{-5}	1.7	65.6 ± 4.3	2×10^{-6}	5.7	2.1 ± 0.2	5×10^{-3}	1.9	56.3 ± 1.2
Shell C	30. Aug 11	8×10^{-6}	2.6	54.8 ± 4.6	8×10^{-7}	3.6	1.4 ± 0.3	2×10^{-3}	6.6	52.2 ± 1.6
Shell D	23. Oct 12	9×10^{-6}	5.5	66.9 ± 4.0	8×10^{-7}	7.1	2.1 ± 0.2	4×10^{-3}	5.1	55.5 ± 1.2
Shell E	23. Oct 12	5×10^{-6}	3.1	58.8 ± 2.5	9×10^{-6}	3.8	1.5 ± 0.1	5×10^{-3}	2.7	53.5 ± 1.3
Shell F	23. Oct 12	1×10^{-5}	2.5	66.2 ± 5.8	8×10^{-7}	5.0	1.7 ± 0.2	4×10^{-3}	2.4	53.8 ± 1.1
Shell G	15. Nov 19	1×10^{-5}	7.1	54.4 ± 2.5	2×10^{-5}	4.2	1.5 ± 0.1	1×10^{-2}	4.9	54.2 ± 1.5
Shell H	15. Nov 19	2×10^{-5}	3.9	58.9 ± 2.2	3×10^{-5}	3.0	1.6 ± 0.1	1×10^{-2}	1.7	53.5 ± 0.8
Shell I	15. Nov 19	5×10^{-6}	3.4	49.9 ± 3.3	1×10^{-5}	4.5	1.2 ± 0.1	3×10^{-3}	4.2	49.8 ± 1.5

Reference materials used for calibration and quality control were analyzed in a similar way. Given the high growth rates in *P. maximus* during the second year of growth (i.e., after the 1st winter growth line), a nearly daily resolution was obtained by sampling every stria from the winter growth mark to the ventral margin. Measured signal intensities were averaged for each line scan as the distribution of trace elements within a single stria was considered to be homogeneous (Barats et al., 2007).

A NewWave Research UP-213 Nd:YAG laser ablation system was used for ablation performing at a repetition rate of 10 Hz with a laser energy density of ca. 15.8 J cm^{-2}. Helium (quality 5.0) served as an initial carrier gas at a flow rate of 0.57 L min^{-1}. After ablation, ion intensities were analyzed using a Thermo Fisher Element 2 single collector sector-field ICP-MS, connected to the laser ablation system, with argon (quality 5.0, flow rate 0.77 L min^{-1}) as carrier gas. The synthetic silicate glass, NIST SRM 612, was used as a reference material and served as an external standard (values obtained from the GeoReM database version 29; http://georem.mpch-mainz.gwdg.de/; last access: 2 July 2021; Jochum et al., 2011), and ^{43}Ca was used as an internal standard.

Data reduction was performed according to the calculations provided by Longerich et al. (1996) and Jochum et al. (2007; 2011) using an in-house Microsoft Excel spreadsheet template. Detection limits (LOD) were computed based on the 3σ criterion using the blank signal of each measurement, i.e., 15 s prior to sample ablation. Element-to-calcium ratios were significantly higher than the calculated detection limits for the target analytes (Table 3.1), with an average LOD of 1×10^{-5} mmol mol^{-1} for Ba, 1×10^{-5} mmol mol^{-1} for Mo and 6×10^{-3} mmol mol^{-1} for Li. Uncertainties of reproducibility were expressed as the relative standard deviation in percent (RSD%) and calculated from repeated NIST SRM 612 measurements. On average, the calculated RSD% was 3.3% for Ba, 4.6% for Mo and 3.6% for lithium. In addition, the synthetic carbonate powder pellet, USGS MACS-3, was used as quality control material and treated as an unknown sample. Table 3.1 summarizes the blindly measured MACS-3 values with an average 59.1 ± 3.8 µg g^{-1} for Ba (ref. value: 59.6 µg g^{-1}), 1.6 ± 0.2 µg g^{-1} for Mo (ref. value: 1.21 µg g^{-1}) and 53.2 ± 1.3 µg g^{-1} for Li (ref. value: 62.9 µg g^{-1}). Published reference values were obtained from the GeoReM database. Due to heterogeneously sized particles of the MACS-3 carbonate pellet, changes in the ablation behavior potentially led to differences in ionization causing deviations between the published reference values and the blindly measured MACS-3 samples. In addition, uncertainties of the non-certified reference material (Jochum et al., 2019) likely also accounted

for observed deviations.

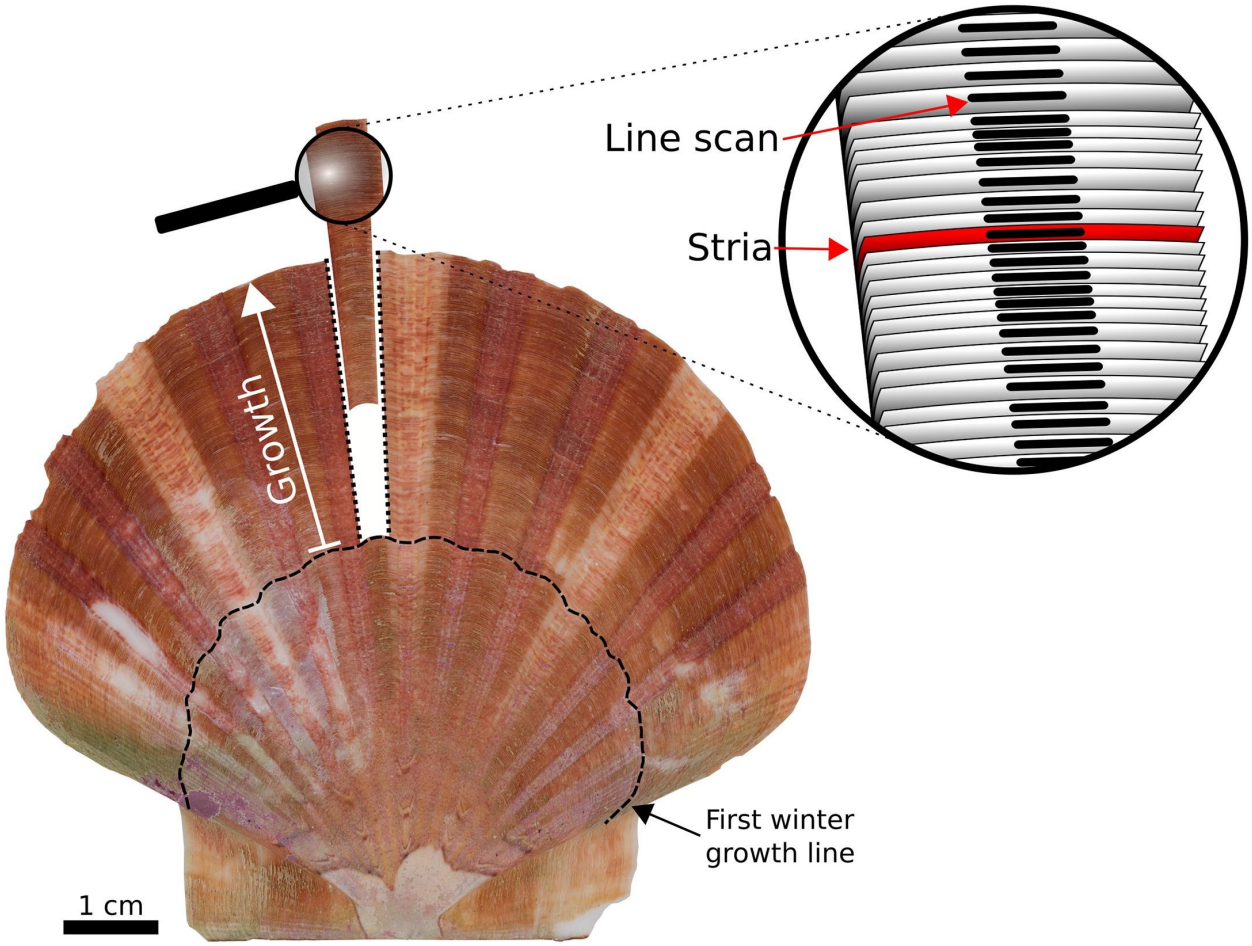

Figure 3.2 Left valve of a *P. maximus* specimen and a schematic representation (magnification) of the analyzed shell portion. All shells used in this study experienced one winter growth line (dashed black line). LA-ICP-MS scans were obtained from a shell section covering the portion between the ventral margin and the winter growth line. Each line scan was positioned on a daily increment (stria) perpendicular to the direction of growth.

3.2.3 Temporal alignment of geochemical information

Shells of *P. maximus* are known to form visible growth increments and lines (aka 'striae') on a daily basis (e.g., Chauvaud et al., 1998; Lorrain et al., 2000). By backdating from the last known increment, i.e., the date of collection corresponding to the last increment visible

at the ventral margin, it was possible to place each stria into a precise temporal context (Fig. 3.2), as long as the shell collection was accomplished during the main growing season. By means of image processing, the clean outer shell surface of each specimen was used for growth pattern analysis. With a Canon EOS 600 DSLR camera connected to a Wild Heerbrugg binocular microscope equipped with a Schott VisiLED MC 1000 light source (sectoral dark field), images were taken along one of the main growth axes between the ventral margin and the first winter line. Obtained, overlapping images were then stitched together using the Image Composite Editor software (version 2.0.3.0; by the Microsoft Research Computational Photography Group). The width of each microgrowth increment was determined by measuring the distance between two adjacent striae and converting the pixel distance into a µm-scale. By including the daily periodicity of striae formation, growth rates were expressed in µm day^{-1}. Since the last formed increments were sometimes hard to identify, because of small fractures at the ventral margin, it was necessary to compare growth patterns of contemporaneous specimens and crossdate the growth curves by minimizing the sum of least squares. As described in previous studies (Thébault et al., 2006; Thébault et al., 2009) difficulties in the visual growth increment determination process and subjective inter-reader discrepancies can lead to small uncertainties in the absolute dating of geochemical data and according to the calculations of a previous study (Fröhlich et al., 2022), a small uncertainty of ± 2 days in the temporal alignment of the geochemical data was considered.

3.2.4 Phytoplankton determination and instrumental data

Phytoplankton data were collected between 13 January and 24 October 2011, between 17 January and 18 December 2012 and between 28 January and 18 December 2019. The sampling frequency in 2011 was twice per week in spring to once per week during the rest of the year, resulting in a total of 52 samples. In 2012, water samples were collected on a weekly basis in spring and biweekly in summer to winter, providing a total of 26 samples. In 2019, a total of 21 water samples were collected on a biweekly basis. Each water sample was collected using a 5 L Niskin bottle that was placed vertically, ca. 1.5 m below the water surface. For phytoplankton species determination, 250 mL of the water sample was carefully filled into a silicon tube, to avoid turbulence and disintegration of intact phytoplankton cells. The phytoplankton cells were fixed in 2.5 mL Lugol's solution within one hour after sampling and stored at a dark place to avoid UV-damaging. The identification of phytoplankton taxa as

well as the calculation of the respective cell concentration were performed using an aliquot of 50 mL of the water sample that was filled into a sedimentation column. After 24 h, the phytoplankton cells settled on a microscope glass slide and the different cells were identified and counted with an inverted microscope (Axio Observer.A1-ZEISS). Due to very small cell sizes and/or only minor differences in cell ornamentations, the assignment to a species-rank was not always unambiguous for some phytoplankton cells. Consequently, these cells were identified according to their phytoplankton genera and/or their cell size. The identification in 2011 and 2012 differed slightly from 2019, e.g., the dinoflagellate genus *Gymnodinium* spp. was subclassed into *Gymnodinium* spp. <20 µm and >20 µm in only 2011 and 2012. In the following, the term phytoplankton bloom refers to an ephemeral, relatively large increase or maximum in the observed cell abundance of a given phytoplankton taxa time-series. Chlorophyll *a* and pheophytin pigment concentration were extracted by filtering water samples with glass fiber filters (GF/F Whatman) and adding 6 mL of 90% acetone. After storing the samples at a dark place for 12 h at 4 °C, each sample was centrifuged (at 3000 rpm for 5 and 10 min) and fluorescence was measured using a Turner Design fluorometer. Finally, pigment concentration were obtained following the calculations provided by (Lorenzen, 1966).

3.2.5 Pseudo-random sampling method to detect potential patterns between trace element profiles and phytoplankton taxa

In order to determine potential relationships between the measured trace element profiles and the phytoplankton data, a pseudo-random sampling method was applied. This algorithmic approach (using the scripting language C++) consisted of multi-step Monte Carlo simulations, where each simulation encompassed 10^7 independent runs (Fig. 3.3). In total 294 simulations were performed, resulting in 2.94 billion runs. The objective of this method was to identify potential relationships in the patterns of trace element profiles, i.e., the relative timing of transient trace element peaks, and those of phytoplankton data.

In general, each run consisted of seven consecutive steps: (1) Choosing the number of different phytoplankton taxa (i.e., number of individual time-series) that are taken into account in the respective run, by pseudo-randomly generating a number (z) between 1 and n (number of considered phytoplankton taxa). (2) Randomly select z phytoplankton time-series among the included taxa (Fig. 3.3A); Supplementary Table S3.1, S3.2). (3) Assign a

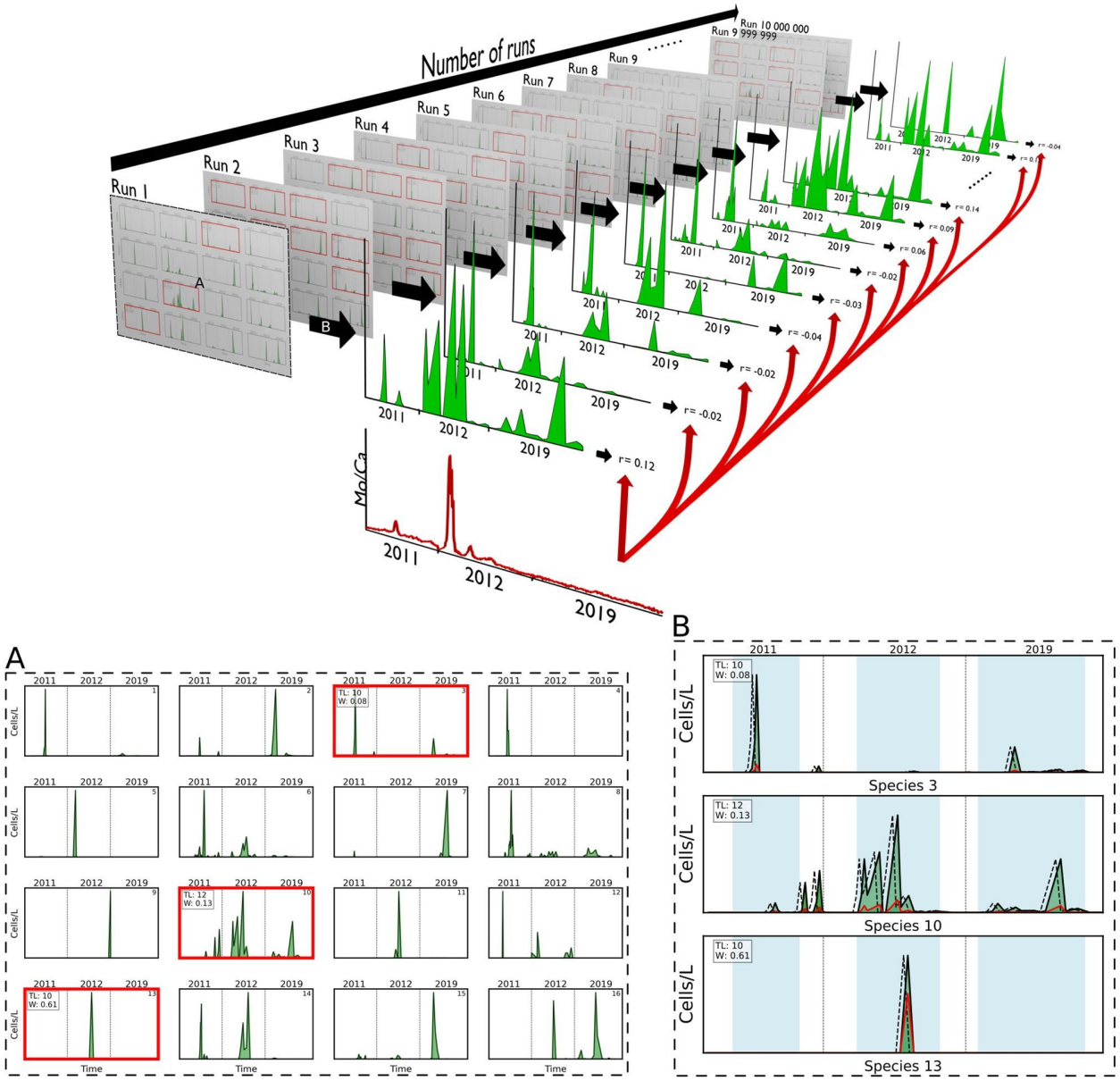

Figure 3.3 Simplified schematic representation of the pseudo-random sampling method used in this study. Exemplarily, 16 different phytoplankton taxa time-series from three years (2011, 2012 and 2019) were included and depicted in **A** (each subplot corresponds to the cell concentration time-series data of one phytoplankton taxon). For each run, a random number of phytoplankton time-series was selected, i.e., subplots marked with a red frame. For instance, in the first run (**A**) the three phytoplankton taxa 3, 10 and 13 were selected. In addition, a time lag (in days between a given range; TL) and a weighting factor (between 0 and 1; W) were randomly generated and assigned to each

Figure 3.3 (continued) phytoplankton time-series. **B** shows how the individual time-series were processed, i.e., the dashed black line displays the original cell concentration data, the green area represents the temporally shifted time-series and the red graph shows the temporally lagged and weighted phytoplankton time-series. The blue area in **B** delimits the region of interest in the processed phytoplankton time-series that is defined by the date of the first and last trace element measurement within the respective year. As a next step, the selected and modified phytoplankton data were combined into a continuous time-series and the Pearson correlation coefficient between the new phytoplankton time-series and the trace element profile was calculated for each run (r). This procedure was repeated iteratively 10^7 times and the best results, according to the Pearson correlation coefficient, were stored.

specific time-lag (in days) to each of the selected phytoplankton time-series. This time lag is randomly selected within a predefined range (Fig. 3.3B). (4) In addition to the temporal lag, a time-series specific weighting factor was randomly assigned to each phytoplankton taxon, where the factor is selected between 0 and 1 (Fig. 3.3B). (5) Generating a continuous phytoplankton time-series based on the specific temporal shifts and weighting factors, by computing the weighted and time-lagged sum of the phytoplankton data that are included in the current run. (6) Compare the obtained phytoplankton time-series to the respective trace element profile by calculating the Pearson correlation coefficient (r). (7) If the Pearson correlation coefficient of the respective run is larger than that of previous runs, store the selected phytoplankton data including time lags and weighting factors (i.e., the 50 best runs, according to the Pearson correlation coefficient, were stored).

Returning the best out of 10^7 runs, according to the Pearson correlation coefficients obtained from one simulation, provided an estimate of the best possible combination. To account for potential patterns at differently lagged phytoplankton time-series, 25 simulations were performed considering predefined time lags (3 days) between 0 and 50 days, i.e., the first simulation covered 0 to 2 days, the second 2 to 4 days, the third 4 to 6 days, and so forth. In addition, 24 simulations were implemented comprising larger time lags (5 days) between 0 and 50 days, i.e., the first simulation encompassed 0 to 4 days, the second 2 to 6 days, etc. This simulation strategy ensured to cover all potential time lags between 0 and 50 days at various temporal windows. As mentioned in section 3.2.4, the phytoplankton identification details slightly differed in the three studied years. Therefore, two sets of simulations were performed: The first covered the main phytoplankton data from all three years (Supplementary Table S3.1) by summarizing individual phytoplankton taxa to phytoplankton

groups, e.g., *Gymnodinium* spp. <20 µm and *Gymnodinium* spp. >20 µm were combined into one *Gymnodinium* spp. group. This grouping strategy ensured to compare phytoplankton groups from all three years but decreased the number of comparable phytoplankton taxa. Since a more detailed phytoplankton determination was available for 2011 and 2012 (Supplementary Table S3.2), the second set of simulations was performed solely focusing on these two years, discarding the less detailed phytoplankton identification in 2019. In order to calculate the Pearson correlation between the phytoplankton data and the trace element profiles, the time-series were cut to the time range covered by the trace element data in the corresponding year (Fig. 3.3B, blue area). To reduce the number of possible combinations and to focus solely on the most dominant taxa, only phytoplankton time-series were included that provided a maximum cell concentration >1000 cells L^{-1} in one of the studied years. In total, 47 phytoplankton groups were taken into account in the first set of simulations and 50 groups in the second set (see Supplementary Tables S3.1 and S3.2). Unlike Ba/Ca_{shell} and Mo/Ca_{shell} profiles, the Li/Ca_{shell} time-series yielded a growth rate related background signal (Thébault and Chauvaud, 2013) that had to be removed from the Li/Ca_{shell} data to extract transient Li peaks and to normalize the background level. This was accomplished by using the Li/Ca_{shell}-to-daily growth rate dependency calculated by Thébault and Chauvaud (2013).

Since no causal relationship could be derived from the purely deterministic calculations, the individual results had to be evaluated separately. To address the quality (i.e., to which extent the temporally shifted and weighted phytoplankton time-series agreed with the trace element profiles) of a simulation at a certain time interval relative to that of other tested time lags, the Pearson correlation coefficients provided a first evaluation. Simulations showing larger correlation coefficients were then manually evaluated by comparing the simulated phytoplankton time-series with the trace element profiles following the premise of a potential relationship. Finally, the hypothetically determined scenarios (or best matching scenarios), i.e., phytoplankton species and time lags used to explain the occurrence of trace element peaks, were contextualized ecologically and interpreted accordingly.

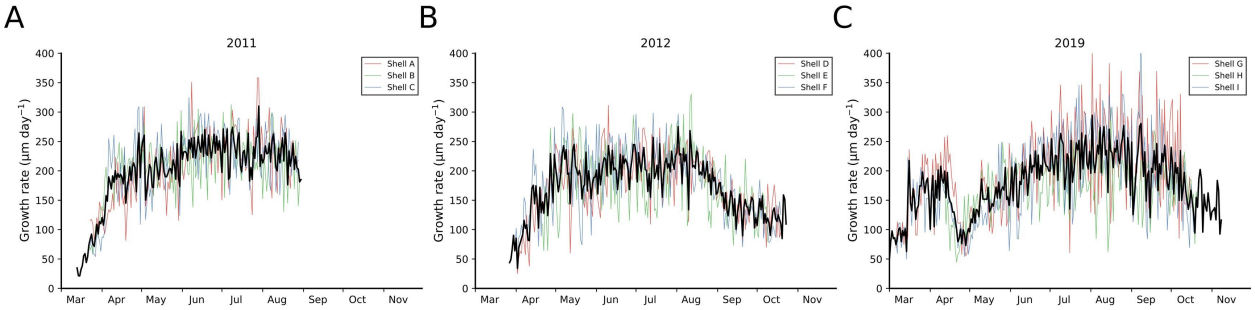

Figure 3.4 Growth rates measured from three contemporaneous specimens from 2011 (**A**), 2012 (**B**) and 2019 (**C**). The black line depicts the average growth rate. The last measured growth rate equals to the date of collection of the three individuals in all three years.

3.3 Results

3.3.1 Growth rate and trace element profiles in *P. maximus*

Although growth rates varied among specimens, especially during the main growing season, the overall growth patterns were largely synchronous among contemporaneous bivalves (Fig. 3.4). In all three studied years, shell growth commenced in March at growth rates between 20 and 60 µm day^{-1}. In 2011 and 2012 (Fig. 3.4A, B), the growth rates gradually increased until early May (reaching average growth rates of ca. 200 µm day^{-1}), whereas in 2019 (Fig. 3.4C), growth rates initially peaked in mid-April (ca. 200 µm day^{-1}) but dropped rapidly until end of April (68 µm day^{-1} on 28 April). After this growth slowdown, the growth rates successively increased reaching maximum values in early August (ca. 280 µm day^{-1}). Similarly, maximum growth in 2011 and 2012 occurred between the end of July and early August with growth rates of ca. 300 µm day^{-1} and 280 µm day^{-1}, respectively. Growth rates started to decline between the end of August and September in all three years.

Trace element profiles of the studied years exhibited a similar pattern among specimens from the same population (Fig. 3.5). In general, a flat baseline level was episodically interrupted by distinct peaks. Average background levels were 0.60 ± 0.06 µmol mol^{-1} for Ba/Ca$_{shell}$, 0.04 ± 0.01 µmol mol^{-1} for Mo/Ca$_{shell}$ and 33.73 ± 4.19 µmol mol^{-1} for Li/Ca$_{shell}$. In 2011, four large Ba/Ca$_{shell}$ peaks were detected with the highest elevation in early August (1.77 µmol mol^{-1}; Fig. 3.5A). From all three years, the largest Ba peak values were determined in August 2012 reaching molar ratios of 3.66 µmol mol^{-1} (Fig. 3.5B). Additionally,

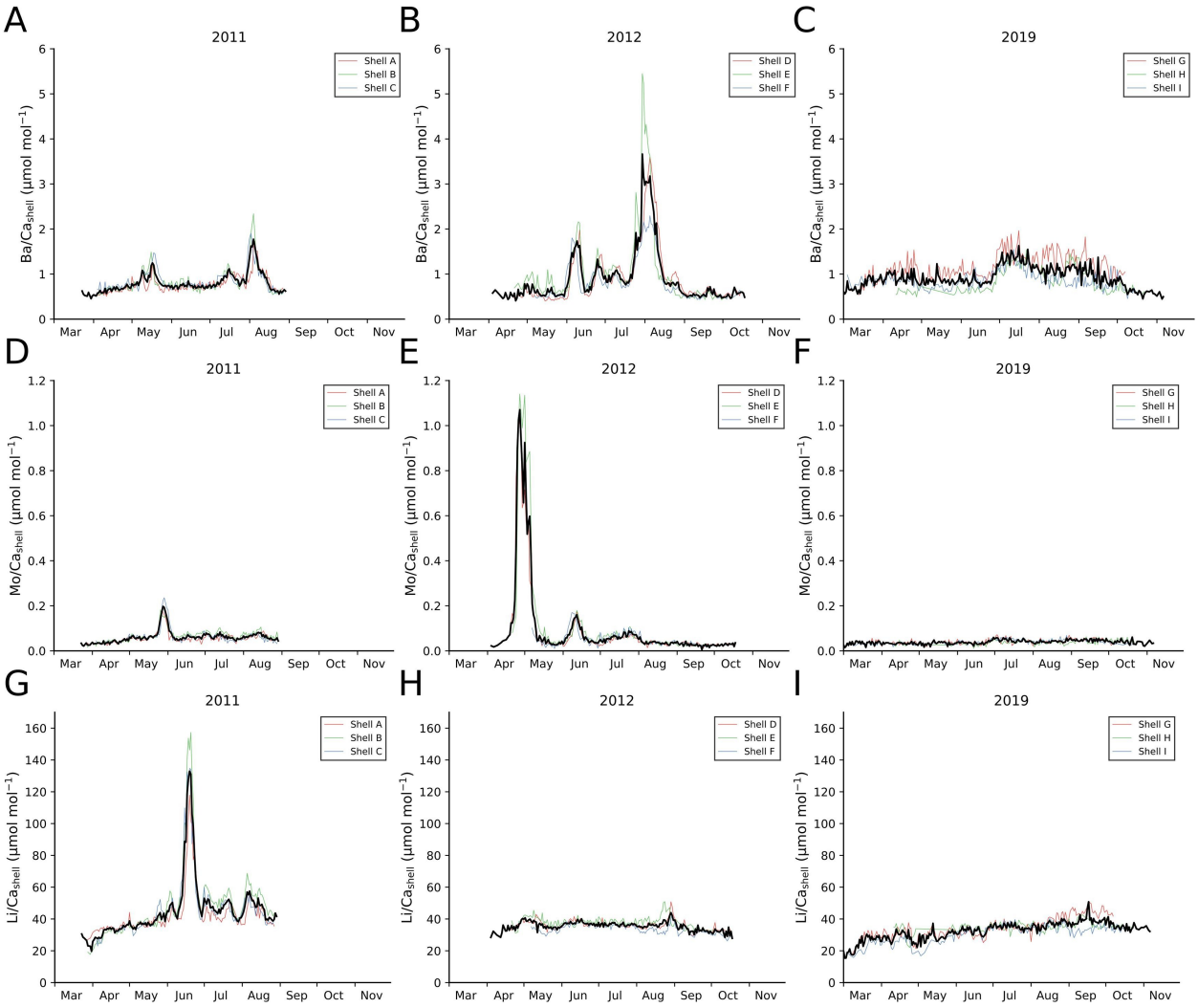

Figure 3.5 Trace element profiles (Li/Ca$_{shell}$, Mo/Ca$_{shell}$ and Ba/Ca$_{shell}$) measured in three contemporaneous *P. maximus* specimens from 2011 (**A**,**D**,**G**), 2012 (**B**,**E**,**H**) and 2019 (**C**,**F**,**I**). Average element-to-calcium ratios are indicated as black line.

three distinct Ba maxima occurred between June and July 2012. In 2019, elevated Ba/Ca_{shell} values (1.63 µmol mol^{-1}) were obtained between early July and August (Fig. 3.5C). The Mo/Ca_{shell} profiles of 2011 showed only one distinct Mo/Ca_{shell} maximum in late May (0.19 µmol mol^{-1}; Fig. 3.5D), whereas in 2012, three ephemeral peaks of decreasing magnitudes were measured between April and July with values in the range of 0.08 and 1.07 µmol mol^{-1} (Fig. 3.5E). No Mo/Ca_{shell} peaks were observed in shells from 2019 (Fig. 3.5F). The Li/Ca_{shell} profiles of all three years exhibit only one sharp Li/Ca_{shell} peak in mid-June 2011 with an average value of 132.93 µmol mol^{-1}. This large peak was enveloped by smaller Li/Ca_{shell} fluctuations between 38 and 58 µmol mol^{-1}.

3.3.2 Phytoplankton dynamics in 2011, 2012 and 2019

In 2011, the phytoplankton dynamics (Fig. 3.6A) showed increasing chlorophyll *a* levels between February (0.67 µg L^{-1}) and early May (5.11 µg L^{-1}) that coincided with the formation of the second largest diatom bloom (up to 742,500 cells L^{-1} on 02 May) in 2011, while pheophytin pigment concentrations were low (between 0.23 and 0.80 µg L^{-1}). Dinoflagellate cell concentration reached its annual maximum of 347,080 cells L^{-1} on 23 May and was accompanied by a peak in pheophytin pigments (1.64 µg L^{-1}). The largest diatom spring bloom occurred on 06 June (4,072,860 cells L^{-1}) with chlorophyll *a* and pheophytin pigment concentration of 3.52 and 1.88 µg L^{-1}, respectively. Until the end of August, neither large diatom nor dinoflagellate blooms developed, as reflected by low levels of chlorophyll *a* fluctuating between 0.97 and 2.19 µg L^{-1}. However, pheophytin concentration consistently showed high values ranging from 1.02 to 1.57 µg L^{-1}. The diatom community was largely dominated by the taxon *Chaetoceros* spp. that made up nearly 80% of the total diatom cells recorded in 2011 (Fig. 3.6A; left panel), followed by *Dactyliosolen fragilissimus* (5.3%), *Guinardia delicatula* (3.4%) and *Leptocylindrus danicus* (3.0%). The dinoflagellates were mainly composed of two taxa, i.e., *Heterocapsa minima* and *Gymnodinium* spp. (size fraction >20 µm) that accounted for 41.1% and 39.1% of the total dinoflagellate cells in 2011.

The phytoplankton dynamics in 2012 (Fig. 3.6B) differed significantly from that observed in 2011 showing two chlorophyll *a* spring peaks, i.e., on 03 April (4.44 µg L^{-1}) and on 10 May (9.77 µg L^{-1}). The first chlorophyll *a* peak was associated with an early diatom bloom (476,990 cells L^{-1}) which was followed by the first and largest dinoflagellate efflorescence in 2012 on 24 April (253,960 cells L^{-1}). Two large diatom summer blooms occurred on 28 June

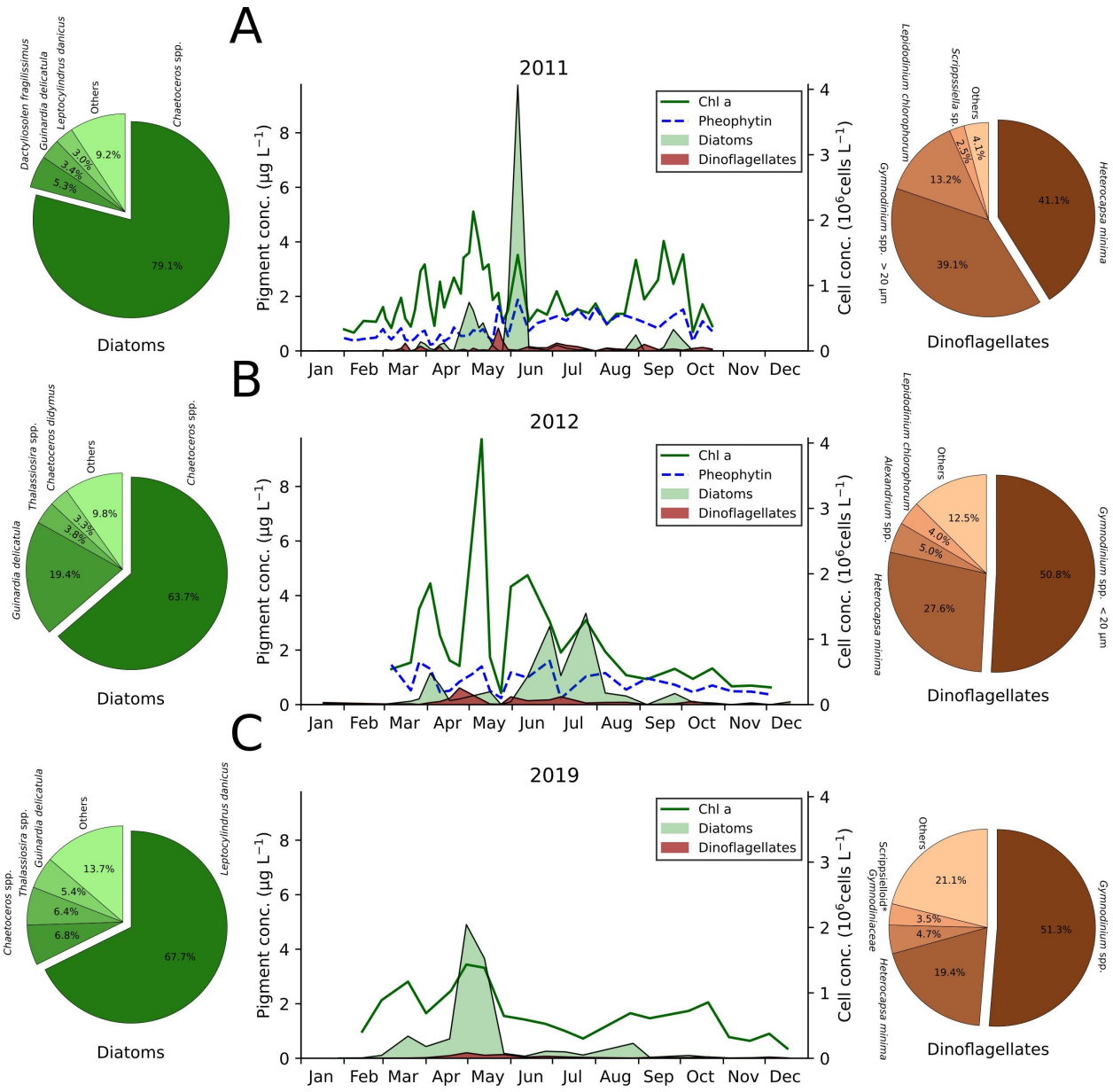

Figure 3.6 Overview of the phytoplankton dynamics observed in the Bay of Brest (Lanvéoc) in 2011 (**A**), 2012 (**B**) and 2019 (**C**). Pigment concentrations represented as solid green and dashed blue lines, i.e., chlorophyll *a* and pheophytin (in 2011 and 2012), respectively. Pie charts display the diatom (left panel) and dinoflagellate (right panel) community composition, according to their relative abundance, observed in the respective years (* dinoflagellate group that comprises cells of *Scrippsiella* spp., *Pentapharsodinium* spp. and *Ensiculifera* spp.).

(1,195,392 cells L^{-1}) and on 24 July (1,395,940 cells L^{-1}) that were preceded by smaller dinoflagellate blooms on 31 May (119,040 cells L^{-1}) and on 06 July (119,680 cells L^{-1}). The summer diatom blooms were related with higher chlorophyll *a* levels between 4.74 and 3.09 µg L^{-1}. The pheophytin pigment concentration roughly followed the chlorophyll *a* pattern with highest concentrations on 26 March (1.55 µg L^{-1}), 10 May (1.40 µg L^{-1}) and 28 June (1.60 µg L^{-1}) followed by lower concentrations throughout the rest of the year (0.62 ± 0.3 µg L^{-1}). Similar to 2011, the majority of diatom cells belonged to the diatom taxon *Chaetoceros* spp. that accounted for 63.7% of the total diatom cells. The dinoflagellate community was dominated by cells of the taxon *Gymnodinium* spp. (size fraction < 20 µm; 50.8%) and *Heterocapsa minima* (27.6%).

In 2019, the phytoplankton dynamics (Fig. 3.6C) was characterized by two chlorophyll *a* maxima in spring, i.e., on 19 March and 30 April with concentrations of 2.81 and 3.44 µg L^{-1}, respectively. These peaks in chlorophyll *a* pigments coincided with two diatom blooms. The first yet small spring bloom occurred on 19 March with cell concentrations reaching 338,340 cells L^{-1} and the second or the largest bloom emerged on 30 April with 2,044,640 cells L^{-1}. A dinoflagellate efflorescence developed (reaching 83,680 cells L^{-1}) contemporaneously to the late diatom spring bloom (30 April). During summer, chlorophyll concentrations remained low (between 0.72 and 1.65 µg L^{-1}) and only smaller diatom blooms evolved with cell concentrations below 228,060 cells L^{-1} (on 28 August). Furthermore, no dinoflagellate blooms were recorded during summer. Unfortunately, pheophytin pigment concentrations were not recorded in 2019. Unlike 2011 and 2012, the dominant diatom species belonged to *Leptocylindrus danicus* that made up 67.7% of the total diatom cells, followed by *Chaetoceros* spp. (6.8%). Similar to 2011 and 2012, the dinoflagellate taxa *Gymnodinium* spp. (51.3%) and *Heterocapsa minima* (19.4%) formed the predominant dinoflagellate groups observed in 2019.

3.3.3 Pseudo-random sampling method results

The simulations used to derive potential patterns that could explain the formation of Ba $/Ca_{shell}$ peaks resulted in Pearson correlation coefficients between 0.67 and 0.90 ($p < 0.05$), with three local maxima of gradually decreasing coefficients at time lags of 8 to 12, 24 to 28 and 36 to 40 days, respectively (Fig. 3.7A, B). Evaluating the generated time-series (temporally lagged and weighted combination of phytoplankton taxa) for these intervals

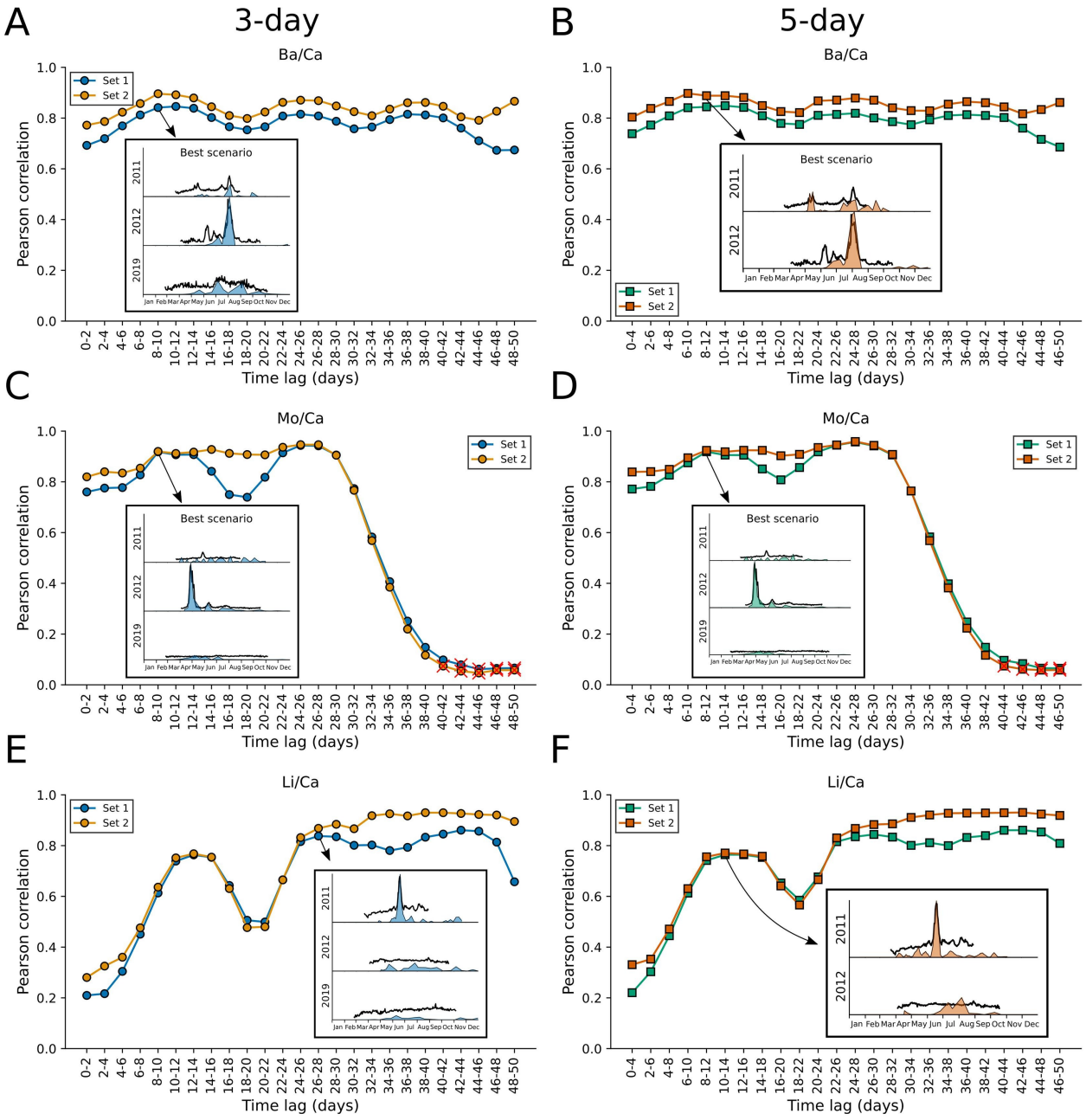

Figure 3.7 Pearson correlation results obtained from the pseudo-random sampling method applied on the various phytoplankton time-series versus Ba/Ca_{shell} (**A**, **B**), Mo/Ca_{shell} (**C**, **D**) and Li/Ca_{shell} (**E**, **F**) profiles at different temporal windows (see section 3.2.5). Correlations that were statistically not significant were indicated with a red cross (**C**, **D**). Plots on the left side show results for the simulated time interval of 3 days and on the right the results for a 5-day interval. Set 1 simulations include lower resolved phytoplankton taxa but were applied to three different years, while set 2

Figure 3.7 (continued) simulations include higher resolved phytoplankton groups but were confined to 2011 and 2012. Small graphs in each subplot depict the best hypothetical scenario obtained, i.e., the temporally shifted and weighted phytoplankton time-series that fitted best to the magnitude and timing of trace element peaks. Results of all simulations are illustrated in the supplementary materials. Since only one large Li/Ca_{shell} peak (in 2011) was observed in the studied years, a single best phytoplankton pattern could not be established. Instead, several scenarios at different time lags provide a good agreement with the Li/Ca_{shell} profiles (see section 3.4.3).

demonstrate that the best agreement to the Ba/Ca_{shell} profiles was obtained for a scenario with a time lag of 8 to 12 days (Fig. 3.7A, B; subplots). At this time lag, the scenario considering a 5-day interval (Set 2) revealed the strongest similarity with the Ba/Ca_{shell} peaks, i.e., all distinct peaks matched with a phytoplankton bloom except for the first Ba/Ca_{shell} peak in 2012 (Fig. 3.7B). Results obtained for other simulations (Supplementary Figs. S3.1 to S3.4) indicate that neither larger or shorter time lags resulted in a sufficiently strong correlation with the trace element profiles. For most of these scenarios, peaks in the phytoplankton data show no consistent pattern with the Ba/Ca_{shell} profiles. The simulations analyzing the time lag between 8 and 12 days revealed a compelling pattern for the diatom species *Thalassionema nitzschioides* with the timing of Ba/Ca_{shell} peaks, i.e., blooms of this diatom taxon coincided with the formation of Ba enrichments in the shell calcite in all three years. In addition, the non-toxic dinoflagellate species *Lepidodinium chlorophorum* and other diatom groups (different species of the genus *Chaetoceros* (*C. socialis*, *C. debilis* and *C. danicus*) as well as aggregated cells of this taxon (*Chaetoceros* spp. chains) and the diatom *Cerataulina pelagica*) also coincided with the timing of subsequent Ba/Ca_{shell} peaks at time lags between 8 and 12 days, but were confined to one or two of the studied years.

Simulations evaluating phytoplankton patterns in relation to Mo/Ca_{shell} profiles (Fig. 3.7C, D) showed a large variability in the Pearson correlation coefficients at different time lags that ranged between 0.05 (statistically not significant; $p > 0.05$) to 0.96 ($p < 0.05$). Correlation coefficients dropped gradually at time intervals >30 days. Although high Pearson correlation coefficients were calculated for time lags of 24 to 28 days, the resulting phytoplankton combinations failed to provide a pattern analogous to the Mo/Ca_{shell} profiles. For instance, the second and third Mo/Ca_{shell} peak in 2012 could not be wiggle–matched to corresponding phytoplankton blooms (Supplementary Figs. S3.5 to S3.8). However, the phytoplankton pattern that was detected for an 8-to-12-day time lag strongly agreed with the measured Mo/Ca_{shell}

peaks in 2012 (subplots in Fig. 3.7C, D). The respective simulations revealed that the shell Mo profiles coincided with the timing of two dinoflagellate genera, i.e., *Gymnodinium* spp. and *Prorocentrum* spp. (including *P. minimum*, *P. cordatum* and *P. balticum*). In particular, time-series of the small dinoflagellate *Gymnodinium* spp. (<20 µm) and *P. balticum* showed a high degree of similarity with the Mo/Ca_{shell} profiles, according to simulations of set 2 with higher taxonomic phytoplankton resolution.

The Pearson correlation coefficients calculated from the simulations on Li/Ca_{shell} at different time lags (Fig. 3.7E, F) exhibited values between 0.21 and 0.93 ($p < 0.05$). The first correlation maximum was observed at a time lag of 10 to 14 days (see subplot in Fig. 3.7F). The high level of synchronicity at this time interval was induced by matching the largest diatom bloom that emerged in all three years (*Chaetoceros* spp.) with the large Li/Ca_{shell} peak in 2011. However, this phytoplankton configuration did not agree well to the Li/Ca_{shell} profile observed in 2012 as well as to the smaller Li/Ca_{shell} peaks observed in 2011. Apart from this, results obtained for larger time lags (Supplementary Figs. S3.9 to S3.12) exhibited high Pearson correlation coefficients with scenarios that fit well to the Li/Ca_{shell} profiles (e.g., subplot in Fig. 3.7E). Accordingly, a best matching scenario could not be determined. This difficulty occurred because only one prominent Li/Ca_{shell} peak was measured within the studied years, which complicated the detection of potential patterns. Instead, several phytoplankton blooms at different time lags fitted to the trace element peak resulting in larger correlation coefficients.

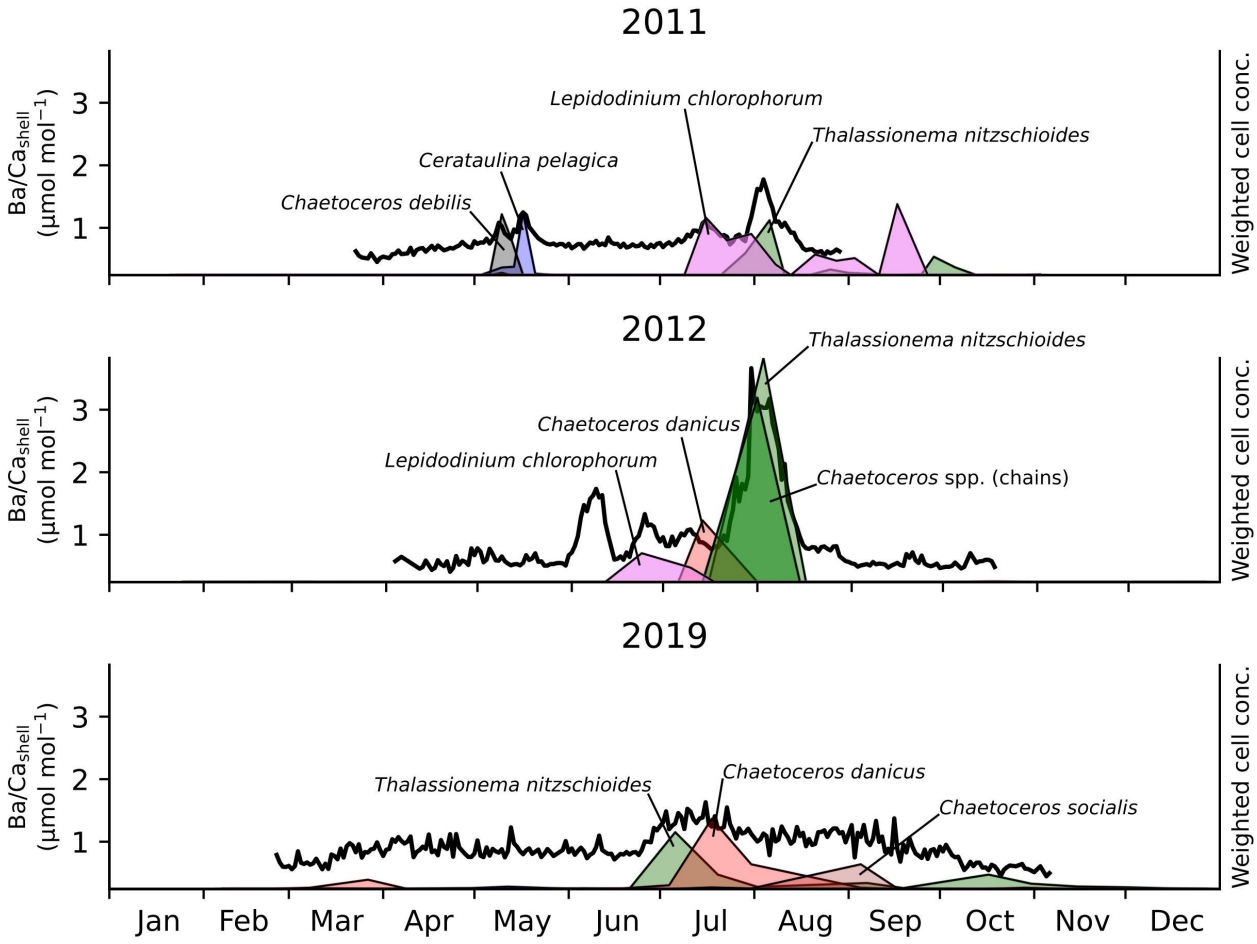

Figure 3.8 Ba/Ca$_{shell}$ profiles of 2011, 2012 and 2019 in relation to blooms of diatoms and dinoflagellates that coincide with Ba/Ca$_{shell}$ peaks after applying a time lag between 8 and 12 days, as provided from the pseudo-random sampling simulations. Weighted cell concentration data are given in arbitrary units. Similar species-specific weighting factors were used in each year. The first Ba/Ca$_{shell}$ peak in 2012, which did not match with a diatom or dinoflagellate bloom, agreed well with the timing of a large flagellate bloom (see Supplementary Fig. S3.13).

3.4 Discussion

The timing as well as the magnitude of transient trace element peaks in profiles of *P. maximus* shells from 2011, 2012 and 2019 exhibited striking similarities among individuals from the same population, confirming previous studies according to which the formation of Ba/Ca_{shell}, Mo/Ca_{shell} and Li/Ca_{shell} enrichments in bivalve shells is environmentally driven (e.g., Gillikin et al., 2008; Thébault et al., 2009; Barats et al., 2010; Thébault and Chauvaud, 2013). The results obtained from the pseudo-random sampling simulations cast new light on the relationship between such trace element peaks and the phytoplankton dynamics that prevailed during shell growth. For all three elements analyzed in this study, a potential explanation could be derived by considering a short time lag of 8 to 12 days between phytoplankton events and trace element peaks in the shell. Ba/Ca_{shell} profiles are likely related to the blooms of diatoms, dinoflagellates and flagellates, whereas Mo/Ca_{shell} patterns may reflect blooms of specific nitrate assimilating dinoflagellates. Mo/Ca_{shell} profiles may also potentially be linked to the timing of diatom aggregates in the water column. Li/Ca_{shell} peaks exhibited patterns similar to the blooms of diatoms that produce neurotoxins under stressful environmental conditions as well as large diatom blooms. Accordingly, shell Ba, Mo and Li profiles could be used as valuable chemical proxies to assess past phytoplankton dynamics.

3.4.1 Phytoplankton and Ba/Ca_{shell} peaks

The high degree of inter-specimen synchronicity of Ba/Ca_{shell} peaks (Fig. 3.5A, B, C) strongly suggests that common environmental drivers regulate the timing of enhanced Ba incorporation into the shell carbonate (Stecher et al., 1996; Vander Putten et al., 2000; Gillikin et al., 2008; Barats et al., 2009; Thébault et al., 2009; Hatch et al., 2013; Marali et al., 2017). Several studies put forward a possible correlation between chlorophyll *a* and Ba/Ca_{shell} profiles in bivalve shells (e.g., Hatch et al., 2013; Doré et al., 2020), however, such a linkage could not be established for the studied years 2011 and 2012 in shells of *P. maximus* (Fröhlich et al., 2022). In addition to these years, chlorophyll *a* concentration in 2019 (Fig. 3.6C) showed no running similarity with the Ba/Ca_{shell} profiles (Fig. 3.5C) observed in shells from the same year, i.e., the spring bloom related chlorophyll *a* maximum occurred in late April, whereas elevated Ba/Ca_{shell} concentrations appeared in late July to August. This further

underscores the limitation of Ba/Ca_{shell} as an indicator of bulk phytoplankton biomass in the ambient water. Likewise, the lack of similarity between total diatom and dinoflagellate cell concentrations and measured Ba/Ca_{shell} profiles in all three years indicates that Ba/Ca_{shell} may not be used as a reliable proxy for bulk diatoms or dinoflagellates in the water column.

It has been proposed that the intake of Ba-rich phytoplankton cells (e.g., diatoms) drives the formation of Ba/Ca_{shell} peaks in the scallop *Comptopallium radula* (Thébault et al., 2009). However, the results obtained from the pseudo-random sampling method indicated no correlation with only a single diatom or dinoflagellate species existed in the studied years. Consequently, Ba/Ca_{shell} peaks could either have a plurispecific cause or are entirely unrelated to the phytoplankton species analyzed in this study. The variable cell-associated Ba concentration reported for various phytoplankton species (Roth and Riley, 1971; Martin and Knauer, 1973; Fisher et al., 1991) supports the notion that different taxa might contribute differently to the formation of Ba/Ca_{shell} peaks (Fröhlich et al., 2022). Moreover, testing potential scenarios of species-specifically weighted time-series at different time lags provide further insights into this relationship between phytoplankton and the formation of Ba/Ca_{shell} peaks. Firstly, phytoplankton time-series did not adequately match the Ba/Ca_{shell} profiles when only a short temporal offset (i.e., 0–2 days and 0–4 days) was considered, as shown by the relatively low Pearson correlation coefficients (Fig. 3.7A, B). Secondly, the best fitting scenario was obtained for a time lag 8 to 12 days, suggesting that Ba could be incorporated into the shell calcite with a delay of 8 to 12 days after a bloom of Ba-rich phytoplankton. In that scenario (subplot in Fig. 3.7B), each Ba/Ca_{shell} peak coincided with a phytoplankton bloom, except the first peak in 2012. Although the simulations covering 3-day intervals showed high correlation coefficients at that time lag (Fig. 3.7A), the best phytoplankton combination was obtained using a 5-day interval (larger degree of freedom compared to a 3-day interval; Fig. 3.7B). Accordingly, time lags hypothetically vary between phytoplankton species by more than about 3 days, which would agree with the time lag of 8 to 12 days. However, it remains to be determined if species-specific differences in sinking velocities (e.g., Bienfang et al., 1982; Alldredge and Gotschalk, 1989; Peperzak et al., 2003) and/or a species-dependent variability in the desorption rate of Ba in the digestive tract of bivalves account for the small variance in the estimated time lags.

Evaluating the phytoplankton species obtained from the simulations covering the best fitting time interval, i.e., 8 to 12 days, demonstrates that the diatom species *T. nitzschioides* shares a striking pattern with the Ba/Ca_{shell} profiles. In all three years, the bloom of this

taxon coincided with a Ba/Ca_{shell} maximum after shifting the time-series about 10 days (Fig. 3.8). Blooms of other diatom taxa match with Ba enrichments after similar time lags (e.g., species of the genus *Chaetoceros*) but were confined to one or two of the studied years (Fig. 3.8). Furthermore, blooms of the dinoflagellate species *L. chlorophorum* are consistent with the timing of Ba/Ca_{shell} peaks in 2011 and 2012 (Fig. 3.8), suggesting that Ba could also originate from dinoflagellates contributing to the observed Ba/Ca_{shell} peaks in addition to diatoms. This conclusion is supported by the findings of Fisher et al. (1991) showing that dinoflagellates accumulate Ba at high concentrations, and Hatch et al. (2013) who observed a dinoflagellate bloom (*Lingulodinium polyedrum*) several days prior to a Ba/Ca_{shell} peak in the bivalve *Donax gouldii*. However, not every Ba/Ca_{shell} peak coincided with a phytoplankton group considered in these simulations, i.e., the first peak in early June 2012 did not match with a diatom or dinoflagellate bloom (Fig. 3.8). Despite the lack of similarity between chlorophyll *a* levels and Ba/Ca_{shell} profiles (Fröhlich et al., 2022) as well as their limited capability to reliably reconstruct phytoplankton biomass (e.g., Desortová, 1981; Kruskopf and Flynn, 2006), the first Ba/Ca_{shell} peak in 2012 coincided with the second chlorophyll *a* maximum observed in that year (Fig. 3.6B), which was associated with a large flagellate bloom (see Supplementary Fig. S3.13). Accordingly, a link between large flagellate blooms and distinct Ba/Ca_{shell} peaks could be hypothesized (as flagellates were not taxonomically identified in detail, no species-specific flagellate-to-Ba relationship could be established). This assumption is supported by the findings of Fisher et al. (1991) showing that flagellates are associated with large quantities of cell-associated Ba. Therefore, it is likely that in addition to diatoms and dinoflagellates, the ingestion of Ba-enriched flagellates contributed to the formation of Ba/Ca_{shell} peaks in *P. maximus*. The pseudo-random sampling results further strengthened the hypothesis of Ba/Ca_{shell} peaks having a dietary origin, because a potential pattern between the occurrence of various phytoplankton species and the formation of Ba/Ca_{shell} peaks was revealed when a temporal offset between one and two weeks was considered.

3.4.2 Phytoplankton and Mo/Ca_{shell} peaks

The transient Mo/Ca_{shell} peaks differ significantly in their timing and magnitude between the studied years indicating that the formation of Mo/Ca_{shell} peaks is likely caused by annually changing environmental factors, most likely originating from a dietary source (Thébault et

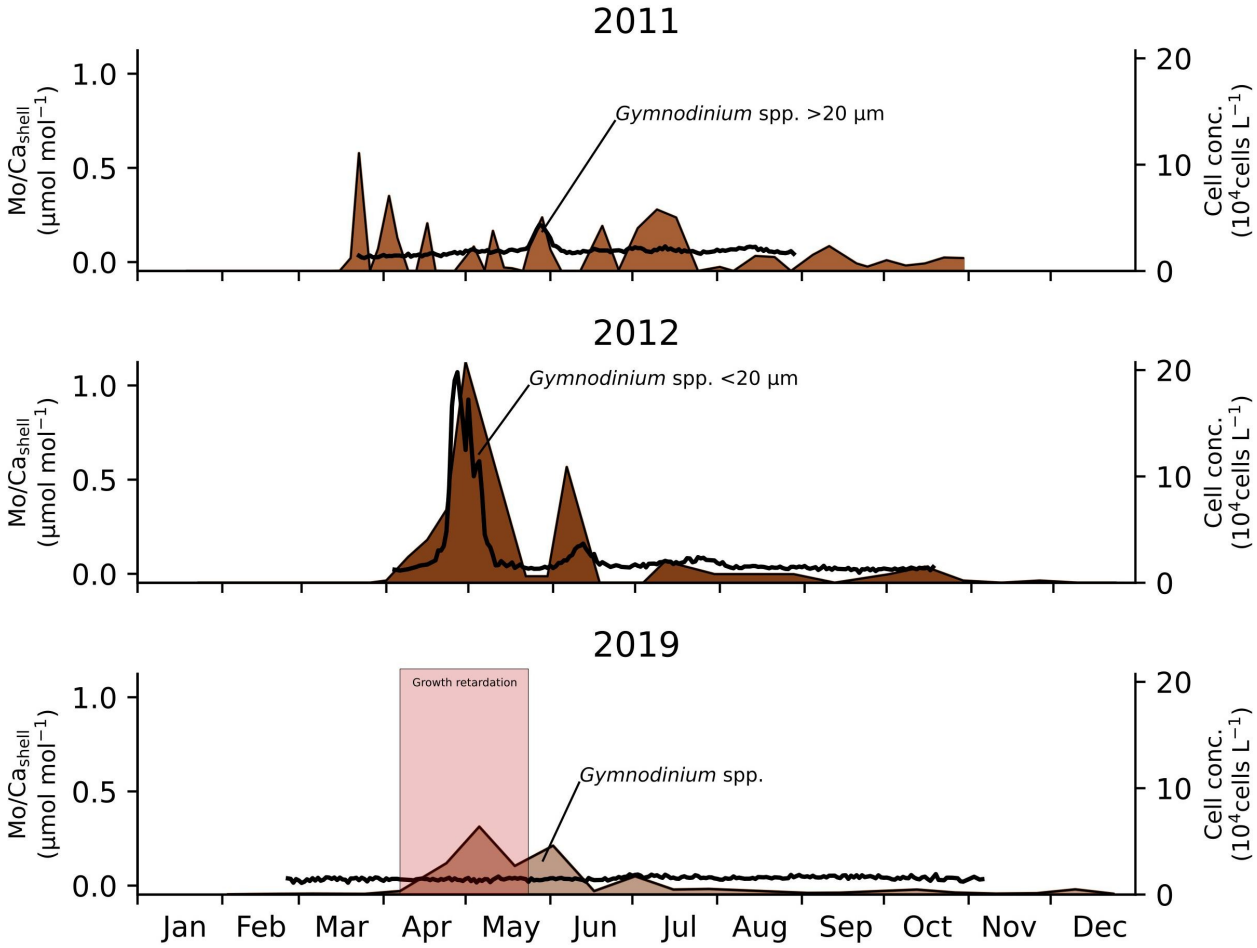

Figure 3.9 Mo/Ca_{shell} profiles of 2011, 2012 and 2019 and the cell concentration time-series of the dinoflagellate *Gymnodinium* spp. at different cell size fractions. Dinoflagellate time-series were temporally shifted about 8 days. Red area depicts the period of large growth rate retardation in *P. maximus* observed in spring 2019.

al., 2009; Tabouret et al., 2012). The pseudo-random sampling simulations revealed a phytoplankton scenario for a time lag of 8 to 12 days (similar to that obtained for Ba/Ca_{shell}) showing a striking similarity with the Mo/Ca_{shell} profiles. In that scenario, blooms of two dinoflagellate genera (*Gymnodinium* spp. and *Prorocentrum* spp.) agreed well with the occurrence of transient Mo/Ca_{shell} peaks. Especially, the time-series of the dominant dinoflagellate *Gymnodinium* spp. shared a similar pattern with the Mo/Ca_{shell} profiles in 2012 with three successively decreasing Mo/Ca_{shell} peaks coinciding with three blooms of decreasing cell concentrations (Fig. 3.9). However, only the size fraction including cells smaller than 20 µm shared this clear pattern with the Mo/Ca_{shell} profiles. In 2011, exclusively cells of *Gymnodinium* spp. larger 20 µm were observed. Interestingly, shifting this time-series (*Gymnodinium* spp. >20 µm) about the same time lag as *Gymnodinium* spp. <20 µm from 2012, shows that the Mo/Ca_{shell} peak in 2011 match with one of the recorded *Gymnodinium* spp. blooms (i.e., the sixth bloom in 2011; Fig. 3.9). Since individual phytoplankton blooms are mostly monospecific (largely dominated by a single phytoplankton taxon), it can be hypothesized that this specific bloom was composed of a smaller *Gymnodinium* species whose cell size fits within the range potentially ingested by *P. maximus*. Conversely, scallops likely filtered out the larger fraction of *Gymnodinium* cells, as particle size is known to be one of the key factors controlling the retention and uptake of phytoplankton cells in scallops (e.g., Shumway et al., 1997; Beninger et al., 2004). In addition to the timing, the magnitude of Mo/Ca_{shell} peaks seems to be resembled by the dinoflagellate cell concentration, except a small deviation of the second Mo/Ca_{shell} peak in 2012. Given the similarity between the *Gymnodinium* spp. time-series and the measured Mo/Ca_{shell} profiles in 2011 and 2012 (Fig. 3.9), a potential link between this dinoflagellate and the development of Mo/Ca_{shell} peaks can be hypothesized. In 2019, no Mo/Ca_{shell} peak was measured although two *Gymnodinium* spp. blooms were monitored. On the one hand, these blooms coincided with a period of significant shell growth retardation (Fig. 3.9). On the other hand, no size classification was made for this dinoflagellate in 2019. Consequently, it is difficult to determine if the absence of a Mo/Ca_{shell} maximum is induced by large (>20 µm), non-ingestible *Gymnodinium* spp. cells (similar to the blooms monitored in 2011; Fig. 3.9) and/or by the strong growth rate reduction that is associated with a restricted food intake (Chauvaud et al., 1998; Lorrain et al., 2000).

A possible mechanism for the observed relationship between *Gymnodinium* spp. blooms and the formation of Mo/Ca_{shell} enrichments is the nitrate assimilation strategy of phyto-

plankton that requires the presence of Mo which is a crucial constituent of the enzyme nitrate reductase (Collier, 1985; Marino et al., 2003). In marine organisms, ammonium is preferentially used instead of nitrate for nitrogen assimilation (Morris and Syrett, 1963; Eppley et al., 1969), which does not require the activity of Mo-containing nitrate reductase. In turn, periods of low ammonium were shown to be associated with nitrate reductase synthesis in phytoplankton (Eppley and Coatsworth, 1968; Eppley et al., 1969), suggesting a potential relationship between phytoplankton cells grown on nitrate and enhanced Mo incorporation into the shell (Thébault et al., 2009). Accordingly, Mo/Ca_{shell} peaks would resemble the timing and magnitude of large phytoplankton blooms grown on nitrates. Yet, this assumption could not be substantiated in this study, because the large Mo/Ca_{shell} peak in 2011 coincided with a peak in ammonium (see Supplementary Fig. S3.14). However, minor fluctuations in the Mo/Ca_{shell} profile from 2011 (in June, July and August) seem to be inversely correlated to measured ammonium concentrations (see Supplementary Fig. S3.14). Unfortunately, ammonium concentrations were not recorded in 2012. Nevertheless, it was demonstrated that some dinoflagellates utilize nitrate instead of ammonium, even when ammonium levels were not limited (Harrison, 1973). Moreover, Yamamoto et al. (2004) showed the affinity of the *Gymnodinium* species *G. catenatum* to assimilate nitrate instead of ammonium, which in turn, requires the presence of nitrate reductase, leading to a high amount of enzyme associated Mo in the dinoflagellate cell. In addition, Ho et al. (2003) observed a 5.6 times higher cellular concentration of Mo in cells of *G. chlorophorum* (13 mmol L^{-1}) compared to other marine phytoplankton taxa reported in that study (2.3 mmol L^{-1}). These findings support the assumption that the ingestion of Mo-rich *Gymnodinium* spp. cells could be linked to the formation of Mo/Ca_{shell} peaks in scallop shells.

In addition to the hypothesis stated previously, Thébault et al. (2022) demonstrated a potential link between the development of diatom aggregates in the water column, especially after large diatom blooms that exhausted nutrient stocks (i.e., silicates), and the formation of Mo/Ca_{shell} peaks in *P. maximus*. These aggregates likely sequester dissolved Mo from the ambient water and lead to the accumulation of Mo in the shell calcite after being ingested by the bivalve. This provides a suitable explanation for the single Mo/Ca_{shell} peak observed in 2011 (Fig. 3.5D) that occurred after a large diatom spring bloom when low nutrient conditions and cell collision rates potentially favored the diatom cells to flocculate (Corzo et al., 2000; Thornton, 2002). Likewise, the first diatom spring bloom in 2012 (end of March; Fig. 3.6B) developed under low silicate conditions (i.e., below the half–saturation constant

(K_m) for silicates around 2 µmol L^{-1}, see Supplementary Fig. S3.15) which potentially led to the formation of aggregates in early 2012 and thus to an enhanced incorporation of Mo into the shell. Accordingly, the development of the first and largest Mo/Ca_{shell} peak in 2012 supports the diatom-aggregate-hypothesis. In 2019, the diatom bloom in early May (Fig. 3.6C) was dominated by the diatom taxa *Chaetoceros* and *Leptocylindrus* which are known to form aggregates (e.g., Bienfang, 1981; Thornton, 2002; Nashad et al., 2017) when growing under nutrient limitations. However, silicate concentrations only reached low levels approx. two weeks after that diatom bloom (see Supplementary Fig. S3.15) suggesting no aggregates developed in 2019 and consequently no Mo/Ca_{shell} peak formed.

Both hypotheses, i.e., the link between Mo/Ca_{shell} peaks and blooms of smaller dinoflagellates species of *Gymnodinium* spp. or, alternatively, the formation of diatom aggregates, provide potential pathways explaining the Mo entrainment into the shell material. Moreover, the observation by Thébault et al. (2022) and the results of this study, showing that Mo/Ca_{shell} maxima coincide with a preceding reduction in growth rate of the bivalve (Fig. 3.4), are consistent with and support both assumptions. On the one hand, blooms of *Gymnodinium* spp. are known to be toxic and negatively affect growth rates in bivalves (Widdows et al., 1979; Chauvaud et al., 1998; Chauvaud et al., 2001). On the other hand, the sedimentation of aggregates can disturb shell growth caused by oxygen depletion and/or gill clogging (Lorrain et al., 2000). Thus, it is likely that the timing and magnitude of Mo/Ca_{shell} peaks record potential changes in phytoplankton dynamics either in the form of large dinoflagellate blooms and/or periods of large diatom blooms coupled to stressful nutrient conditions, which makes Mo/Ca_{shell} a valuable proxy for ecological reconstructions.

3.4.3 Phytoplankton and Li/Ca_{shell} peaks

In contrast to Ba/Ca_{shell} and Mo/Ca_{shell} profiles, the only major Li/Ca_{shell} peak occurred in 2011 (Fig. 3.5G) and no distinct peak was observed in shells from 2012 and 2019 (Fig. 3.5H, I). This made it difficult to detect potential patterns between trace element profiles and phytoplankton dynamics from different years. Simulating phytoplankton scenarios that can potentially describe the measured Li/Ca_{shell} profiles in all three years suggested an immediate relationship between the timing of a phytoplankton bloom and the formation of Li/Ca_{shell} peaks to be unlikely, as shown by the low Pearson correlation coefficients at small time intervals (0 to 4 days; Fig. 3.7E, F). For scenarios deduced from simulations considering larger

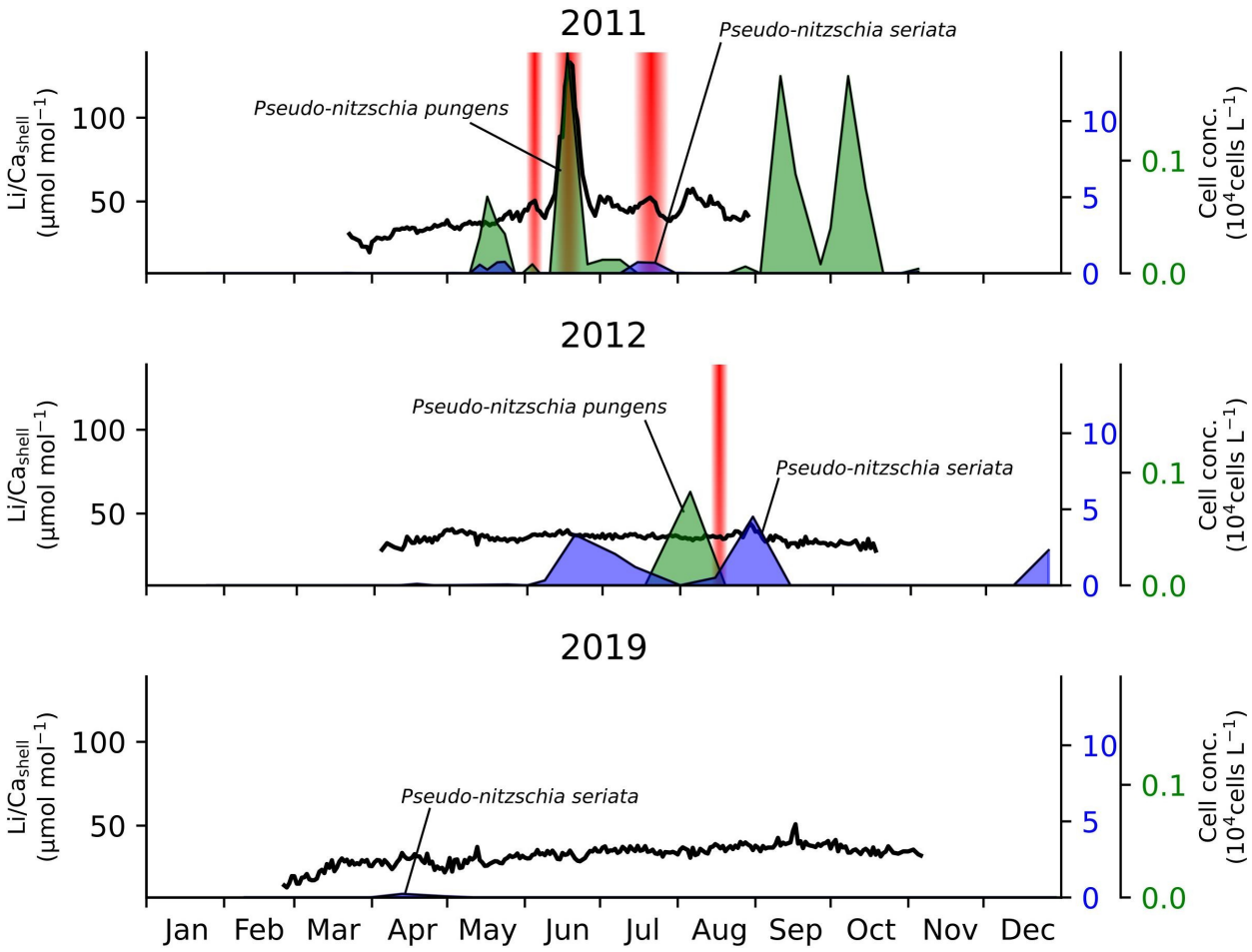

Figure 3.10 Li/Ca$_{shell}$ profiles of 2011, 2012 and 2019 and the timing and magnitude of *Pseudo-nitzschia pungens* and *P. seriata* blooms after a short time lag of 8 to 12 days. Red vertical bars indicate periods of stressful conditions (temporally shifted about 12 days), i.e., nutrient limitation and high grazing activity of zooplankton.

time intervals (>14 days), no suitable pathway could be derived that provides an appropriate ecological interpretation to explain the Li/Ca_{shell} profiles. However, the simulations returned a relatively high correlation with the Li/Ca_{shell} profiles when shifting the most dominant diatom taxon *Chaetoceros* spp. about 10 to 14 days (subplot in Fig. 3.7F). This observation is in agreement with the findings of Thébault et al. (2022) suggesting that the mass occurrence of diatoms about two weeks earlier could be associated with diatom frustules enriched in Li, similar to Ba (Sternberg et al., 2005). Thus, the frustules transport large quantities of this trace element to the sediment water interface where it is taken up by the scallops. Unlike 2011, no Li/Ca_{shell} peaks were formed in 2012 and 2019 following blooms of the main diatom genus *Chaetoceros*, possibly as a result of much lower cell concentrations.

Evaluating other hypothetical scenarios obtained from the pseudo-random sampling simulations revealed another phytoplankton pattern that match the Li/Ca_{shell} profiles. For shorter time intervals (4–6, 6–8, 8–10 days) the best fitting time-series is obtained for the diatom species *Pseudo-nitzschia pungens* that shares an appealing resemblance to the Li/Ca_{shell} profile in 2011. In fact, performing the pseudo-random simulations for a time lag of 8 to 12 days but excluding the *Chaetoceros* spp. time-series revealed *P. pungens* to match best with the Li/Ca_{shell} profile, although the correlation metrics was slightly lower. The lower Pearson correlation coefficients can be explained by the first *P. pungens* bloom as well as the bloom in 2012 that do not coincide with a Li/Ca_{shell} peak in 2011, when shifting about 8 to 12 days (Fig. 3.10). However, the second, third and fourth bloom match with the timing of Li/Ca_{shell} maxima (Fig. 3.10). The link between blooms of *Pseudo-nitzschia* and Li/Ca_{shell} peaks in scallop shells was already proposed by Thébault and Chauvaud (2013). It was hypothesized that the synthesis of domoic acid (DA), a potent neurotoxin produced by *Pseudo-nitzschia* (Bates et al., 1989), demands the presence of Li (Subba Rao et al., 1998) and lead to the formation of Li/Ca_{shell} peaks after ingestion (Thébault and Chauvaud, 2013). Since the sampling site of phytoplankton and scallops were different in that study (Thébault and Chauvaud, 2013), it was difficult to establish a reliable relationship between the timing and magnitude of blooms and Li/Ca_{shell} peaks due to the spatial variability of *Pseudo-nitzschia*. The present study shows the similarity between the timing of *P. pungens* blooms and Li/Ca_{shell} peaks observed for 2011 supporting the hypothesis by Thébault and Chauvaud (2013). Furthermore, other species of this diatom genus could also produce DA (Bates et al., 2018), suggesting that not only *P. pungens* but also other taxa such as *P. seriata* can potentially contribute to the formation of Li/Ca_{shell} peaks. Indeed, the small

Li/Ca_{shell} peaks in July 2011 match with the bloom of *P. seriata* when shifting the time-series about 8 to 12 days (Fig. 3.10). Yet, a discrepancy is obtained for the year 2012 that experienced blooms of *P. pungens* and *P. seriata* while no Li/Ca_{shell} peaks were measured (Fig. 3.10). A possible explanation for this inconsistency is that DA is synthesized only when the diatoms are stressed, i.e., by nutrient limitation (Pan et al., 1996) and/or by enhanced grazing activity of zooplankton (Bates et al., 2018). Interestingly, when considering a time lag of 8 to 12 days, the Li/Ca_{shell} peaks in 2011 coincide with periods of high pheophytin levels (an approximation of grazing activity; Lorenzen, 1967; Strom, 1993; Chauvaud et al., 2000) and low levels of silicate, i.e., stressful conditions for *Pseudo-nitzschia* cells (Fig. 3.10; Supplementary Fig. S3.15; red vertical bars). *Pseudo-nitzschia* blooms that could not be associated with the formation of subsequent Li/Ca_{shell} peaks developed under non-stressful conditions, especially in 2012 when these conditions solely occurred between two successive blooms of *Pseudo-nitzschia* (Fig. 3.10). These findings support the assumption that the formation of Li/Ca_{shell} peaks could be related to blooms of *Pseudo-nitzschia* but only under certain environmental conditions that triggers the formation of DA. In addition to *Pseudo-nitzschia* species, a potential influence of the benthic diatom *Nitzschia* spp. on the development of Li/Ca_{shell} peaks should be considered in future studies, as this diatom is known to produce DA similar to *Pseudo-nitzschia*.

3.4.4 Limitations of the pseudo-random sampling method

The methodology applied in this study tested the underlying assumption that the formation of distinct trace element-to-Ca peaks (Ba/Ca_{shell}, Mo/Ca_{shell} and Li/Ca_{shell}) was induced by an enhanced ingestion of trace element-enriched cells of a single or multiple phytoplankton species. Although the pseudo-random sampling method (section 3.2.5) provides a practical strategy to find potential patterns between a large set of complex phytoplankton time-series and trace element profiles, it also inherits some limitations. (1) The cell concentration data of the various diatom and dinoflagellate species formed the basis of the calculations and were used to quantify the relative abundance of the individual phytoplankton taxa. Accordingly, the method considered the ingestion of phytoplankton cells to be proportional to the number of cells in the water column, without accounting for possible changes in the feeding behavior of the scallops. (2) The simulations considered different time lags between 0 and 50 days by sequentially testing short time windows (3 and 5-day intervals). This technique narrows the

maximum time lag difference that two species can hypothetically encounter to a few days, i.e., the duration between the appearance of phytoplankton cells in the water column and the uptake of a particular trace element into the shell between two species can differ only by 3 or 5 days. Consequently, a scenario in which a bloom of one species takes 8 days to be recorded in the shell whereas a bloom of another species needs 20 days, was not encompassed by the simulations. (3) The underlying pathway for the uptake of trace elements is assumed to be similar between the studied years, discarding possible inter-annual differences. In addition, the amount of trace elements at the level of a single phytoplankton cell and/or filtration behavior of the bivalves are likely affected by environmental variables (e.g., currents, salinity, temperature, nutrient availability and dissolved trace element concentration in the surrounding water), which was not considered in the simulations and have to be addressed separately in the future. (4) The temporal resolution of the phytoplankton concentration data differed from that of the trace element profiles and among years, adding challenges to detect and interpret potential patterns between the time-series. The limitations clearly demonstrate the necessity of an ecological interpretation of the obtained results. Despite these constraints, the statistical approach used herein provided the chance to analyze a complex coastal ecosystem and allowed to derive potential relationships between environment and shell chemistry.

3.5 Summary and conclusions

Based on the results obtained in this study, trace element peaks (Ba/Ca_{shell}, Mo/Ca_{shell} and Li/Ca_{shell}) in shells of *P. maximus* most likely have a dietary origin that can be related to the activity of individual phytoplankton taxa in the water column. Herein, pseudo-random simulations allowed to decipher this linkage considering various time lags between phytoplankton events and the timing of enhanced trace element incorporation into the shell. The results demonstrated that phytoplankton time-series agreed best to the trace element profiles when a time lag of 8 to 12 days was considered. In other words, the peaks of Ba/Ca_{shell}, Mo/Ca_{shell} and Li/Ca_{shell} show a high degree of similarity to the phytoplankton data when lagged by that time interval. However, potential explanations for the origin of the trace element maxima vary considerably between the different elements. Ba/Ca_{shell} peaks are likely linked to the blooms of ingestible diatoms, dinoflagellates and flagellates. Especially the diatom species *Thalassionema nitzschioides* provided a striking similarity in

the timing and magnitude of blooms and the subsequent formation of Ba/Ca_{shell} peaks after 10 days, in all three years. In addition, the simulations indicated that Ba/Ca_{shell} profiles likely have a plurispecific origin, i.e., various phytoplankton taxa enriched in Ba contributed to the measured Ba/Ca_{shell} profiles. However, it remains to be clarified to what extent different taxa control the formation of Ba/Ca_{shell} peaks, which could be tested in subsequent tank experiments by sequentially feeding bivalves with different phytoplankton species and analyzing their geochemical response in the shell carbonate. Measured Mo/Ca_{shell} peaks were shown to be potentially related to the formation of preceding dinoflagellate blooms. In particular, the dinoflagellate species *Gymnodinium* spp. agreed well to the observed Mo/Ca_{shell} profiles when considering the smaller cell size fraction and a small temporal offset. It is hypothesized that the enzyme activity of nitrate reductase, used for nitrate assimilation, triggered the formation of Mo/Ca_{shell} peaks which is shown to be high in *Gymnodinium* spp. cells. In addition to this hypothesis, the results also support the assumption that Mo/Ca_{shell} peaks could be linked to the timing of diatom aggregate formation. Thus, further tank experiments can validate the pathway of Mo from the environment into the shell calcite by e.g., setting up rolling tanks to simulate aggregate forming and expose the shells to those aggregates, as well as species-specific feeding experiments using *Gymnodinium* spp. cells. In contrast to Ba/Ca_{shell} and Mo/Ca_{shell}, the simulations could not establish a clear pattern between phytoplankton and Li/Ca_{shell} peaks. Instead, the data favor two possible scenarios that could describe the formation of Li/Ca_{shell} peaks. On the one hand, the mass occurrence of diatoms, i.e., large bloom of *Chaetoceros* spp., could have favored the accumulation of Li in the shell after a short time lag. On the other hand, a potential link to the formation of harmful diatom blooms could be deduced. As demonstrated, blooms of the diatom *Pseudo-nitzschia* match the timing of Li/Ca_{shell} maxima when a short time lag is implemented in the model. Since not all *Pseudo-nitzschia* blooms could be associated with a Li/Ca_{shell} peak, it is proposed that the synthesis of the neurotoxin domoic acid is linked to stressful conditions in the ambient water such as nutrient limitation and/or high grazing activity of zooplankton. This toxin sequesters Li which is then ingested by scallops and potentially accounts for the enrichment of Li in the shell. Shells from additional years with transient Li/Ca_{shell} peaks are required to confirm either of these hypotheses as a large Li/Ca_{shell} maximum was only measured in one of the three studied years. If the demonstrated assumptions can be further developed and verified, Ba/Ca_{shell}, Mo/Ca_{shell} and Li/Ca_{shell} profiles will establish powerful proxies to reconstruct past phytoplankton dynamics that prevailed in the water

column. Ba/Ca_{shell} peaks could then be utilized as plurispecific indicators for the timing and magnitude of phytoplankton species enriched in Ba. Mo/Ca_{shell} profiles will establish a powerful tool to assess dynamics of specific dinoflagellate species growing on nitrates or the timing of diatom aggregate formation. Finally, the Li/Ca_{shell} peaks can reveal information about large diatom blooms or the timing and frequency of toxic diatom blooms as well as periods of enhanced zooplankton activity in the water column.

3.6 Supplementary material

Table S3.1 Phytoplankton groups that were used in the first set of simulations including the years 2011, 2012 and 2019.

Identified phytoplankton group	Max. cell concentration in 2011 (cells L^{-1})	Max. cell concentration in 2012 (cells L^{-1})	Max. cell concentration in 2019 (cells L^{-1})	Index
Alexandrium spp.	0	46,310	200	0
Cerataulina pelagica	190,900	0	7,000	1
Chaetoceros curvisetus + debilis	37,170	200	135,360	2
Chaetoceros danicus	0	4,000	4,560	3
Chaetoceros didymus	70,350	85,100	1,200	4
Chaetoceros pseudobrevis	17,110	0	0	5
Chaetoceros socialis	1,080	0	12,360	6
Chaetoceros sp. (chains)	0	46,310	0	7
Chaetoceros spp.	4,060,000	1,230,000	92,160	8
Coscinodiscus wailesii	400	44,310	0	9
Cyclotella sp.	26,180	10,100	0	10
Dactyliosolen fragilissimus	222,880	2,500	58,080	11
Diatoma vulgare	0	1,510	0	12
Dinophysis acuminata	1,500	120	200	13
Guinardia delicatula	129,900	302,100	166,080	14
Guinardia flaccida	3,000	2,300	42,000	15
Guinardia striata	1,250	500	7,200	16
Gymnodinium spp.	110,770	207,440	63,840	17
Gyrodinium spp.	1,200	26,180	1,560	18
Haslea wawrickae	1,750	1,760	0	19
Heterocapsa minima	292,000	47,330	14,560	20
Heterocapsa triquetra	3,250	0	240	21
Lauderia annulata	0	21,650	400	22

Lepidodinium chlorophorum	69,480	28,190	0	23
Leptocylindrus danicus	144,720	0	2,011,200	24
Leptocylindrus minimus	0	0	20,160	25
Lithodesmium undulatum	0	120	4,000	26
Minidiscus sp.	2,000	30,210	0	27
Navicula spp.	0	4,000	1,840	28
Naviculodes sp.	320	2,250	0	29
Nitzschia longissima + *Cylindrotheca closterium*	1,630	1,500	6,280	30
Nitzschia spp.	1,630	1,000	720	31
Prorocentrum micans	2,500	2,250	1,120	32
Prorocentrum minimum + *cordatum* + *balticum*	1,200	8,060	160	33
Prorocentrum triestinum	5,880	80	1,400	34
Protoperidinium bipes	1,000	5,000	6,240	35
Protoperidinium depressum	1,350	0	760	36
Pseudo-nitzschia delicatissima	22,610	5,750	2,760	37
Pseudo-nitzschia pungens	1,960	830	0	38
Pseudo-nitzschia seriata	7,540	45,130	2,360	39
Rhizosolenia imbricata	2,800	32,530	560	40
Rhizosolenia setigera	2,750	1,380	1,880	41
Scrippsiella spp. + *Pentapharsodinium* spp. + *Ensiculifera* spp.	20,270	3,500	2,920	42
Skeletonema marinoi	2,400	12,100	0	43
Thalassionema nitzschioides	12,560	51,350	13,000	44
Thalassiosira spp.	44,310	88,620	298,760	45
Tripos kofoidii	1,120	7,510	2,160	46

Table S3.2 Phytoplankton groups that were utilized in the second set of simulations including the years 2011 and 2012.

Identified phytoplankton group	Max. cell concentration in 2011 (cells L^{-1})	Max. cell concentration in 2012 (cells L^{-1})	Index
Alexandrium spp.	0	46,310	0
Cerataulina pelagica	190,900	0	1
Chaetoceros curvisetus	8,760	0	2
Chaetoceros danicus	0	4,000	3
Chaetoceros debilis	37,170	200	4
Chaetoceros didymus	70,350	85,100	5
Chaetoceros pseudobrevis	17,110	0	6
Chaetoceros socialis	1,080	0	7
Chaetoceros sp. (chains)	0	46,310	8
Chaetoceros spp.	4,060,000	1,230,000	9
Coscinodiscus wailesii	400	44,310	10
Cyclotella sp.	26,180	10,100	11
Cylindrotheca closterium	1,500	1,500	12
Dactyliosolen fragilissimus	222,880	2,500	13
Diatoma vulgare	0	1,510	14
Dinophysis acuminata	1,500	120	15
Guinardia delicatula	129,900	302,100	16
Guinardia flaccida	3,000	2,300	17
Guinardia striata	1,250	500	18
Gymnodinium spp. <20 µm	0	207,440	19
Gymnodinium spp. >20 µm	110,770	11,070	20
Gyrodinium flagellare	8,060	13,250	21
Gyrodinium spp.	1,200	26,180	22
Haslea wawrickae	1,750	1,760	23
Heterocapsa minima	292,000	47,330	24

Heterocapsa triquetra	3,250	0	25
Lauderia annulata	0	21,650	26
Lepidodinium chlorophorum	69,480	28,190	27
Leptocylindrus danicus	144,720	0	28
Minidiscus sp.	2,000	30,210	29
Navicula sp. (8–10 µm)	0	4,000	30
Naviculodes spp.	320	2,250	31
Nitzschia longissima	1,630	0	32
Nitzschia spp.	0	1,000	33
Prorocentrum balticum	1,200	8,060	34
Prorocentrum micans	2,500	2,250	35
Prorocentrum triestinum	5,880	80	36
Protoperidinium bipes	1,000	5,000	37
Protoperidinium depressum	1,350	0	38
Pseudo-nitzschia delicatissima	22,610	5,750	39
Pseudo-nitzschia pungens	1,960	830	40
Pseudo-nitzschia seriata	7,540	45,130	41
Rhizosolenia imbricata	2,800	32,530	42
Rhizosolenia setigera	1,750	1,380	43
Rhizosolenia setigera (fine)	1,000	0	44
Scrippsiella sp.	20,270	3,500	45
Skeletonema marinoi	2,400	12,100	46
Thalassionema nitzschioides	12,560	51,350	47
Thalassiosira spp.	44,310	88,620	48
Tripos kofoidii	1,120	7,510	49

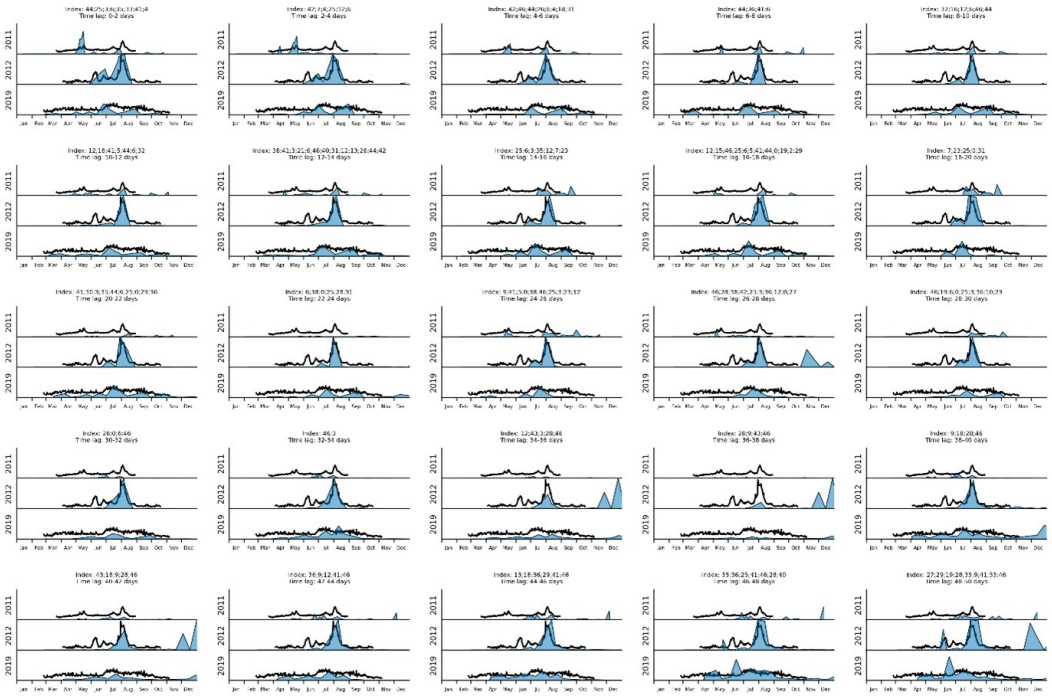

Figure S3.1 Ba/Ca_{shell} profiles Set 1 - 3 days interval.

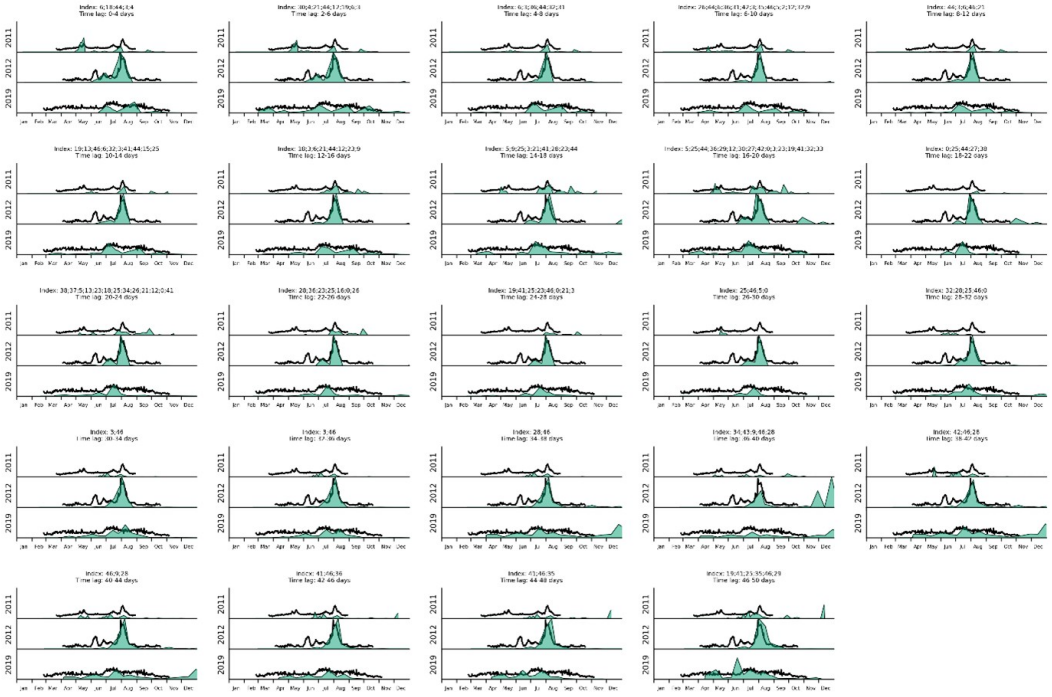

Figure S3.2 Ba/Ca_{shell} profiles Set 1 - 5 days interval.

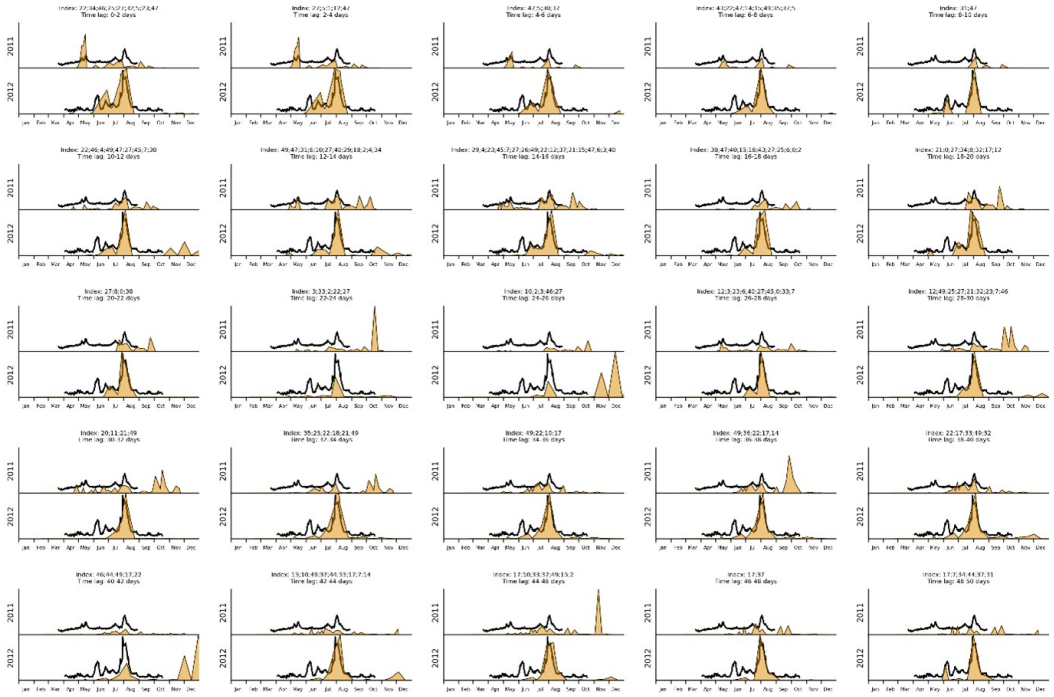

Figure S3.3 Ba/Ca_{shell} profiles Set 2 - 3 days interval.

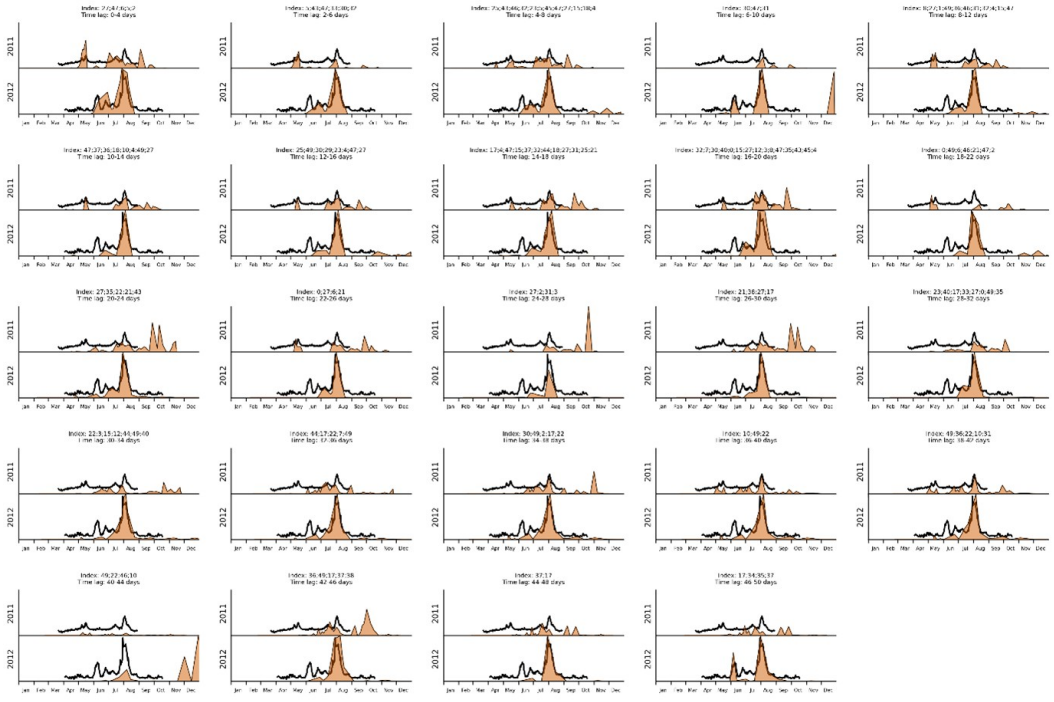

Figure S3.4 Ba/Ca_{shell} profiles Set 2 - 5 days interval.

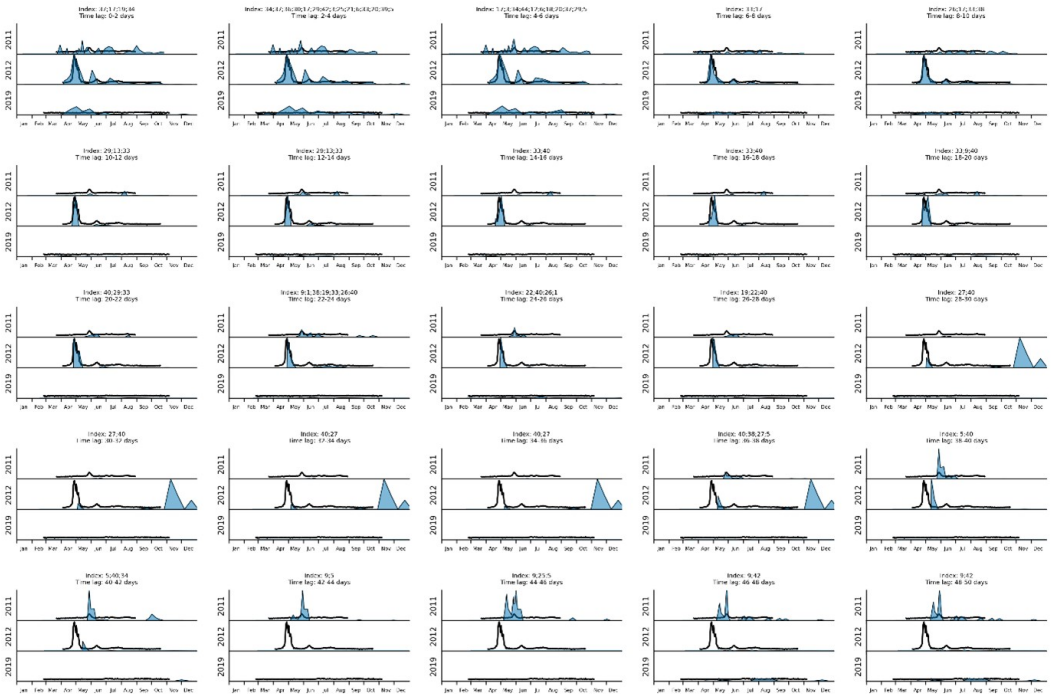

Figure S3.5 Mo/Ca_{shell} profiles Set 1 - 3 days interval.

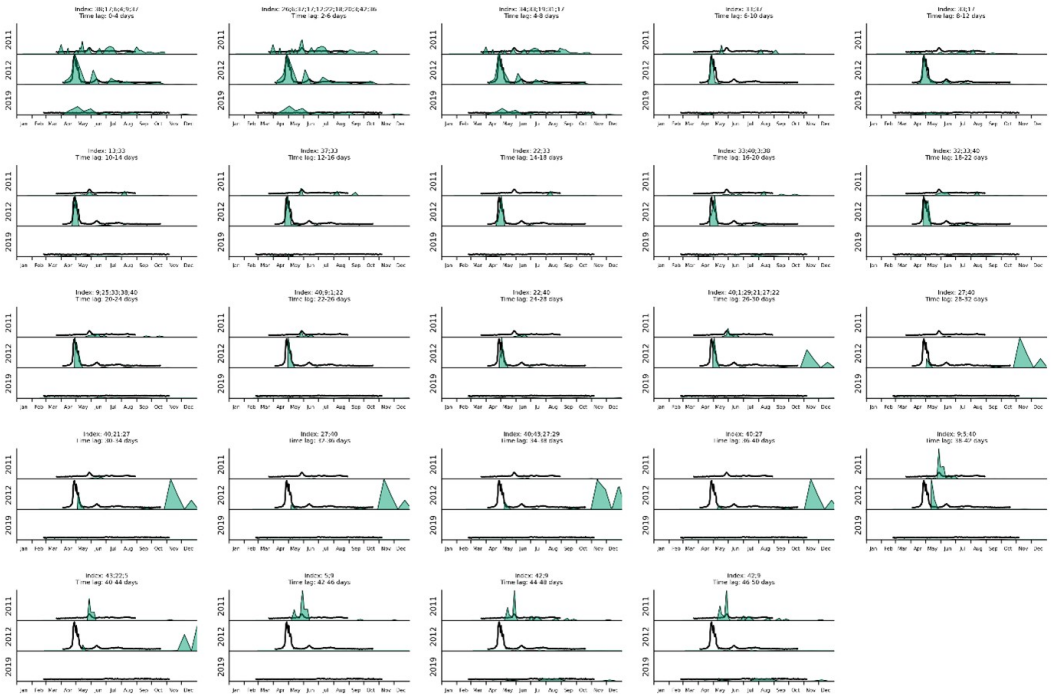

Figure S3.6 Mo/Ca_{shell} profiles Set 1 - 5 days interval.

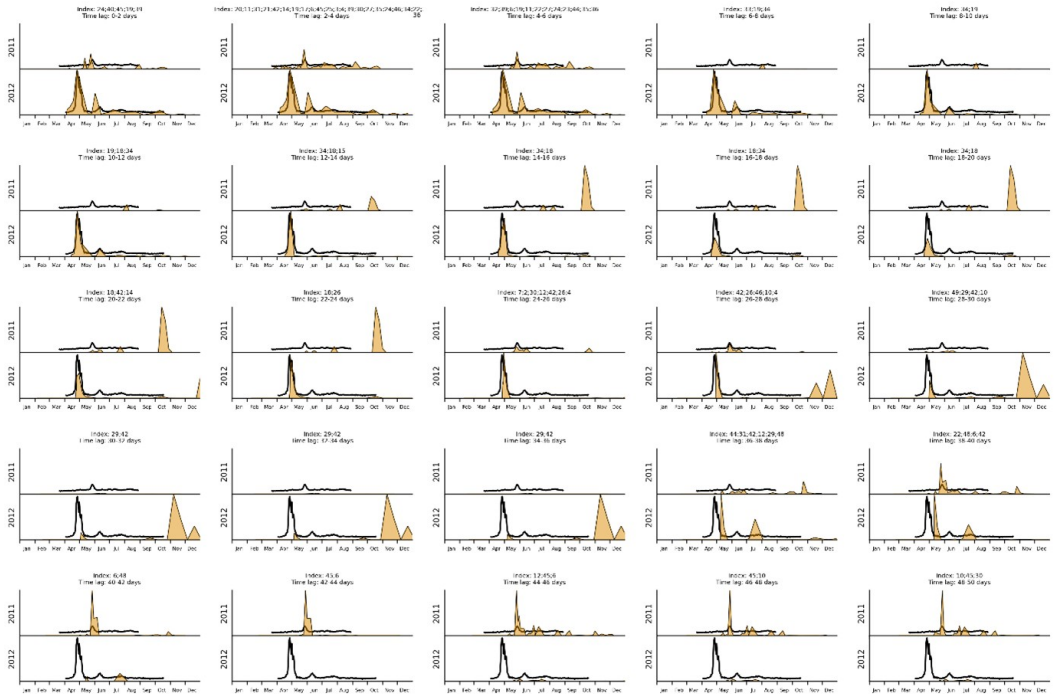

Figure S3.7 Mo/Ca_{shell} profiles Set 2 - 3 days interval.

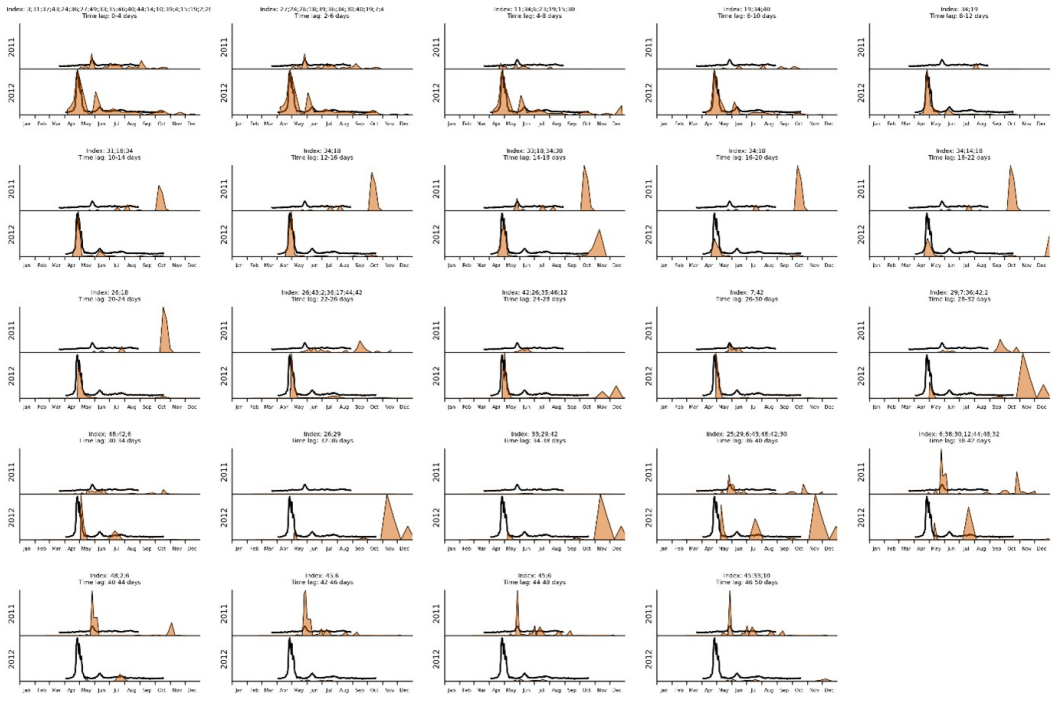

Figure S3.8 Mo/Ca_{shell} profiles Set 2 - 5 days interval.

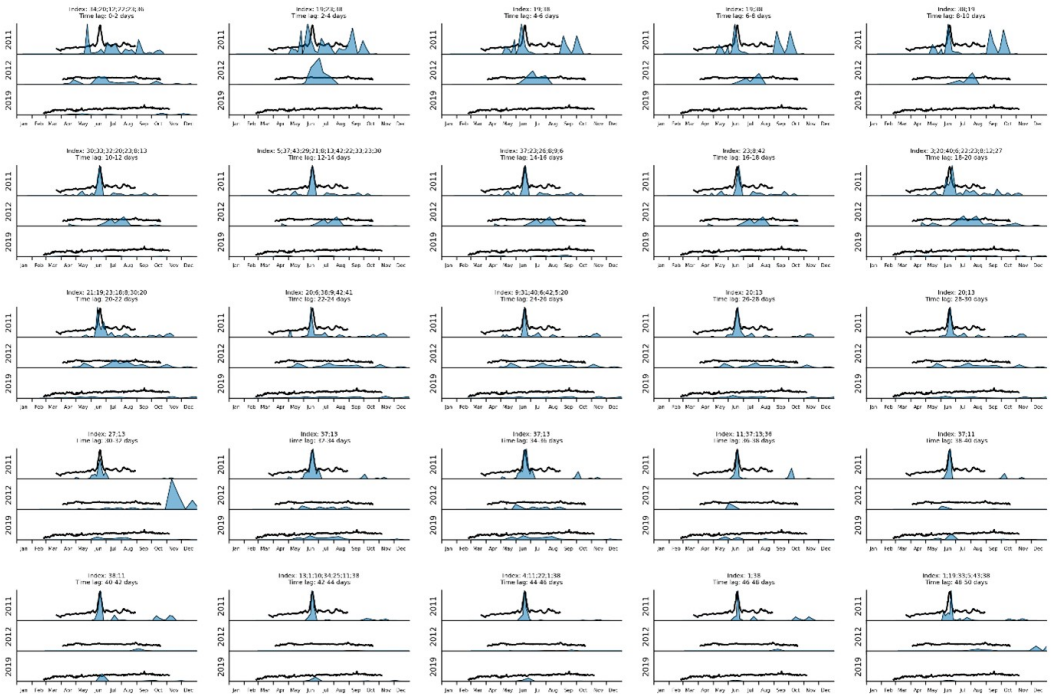

Figure S3.9 Li/Ca_{shell} profiles Set 1 - 3 days interval.

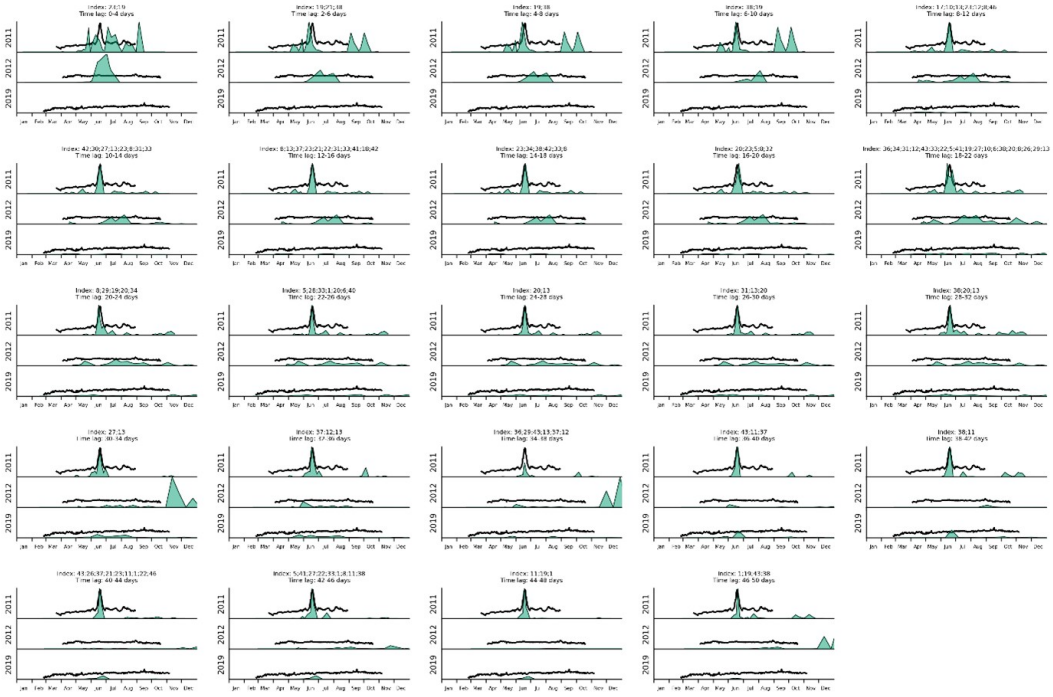

Figure S3.10 Li/Ca_{shell} profiles Set 1 - 5 days interval.

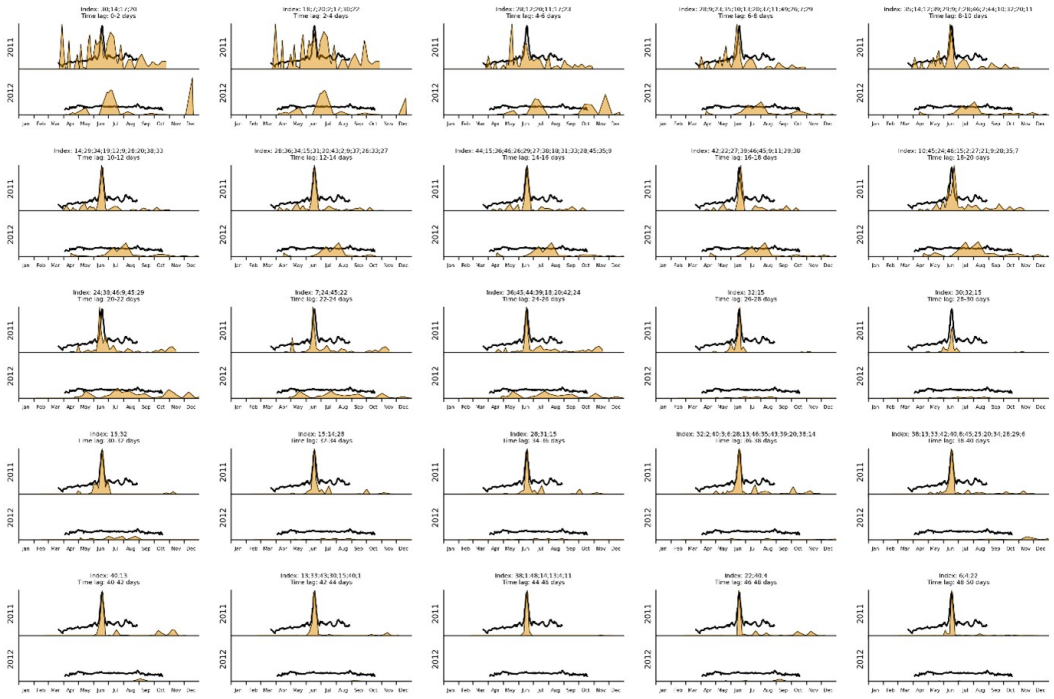

Figure S3.11 Li/Ca_{shell} profiles Set 2 - 3 days interval.

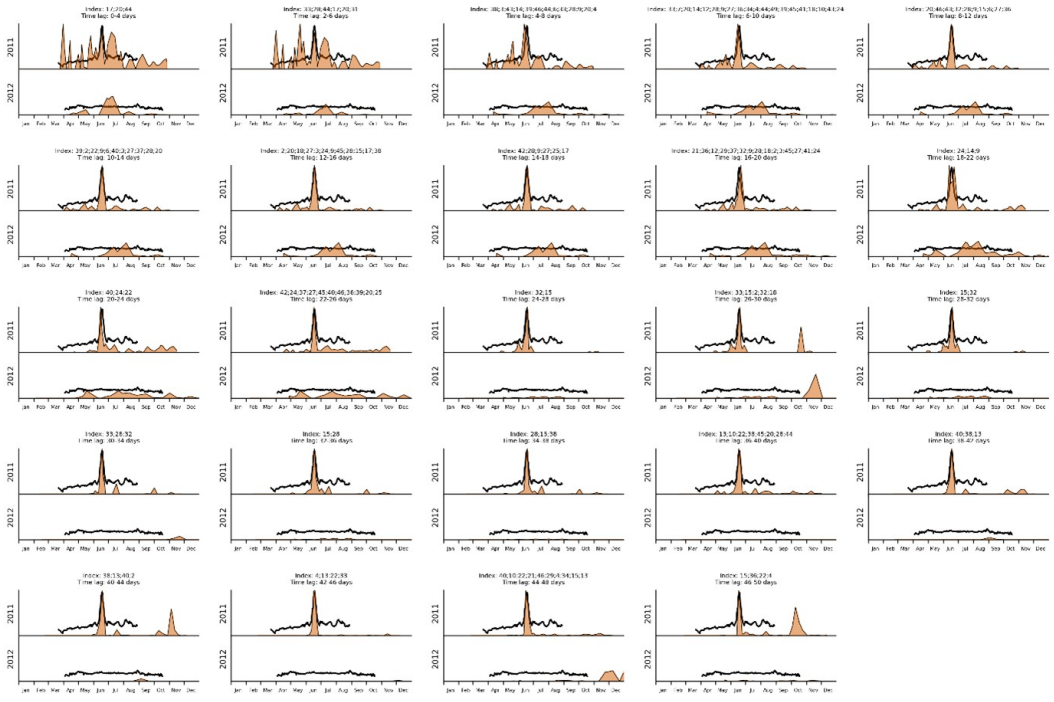

Figure S3.12 Li/Ca_{shell} profiles Set 2 - 5 days interval.

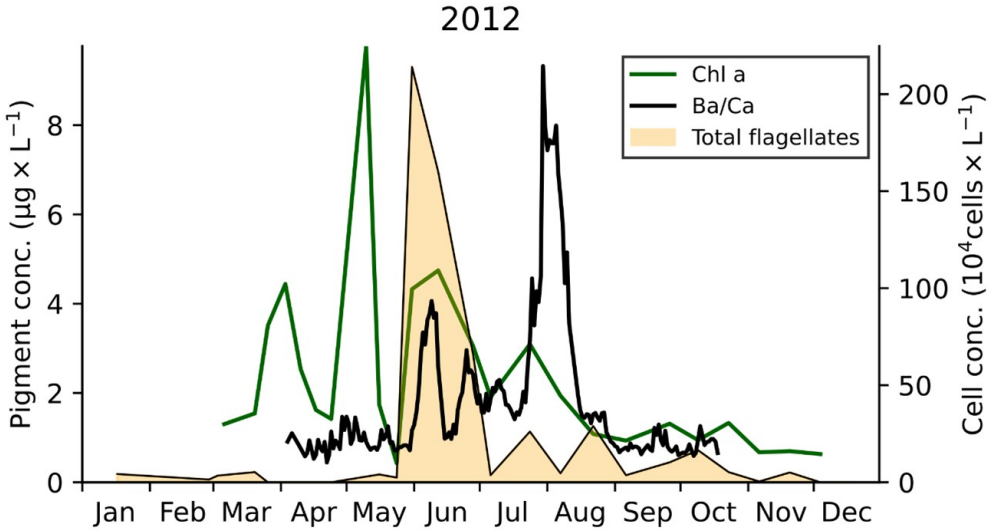

Figure S3.13 Chlorophyll *a* pigment concentration and total flagellates cell concentration recorded in 2012 at the sampling site in Lanvéoc. Average Ba/Ca_{shell} profiles (black graph) measured in three contemporaneous shells.

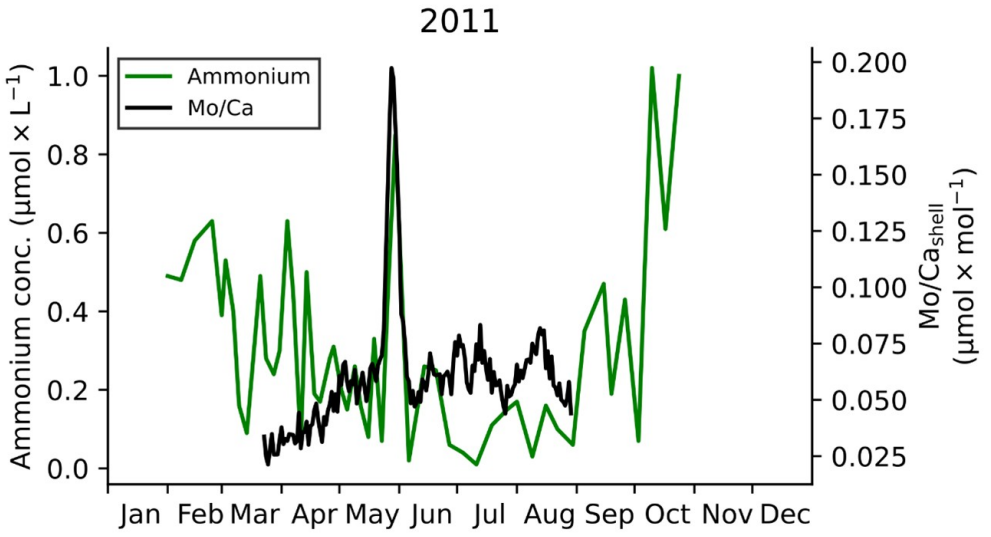

Figure S3.14 Ammonium (NH_4^+) concentration in 2011 in relation to the average Mo/Ca_{shell} profile.

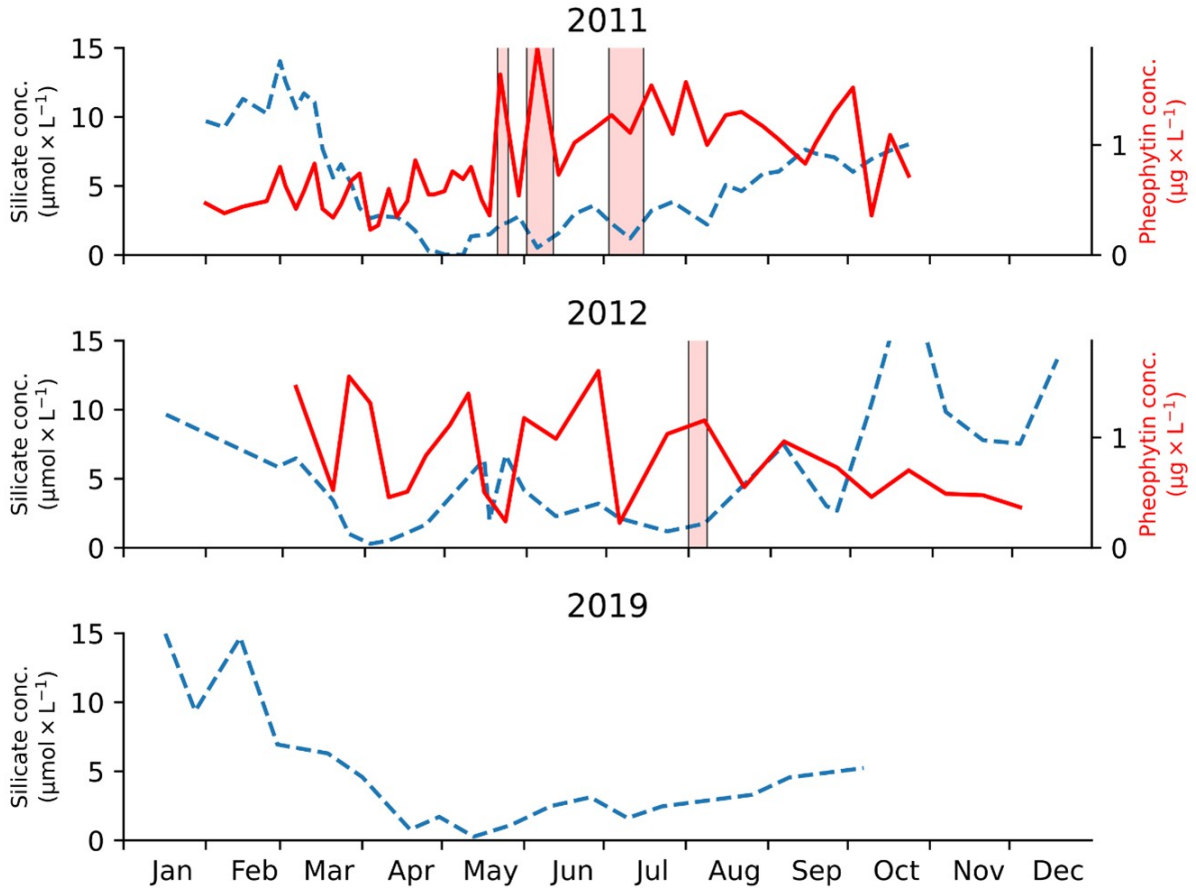

Figure S3.15 Silicic acid ($SiOH_4$) and pheophytin pigment concentrations in 2011, 2012 and 2019. No pheophytin pigments were recorded in 2019. Red vertical bars indicate periods (>3 days) of high pheophytin levels (>1.1 µg L^{-1}) at contemporaneously low silicate levels (<2.5 µmol L^{-1}) in 2011 and 2012.

References

Alldredge, A. L., Gotschalk, C. C., 1989. Direct observations of the mass flocculation of diatom blooms: Characteristics, settling velocities and formation of diatom aggregates. Deep Sea Research Part A, Oceanographic Research Papers 36, 159–171.

Barats, A., Amouroux, D., Chauvaud, L., Pécheyran, C., Lorrain, A., Thébault, J., Church, T. M., Donard, O. F., 2009. High frequency barium profiles in shells of the great scallop *Pecten maximus*: A methodical long-term and multi-site survey in Western Europe. Biogeosciences 6, 157–170.

Barats, A., Amouroux, D., Pécheyran, C., Chauvaud, L., Thébault, J., Donard, O. F. X., 2010. Spring molybdenum enrichment in scallop shells: A potential tracer of diatom productivity in temperate coastal environments (Brittany, NW France). Biogeosciences 7, 233–245.

Barats, A., Pécheyran, C., Amouroux, D., Dubascoux, S., Chauvaud, L., Donard, O. F. X., 2007. Matrix-matched quantitative analysis of trace-elements in calcium carbonate shells by laser-ablation ICP-MS: Application to the determination of daily scale profiles in scallop shell (*Pecten maximus*). Analytical and Bioanalytical Chemistry 387, 1131–1140.

Barbier, E. B., Hacker, S. D., Kennedy, C., Koch, E. W., Stier, A. C., Silliman, B. R., 2011. The value of estuarine and coastal ecosystem services. Ecological Monographs 81, 169–193.

Bates, S. S., Bird, C. J., de Freitas, A. S. W., Foxall, R., Gilgan, M., Hanic, L. A., Johnson, G. R., McCulloch, A. W., Odense, P., Pocklington, R., Quilliam, M. A., Sim, P. G., Smith, J. C., Subba Rao, D. V., Todd, E. C. D., Walter, J. A., Wright, J. L. C., 1989. Pennate diatom *Nitzschia pungens* as the primary source of domoic acid, a toxin in shellfish from eastern Prince Edward Island, Canada. Canadian Journal of Fisheries and Aquatic Sciences 46, 1203–1215.

Bates, S. S., Hubbard, K. A., Lundholm, N., Montresor, M., Leaw, C. P., 2018. *Pseudo-nitzschia*, *Nitzschia*, and domoic acid: New research since 2011. Harmful Algae 79, 3–43.

Beman, J. M., Arrigo, K. R., Matson, P. A., 2005. Agricultural runoff fuels large phytoplankton blooms in vulnerable areas of the ocean. Nature 434, 211–214.

Beninger, P. G., Decottignies, P., Rincé, Y., 2004. Localization of qualitative particle selection sites in the heterorhabdic filibranch *Pecten maximus* (Bivalvia: Pectinidae). Marine Ecology Progress Series 275, 163–173.

Bienfang, P. K., Harrison, P. J., Quarmby, L. M., 1982. Sinking rate response to depletion of nitrate, phosphate and silicate in four marine diatoms. Marine Biology 67, 295–302.

Bienfang, P. K., 1981. Sinking rates of heterogeneous, temperate phytoplankton populations. Journal of Plankton Research 3, 235–253.

Bishop, J. K. B., 1988. The barite-opal-organic carbon association in oceanic particulate matter. Nature 332, 341–343.

Cardinale, B. J., Srivastava, D. S., Duffy, J. E., Wright, J. P., Downing, A. L., Sankaran, M., Jouseau, C., 2006. Effects of biodiversity on the functioning of trophic groups and ecosystems. Nature 443, 989–992.

Chauvaud, L., Donval, A., Thouzeau, G., Paulet, Y. M., Nézan, E., 2001. Variations in food intake of *Pecten maximus* (L.) from the Bay of Brest (France): Influence of environmental factors and phytoplankton species composition. Comptes Rendus de l'Académie des Sciences - Series III - Sciences de la Vie 324, 743–755.

Chauvaud, L., Jean, F., Ragueneau, O., Thouzeau, G., 2000. Long-term variation of the Bay of Brest ecosystem: Benthic-pelagic coupling revisited. Marine Ecology Progress Series 200, 35–48.

Chauvaud, L., Lorrain, A., Dunbar, R. B., Paulet, Y. M., Thouzeau, G., Jean, F., Guarini, J. M., Mucciarone, D., 2005. Shell of the great scallop *Pecten maximus* as a high-frequency archive of paleoenvironmental changes. Geochemistry, Geophysics, Geosystems 6, Q08001.

Chauvaud, L., Thébault, J., Clavier, J., Lorrain, A., Strand, Ø., 2011. What's hiding behind ontogenetic δ^{13}C variations in mollusk shells? New insights from the great scallop (*Pecten maximus*). Estuaries and Coasts 34, 211–220.

Chauvaud, L., Thouzeau, G., Paulet, Y. M., 1998. Effects of environmental factors on the daily growth rate of *Pecten maximus* juveniles in the Bay of Brest (France). Journal of Experimental Marine Biology and Ecology 227, 83–111.

Cloern, J. E., 2001. Our evolving conceptual model of the coastal eutrophication problem. Marine Ecology Progress Series 210, 223–253.

Collier, R. W., 1985. Molybdenum in the Northeast Pacific Ocean. Limnology and Oceanography 30, 1351–1354.

Corzo, A., Morillo, J. A., Rodríguez, S., 2000. Production of transparent exopolymer particles (TEP) in cultures of *Chaetoceros calcitrans* under nitrogen limitation. Aquatic Microbial Ecology 23, 63–72.

Dehairs, F., Chesselet, R., Jedwab, J., 1980. Discrete suspended particles of barite and the barium cycle in the open ocean. Earth and Planetary Science Letters 49, 528–550.

Del Amo, Y., Quéguiner, B., Tréguer, P., Breton, H., Lampert, L., 1997. Impacts of high-nitrate freshwater inputs on macrotidal ecosystems. II. Specific role of the silicic acid pump in the year-round dominance of diatoms in the Bay of Brest (France). Marine Ecology Progress Series 161, 225–237.

Desortová, B., 1981. Relationship between chlorophyll-*a* concentration and phytoplankton biomass in several reservoirs in Czechoslovakia. Internationale Revue der gesamten Hydrobiologie und Hydrographie 66, 153–169.

Doré, J., Chaillou, G., Poitevin, P., Lazure, P., Poirier, A., Chauvaud, L., Archambault, P., Thébault, J., 2020. Assessment of Ba/Ca in *Arctica islandica* shells as a proxy for phytoplankton dynamics in the Northwestern Atlantic Ocean. Estuarine, Coastal and Shelf Science 237, 106628.

Dymond, J., Collier, R., McManus, J., Honjo, S., Manganini, S., 1997. Can the aluminum and titanium contents of ocean sediments be used to determine the paleoproductivity of the oceans? Paleoceanography 12, 586–593.

Eppley, R. W., Coatsworth, J. L., Solórzano, L., 1969. Studies of nitrate reductase in marine phytoplankton. Limnology and Oceanography 14, 194–205.

Eppley, R. W., Coatsworth, J. L., 1968. Uptake of nitrate and nitrite by *Ditylum brightwellii* – kinetics and mechanisms. Journal of Phycology 4, 151–156.

Field, C. B., Behrenfeld, M. J., Randerson, J. T., Falkowski, P., 1998. Primary production of the biosphere: Integrating terrestrial and oceanic components. Science 281, 237–240.

Fisher, N. S., Guillard, R. R. L., Bankston, D. C., 1991. The accumulation of barium by marine phytoplankton grown in culture. Journal of Marine Research 49, 339–354.

Fröhlich, L., Siebert, V., Walliser, E. O., Thébault, J., Jochum, K. P., Chauvaud, L., Schöne, B. R., 2022. Ba/Ca profiles in shells of *Pecten maximus* – A proxy for specific primary producers rather than bulk phytoplankton. Chemical Geology 593, 120743.

Gillikin, D. P., Dehairs, F., Lorrain, A., Steenmans, D., Baeyens, W., André, L., 2006. Barium uptake into the shells of the common mussel (*Mytilus edulis*) and the potential for estuarine paleo-chemistry reconstruction. Geochimica et Cosmochimica Acta 70, 395–407.

Gillikin, D. P., Lorrain, A., Paulet, Y. M., André, L., Dehairs, F., 2008. Synchronous barium peaks in high-resolution profiles of calcite and aragonite marine bivalve shells. Geo-Marine Letters 28, 351–358.

Gordon, H. R., Clark, D. K., Mueller, J. L., Hovis, W. A., 1980. Phytoplankton pigments from the nimbus-7 coastal zone color scanner: Comparisons with surface measurements. Science 210, 63–66.

Hallmann, N., Schöne, B. R., Strom, A., Fiebig, J., 2008. An intractable climate archive – Sclerochronological and shell oxygen isotope analyses of the Pacific geoduck, *Panopea abrupta* (bivalve mollusk) from Protection Island (Washington State, USA). Palaeogeography, Palaeoclimatology, Palaeoecology 269, 115–126.

Hare, C. E., Leblanc, K., DiTullio, G. R., Kudela, R. M., Zhang, Y., Lee, P. A., Riseman, S., Hutchins, D. A., 2007. Consequences of increased temperature and CO_2 for phytoplankton community structure in the Bering Sea. Marine Ecology Progress Series 352, 9–16.

Harrison, W. G., 1973. Nitrate reductase activity during a dinoflagellate bloom. Limnology and Oceanography 18, 457–465.

Hatch, M. B. A., Schellenberg, S. A., Carter, M. L., 2013. Ba/Ca variations in the modern intertidal bean clam *Donax gouldii*: An upwelling proxy? Palaeogeography, Palaeoclimatology, Palaeoecology 373, 98–107.

Ho, T. Y., Quigg, A., Finkel, Z. V., Milligan, A. J., Wyman, K., Falkowski, P. G., Morel, F. M. M., 2003. The elemental composition of some marine phytoplankton. Journal of Phycology 39, 1145–1159.

Hovis, W. A., Clark, D. K., Anderson, F., Austin, R. W., Wilson, W. H., Baker, E. T., Ball, D., Gordon, H. R., Mueller, J. L., El-Sayed, S. Z., Sturm, B., Wrigley, R. C., Yentsch, C. S., 1980. Nimbus-7 coastal zone color scanner: System description and initial imagery. Science 210, 60–63.

Iglesias-Rodriguez, M. D., Halloran, P. R., Rickaby, R. E. M., Hall, I. R., Colmenero-Hidalgo, E., Gittins, J. R., Green, D. R. H., Tyrrell, T., Gibbs, S. J., von Dassow, P., Rehm, E., Armbrust, E. V., Boessenkool, K. P., 2008. Phytoplankton calcification in a high-CO_2 world. Science 320, 336–340.

Jochum, K. P., Garbe-Schönberg, D., Veter, M., Stoll, B., Weis, U., Weber, M., Lugli, F., Jentzen, A., Schiebel, R., Wassenburg, J. A., Jacob, D. E., Haug, G. H., 2019. Nano-powdered calcium carbonate reference materials: Significant progress for microanalysis? Geostandards and Geoanalytical Research 43, 595–609.

Jochum, K. P., Stoll, B., Herwig, K., Willbold, M., 2007. Validation of LA-ICP-MS trace element analysis of geological glasses using a new solid-state 193 nm Nd:YAG laser and matrix-matched calibration. Journal of Analytical Atomic Spectrometry 22, 112–121.

Jochum, K. P., Weis, U., Stoll, B., Kuzmin, D., Yang, Q., Raczek, I., Jacob, D. E., Stracke, A., Birbaum, K., Frick, D. A., Günther, D., Enzweiler, J., 2011. Determination of reference values for NIST SRM 610-617 glasses following ISO guidelines. Geostandards and Geoanalytical Research 35, 397–429.

Kruskopf, M., Flynn, K. J., 2006. Chlorophyll content and fluorescence responses cannot be used to gauge reliably phytoplankton biomass, nutrient status or growth rate. New Phytologist 169, 525–536.

Lionard, M., Muylaert, K., Tackx, M., Vyverman, W., 2008. Evaluation of the performance of HPLC-CHEMTAX analysis for determining phytoplankton biomass and composition in a turbid estuary (Schelde, Belgium). Estuarine, Coastal and Shelf Science 76, 809–817.

Longerich, H. P., Jackson, S. E., Günther, D., 1996. Laser ablation inductively coupled plasma mass spectrometric transient signal data acquisition and analyte concentration calculation. Journal of Analytical Atomic Spectrometry 11, 899–904.

Lorenzen, C. J., 1966. A method for the continuous measurement of *in vivo* chlorophyll concentration. Deep-Sea Research and Oceanographic Abstracts 13, 223–227.

Lorenzen, C. J., 1967. Vertical distribution of chlorophyll and phaeo-pigments: Baja California. Deep-Sea Research and Oceanographic Abstracts 14, 735–745.

Lorrain, A., Paulet, Y. M., Chauvaud, L., Savoye, N., Nézan, E., Guérin, L., 2000. Growth anomalies in *Pecten maximus* from coastal waters (Bay of Brest, France): Relationship with diatom blooms. Journal of the Marine Biological Association of the United Kingdom 80, 667–673.

Marali, S., Schöne, B. R., Mertz-Kraus, R., Griffin, S. M., Wanamaker, A. D., Matras, U., Butler, P. G., 2017. Ba/Ca ratios in shells of *Arctica islandica* – Potential environmental proxy and crossdating tool. Palaeogeography, Palaeoclimatology, Palaeoecology 465, 347–361.

Marino, R., Howarth, R. W., Chan, F., Cole, J. J., Likens, G. E., 2003. Sulfate inhibition of molybdenum-dependent nitrogen fixation by planktonic cyanobacteria under seawater conditions: A non-reversible effect. Hydrobiologia 500, 277–293.

Marinov, I., Doney, S. C., Lima, I. D., 2010. Response of ocean phytoplankton community structure to climate change over the 21st century: Partitioning the effects of nutrients, temperature and light. Biogeosciences 7, 3941–3959.

Martin, J. H., Knauer, G. A., 1973. The elemental composition of plankton. Geochimica et Cosmochimica Acta 37, 1639–1653.

Morris, I., Syrett, P. J., 1963. The development of nitrate reductase in *Chlorella* and its repression by ammonium. Archiv für Mikrobiologie 47, 32–41.

Nashad, M., Menon, N. N., Joseph, C. A., Pettersson, L. H., Menon, N. R., 2017. First report of *Leptocylindrus* sp. bloom in the coastal waters of Kerala, southeast Arabian Sea. Journal of Marine Biological Association, India 59, 87–92.

Nixon, S. W., 1995. Coastal marine eutrophication: A definition, social causes, and future concerns. Ophelia 41, 199–219.

Pan, Y., Subba Rao, D. V., Mann, K. H., Li, W. K. W., Harrison, W. G., 1996. Effects of silicate limitation on production of domoic acid, a neurotoxin, by the diatom *Pseudo-nitzschia multiseries*. II. Continuous culture studies. Marine Ecology Progress Series 131, 235–243.

Peperzak, L., Colijn, F., Koeman, R., Gieskes, W. W. C., Joordens, J. C. A., 2003. Phytoplankton sinking rates in the Rhine region of freshwater influence. Journal of Plankton Research 25, 365–383.

Radach, G., Berg, J., Hagmeier, E., 1990. Long-term changes of the annual cycles of meteorological, hydrographic, nutrient and phytoplankton time series at Helgoland and at LV ELBE 1 in the German Bight. Continental Shelf Research 10, 305–328.

Ragueneau, O., Varela, E. D. B., Treguer, P., Queguiner, B., Del Amo, Y., 1994. Phytoplankton dynamics in relation to the biogeochemical cycle of silicon in a coastal ecosystem of Western Europe. Marine Ecology Progress Series 106, 157–172.

Richardson, C. A., Crisp, D. J., Runham, N. W., 1980. An endogenous rhythm in shell deposition in *Cerastoderma edule*. Journal of the Marine Biological Association of the United Kingdom 60, 991–1004.

Richardson, K., Heilmann, J. P., 1995. Primary production in the Kattegat: Past and present. Ophelia 41, 317–328.

Roth, I., Riley, J. P., 1971. The distribution of trace elements in some species of phytoplankton grown in culture. Journal of the Marine Biological Association of the United Kingdom 51, 63–72.

Schöne, B. R., 2008. The curse of physiology – Challenges and opportunities in the interpretation of geochemical data from mollusk shells. Geo-Marine Letters 28, 269–285.

Shumway, S. E., Cucci, T. L., Lesser, M. P., Bourne, N., Bunting, B., 1997. Particle clearance and selection in three species of juvenile scallops. Aquaculture International 5, 89–99.

Shuter, B., 1979. A model of physiological adaptation in unicellular algae. Journal of Theoretical Biology 78, 519–552.

Sigman, D. M., Boyle, E. A., 2000. Glacial/interglacial variations in atmospheric carbon dioxide. Nature 407, 859–869.

Smith, V. H., 2003. Eutrophication of freshwater and coastal marine ecosystems: A global problem. Environmental Science and Pollution Research 10, 126–139.

Stecher, H. A., Krantz, D. E., Lord, C. J., Luther, G. W., Bock, K. W., 1996. Profiles of strontium and barium in *Mercenaria mercenaria* and *Spisula solidissima* shells. Geochimica et Cosmochimica Acta 60, 3445–3456.

Sternberg, E., Tang, D., Ho, T. Y., Jeandel, C., Morel, F. M. M., 2005. Barium uptake and adsorption in diatoms. Geochimica et Cosmochimica Acta 69, 2745–2752.

Strom, S. L., 1993. Production of pheopigments by marine protozoa: Results of laboratory experiments analysed by HPLC. Deep Sea Research Part I: Oceanographic Research Papers 40, 57–80.

Subba Rao, D. V., Pan, Y., Mukhida, K., 1998. Production of domoic acid by *Pseudonitzschia multiseries* Hasle, affected by lithium. Marine Ecology 19, 31–36.

Tabouret, H., Pomerleau, S., Jolivet, A., Pécheyran, C., Riso, R., Thébault, J., Chauvaud, L., Amouroux, D., 2012. Specific pathways for the incorporation of dissolved barium and molybdenum into the bivalve shell: An isotopic tracer approach in the juvenile great scallop (*Pecten maximus*). Marine Environmental Research 78, 15–25.

Thébault, J., Chauvaud, L., 2013. Li/Ca enrichments in great scallop shells (*Pecten maximus*) and their relationship with phytoplankton blooms. Palaeogeography, Palaeoclimatology, Palaeoecology 373, 108–122.

Thébault, J., Chauvaud, L., Clavier, J., Fichez, R., Morize, E., 2006. Evidence of a 2-day periodicity of striae formation in the tropical scallop *Comptopallium radula* using calcein marking. Marine Biology 149, 257–267.

Thébault, J., Chauvaud, L., L'Helguen, S., Clavier, J., Barats, A., Jacquet, S., Pécheyran, C., Amouroux, D., 2009. Barium and molybdenum records in bivalve shells: Geochemical proxies for phytoplankton dynamics in coastal environments? Limnology and Oceanography 54, 1002–1014.

Thébault, J., Jolivet, A., Waeles, M., Tabouret, H., Sabarot, S., Pécheyran, C., Leynaert, A., Jochum, K. P., Schöne, B. R., Fröhlich, L., Siebert, V., Amice, E., Chauvaud, L., 2022. Scallop shells as geochemical archives of phytoplankton-related ecological processes in a temperate coastal ecosystem. Limnology and Oceanography 67, 187–202.

Thornton, D. C. O., 2002. Diatom aggregation in the sea: Mechanisms and ecological implications. European Journal of Phycology 37, 149–161.

Vander Putten, E., Dehairs, F., Keppens, E., Baeyens, W., 2000. High resolution distribution of trace elements in the calcite shell layer of modern *Mytilus edulis*: Environmental and biological controls. Geochimica et Cosmochimica Acta 64, 997–1011.

Wang, J. X., Kong, F. Z., Geng, H. X., Zhang, Q. C., Yuan, Y. Q., Yu, R. C., 2021. CHEMTAX analysis of phytoplankton assemblages revealed potential indicators for blooms of haptophyte *Phaeocystis globosa*. Ecological Indicators 131, 108177.

Warner, A. J., Hays, G. C., 1994. Sampling by the continuous plankton recorder survey. Progress in Oceanography 34, 237–256.

Westberry, T., Behrenfeld, M. J., Siegel, D. A., Boss, E., 2008. Carbon-based primary productivity modeling with vertically resolved photoacclimation. Global Biogeochemical Cycles 22, 1–18.

Widdows, J., Moore, M. N., Lowe, D. M., Salkeld, P. N., 1979. Some effects of a dinoflagellate bloom (*Gyrodinium aureolum*) on the mussel, *Mytilus edulis*. Journal of the Marine Biological Association of the United Kingdom 59, 522–524.

Wiltshire, K. H., Manly, B. F., 2004. The warming trend at Helgoland Roads, North Sea: Phytoplankton response. Helgoland Marine Research 58, 269–273.

Winder, M., Sommer, U., 2012. Phytoplankton response to a changing climate. Hydrobiologia 698, 5–16.

Worm, B., Barbier, E. B., Beaumont, N., Duffy, J. E., Folke, C., Halpern, B. S., Jackson, J. B. C., Lotze, H. K., Micheli, F., Palumbi, S. R., Sala, E., Selkoe, K. A., Stachowicz, J. J., Watson, R., 2006. Impacts of biodiversity loss on ocean ecosystem services. Science 314, 787–790.

Wright, S. W., van den Enden, R. L., Pearce, I., Davidson, A. T., Scott, F. J., Westwood, K. J., 2010. Phytoplankton community structure and stocks in the Southern Ocean (30–80°E) determined by CHEMTAX analysis of HPLC pigment signatures. Deep Sea Research Part II: Topical Studies in Oceanography 57, 758–778.

Yamamoto, T., Oh, S. J., Kataoka, Y., 2004. Growth and uptake kinetics for nitrate, ammonium and phosphate by the toxic dinoflagellate *Gymnodinium catenatum* isolated from Hiroshima Bay, Japan. Fisheries Science 70, 108–115.

4 Uptake of barium, molybdenum, and lithium and incorporation into scallop shells: Refining proxies for primary production dynamics

Lukas Fröhlich[1], Valentin Siebert[2], Qian Huang[1], Julien Thébault[2], Brivaëla Moriceau[2], Klaus Peter Jochum[3], Bernd R. Schöne[1],

[1] *Johannes Gutenberg University, Mainz, Germany*
[2] *Univ Brest, CNRS, IRD, Plouzané, France*
[3] *Climate Geochemistry Department, Max Planck Institute for Chemistry, Mainz, Germany*

Reference:

Fröhlich, L., Siebert, V., Huang, Q., Thébault, J., Moriceau, B., Jochum, K. P., Schöne, B. R., 2023. Uptake of barium, molybdenum, and lithium and incorporation into scallop shells: Refining proxies for primary production dynamics. Limnology and Oceanography 68, 2544-2561.

This chapter addressed and compared the geochemical variations of Ba/Ca_{shell}, Mo/Ca_{shell} and Li/Ca_{shell} of *P. maximus* specimens that lived naturally on the sediment surface with contemporaneous scallops that lived inside a cage above the seafloor. This allowed to evaluate how phytoplankton-related mechanisms and biogeochemical cycles inside the water column may influence the element ratios in scallop shells. This research demonstrated that both sediment-lived and cage-lived scallops exhibit synchronous periods of trace element enrichments caused by the trophic uptake of respective elements. Geochemical differences between the two groups could be attributed to influences caused by specimen-specific physiological parameters, like growth rates and filtration rates. This manuscript was published in the journal 'Limnology and Oceanography'. For this study, I contributed to the conceptualization, methodology, formal analysis, data acquisition, investigation, visualization, as well as the writing and reviewing of the original draft. This study was co-funded by the German Research Foundation (DFG) grant to BRS (SCHO 793/21) and the French National Research Agency (ANR) grant to JT, within the framework of the HIPPO project.

Author contributions:

LF – Conceptualization, Formal analysis, Data acquisition, Investigation, Methodology, Visualization, Writing - original draft, Writing - review and editing

VS – Investigation, Formal analysis, Data acquisition, Writing - review and editing

QH – Conceptualization, Methodology, Formal analysis, Supervision, Writing - review and editing

JT – Project administration, Investigation, Resources, Validation, Supervision, Writing - review and editing

BM – Resources, Supervision, Writing - review and editing

KPJ – Resources, Validation, Writing - review and editing

BRS – Resources, Conceptualization, Formal analysis, Funding Acquisition, Supervision, Validation, Writing - original draft, Writing - review and editing

Abstract

Ba/Ca_{shell}, Mo/Ca_{shell}, and Li/Ca_{shell} chronologies of *Pecten maximus* can provide information on past phytoplankton dynamics. Distinct Ba, Mo, and Li peaks in the shells are associated with algal blooms. This study evaluated the underlying hypothesis that respective element profiles reliably record variations in phytoplankton dynamics occurring within the water column. Therefore, the chemical content of scallops from the Bay of Brest, France, that lived on the sediment surface was compared to conspecific specimens living in a cage above the seafloor and compared with the phytoplankton abundance and the physicochemical properties of the water column. As demonstrated, Ba/Ca_{shell} and Mo/Ca_{shell} peaks occurred contemporaneously in specimens within the cage and on the sediment, but were higher in the latter. Furthermore, element/Ca peaks agreed with the timing of particulate Ba and Mo enrichments in the seawater. These data support the assumption of a dietary uptake of both elements. Differences in peak heights between shells living in a cage and on the seafloor were controlled by rates of filtration and biomineralization. While the timing and magnitude of Ba/Ca_{shell} peaks were linked to Ba-containing diatoms, Mo/Ca_{shell} peaks were related to blooms of Mo-enriched dinoflagellate and diatom aggregation events. Two episodes of slight Li enrichment occurred synchronously in cage and sediment shells. Although the exact mechanism causing such Li increases remains unresolved, the findings suggest a link to large diatom blooms or the presence of a specific diatom taxon. This study refines previously hypothesized relationships between trace element enrichments in scallop shells and phytoplankton dynamics.

4.1 Introduction

The health of aquatic ecosystems is strongly influenced by phytoplankton. Besides producing oxygen and sequestering atmospheric CO_2 (Field et al., 1998; Westberry et al., 2008), phytoplankton also impacts marine food webs (e.g., Turner and Tester, 1997). Increasing surface water temperature (Winder and Sommer, 2012), ocean acidification (Iglesias-Rodriguez et al., 2008) and imbalanced levels of nutrients caused by inputs of anthropogenic pollutants and artificial fertilizers (Vitousek et al., 1997) can affect the phytoplankton species abundance and community structure. Nearshore areas that provide the habitat for many organisms and serve as valuable sites for human activities (e.g., Worm et al., 2006; Barbier et al., 2011) are particularly vulnerable to eutrophication-induced changes in the phytoplankton species composition. For example, the transition from a phytoplankton community dominated by diatoms to such largely dominated by non-siliceous species such as dinoflagellates (e.g., Wasmund et al., 2017; Spilling et al., 2018), can lead to an increase in harmful algal blooms (Hallegraeff, 1993; Lewitus et al., 2012). To evaluate future trends in phytoplankton community structures, it is crucial to understand the preindustrial phytoplankton dynamics. Such an approach requires temporally well-constrained archives, for example, shells of bivalve mollusks, which reliably record ephemeral variations in phytoplankton species dynamics.

Bivalves record paleoenvironmental information in their shells at high temporal resolution, specifically in the form of geochemical properties, including stable isotopes (e.g., Schöne et al., 2003; McConnaughey and Gillikin, 2008) as well as trace and minor elements (e.g., Thébault et al., 2009b; Zhao et al., 2017; Schöne et al., 2021). Daily, fortnightly and annual growth increments and lines (e.g., Chauvaud et al., 1998; Clark, 2005) can be used to temporally contextualize these geochemical properties. Temporally constrained barium-to-calcium ratios in shells (Ba/Ca_{shell}) of different bivalve species, for example, *Arctica islandica*, *Glycymeris pilosa*, and *Pecten maximus*, were identified as proxies for phytoplankton dynamics (e.g., Stecher et al., 1996; Gillikin et al., 2006). Respective time-series were characterized by a low background that was interrupted by sharp, erratic peaks. Notably, Ba/Ca_{shell} peaks occurred highly synchronously among specimens growing at the same locality and time (e.g., Gillikin et al., 2008; Barats et al., 2009; Thébault et al., 2009a). Whereas Ba/Ca_{shell} peaks typically correlate weakly with chlorophyll *a* concentration (e.g., Gillikin et al., 2008; Fröhlich et al., 2022b; Schöne et al., 2023), they seem to be strongly linked to blooms of specific phytoplankton taxa, especially diatoms containing species-specific loads of

cellular Ba (e.g., Roth and Riley, 1971; Fisher et al., 1991; Sternberg et al., 2005). Furthermore, profiles of molybdenum-to-calcium ratios (Mo/Ca_{shell}) and lithium-to-calcium ratios (Li/Ca_{shell}) in scallop shells exhibited similar patterns as Ba/Ca_{shell}. These patterns include a low background level interrupted by sharp peaks and were likewise associated with phytoplankton dynamics (Thébault et al., 2009a; Barats et al., 2010; Thébault and Chauvaud, 2013; Thébault et al., 2022). However, the underlying mechanisms leading to the formation of Mo/Ca_{shell} and Li/Ca_{shell} peaks differed notably from those of Ba/Ca_{shell} peaks. Enhanced dietary uptake of Mo by *P. maximus* (Barats et al., 2010; Tabouret et al., 2012) seems to be related to the ingestion of small Mo-enriched aggregates of phytoplankton cells (Thébault et al., 2022) and specific dinoflagellates with a high load of cellular Mo (Fröhlich et al., 2022a). Yet, it remains unresolved if these mechanisms provide sufficient quantities of Mo that can explain the formation and magnitude of Mo/Ca_{shell} peaks. The timing of Li/Ca_{shell} peaks in shells of *P. maximus* suggested a relationship to blooms of diatoms adsorbing Li from the water column (Thébault and Chauvaud, 2013; Thébault et al., 2022). Thus, Ba/Ca_{shell}, Mo/Ca_{shell}, and Li/Ca_{shell} profiles of scallops seem to serve as highly valuable sclerochronological tools to derive information about past phytoplankton dynamics. However, despite an increasing number of implications for a trophic uptake of Ba, Mo, and Li, uncertainties remain to what extent the complex dynamics of phytoplankton contribute to the shell geochemistry and which pathways (uptake of these elements, transport within the body and incorporation into the shell) are involved. For instance, the large variation of cellular Ba reported in various marine phytoplankton taxa (e.g., Fisher et al., 1991; Masuzawa et al., 1999; Lobus et al., 2021) makes it difficult to precisely attribute Ba/Ca_{shell} peaks to the presence of specific phytoplankton taxa. To use Ba/Ca_{shell}, Mo/Ca_{shell}, and Li/Ca_{shell} as qualitative and quantitative proxies for phytoplankton dynamics, more detailed information is required on the elemental uptake and shell incorporation, which control the formation of peaks in the trace element-to-calcium profiles.

This study combines highly resolved time-series of Ba/Ca_{shell}, Mo/Ca_{shell}, and Li/Ca_{shell} measured in contemporaneous *P. maximus* specimens (Bay of Brest, France) with detailed environmental monitoring data (Siebert et al., 2023), aiming to verify and refine proposed hypotheses about the uptake of Ba, Mo, and Li from the ambient environment into the shells. Specifically, it was tested that phytoplankton-related processes occurring within the water column affect the chemical composition of scallop shells, substantiating these shells as reliable geochemical archives to accurately record respective events. This was achieved

by comparing element chemical properties of scallops that thrived naturally on the sediment surface to such specimens that lived inside a cage deployed above the seafloor. Geochemical data from the two settings (sediment floor and cage) were also compared with the chemistry of the ambient seawater and the prevailing phytoplankton dynamics. Together with specimen-specific physiological parameters, the molar element-to-calcium ratios were used to deduce absolute concentrations of trace elements that were potentially taken up by the scallops. This novel approach allowed us to quantitatively evaluate if the proposed uptake mechanisms provide sufficient quantities of trace elements to explain their enrichment in the shells. The results of this study can increase the understanding of how Ba/Ca_{shell}, Mo/Ca_{shell}, and Li/Ca_{shell} of *P. maximus* respond to variations in the ambient environment and facilitate the use of the shells as archives for past phytoplankton dynamics.

4.2 Material and methods

4.2.1 Study locality, shell collection, and experimental setup

In October 2021, living specimens of *P. maximus* were collected by SCUBA divers in the southern part of the Bay of Brest (Pointe de Lanvéoc, 48°17′39″N, 004°27′12″W [WGS84]; Supporting Information Fig. S4.1). The bay is a typical shallow (8–15 m depth) and semi-enclosed coastal ecosystem in northwestern France that has been extensively researched in ecological and phytoplankton-related studies over the past years. This constitutes the Bay of Brest as an ideal location to study potential geochemical responses in scallop shells to environmental signals such as large phytoplankton blooms whose initiation is largely controlled by sea surface temperature, nutrient inputs, light conditions, and ocean currents (e.g., Poppeschi et al., 2022). Six specimens were collected from their natural habitat, specifically, scallops that lived and grew on the sediment surface (at approximately 8 m below sea surface; hereafter, these shells are referred to as 'sediment shells'), and six specimens were retrieved from cages (hereafter referred to as 'cage shells') positioned about 1 m above the sediment–water interface (i.e., thin layer at the boundary between sediment surface and water column; SWI) (see Supporting Information Table S4.1). These large-meshed cages (approximately 0.5 cm mesh size, 60 cm × 80 cm × 25 cm) were deployed on 22 February 2021 and juvenile scallops (obtained from the Tinduff Hatchery in Plougastel-Daoulas, France, with a shell height between 2.5 and 3 cm) placed inside (30 scallops per cage). All specimens

used in this study have encountered one winter (age class 1) showing a prominent winter growth line (Supporting Information Fig. S4.1). *P. maximus* precipitates most of the shell carbonate during the second year of life. The respective shell portion, therefore, provides the highest temporal resolution for sclerochronological analyses. After collection, the bivalves were dissected, eviscerated, and epibionts gently removed with a nylon brush. For shell growth pattern and element chemical analyses (for a detailed description of LA-ICP-MS and growth pattern analyses as well as temporal contextualization of geochemical data, see Supporting Information), only the left (flat) valves were utilized because these valves show the most distinct daily growth patterns (growth increments and growth lines, aka 'striae'; Chauvaud et al., 1998). In all cage specimens, shell portions representing the beginning of the growing period in March/April were infested by epibionts, leading to difficulties in the identification of individual growth increments and in situ element analyses. Accordingly, only shell portions without epibionts were used in this study. Water samples collected at the same locality as the scallop specimens were analyzed for their phytoplankton compositions, element chemical properties in the particulate fraction (PBa, PMo, and PLi) as well as for their particulate organic carbon (POC) content (details provided in the Supporting Information).

4.2.2 Trace element uptake by scallops and relation to phytoplankton

Based on the molar trace element-to-calcium ratios measured in the scallop shells, the absolute amount of trace elements incorporated into the shell per day was calculated following the method described by Thébault et al. (2009a). In addition, the quantity of a trace element contained in each liter of filtered seawater was deduced from the Ba/Ca_{shell}, Mo/Ca_{shell}, and Li/Ca_{shell} profiles. Briefly, the calculations were based on the following model, with daily growth rates and molar element-to-calcium ratios as input parameters (model described and illustrated in the Supporting Information and Supporting Information Fig. S4.2A): (1) The shell growth rates were used to calculate the total shell height at each day. (2) The soft tissue dry weight was estimated using the previously determined relationship between shell height and soft tissue dry weight that was previously described for *P. maximus* (Lorrain et al., 2004). (3) Similarly, the shell height was used to account for the shell weight using the shell height-to-shell weight relationship of *P. maximus* (Lorrain et al., 2004). (4) Daily filtration rates were deduced from the soft tissue weight and a soft tissue dry weight-standardized

filtration rate of $\sim 5\,\mathrm{L\,h^{-1}\,g^{-1}}$ (Palmer, 1980; Laing, 2004; Thébault et al., 2009a). (5) The shell weight was used to estimate the amount of shell material that was precipitated each day. (6) The absolute amount of a trace element that was incorporated into the shell during each day was estimated according to the measured trace element-to-calcium ratios and a relative Ca content of 38 wt% (determined for *P. maximus* by Richard 2009 and *A. islandica* shells by Marali et al., 2017) of the total shell material. Background subtraction was performed for the Ba/Ca_{shell} and Mo/Ca_{shell} profiles to remove the influence of dissolved Ba and Mo on the measured element-to-calcium ratios, using the partition coefficient for Ba ($D_{Ba} = 0.11$; Barats et al., 2009) and Mo ($D_{Mo} = 1.5 \times 10^{-4}$; Barats et al., 2010). The relationship between daily growth rates and Li/Ca_{shell} background was used to account for excess Li/Ca_{shell} (Thébault and Chauvaud, 2013). (7) The amount of trace elements that was contained in each liter of filtered seawater (hereafter referred to as $TE_{filtered\ seawater}$) was estimated considering the total load of trace elements incorporated into the bivalve (assuming that 63% of the total Ba and 27% of the total Mo ends up in the shell matrix according to preliminary data from Barats, 2006) each day and the daily filtration rate. Absolute estimates of $Li_{filtered\ seawater}$ were not obtained as the relative distribution of Li among the soft tissue and shell material was not available.

To quantify the potential trace element content in phytoplankton, the estimated $TE_{filtered\ seawater}$ levels were compared with the measured phytoplankton cell concentration data based on previously hypothesized relationships between trace element incorporation rates and phytoplankton dynamics. The uptake mechanisms were quantitatively evaluated for Ba and Mo, but only qualitatively for Li because absolute values for $Li_{filtered\ seawater}$ could not be obtained (see above). Accordingly, $Mo_{filtered\ seawater}$ levels were related to the cell concentration data of the dinoflagellate genus *Gymnodinium* spp. (Fröhlich et al., 2022a). In contrast to Mo/Ca_{shell}, the patterns of the Ba/Ca_{shell} profiles were hypothesized to be controlled by the abundance of multiple phytoplankton species, primarily diatoms (Thébault et al., 2009a; Fröhlich et al., 2022a; Fröhlich et al., 2022b). To detect potential patterns between the Ba/Ca_{shell} profiles and diatoms, the pseudo-random Monte Carlo (MC) approach described in Fröhlich et al. (2022a) was used. Given the premise that Ba/Ca_{shell} peaks follow the timing and intensity of phytoplankton blooms, along with species-specific amounts of cell-associated Ba, this method evaluated numerous potential scenarios (i.e., 1.8×10^9) and identified the statistically most relevant one. To this avail, combinations of phytoplankton cell concentration data (determined for specific phytoplankton taxa) were pseudo-randomly selected, tempo-

rally shifted (within a predefined time window, i.e., time lag), weighted (between 0 and 1), and merged into artificially generated time-series (for details see Fröhlich et al., 2022a). Then, the resulting time-series were correlated with the Ba/Ca_{shell} profile using the Pearson correlation coefficient as a metric. Note that uncertainties in the temporal alignment of the geochemical shell data, as well as the low sampling frequency of the phytoplankton data (i.e., the exact timing when a phytoplankton bloom reaches the highest cell concentration remains unknown), largely influence the direct assignment of a given phytoplankton bloom to a Ba/Ca_{shell} peak during the MC calculations. In addition, a short time lag of up to 12 d between the occurrence of a given phytoplankton species and a Ba/Ca_{shell} peak had to be assumed (Fröhlich et al., 2022a; Fröhlich et al., 2022b). Therefore, stepwise testing of different time windows (i.e., 4-d window) was necessary to determine the combination of different phytoplankton species that agreed best with the measured Ba/Ca_{shell} profile. As no phytoplankton data were available for the time between late July and early September, the MC approximations were performed, excluding this time interval. The MC-estimated species-specific weighting coefficients served as relative Ba-enrichment factors and were used together with $Ba_{filtered\ seawater}$ to account for the minimum content of diatom-associated Ba in 1 L of seawater that was potentially ingested by the scallops (see Fig. S4.2B).

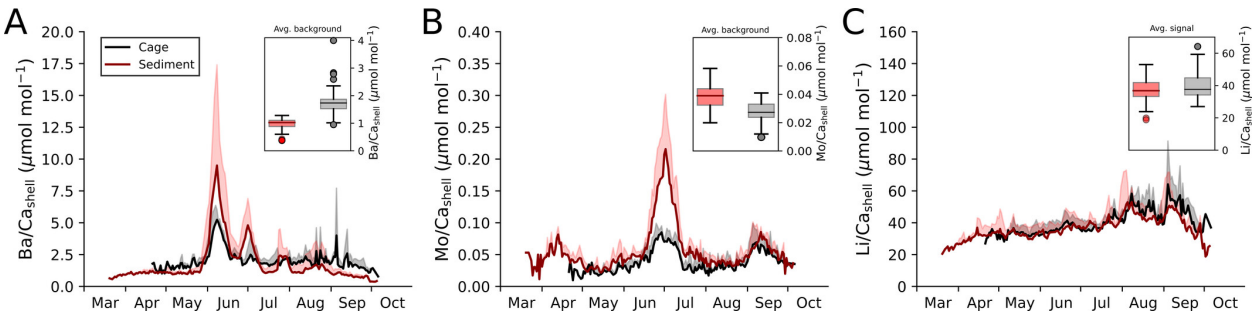

Figure 4.1 Averaged Ba/Ca_{shell} (**A**), Mo/Ca_{shell} (**B**), and Li/Ca_{shell} (**C**) profiles ($+1\sigma$) obtained from three *Pecten maximus* specimens grown inside a cage (black) and on the sediment surface (red) during 2021. Box plots indicate differences in the background signals between cage and sediment shells of average Ba/Ca_{shell} and Mo/Ca_{shell} profiles and the average signal of Li/Ca_{shell} ratios.

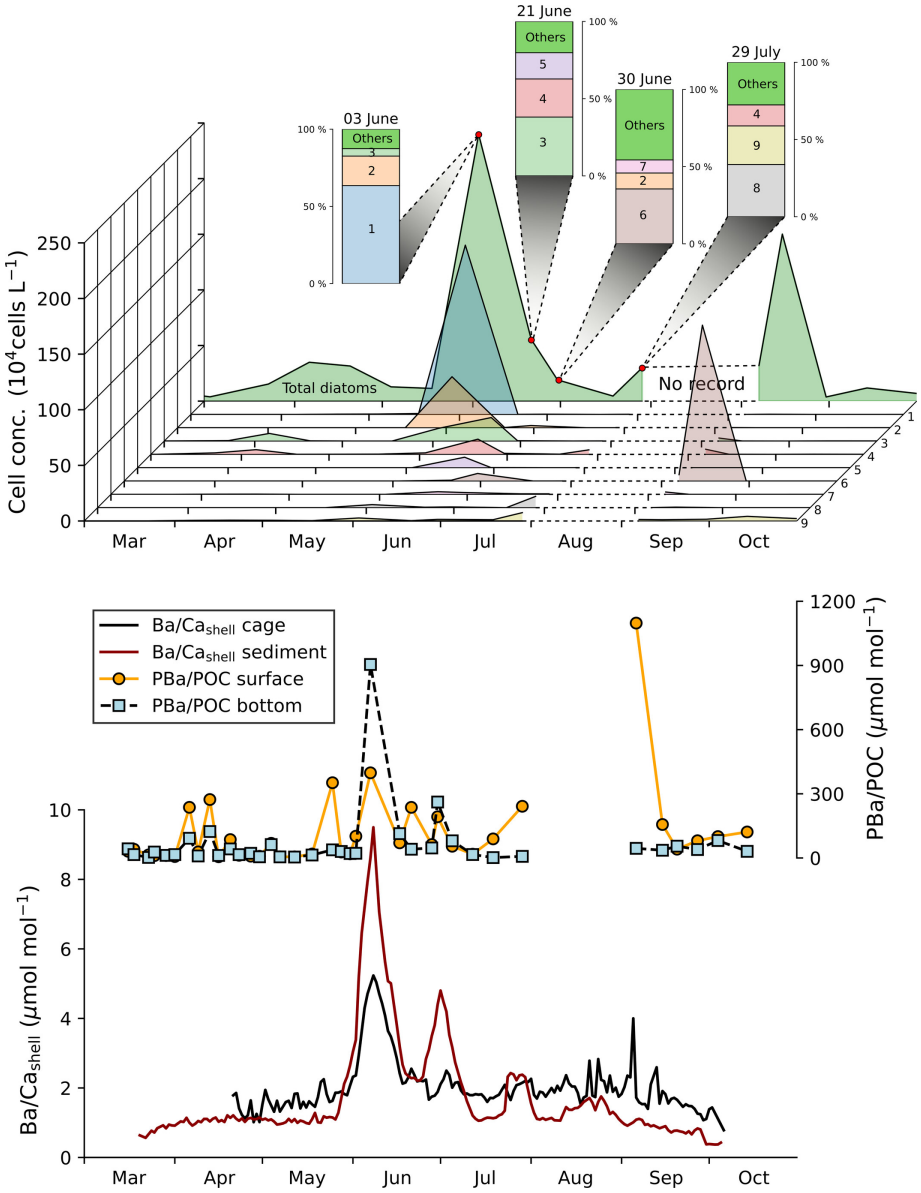

Figure 4.2 Average Ba/Ca_{shell} profiles from cage and sediment shells (from 2021), the temporal variation in the PBa/POC ratios measured in surface and bottom waters and the cell concentration time-series of the most abundant diatom species that were recorded in the water column (at the studied locality in Lanvéoc, France). The vertical bar plots in the upper panel indicate the relative community compositions at four different dates with the three most abundant diatom taxa (1—*Leptocylindrus danicus*, 2—*Tenuicylindrus belgicus*, 3—*Chaetoceros curvisetus*, 4—*Chaetoceros* spp., 5—*Chaetoceros socialis*, 6—*L. danicus* and *Leptocylindrus convexus*, 7—*C. socialis*, 8—*Pseudo-nitzschia delicatissima*, *Pseudo-nitzschia pseudodelicatissima*, and *Pseudo-nitzschia cuspidata*, 9—*Lennoxia faveolata*).

4.3 Results

4.3.1 Ba in shells, seawater, and relation to diatom blooms

All studied cage shells (Fig. 4.1A; Supporting Information Fig. S4.4A) showed one prominent Ba/Ca_{shell} peak at ca. 08 June that occurred simultaneously in all specimens from the cage (on average, $5.23 \pm 0.79\,\mu mol\,mol^{-1}$). This peak was followed by another, smaller Ba/Ca_{shell} enrichment (04 July; on average $2.37\,\mu mol\,mol^{-1}$), which was, however, only well-pronounced in one of the three studied specimens (Shell B; Supporting Information Fig. S4.4A). Similarly, in late July, another Ba/Ca_{shell} peak was only observed in one of the three specimens (Shell C; Supporting Information Fig. S4.4A). On average, the measured Ba/Ca_{shell} background in cage shells was around $1.73 \pm 0.41\,\mu mol\,mol^{-1}$. In the ontogenetically older shell portions (starting from mid-August), larger deviations from this background level were observed as short-term (< 2 d) enrichments showing Ba/Ca_{shell} ratios reaching up to $8.23\,\mu mol\,mol^{-1}$ on 05 September in Shell A (Fig. 4.1A).

In contrast to the cage shells, the Ba/Ca_{shell} profiles of sediment specimens revealed a more stable background level of about $0.96 \pm 0.20\,\mu mol\,mol^{-1}$ (Fig. 4.1A). This background was interrupted by a large double peak between late May and end of June, with average values of 9.50 and $4.80\,\mu mol\,mol^{-1}$ on 08 June and 01 July, respectively (Fig. 4.1A). Although the first Ba/Ca_{shell} peak occurred nearly synchronously in all three specimens (i.e., within a few days), the peak magnitude of Shell D ($18.58\,\mu mol\,mol^{-1}$) was notably larger than that of Shell E and F (5.95 and $7.43\,\mu mol\,mol^{-1}$, respectively; Supporting Information Fig. S4.4A). In late July, another Ba/Ca_{shell} enrichment episode was observed in all three shells with average values of up to $2.43\,\mu mol\,mol^{-1}$ (25 July). The fourth and last Ba/Ca_{shell} enrichment ($3.86\,\mu mol\,mol^{-1}$) was recorded in August in only one specimen from the sediment (Shell F), while no peak was present in the other two shells (Shells D and E; Supporting Information Fig. S4.4A). The average background signals differed significantly between cage and sediment shells (approximately 80% higher median in cage shells than in sediment shells), as indicated by a Kruskal–Wallis test ($p < 0.001$, $H[\chi^2] = 135.7$; details about statistics provided in the Supporting Information).

Ratios of PBa to POC (PBa/POC) range from 1.86 to $904.58\,\mu mol\,mol^{-1}$ in bottom waters and 5.23 to $1098.04\,\mu mol\,mol^{-1}$ in surface waters (Fig. 4.2). PBa/POC profiles at both settings (surface and bottom) were characterized by a very low and flat baseline episodi-

cally interrupted by sharp peaks. The largest values were recorded on 07 June in bottom waters and 06 September in surface waters. Notably, all episodes of enhanced PBa/POC ratios that were measured in bottom waters occurred simultaneously with PBa/POC peaks in surface waters, although to different magnitudes. A significant correlation existed between Ba/Ca_{shell} profiles (cage and sediment) and PBa/POC ratios of bottom waters (see Supporting Information Fig. S4.5).

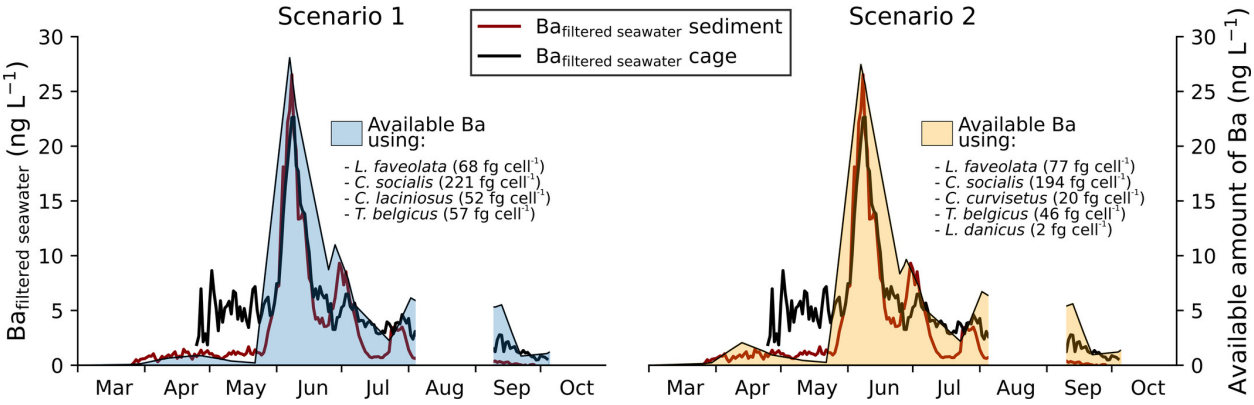

Figure 4.3 Considering shell height, growth rates, and filtration rates (i.e., 5 L h^{-1} g^{-1} soft tissue dry weight), the $Ba_{filtered\ seawater}$ concentration was estimated from the Ba/Ca_{shell} profiles. Two potential diatom scenarios obtained by Monte Carlo simulations were used to estimate the diatom-associated amount of Ba following the assumption that the ingestion of diatoms triggered the formation of the Ba/Ca_{shell} peaks (see calculations described in the Supporting Information).

The different Ba/Ca_{shell} enrichments were associated with uniqe diatom assemblages (Fig. 4.2). For instance, the two large Ba/Ca_{shell} peaks in shells from the sediment (i.e., in early June and early July; Fig. 4.2) occurred contemporaneously with blooms of the diatom genus *Leptocylindrus* (i.e., *Leptocylindrus danicus* on 03 June and *L. danicus* + *Leptocylindrus convexus* on 30 June, respectively), while different diatoms of the genus *Chaetoceros* made up the majority of diatom cells on 21 June that coincided with only a very small Ba/Ca_{shell} enrichment in the cage shells (Fig. 4.2). No apparent correlation existed between bulk diatom dynamics and Ba/Ca_{shell} profiles. Instead, the pseudo-random MC method revealed potential patterns between Ba/Ca_{shell} profiles and the main abundant diatom taxa (see caption Fig. 4.2). The strongest correlation (Pearson coefficient: 0.91 with $p < 0.05$) between MC-approximated patterns and the Ba/Ca_{shell} profile was obtained for a time lag of 5-8 d (Supporting Information Fig. S4.6). However, the timing and magnitude of the diatom

occurrences agreed better with the Ba/Ca_{shell} profiles at a shorter time lag of 4-7 d (with slightly lower Pearson correlation coefficients). According to this, the best diatom combination (hereafter referred to as 'scenario 1,' containing the diatom species *Lennoxia faveolata*, *Chaetoceros socialis* and *Chaetoceros laciniosus*, and *Tenuicylindrus belgicus*) coincides with the timing of the two large Ba/Ca_{shell} peaks in June and July and the smaller enrichment at the end of July (Fig. 4.3; Supporting Information Fig. S4.6). In a second, slightly modified set of MC calculations, the cell concentration data of *L. danicus* were forced to be included in each tested combination performed by the pseudo-random simulation (set 2; Supporting Information Fig. S4.6). The reason for considering set 2 is that the mass occurrence of this specific diatom taxon, by far the most abundant diatom species in the studied year (Fig. 4.2), coincided with the timing of the largest Ba/Ca_{shell} peak in cage and sediment shells and thus suggested to be directly related to the Ba enrichment in the shell. In agreement with simulations of set 1, the most suitable combination was detected for a potential time lag of 4-7 d (in the following referred to as 'scenario 2' considering *L. faveolata*, *C. socialis*, *Chaetoceros curvisetus*, *T. belgicus*, and *L. danicus*; Fig. 4.3; Supporting Information Fig. S4.6). Because the obtained species-specific weighting factors were affected by the time lag that was artificially applied to each diatom species, various tested time lags produced slightly different outcomes (Supporting Information Fig. S4.6). In this study, the short time lag (i.e., in the expected range which was previously approximated between phytoplankton bloom and geochemical response; Fröhlich et al., 2022a) was exclusively used to determine the potential phytoplankton combination (with weighting factors) that best matched the Ba/Ca_{shell} profile. As depicted in Supporting Information Fig. S4.7, the daily amount of Ba that ended up in the bivalve varied considerably between specimens in the cage (maximum of $1.6\,\mu g\,d^{-1}$) and on the sediment (maximum of $3.6\,\mu g\,d^{-1}$). However, an almost equal amount of Ba in 1 L of ingested seawater was needed to trigger the formation of the largest Ba/Ca_{shell} peaks in early June (Supporting Information Fig. S4.7) for shells from the cage (approximately $23\,ng\,L^{-1}$) and the sediment (approximately $27\,ng\,L^{-1}$) after taking the shell growth and filtration rates into consideration. Following the approximations performed for scenario 1 (Fig. 4.3), the hypothetically calculated amount of Ba (see Fig. S4.2) ranged between 52 and $221\,fg\,cell^{-1}$ (for the diatom taxa *T. belgicus* and *C. socialis*, respectively). Based on the estimates of scenario 2, an adequate amount of phytoplankton-associated Ba was potentially abundant in the seawater if the diatom cells contained between 2 (*L. danicus*) and 194 (*C. socialis*) $fg\,Ba\,cell^{-1}$ (Fig. 4.3).

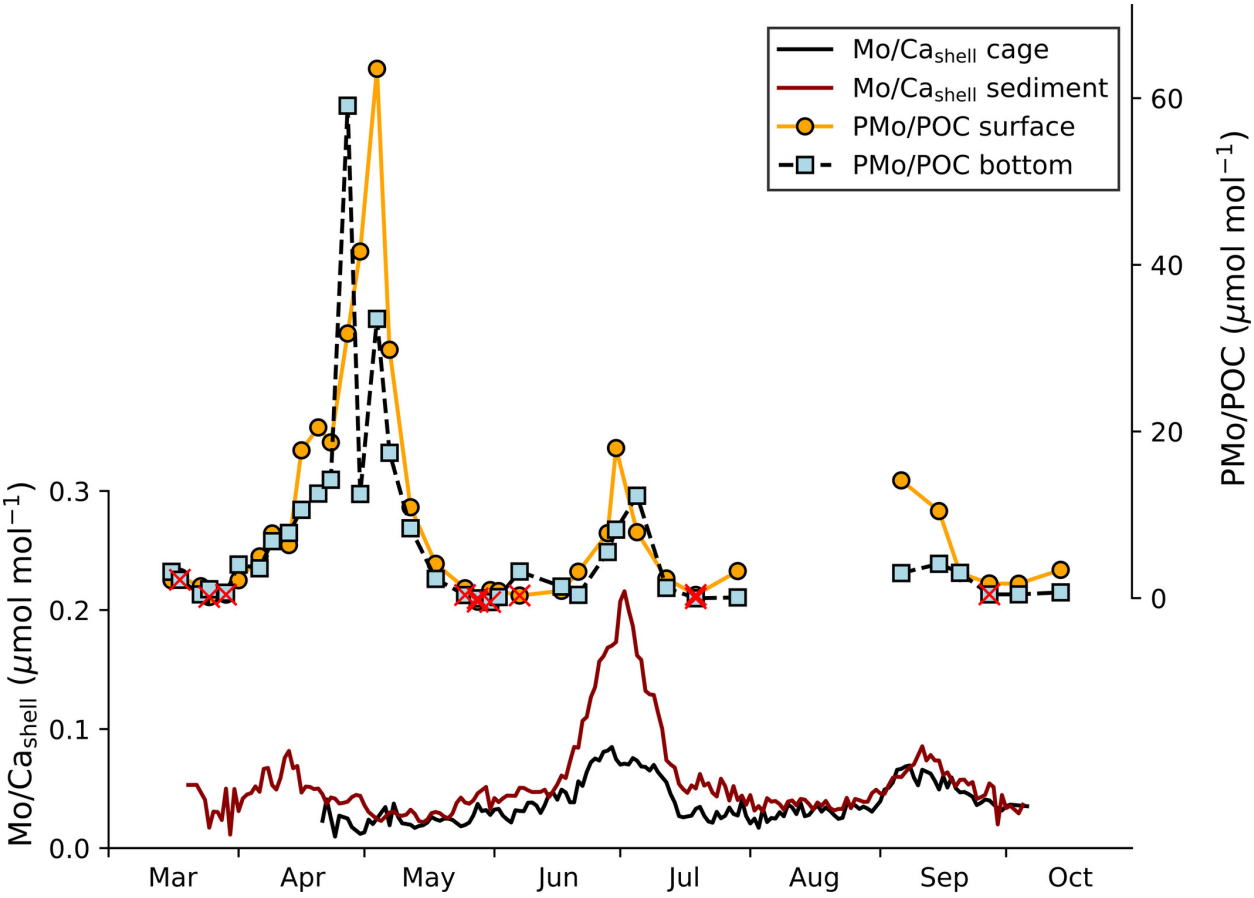

Figure 4.4 Average Mo/Ca$_{shell}$ profiles from cage and sediment shells (from 2021) and the variation in PMo/POC ratios measured in surface and bottom waters. Note that some analyses of PMo remained below the limit of detection (indicated with a red cross).

4.3.2 Mo in shells, seawater, dinoflagellate blooms, and aggregation events

Mo/Ca$_{shell}$ profiles (Figs. 4.1B, 4.4) of the cage shells showed two episodes of elevated Mo content, that is, at 29 June (0.08 ± 0.01 µmol mol^{-1}) and 08 September (0.07 ± 0.02 µmol mol^{-1}). Peak heights were nearly identical between the three specimens and clearly stood out from the background (approximately 0.03 ± 0.01 µmol mol^{-1}, Fig. 4.1B). In specimens from the sediment, a large Mo/Ca$_{shell}$ peak occurred at around the same time of the year (on 02 July) but was nearly threefold larger than in cage specimens (0.22 ± 0.09 µmol mol^{-1}; Fig. 4.1B). As in the cage shells, another Mo/Ca$_{shell}$ enrichment was observed in early September with an average magnitude of 0.09 ± 0.01 µmol mol^{-1}. Sediment specimens also revealed

elevated Mo/Ca_{shell} values (approximately 0.08 µmol mol^{-1}) in shell portions deposited in early April. The contemporaneous shell portions could not be studied in cage shells due to epibiont overgrowth. Sediment specimens contained, on average, 25% higher Mo/Ca_{shell} values (0.04 ± 0.01 µmol mol^{-1}) than cage shells (Kruskal–Wallis test; $p < 0.001$, H[χ^2] = 74). The total (shell plus soft tissue) daily Mo incorporation ranged between 3 and 63 ng d^{-1} for cage specimens and 8 and 147 ng d^{-1} for sediment specimens (Fig. 4.5A). Considering the daily filtered water volume (Fig. 4.5A), $Mo_{filtered\ seawater}$ ranged between 0.03 to 0.78 ng Mo L^{-1} (Fig. 4.5B).

Levels of PMo/POC ratios likewise showed a flat baseline (note that low PMo/POC levels were slightly below the detection limit obtained for particulate Mo) with episodes of high PMo/POC levels (Fig. 4.4). In both bottom and surface waters, three PMo/POC events were observed in late April to early May (up to 59.10 and 63.53 µmol mol^{-1}, respectively), late June (reaching 12.29 and 18.01 µmol mol^{-1}, respectively), and early to mid-September (mainly occurring in surface water samples with ratios of 14.13 µmol mol^{-1}). Eight phytoplankton aggregation events were determined (V. Siebert unpubl.) to occur in the water column during 2021 (30 March; 12 and 27 April; 13 May; 06, 14, and 27 June; 02 October). Among these events, the aggregates observed in June showed notable enrichment in Mo (Fig. 4.5). The most abundant dinoflagellate species identified in 2021 belonged to the genus *Gymnodinium* with a maximum cell concentration of 33,440 cells L^{-1} on 04 May (V. Siebert unpubl.). More than half of these cells (68%) were smaller than 10 µm. Distinct blooms of this dinoflagellate occurred in early May, mid-June, and mid-September (Fig. 4.5B), contemporaneously with PMo/POC enrichments. Estimating the cellular Mo content (described in Discussion) of individual *Gymnodinium* spp. cells smaller than 10 µm (in length and diameter) yielded amounts of up to 500 fg cell^{-1} (Fig. 4.5C; see Discussion for calculations).

4.3.3 Li in shells and seawater

Cage and sediment shells revealed similar Li/Ca_{shell} profiles (Fig. 4.1C) that were characterized by low values in early 2021 (on average, 32.65 ± 2.04 and 30.61 ± 3.71 µmol mol^{-1} until June in cage and sediment shells, respectively) and steadily increasing ratios during the main growing season in June and July (on average, 37.70 ± 3.35 µmol mol^{-1} in cage and 36.97 ± 2.98 µmol mol^{-1} in sediment specimens). Between August and mid-September, Li/Ca_{shell} values were slightly higher in cage shells (49.20 ± 5.77 µmol mol^{-1}) than in sedi-

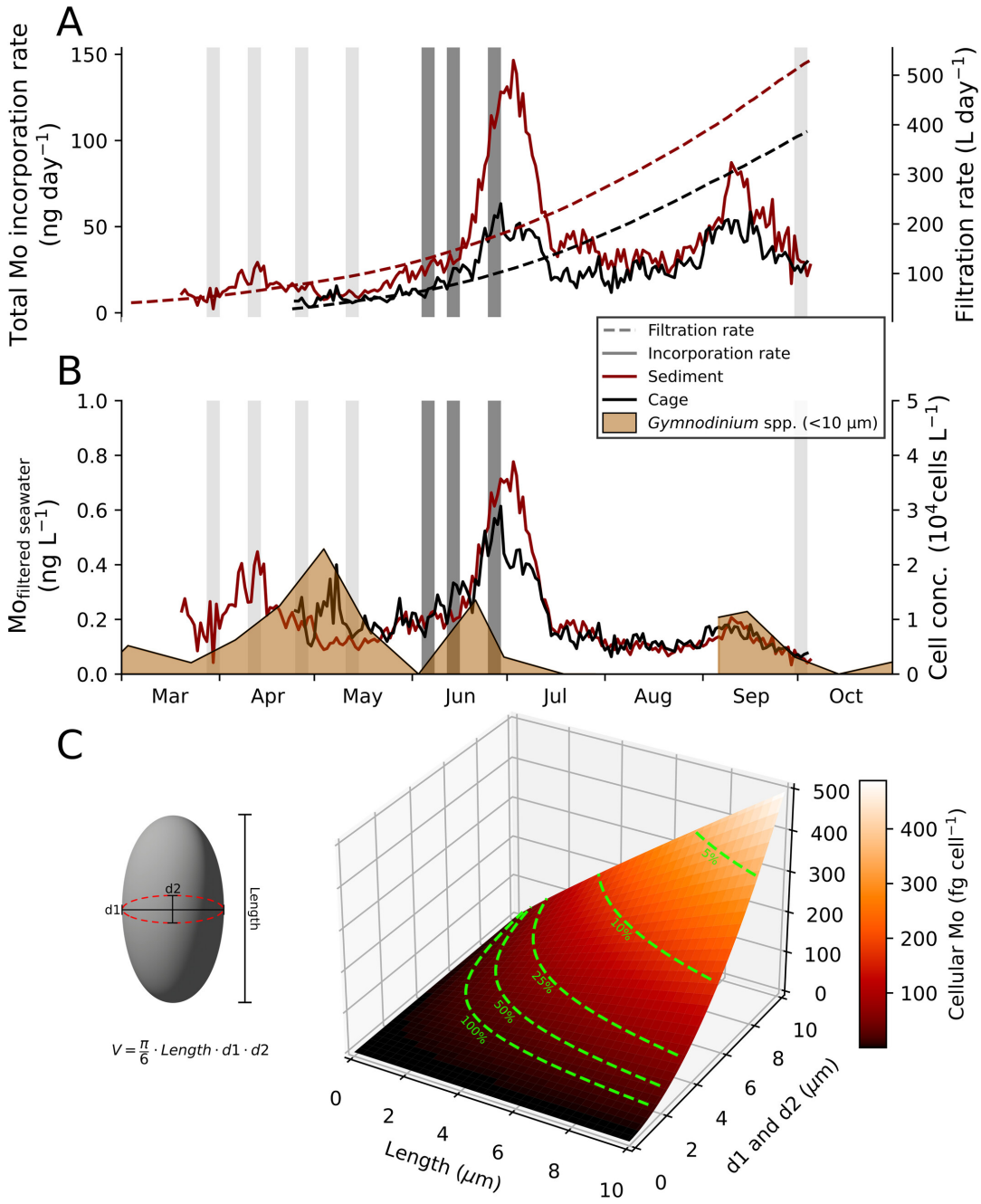

Figure 4.5 Approximated total Mo incorporation rate into the scallops and filtration rate (at 5 L h^{-1} g^{-1} of soft tissue dry weight) for cage and sediment shells (**A**). The Mo$_{\text{filtered seawater}}$ concentration (based on the total Mo incorporation rate, growth, and filtration rate) and the temporal dynamics of the dominant dinoflagellate *Gymnodinium* spp. monitored at the study site (**B**). Periods of aggregate formation (determined by V. Siebert unpubl.) are indicated as light gray, vertical bars (**A** and **B**).

Figure 4.5 (continued) Dark gray bars depict aggregation episodes during which significant loads of Mo were transported from the water column toward the SWI (V. Siebert unpubl.). The cellular Mo content at various cell volumes (**C**) was estimated using the cell geometry for *Gymnodinium* (Hillebrand et al., 1999; Sun and Liu, 2003), the volume-to-carbon relationship for dinoflagellates (Menden-Deuer and Lessard, 2000) and the elemental Mo/P (phosphorous) and C/P composition determined for the dinoflagellate *Gymnodinium chlorophorum* (Ho et al., 2003). The green graphs in the three-dimensional plot (**C**) illustrate potential values for cell parameters (if 100%, 50%, 25%, 10%, or 5% of the *Gymnodinium* spp. cells per liter were ingested by the scallops) that are required to provide an adequate amount of cellular Mo to meet the trace element requirement in the ingested seawater (estimated in **B**) to explain the observed Mo/Ca_{shell} peaks.

ment shells ($45.40 \pm 3.74\,\mu mol\,mol^{-1}$). Although no large, distinct peaks were observed in the Li/Ca_{shell} chronologies (Fig. 4.1C), two smaller enrichment episodes were present during late summer (August to mid-September), with average values reaching 58.20-64.18 $\mu mol\,mol^{-1}$ in cage shells and 50.73-52.99 $\mu mol\,mol^{-1}$ in sediment shells. Until the end of shell growth in early October, Li/Ca_{shell} ratios decreased rapidly in both groups (cage: $40.51\,\mu mol\,mol^{-1}$; sediment: $31.52\,\mu mol\,mol^{-1}$). Li/Ca_{shell} data differed significantly between cage and sediment shells (Kruskal–Wallis test, $p < 0.05$, $H[\chi^2] = 6.0$). It is noteworthy that similar results were obtained after removing the estimated background signal from the measured Li/Ca_{shell} data.

Ratios of PLi to POC exhibited values ranging between 1.15 and 1289.74 in bottom and surface waters (Fig. 4.6). Aside from a large PLi/POC peak in March, two additional enrichments occurred in bottom PLi/POC ratios on 07 June ($656.47\,\mu mol\,mol^{-1}$) and 15 September ($384.88\,\mu mol\,mol^{-1}$). The latter coincided with the maximum PLi/POC ratio in surface waters.

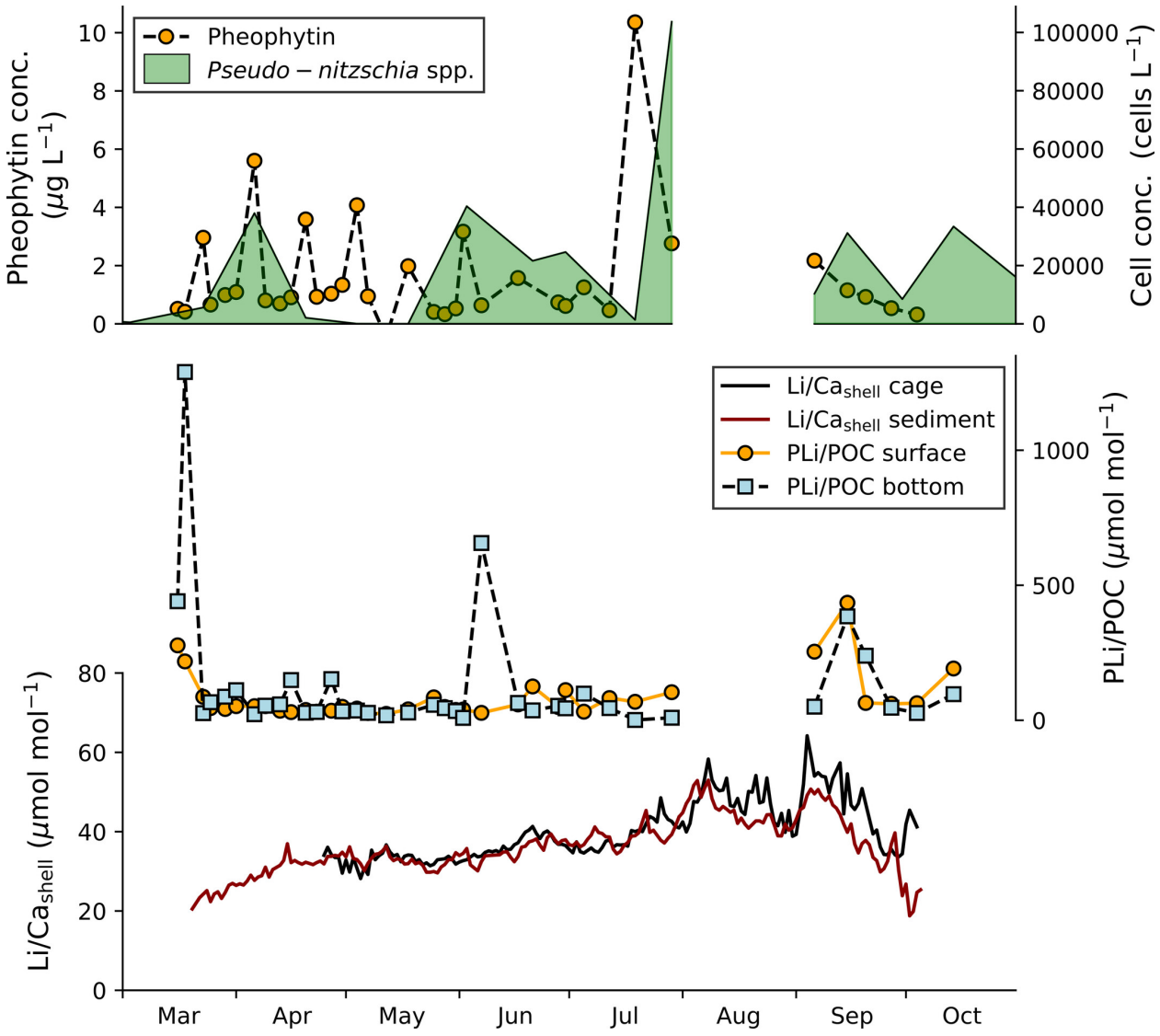

Figure 4.6 Cell concentration time-series of the diatom *Pseudo-nitzschia* spp. and pheophytin pigment concentration in 2021. Temporal variation of PLi/POC recorded in surface and bottom waters with averaged Li/Ca_{shell} profiles measured in cage and sediment shells.

4.4 Discussion

4.4.1 Ba/Ca_{shell} profiles

The synchronicity of the Ba/Ca_{shell} peaks (in cage and sediment specimens) and PBa/POC ratios of the water column (Fig. 4.2) suggests that shell Ba enrichments likely originated from the particulate phase (PBa), which is derived from the ambient water rather than the sediment. This finding corroborates the hypothesized trophic uptake of Ba-enriched suspended particles by scallop shells (e.g., Gillikin et al., 2008; Barats et al., 2009; Tabouret et al., 2012) that either originate from Ba accumulated on phytoplankton cell walls (Sternberg et al., 2005) or from enhanced barite precipitation (during the decay of phytoplankton blooms or the presence of acantharians in the water column) (e.g., Bishop, 1988; Ganeshram et al., 2003). Direct ingestion of cellular Ba from living phytoplankton cells provides a reasonable explanation for elevated shell Ba levels because Ba/Ca_{shell} peaks occur simultaneously with blooms of certain diatom species and a strong increase in the PBa/POC ratio in early June (Fig. 4.2). This agrees to previous findings demonstrating that the occurrence of Ba/Ca_{shell} peaks is linked to the formation of phytoplankton blooms (i.e., mainly diatom blooms) (Thébault et al., 2009a; Fröhlich et al., 2022a; Fröhlich et al., 2022b). During the blooms, dissolved Ba from the ambient water is adsorbed onto phytoplankton cell walls (Sternberg et al., 2005) and the ingestion of those Ba-enriched cells by scallops leads to an elevated Ba concentration in the shell calcite after a few days. The hypothesis is further substantiated by a negative correlation between dissolved Ba and PBa in the seawater (V. Siebert unpubl.). While large phytoplankton blooms generate microenvironments facilitating the precipitation of barite (e.g., Dehairs et al., 1980; Bishop, 1988), the ingestion of such particles could not sufficiently explain the formation of Ba/Ca_{shell} peaks in the scallop, *Comptopallium radula* (Thébault et al., 2009a). Moreover, the ingestion of rapidly sinking barite particles in decaying phytoplankton (Stecher and Kogut, 1999) would have caused a larger Ba uptake by sediment specimens than by cage specimens because of the accumulation of large amounts of barite crystals at the SWI. However, after removing the influence of shell precipitation and filtration rates on the Ba/Ca_{shell} peaks, the $Ba_{filtered\ seawater}$ was nearly identical between cage and sediment shells (see Supporting Information Fig. S4.7), indicating that barite ingestion played only a minor role in the formation of shell Ba enrichments. Although the development of barite particles potentially contributed to the observed enrichments of PBa/POC

in the water column, a pathway via barite uptake leading to the formation of the observed Ba/Ca_{shell} peaks in cage and sediment shells is less likely.

Consistent with previous findings (e.g., Barats et al., 2009; Fröhlich et al., 2022b), the variation in bulk phytoplankton or gross diatom abundance (Fig. 4.2) provided no striking similarities to the Ba/Ca_{shell} chronologies within the studied year (except the large peak in early June), reinforcing the assumption that phytoplankton or diatoms as a whole cannot explain the variability of Ba/Ca_{shell} peaks. This complicates the applicability of Ba/Ca_{shell} as a direct paleoproductivity proxy. The quantity of cell-associated Ba varies significantly between different phytoplankton species (Roth and Riley, 1971; Fisher et al., 1991), indicating that the ingestion of some phytoplankton taxa contributes more to the measured Ba/Ca_{shell} peaks than other species (Fröhlich et al., 2022b). The pseudo-random MC calculations (considering species-specific amounts of cell-associated Ba) returned two possible scenarios (Fig. 4.3), which qualitatively illustrated that the dynamics of only four (scenario 1; Fig. 4.3) or five (scenario 2; Fig. 4.3) diatom species are sufficient to explain the observed Ba/Ca_{shell} patterns. Although both scenarios include chain-forming diatoms (i.e., *C. socialis* and *L. danicus*), which can potentially inhibit the shell growth of scallops due to gill clogging (Chauvaud et al., 1998; Lorrain et al., 2000), these diatom species cannot be excluded as potential food sources because no distinct reductions in growth rate (details about growth rates are provided in the Supporting Information) were observed during the formation of Ba/Ca_{shell} peaks. Aside from the diatom genus *Chaetoceros*, a well-known dietary component of *P. maximus* (e.g., Laing, 2004), no further information about feeding preference or gut content was available for the studied scallops. Therefore, none of the potential diatom scenarios can be ruled out. Moreover, the small discrepancy in the estimated time lag (4–7 d; Supporting Information Fig. S4.6B) compared to the previously reported delay between phytoplankton blooms and geochemical response in the Ba/Ca_{shell} profiles (8-12 d; Fröhlich et al., 2022a; Fröhlich et al., 2022b) were most likely due to the low temporal resolution of the phytoplankton record and small uncertainties in the temporal alignment of the geochemical data. In fact, species-specific Ba loads between 2 and 221 $fg\,cell^{-1}$ were estimated for the selected diatom species (Fig. 4.3), which fall in the range of cellular Ba content in different marine phytoplankton species (up to 245 $fg\,cell^{-1}$ Fisher et al., 1991). In particular, a cell-associated Ba load of 60 $fg\,cell^{-1}$ can be approximated for *Chaetoceros* (using an average Ba concentration of 75.33 $\mu g\,g^{-1}$ of dry weight (Lobus et al., 2021) at a maximum cellular dry weight for *C. gracilis* of approximately 0.8 $ng\,cell^{-1}$ (Tachihana et al.,

2020)), which is notably consistent with the cellular Ba range computed in the present study. Such combinations of qualitative and quantitative approaches provide ecologically reasonable estimates and suggest that the cell abundance of only a few diatom species containing a reasonable amount of Ba can induce the formation of maxima in the Ba/Ca_{shell} chronology of *P. maximus*.

Interestingly, the significant difference in peak magnitudes of the elemental Ba/Ca_{shell} ratios between cage and sediment shells in early June (Fig. 4.2) was diminished after converting Ba/Ca_{shell} profiles to $Ba_{filtered\ seawater}$ (Fig. 4.3; Supporting Information Fig. S4.7). This suggests that the filtered seawater for both cage and sediment scallops contained nearly the same amount of Ba (during the formation of Ba/Ca_{shell} peaks), which could be induced by a diatom bloom in the ambient water. The higher Ba/Ca_{shell} peaks of sediment shells, on the other hand, seem to be mainly controlled by higher filtration and shell precipitation rates (Supporting Information Fig. S4.7). Aside from the difference in the averaged Ba/Ca_{shell} ratios of cage and sediment shells, a relatively large inter-specimen variation existed in the Ba/Ca_{shell} peak heights among sediment shells (i.e., the most distinct difference occurred between Shell D and Shell E in early June during the formation of the largest Ba/Ca_{shell} peak with 3.1 times higher values measured in Shell D; Supporting Information Fig. S4.4A). By computing the $Ba_{filtered\ seawater}$ contents for Shell D and Shell E according to their individual growth rate and filtration rate, this in-situ measured Ba/Ca_{shell} discrepancy became less pronounced and differed by around $16\,ng\,L^{-1}$ (1.7 times higher in Shell D compared to Shell E; Supporting Information Fig. S4.8). Nevertheless, it needs to be noted that an equal weight-standardized filtration rate of $5\,L\,h^{-1}\,g^{-1}$ was considered for the calculation of $Ba_{filtered\ seawater}$ of Shell D and Shell E. Given that asynchronous, short-term changes in individual filtration activities were observed for scallops cultured in the same tank with identical conditions (Strohmeier et al., 2009), it is likely that individual variations in filtration rate might have induced such differences in peak heights. Alternatively, if the same amount of Ba (i.e., $Ba_{filtered\ seawater}$) was available in the water for Shell D and Shell E in early June, the filtration rate should have been slightly higher in Shell D to explain the larger Ba/Ca_{shell} peak magnitude (e.g., given a scenario in which Shell D possessed a higher, yet realistic, relative filtration rate of about $8.6\,L\,h^{-1}\,g^{-1}$ instead of $5\,L\,h^{-1}\,g^{-1}$, both specimens exhibited similar $Ba_{filtered\ seawater}$ levels; Supporting Information Fig. S4.8). Therefore, small individual differences in growth rate and filtration rate can result in significant differences in the measured Ba/Ca_{shell} profiles, which could affect the inter-specimen reproducibility of

Ba/Ca_{shell} profiles. These findings suggest to adjust elemental Ba/Ca_{shell} ratios measured in *P. maximus* for filtration rate and shell growth rate before the data can be used as a potential quantitative indicator of past phytoplankton dynamics. Additional information about uncertainties in the estimations applied in this study is provided in the Supporting Information.

The Ba/Ca_{shell} background level of cage shells was significantly higher than that of sediment shells (Fig. 4.1A), even after approximating the $Ba_{filtered\ seawater}$ content (Fig. 4.3). This finding is potentially coupled to the observation of higher growth rates measured in cage-grown specimens (Supporting Information Fig. S4.3), a phenomenon previously reported for other scallop taxa, for example, *Crassadoma gigantea* (Leighton, 1979), *Placopecten magellanicus* (MacDonald, 1986), and *Lyropecten nodosus* (Mendoza et al., 2003). The higher growth rate in cage-grown scallops may be primarily associated with higher food availability (MacDonald, 1986) because the cage was placed within the water column where bivalves potentially had better access to living planktonic organisms, such as diatoms. Thus, the constant provision of Ba-containing cells, selectively retained by scallop gills (Shumway et al., 1997; Beninger et al., 2004), potentially led to elevated Ba/Ca_{shell} background levels. Sediment particles within the digestive tract of scallops from the sediment (as reported by Shumway et al., 1987) could also affect the bivalves to efficiently assimilate their food, altering the gut pH and/or the retention time of food particles in the gut (e.g., Wang et al., 1995). This potential influence might have contributed to the observed differences in Ba/Ca_{shell} background, yet it needs to be confirmed in future studies by analyzing the gut content of scallops. The high variability in the Ba/Ca_{shell} profiles observed in cage shells compared to the more stable Ba/Ca_{shell} background measured in sediment shells (Fig. 4.1A) could be related to enhanced competition for resources between the cage scallops, given the high specimen density in the cage and the fact that scallops were reported to actively avoid high spatial population densities (e.g., MacDonald and Bajdik, 1992). An inter-species food competition for cage scallops is also likely, as a large number of naturally growing, filter-feeding ascidians colonized the cage. Accordingly, scallops living on the sediment surface may have had limited access to large amounts of planktonic diatoms, but rather fed on a mixture of detritus and benthic microalgae. After phytoplankton bloom events, the decaying cells sank toward the SWI, where they got ingested by the scallops and triggered the formation of Ba/Ca_{shell} peaks provided that the quantity of cellular Ba together with the cell abundance in the water was sufficient to cause a respective enrichment in the shells.

Although it remains unknown to which extent the various factors (i.e., growth and filtration rates, food availability, resource competition, the spatial distribution of food, and phytoplankton dynamics) contributed to the observed differences in cage and sediment Ba/Ca_{shell} background levels, the findings indicate that *P. maximus* sensitively reacted to changes in their direct environment which subsequently affected the Ba/Ca_{shell} ratios.

4.4.2 Mo/Ca_{shell} profiles

Similar to Ba/Ca_{shell} profiles, the Mo/Ca_{shell} profiles of cage and sediment shells shared a remarkably similar pattern with the PMo/POC data recorded in the water column with three contemporaneous episodes of Mo enrichment (Fig. 4.4). This observation supports the assumption that shell Mo originates from the particulate phase (PMo) (Tabouret et al., 2012; Thébault et al., 2022). However, the magnitude of PMo/POC elevations (e.g., during late April to early May) does not correspond to the patterns measured in the Mo/Ca_{shell} profiles, suggesting that the scallops seem to have incorporated a non-proportionate amount of Mo from the PMo pool. Interestingly, after accounting for filtration (Fig. 4.5A) and shell growth rate, an episode of enhanced Mo concentration in the water ($Mo_{filtered\ seawater}$) was identified for cage shells in late April to early May (Fig. 4.5B), which was not obvious from the original Mo/Ca_{shell} profile (Fig. 4.4). This $Mo_{filtered\ seawater}$ enrichment exhibited very similar levels to that determined for sediment shells in April. Although a temporal offset exists, it can be assumed that the enhanced $Mo_{filtered\ seawater}$ concentrations for both cage and sediment shells were potentially induced by the same external event that occurred in the water column. The short temporal discrepancy between $Mo_{filtered\ seawater}$ of cage and sediment shells during this period (late April to early May) is likely an artifact of uncertainties in the absolute temporal alignment of the geochemical data (especially in growth increments closer to the first winter growth cessation). Furthermore, the approximation of $Mo_{filtered\ seawater}$ indicates that a comparable quantity of Mo was filtered from the ingested water by cage and sediment shells in early July, making the distinctively lower Mo/Ca_{shell} peak magnitudes in cage shells less pronounced (Fig. 4.5B). Following previous observations, Mo/Ca_{shell} peaks in scallops (*P. maximus* and *C. radula*) are associated with transport of Mo-enriched biogenic particles toward the SWI where they got ingested by the bivalves (Thébault et al., 2009a; Barats et al., 2010). More specifically, stressed phytoplankton cells (e.g., due to nutrient limitation, Toullec et al., 2021, or grazing by zooplankton, Toullec et al., 2019) tend to stick together,

forming large particles, such as aggregates (e.g., Alldredge and Gotschalk, 1988; Alldredge and Gotschalk, 1989), which were proposed to sequester Mo from the dissolved phase (Dellwig et al., 2007; Mori et al., 2021) and induce Mo/Ca_{shell} peaks after digestion by the scallops (Thébault et al., 2009a; Thébault et al., 2022). Siebert et al. (V. Siebert unpubl.) identified multiple episodes of aggregate formations in the water column throughout the studied year (Fig. 4.5A, B; gray bars) and concluded that not all aggregation episodes were linked to a significant transport of PMo toward the SWI, but only three aggregation events in June were associated with an enhanced PMo transfer (Fig. 4.5A, B; dark gray bars). Accordingly, the largest Mo/Ca_{shell} peak observed in both sediment and cage shells occurred shortly after those three Mo-associated aggregation episodes (Figs. 4.4, 4.5), substantiating the aforementioned relationship between scallops and potentially ingested aggregates. However, the two remaining Mo/Ca_{shell} enrichments in April and September did not occur contemporaneously with aggregation events (Figs. 4.4, 4.5). Since the phytoplankton genus *Gymnodinium* is naturally enriched in Mo (Ho et al., 2003) and the most dominant dinoflagellate genus of the studied year, a large bloom event may have contributed to an excessive transfer of Mo from the dissolved phase to the particulate phase, which potentially accounted for the large PMo/POC ratio measured in early May (V. Siebert unpubl.). Compelling synchronicity in early May and September existed between the timing and magnitude of blooms of this dinoflagellate taxon (i.e., *Gymnodinium* spp. from the size fraction $< 10\,\mu m$) and the variation of enhanced $Mo_{filtered\ seawater}$ levels estimated for cage and sediment scallops (Fig. 4.5B). This is in agreement with the findings by Fröhlich et al. (2022a) reporting qualitative similarities in the occurrence of small cells ($<20\,\mu m$) of the dinoflagellate *Gymnodinium* spp. and peaks in Mo/Ca_{shell} profiles of scallop shells from three studied years. Aside from the blooms of *Gymnodinium* spp. in early May and September, a third mass occurrence of this dinoflagellate developed in June, shortly before the largest shell Mo enrichment observed in this year (Fig. 4.5B). Similar to Ba/Ca_{shell}, a short time lag of a few days existed between a *Gymnodinium* spp. bloom and a Mo/Ca_{shell} peak (Fröhlich et al., 2022a), but this appears to be negligible given the uncertainties in absolute dating of the shell data and the low temporal resolution of phytoplankton monitoring. Assuming a linear relationship between cell abundance and Mo uptake, the cell concentration of *Gymnodinium* spp. during this bloom would have resembled the approximated $Mo_{filtered\ seawater}$ contents, which was not observed in this study. As described above, it is therefore likely that episodes of aggregate formation observed in June resulted in loads of PMo transported toward the SWI (Dellwig

et al., 2007). Furthermore, the retention of small aggregate particles (Thébault et al., 2022), in addition to the ingestion of Mo-enriched cells of *Gymnodinium* spp., led to an enhanced Mo uptake by the scallops. The contemporaneity of *Gymnodinium* spp. blooms and phytoplankton aggregation may represent an allelopathic relationship (i.e., one organism produced biochemical compounds affecting the growth or survival of another) between dinoflagellates and other phytoplankton taxa. The allelopathic relation may have stressed the phytoplankton in competition with the dominant *Gymnodinium* genus (e.g., Kubanek et al., 2005). Such stress may either induce cell lysis or promote the excretion of large amounts of sticky polymers, both mechanisms triggering the aggregation of phytoplankton cells. The small difference in the $Mo_{\text{filtered seawater}}$ concentration between cage and sediment shells in early July (Fig. 4.5B) could be a result of aggregate particles that sank rapidly toward the SWI and resided shortly in the water column, making them more available to scallops living on the sediment surface. This hypothesis can hardly be validated in the current study because the estimations contain several uncertainties (see Supporting Information) that potentially contributed to differences in the absolute trace element uptake. However, these findings confirm that the patterns in Mo/Ca_{shell} profiles are potentially influenced by phytoplankton dynamics within the water column, where both *Gymnodinium* spp. blooms and aggregation events play a role in Mo/Ca_{shell} peak formation.

Based on the hypothesis that the formation of Mo/Ca_{shell} peaks can be triggered by the ingestion of small *Gymnodinium* spp. cells ($< 10\,\mu m$), the intracellular Mo content of this dinoflagellate was estimated to evaluate if this pathway can provide a sufficient load of PMo to explain respective trace element enrichments in the scallop shells. Unlike most phytoplankton (e.g., Morris and Syrett, 1963; Eppley et al., 1969), this dinoflagellate is inferred to potentially use nitrate instead of ammonium for nitrogen assimilation (Yamamoto et al., 2004). The utilization of nitrate requires the synthesis of the Mo-containing enzyme nitrate reductase (Collier, 1985; Marino et al., 2003), which could be the cause for the enhanced Mo content observed in *Gymnodinium* cells (Fröhlich et al., 2022a). Ho et al. (2003) determined the element ratios of Mo and carbon (C), both normalized to phosphorus (P), in the dinoflagellate species *Gymnodinium chlorophorum*, suggesting a molar Mo/C ratio of $0.8\,mmol\,mol^{-1}$ (using Mo/P of $0.11\,mol\,mol^{-1}$ and C/P of $137\,mol\,mol^{-1}$). An empirical relationship between carbon content and cell volume was defined for dinoflagellates ($pg\,C\,cell^{-1} = 0.216 \times volume^{0.939}$; Menden-Deuer and Lessard, 2000), where the cell volume can be estimated by a geometric model for *Gymnodinium* cells (Fig. 4.5C; Hillebrand et al., 1999; Sun and

Liu, 2003). These features allowed to estimate the range of absolute cellular Mo content at various possibilities in the shape of *Gymnodinium* cells (i.e., length, diameter d1 and d2; Fig. 4.5C). Considering that the total pool of *Gymnodinium* cells within each liter of filtered seawater was retained by the scallops, a cellular Mo load of 17.5 fg cell^{-1} (Fig. 4.5C; green 100% graph) was calculated (e.g., 0.4 ng Mo L^{-1} of filtered water at 22,880 cells L^{-1} in early May; Fig. 4.5B). Based on the above-described cell geometry-to-Mo content relationship, the *Gymnodinium* cell volumes would have been about 14.7 µm^3, considering a cell length of 7 µm and a diameter of 2 µm for d1 and d2 (Fig. 4.5C), which agrees with the observed phytoplankton in this study (a length of < 10 µm of the recorded *Gymnodinium* spp. cells). Given that many species of *Gymnodinium* have been reported toxic and could hamper shell growth in bivalves (Widdows et al., 1979; Chauvaud et al., 2001), cells of *Gymnodinium* are likely not the preferred diet of *P. maximus* and only ingested by smaller amounts. In fact, a reduction in growth rate was observed for sediment scallops during the first large *Gymnodinium* bloom in early May (Supporting Information Fig. S4.3). Therefore, a scenario in which only 5% of the total *Gymnodinium* spp. cells were ingested (i.e., corresponding to a cell concentration as low as 1144 cells L^{-1} in early May) is likely, which would result in a cellular Mo load of up to 349.7 fg cell^{-1} to account for the estimated $Mo_{filtered\ seawater}$ requirement of 0.4 ng Mo L^{-1} for the cage and sediment shells (in early May). Interestingly, even this high cellular Mo content can be contained in *Gymnodinium* cells with a length and diameter not exceeding 10 µm (e.g., at a length of 8.4 and 9 µm in diameter d1 and d2; Fig. 4.5C; green 5% graph). In other words, the ingestion of cells of only a very small portion (<5%) of the total *Gymnodinium* spp. (<10 µm) pool provided a sufficient concentration of $Mo_{filtered\ seawater}$ to induce the formation of the Mo/Ca_{shell} peaks in the cage and sediment shells. Although these calculations were based on multiple assumptions, this line of evidence supports that a potential link exists between the dinoflagellate genus *Gymnodinium* and Mo/Ca_{shell} peaks. Despite the fact that ammonium assimilating diatoms leading to the formation of Ba/Ca_{shell} peaks are assumed to contain only low amounts of cellular Mo (repressed synthesis of the Mo-containing enzyme nitrate reductase), such diatom blooms could have eventually contributed slightly to the large Mo/Ca_{shell} peak during summer. To investigate the impact of various phytoplankton taxa cultivated using different nitrogen sources on the Mo content in scallop shells, future studies should incorporate feeding experiments. These experiments will provide valuable insights into the relationship between phytoplankton composition and nitrogen sources in relation to Mo accumulation in scallop shells.

Despite small differences observed in the Mo/Ca_{shell} background levels (Fig. 4.1B), after accounting for growth and filtration rates (Fig. 4.5A), the $Mo_{filtered\ seawater}$ concentration revealed closely similar levels between cage and sediment shells outside Mo enrichment episodes (Fig. 4.5B). Compared to the significant deviations in the Ba/Ca_{shell} background levels that can be explained by small differences in the ambient environment of the scallops, the more similar Mo requirements in cage and sediment shells suggest that such small environmental variations did not affect Mo/Ca_{shell} background levels. Instead, only during distinct events in the water column (e.g., aggregation episodes and/or large dinoflagellate blooms), enhanced loads of Mo enter the scallops and lead to the formation of Mo/Ca_{shell} peaks. This is in agreement with previous findings showing that the digestive gland is the most Mo-enriched organ (about 69% of the total shell Mo content; Barats et al., 2010; Thébault et al., 2022) and that variations of dissolved Mo in seawater contribute insignificantly to the Mo/Ca_{shell} profiles (Barats et al., 2010; Tabouret et al., 2012).

4.4.3 Li/Ca_{shell} profiles

Unlike past Li/Ca_{shell} chronologies of *P. maximus*, respective profiles of cage and sediment specimens in the present study did not show large and distinct peaks (e.g., a Li/Ca_{shell} peak off approximately $159\,\mu mol\,mol^{-1}$ was measured in scallops by Thébault et al., 2022). However, two small Li/Ca_{shell} enrichments in August and September occurred contemporaneously in cage and sediment shells (Fig. 4.6). These Li enrichments were even more pronounced when converted to an absolute daily Li incorporation rate (Supporting Information Fig. S4.9), using the relationship between daily shell growth rates and the Li/Ca_{shell} background (Thébault and Chauvaud, 2013) together with the daily Ca precipitation rate (Supporting Information Fig. S4.2). This indicates a common environmental forcing acting upon Li incorporation into the shells. It was previously hypothesized that Li from the dissolved phase is removed by the production of biogenic opal (Coplen et al., 2002) in diatom frustules that can lead to the transport of large quantities of Li toward the SWI, triggering the formation of Li/Ca_{shell} peaks in scallops (Thébault and Chauvaud, 2013; Thébault et al., 2022). The large diatom blooms in early June and mid-September (Fig. 4.2) occurred contemporaneously with increased PLi/POC levels in bottom waters, while increased PLi/POC values were only detected at the surface water in mid-September (Fig. 4.6). The latter PLi/POC event (September) also coincided with a Li/Ca_{shell} enrichment, corroborating a

link between diatom abundance and shell Li enrichments. However, no respective Li/Ca_{shell} peak occurred in June after the formation of the largest diatom bloom (Fig. 4.2). A possible explanation for the absence of a respective Li/Ca_{shell} enrichment in early June is that either particulate Li was associated with a diatom species that was not ingested by the scallops or another process was involved that caused the recorded peak in PLi/POC at the SWI, such as the resuspension of Li-enriched sediment particles (Tardy et al., 1972) that were not filtered and retained by the scallops. Alternatively, Thébault et al. (2022) demonstrated that after large diatom blooms, the recycling of biogenic silica at the SWI also releases frustule-associated Li into the ambient water, causing distinct Li/Ca_{shell} peaks in scallops. The lack of a Li/Ca_{shell} peak following the large diatom bloom in June could potentially be linked to the observation that a large number of epifaunal brittlestars, *Ophiocomina nigra*, colonized the seabed. This omnivorous echinoderm species could have consumed most of the organic-enriched particles at the SWI, including deposited diatom frustules, which, in turn, prohibited the dissolution of Li into the water column. Unfortunately, no environmental monitoring data are available for August during the formation of the first small Li/Ca_{shell} enrichment to further constrain these links.

Another proposed hypothesis describes a potential relationship between the diatom genus *Pseudo-nitzschia* spp. and the formation of transient Li/Ca_{shell} peaks in *Pecten maximus* (Thébault and Chauvaud, 2013; Fröhlich et al., 2022a). Under stressful conditions, such as nutrient limitations and/or enhanced predatory activity by zooplankton (Pan et al., 1996; Bates et al., 2018), *Pseudo-nitzschia* spp. cells produce the neurotoxin domoic acid which requires the presence of intracellular Li (Subba Rao et al., 1998). The ingestion of those cells by scallops can lead to elevated Li/Ca_{shell} levels. In the studied year, several *Pseudo-nitzschia* spp. blooms were recorded (Fig. 4.6), including large blooms in June, at the end of July (i.e., the most abundant diatom genus; Fig. 4.2), and in September. However, only during the end of July high concentrations of pheophytin pigments (an indicator for increased predation activity of zooplankton; Lorenzen, 1967) were observed at the beginning of the development of a *Pseudo-nitzschia* spp. bloom (Fig. 4.6), generating conditions for this diatom to produce the Li-associated neurotoxin. Considering a short time lag between the timing of the diatom bloom and the formation of Li/Ca_{shell} enrichments (cf. Fröhlich et al., 2022a), this pathway seems to provide a possible explanation for the Li enrichment in cage and sediment shells in August. A similar pattern occurred in September, during the presence of elevated pheophytin levels ($2\,\mu g\,L^{-1}$) and the development of a *Pseudo-nitzschia* spp. bloom (Fig. 4.6). This may

have induced the formation of the second episode of elevated Li/Ca_{shell}. However, as blooms of this diatom also occurred prior to the two Li/Ca_{shell} enrichment episodes (i.e., in April and June) at slightly increased pheophytin pigment concentrations (Fig. 4.6), the absence of respective trace element peaks in the scallop shells argues against the proposed link. The observed discrepancies may be explained by a species-specific filtration of scallops because these blooms were composed of different *Pseudo-nitzschia* species.

The exact uptake mechanisms of Li from the water column to the incorporation into the scallop shells need to be further validated by a longer time-series of Li/Ca_{shell} and environmental records. Nonetheless, the hypotheses of Li formation in scallop shells discussed in this study may also apply to the formation of larger, distinct Li/Ca_{shell} peaks (e.g., Thébault et al., 2022), making Li/Ca_{shell} chronologies a geochemical proxy for recording short-term changes in the water column. A reliable estimation of the absolute amount of Li filtered from the water (like $Ba_{filtered\ seawater}$ and $Mo_{filtered\ seawater}$) could not be performed because no information about the relative distribution of this trace element in soft tissue and the shell was available. However, when considering differences in the volume of filtered seawater between cage and sediment specimens (Supporting Information Fig. S4.7), it can be estimated that scallops from the sediment filtered seawater that contained about 36% less Li relative to cage scallops during the Li enrichments in August and September (Supporting Information Fig. S4.9). Accordingly, Li potentially derived from planktonic particles which might have been more accessible to the cage scallops, analogous to the observation of the enhanced ingestion of Ba-enriched phytoplankton for cage shells.

4.5 Summary and conclusions

Shell Ba/Ca and Mo/Ca profiles of *P. maximus* differed among specimens grown on the seafloor and in a cage 1 m above the sediment-water interface. A close link existed between elements bound to organic particles in the water column and Ba/Ca_{shell} and Mo/Ca_{shell} data, supporting previously proposed hypotheses on the trophic uptake of those elements by scallops. Computing the trace element concentrations in the seawater filtered by the scallops using a novel model that combines element-to-calcium ratios with physiological parameters such as shell height, growth rates, and filtration rates showed that the theoretical filtered Ba and Mo loads in the seawater were nearly identical between sediment and cage scallops during Ba/Ca_{shell} and Mo/Ca_{shell} peak formation. The observed geochemical differences were rather

related to growth conditions than different food or water conditions. The approximations obtained from the MC simulations indicated that the timing and magnitude of Ba/Ca_{shell} peaks can be quantitatively modeled by blooms of specific diatom species containing different amounts of cellular Ba. The Mo/Ca_{shell} profiles appeared to be related to the timing of Mo-enriched dinoflagellate species (*Gymnodinium* spp.) as well as to the occurrence of aggregate-forming diatoms transporting particulate Mo toward the SWI. Li/Ca_{shell} profiles did not show distinct peaks. However, two small Li enrichments occurred in all studied shells contemporaneously with elevated particulate Li concentration in the water, supporting assumptions according to which Li is derived not only from the dissolved phase but also from the particulate fraction. These findings add new insights into uptake mechanisms of Ba, Mo, and Li from the seawater into the shells of scallops, allowing further refined Ba/Ca_{shell}, Mo/Ca_{shell}, and Li/Ca_{shell} ratios as proxies for short-term phytoplankton dynamics. However, future studies should focus on the geochemical records of Li/Ca_{shell} ratios before considering their application as a potential phytoplankton proxy. As demonstrated herein, the strong influence of specimen-specific physiological parameters (filtration rate, growth rate, and shell height) on shell chemistry highlights the necessity to adjust element chemical data before they can serve as quantitative paleoenvironment proxies. Since each element alone suggests to be a potential indicator for phytoplankton dynamics, future studies might also focus on determining whether the combination of all three elements in a multi-proxy approach can be effective and what additional information about marine biogeochemical cycles can be derived from it.

4.6 Supporting Information

4.6.1 LA-ICP-MS analysis

Separated portions of the *P. maximus* shells were measured for their Ba, Mo and Li (^{137}Ba, ^{97}Mo and ^{7}Li as analytes) content by means of a Laser Ablation-Inductively Coupled Plasma-Mass Spectrometry (LA-ICP-MS) system (Max Planck Institute for Chemistry in Mainz, Germany). To fit the shell samples into the ablation chamber of the laser system, an approx. 5 mm broad slab was cut from the left valves along the axis of maximum growth using a 150 µm-thin, diamond coated (galvanically bonded) disk (Art.–Number: 6911H.-104.220, Komet – Dental Gebr. Brasseler GmbH & Co. KG) connected to a manual drilling device. Measurements were accomplished between two radial ribs. The focus was placed on the portion between the first winter growth mark and the last formed growth increment (ventral margin; Fig. S4.1). Prior to the in-situ chemical analysis, shell slabs were immersed in 10 vol% acetic acid for ca. 1 min and ultrasonically cleaned with deionized water for about 3 min. This procedure removed sediments and epibionts that were trapped within the surface sculpture of the scallop shells. In addition, the laser performed a pre-ablation procedure (line scan) to avoid potential surface contamination by ablating at a speed of 80 µm s^{-1} with a laser spot size of 100 µm. Measurements were conducted in line scan mode (length of 600 µm) at a constant speed of 5 µm s^{-1} and a spot size of 80 µm on the outer surface of the shell, perpendicular to the direction of growth. Signal intensities measured from each scan were averaged because a homogeneous distribution of the studied elements within individual striae has been demonstrated (Barats et al., 2007). The daily periodicity of shell formation (Chauvaud et al., 1998; Lorrain et al., 2000) allowed to extract elemental time-series with a temporal resolution from one to two day days.

The laser system (NewWave Research UP-213 Nd:YAG laser) operated at a repetition rate of 10 Hz and a laser energy density of approx. 15.8 J cm^{-2}, using helium (quality 5.0) as a carrier gas (0.57 L min^{-1}). With a Thermo Fisher Element 2 single collector sector-field ICP-MS system, the ion intensities were measured after each ablation, with argon (quality 5.0) as a carrier gas (0.77 L min^{-1}). To calibrate the obtained raw signals, a synthetic silicate glass (NIST SRM 612) was used as an external standard, ^{43}Ca as an internal standard and a pressed carbonate powder pellet (USGS MACS-3) was analyzed as blind sample to account for quality control. Reference materials were analyzed similar to the shell samples (i.e., in

a line scan mode using similar laser system settings) and reference values derived from the GeoReM database (version 33; http://georem.mpch-mainz.gwdg.de/; last access: 16 August 2022; Jochum et al., 2011).

An in-house script (C++) was used to process raw signal intensities following the equations provided by Longerich et al. (1996) and Jochum et al. (2007; 2011) and convert them into element-to-calcium ratios such as Ba/Ca_{shell}, Mo/Ca_{shell} and Li/Ca_{shell} (in $\mu mol\,mol^{-1}$). Based on the 3σ criterion, the limits of detection (LOD) were calculated from the blank signal of the calibration material (NIST SRM 612) obtained from 15 s before the laser started to ablate. Values below average LODs (Table S4.1) were discarded. To account for a potential time-dependent machine drift, each sequence was processed following a batchwise calibration. Thus, a batch of shell and quality control samples was calibrated using repeated measurements of reference materials (NIST SRM 612). Based on these replicate measurements of the external reference material, the relative standard deviation in percent (RSD%) was calculated to report the reproducibility for each measurement. For Ba, Mo and Li, the average RSD% was 1.2%, 1.3% and 1.2%, respectively (Table S4.1). The blindly measured quality control material (USGS MACS-3) was used to account for accuracy with average deviations from the reference values of 6% for Ba and Mo, and 17% for Li. These deviations (Table S4.1) are potentially induced by an uneven ablation behavior of the pressed synthetic carbonate powder pellet (heterogeneity of particle sizes) which can lead to ionization differences and/or uncertainties in reported values of the non-certified quality control material (Jochum et al., 2019).

4.6.2 Temporal contextualization of measured shell data

The outer shell surface was photographed with a Canon EOS 600 DSLR camera mounted to a binocular microscope (Wild Heerbrugg) equipped with sectoral dark field illumination (Schott VisiLED MC 1000, reflected light). Photographs were used to measure pixel-distances between successive microgrowth lines (daily striae) and converted into µm-distance (reported in $\mu m\,day^{-1}$). Since the specimens were collected alive, the last growth increment at the ventral margin corresponds to the date of death allowing to assign precise calendar dates to each shell portion. However, the identification of individual striae was not always unambiguous (see Thébault et al., 2006; Thébault et al., 2009a) because of fractures that mainly occurred at the ventral margin. This led to uncertainties in the shell growth reading

procedure and to inter-reader differences. To account for these discrepancies, the growth curves of multiple specimens were crossdated to form an average chronology which was used to temporally constrain the growth record. In this study, six specimens from the cage and six specimens from the sediment were used for growth pattern analysis (Table S4.1). Since elemental analyses were conducted on the outer shell surface, each LA-ICP-MS scan could be visually associated with a specific growth increment and thus assigned to a calendar date.

4.6.3 Environmental monitoring

Water samples (250 mL) from approx. 1.5 m below the sea surface were analyzed for their phytoplankton content. After biweekly water collection, the samples were transferred into silicon tubes and 8 mL of Lugol's solution was added to fix the phytoplankton cells. The phytoplankton content from a 50 mL aliquot was then analyzed (identification and cell counting) with an inverted microscope (Axio Observer.A1-ZEISS) after the cells sedimented on a glass slide for about 24 h. The samples for analyzing particulate Ba (PBa), Mo (PMo) and Li (PLi) content were collected from the surface water (approx. 1 m below sea surface) and from the bottom water (approx. 0.20 m above the SWI). Samples were obtained by SCUBA diving twice per week between March and June and once per week from July to October. The water was filtered (using MF-Millipore^{TM} mixed cellulose ester filter, mesh size 0.45 µm) and the particulate trace element content was analyzed by means of ICP-MS (inductively coupled plasma mass spectrometry; Thermo Scientific Quad XSeries 2). In addition, the filtered fraction of the water samples (using Whatman GF/F filters; mesh size 0.7 µm) were dried at 50 C °C and analyzed for their particulate organic carbon (POC) content using a CHN elemental analyzer (Thermo Fisher Flash 2000). The pheophytin pigment concentrations were calculated based on the method described by Lorenzen (1966). A detailed description about the entire environmental monitoring is provided by Siebert et al. (2023).

4.6.4 Relationship between phytoplankton-associated trace element load, shell physiology and shell geochemistry to approximate the trace element uptake by scallops

Episodes of trace element enrichments in scallop shells (i.e., Ba/Ca_{shell}, Mo/Ca_{shell} and Li/Ca_{shell}) were demonstrably related to phytoplankton dynamics occurring in the water col-

umn (see discussion in the main text). For instance, the timing and magnitude of Ba/Ca_{shell} peaks were attributed to blooms of various phytoplankton species (mainly diatoms) that contain species-specific amounts of cellular Ba. Based on this underlying assumption, the amount of diatom-associated Ba in the seawater is controlled by the abundance of a given diatom species (cell concentration) and the Ba load contained in each cell (Fig. S4.2; Step 1 and 2). The daily shell growth rate measured on the shell surface (Fig. S4.2; Step 3) can be converted into total daily shell height (ht_{shell}; in mm; Fig. S4.2; Step 4) allowing to estimate the soft tissue dry weight ($wt_{soft\,tissue}$; in g) according to the allometric relationship:

$$wt_{soft\,tissue} = 2.974 \times 10^{-7} \times ht_{shell}^{3.817} \tag{4.1}$$

provided by Lorrain et al. (2004). Additionally, the soft tissue dry weight (Fig. S4.2; Step 5) can be used to approximate the filtration rate at each day (Fig. S4.2; Step 6), according to the weight standardized filtration rate of $5\,L\,h^{-1}\,g^{-1}$ of soft tissue dry weight (value discussed in the main text). On a theoretical basis, the amount of Ba that is ingested by a scallop at each day (Fig. S4.2; Step 7) can then be deduced using the amount of water that was filtered per day and the diatom-associated Ba concentration in the seawater (Fig. S4.2; Step 2), assuming that the total pool of diatoms in each liter is retained and digested by the bivalve. Aside from the soft tissue dry weight, the shell weight (wt_{shell}; in g) can also be determined given the allometric relationship to shell height (Lorrain et al., 2004):

$$wt_{shell} = 4.09 \times 10^{-4} \times ht_{shell}^{2.701} \tag{4.2}$$

This information about the shell weight (Fig. S4.2; Step 8) is required to compute the absolute amount of Ca that got precipitated at each day (Fig. S4.2; Step 9). Given that the shell material is composed of calcium carbonate ($CaCO_3$) as well as a small amount of carbonate bound organic matter ($< 5\,wt\%$), a pure Ca content of 38 wt% can be assumed which is in agreement with previous Ca measurements on bivalve shells (Richard, 2009; Marali et al., 2017). Accordingly, the Ca precipitation rate ($Ca_{prec.}$; in $g\,day^{-1}$) is calculated as:

$$Ca_{prec.} = \left[wt_{shell(d)} - wt_{shell(d-1)}\right] \times 0.38 \tag{4.3}$$

i.e., the Ca-proportion of the shell material deposited between two consecutive days (i.e.,

$wt_{shell(d)}$ and $wt_{shell(d-1)}$). Considering that about 63% of the total Ba content of scallops (soft tissues plus shell) is located in the shell (Barats, 2006), the amount of Ba incorporated into the shell material during each day (Fig. S4.1; Step 10) can be approximated from the totally ingested Ba (Fig. S4.2; Step 7). In combination with the daily precipitated amount of Ca (Fig. S4.2; Step 9), the Ba/Ca_{shell} weight ratios (Fig. S4.2; Step 11) as well as the molar ratios (Fig. S4.2; Step 12) can be calculated. Finally, the theoretically measured Ba/Ca_{shell} profile can be obtained taking into consideration that apart from the Ba in the particulate phase, the dissolved Ba also contributed to the Ba/Ca_{shell} background. This Ba/Ca_{shell} background signal can be approximated from the dissolved Ba/Ca ratio in the seawater ($Ba/Ca_{seawater}$) and a previously determined partition coefficient (D_{Ba}) of 0.11 (Barats et al., 2009):

$$Ba/Ca_{shell} = D_{Ba} \times Ba/Ca_{seawater} \tag{4.4}$$

Note that these steps are based on the presumption that the geochemical information measured on the shell surface of a specific shell portion is representative of the entire, contemporaneously formed shell material.

In this study, the above-described dependencies between growth rate, filtration rate and available Ba in the environment and their effect on Ba/Ca_{shell} data were used to reconstruct the theoretical amount of Ba that was potentially associated with Ba-containing phytoplankton in the water filtered by the scallops. Specifically, in a first step, the Ba/Ca_{shell} background level was subtracted from the Ba/Ca_{shell} profile (Fig. S4.2; Step 13 to 12), to remove the influence from the dissolved Ba content in the seawater. Then, the molar ratios were converted to weight ratios (Fig. S4.2; Step 11) and combined with the amount of precipitated Ca (Fig. S4.2; Step 9) to obtain an estimate about the absolute amount of Ba that was incorporated into the shell each day (Fig. S4.2; Step 10) and into the bivalve including soft tissues (Fig. S4.2; Step 7), which was considered to be equal to the total amount of Ba taken up by the scallop from the particulate seawater fraction at each day. This amount of Ba was then used together with the volume of daily filtered seawater (Fig. S4.2; Step 6) to gain an approximation of the particulate Ba content (i.e., phytoplankton associated) that was present in the filtered seawater ($Ba_{\text{filtered seawater}}$; Fig. S4.2; Step 2). For the Mo/Ca_{shell} profiles, a similar approach was used to approximate the daily Mo incorporation and $Mo_{\text{filtered seawater}}$ content, using different Mo/Ca_{shell} background estimations ($D_{Mo} = 1.5 \times 10^{-4}$ Barats et al., 2010) and

a relative Mo distribution into the shell material of 27% (value derived from Barats, 2006). Absolute Li incorporation rates were not calculated from the Li/Ca_{shell} profiles as important information on the relative Li distribution among the soft tissues and shell material was not available.

4.6.5 Statistics

To statistically evaluate differences between the average shell growth patterns of cage and sediment specimens, a two-way factorial analysis of variance (i.e., two-way ANOVA test) was used. Sample site (cage vs sediment) and the timing of shell growth (comparison of monthly pooled growth rates; May to September) were considered as orthogonal and fixed factors. Shapiro–Wilk tests were performed to satisfy the underlying assumption of normally distributed data, and Bartlett tests were used to check for the homogeneity of variance. Finally, a Tukey's post-hoc test identified which specific groups were significantly different. The average trace element-to-calcium chronologies were analyzed for statistical differences in the background levels (Ba/Ca_{shell} and Mo/Ca_{shell}) or mean profiles (Li/Ca_{shell}) between cage and sediment specimens. Therefore, episodes of pronounced Ba/Ca_{shell} and Mo/Ca_{shell} peaks, defined as any period longer than one week with values exceeding the median, were approximately delineated from the background signal. The trace element-to-calcium profiles were evaluated using the non-parametric Kruskal–Wallis test due to the lack of normality and homogeneity. All statistical analyses were performed using the programming language Python (version 3.7.4).

4.6.6 Growth rates of sediment and cage shells

According to growth pattern analysis, the main growing season of sediment scallops started in early March (Fig. S4.3). In cage shells, epibionts made the reliable identification of striae formed between early March and mid-April impossible. Between March and April, sediment shells grew from 70 to 175 µm day^{-1} with increasing rates until mid-April. High growth rates of about 190 µm day^{-1} at the end of April were measured for cage shells. At the beginning of May, growth rates in cage shells remained high (up to 240 µm day^{-1}), while a growth rate reduction was observed in contemporaneous specimens from the sediment (<140 µm day^{-1} in early May). Growth rates in sediment shells progressively increased until July, reaching a maximum of 220 µm day^{-1}, and slowly decreased until early October.

Cage shells experienced a reduction in growth rate at the end of May (reaching 170 µm day^{-1}) followed by a steady increase until mid-July (up to 267 µm day^{-1}) and a moderate decline until October. Testing for statistical differences in growth rates between sediment and cage shells for the months from May to September (Fig. S4.3; Table S4.2 and S4.3) indicated that the position (i.e., sediment surface or 1 m above the substrate) as well as the timing of growth caused a significant difference in growth (ANOVA: $F = 14.26$, $df = 4$, $p < 0.001$). Furthermore, the growth rates between May and August were significantly different between cage and sediment shells (Tukey multiple comparison test, $p < 0.001$). Accordingly, shells grown 1 m above the SWI grew faster (except in September) compared to shells that lived on the sediment surface (Fig. S4.3).

4.6.7 Uncertainties in the trace element-related estimations

The model used to back-calculate $Ba_{\text{filtered seawater}}$, $Mo_{\text{filtered seawater}}$, and total Li incorporation rates as well as the amount of cellular Ba and Mo in specific phytoplankton taxa (see Fig. S4.2), was based on the following presumptions that might have affected the final results. (1) The amount of daily filtered seawater was calculated using the shell height-to-soft tissue dry weight relationship proposed by Lorrain et al. (2004) and the assumption of a relative filtration rate of about 5 L h^{-1} g^{-1} of soft tissue dry weight, which is in the range previously determined for bay scallops (Palmer, 1980) and juvenile king scallops at optimal temperature settings (Laing, 2004). For simplification, the relative filtration rate was assumed to be constant throughout the year despite potential influences of temperatures as well as food particle density and quality on the filtration rate of the scallops (Laing, 2004). For instance, at very low seston conditions (i.e., chlorophyll *a* concentration below 0.88 µg L^{-1}) the filtration rate in *P. maximus* was shown to reach 12 L h^{-1} g^{-1} (Strohmeier et al., 2009), more than twice the rate that was considered herein. Note, according to a higher filtration scenario of scallops, the estimated cellular Ba contents for the selected diatom species would notably decrease, e.g., a maximum of 221 fg Ba cell^{-1} was calculated at a filtration rate of 5 L h^{-1} g^{-1} compared to 92 fg Ba cell^{-1} at 12 L h^{-1} g^{-1} for the diatom species *C. socialis* (scenario 1; Fig. S4.6C). (2) Using the described relationship between the dissolved Ba/Ca and Mo/Ca ratio in the surrounding media and the Ba/Ca_{shell} and Mo/Ca_{shell} background (Gillikin et al., 2006; Gillikin et al., 2008; Barats et al., 2009; Barats et al., 2010), the influence of the dissolved phase was estimated considering constant Ba and Mo partition coefficients. As

the dissolved Ba/Ca and Mo/Ca ratios in the seawater (Fig. S4.10) were assumed to be vertically homogenous within the range of 1 m (distance between sediment and cage), the estimated background signal was subtracted from the measured Ba/Ca_{shell} and Mo/Ca_{shell} profiles for both cage and sediment shells. However, the temporal variation and biological influence onto the partition coefficients remain uncertain, as the values were obtained from different years and small differences in reported partition coefficients exists between studies (e.g., Gillikin et al., 2008; Barats et al., 2010; Tabouret et al., 2012). (3) The species-specific amount of cellular Ba and Mo in phytoplankton was considered stable and potential environmental influences such as pH or Fe concentration in the seawater that can affect the Ba adsorption onto diatoms (Sternberg et al., 2005) were not included. (4) It was assumed that the distribution of the totally ingested Ba and Mo pool that ended up in the shell relative to the soft tissues remained constant during shell growth. (5) To approximate the cellular Ba contents of diatoms, the total amount of phytoplankton cells per liter of filtered seawater (measured in the water column) was expected to be retained and ingested by the scallops, without considering species-specific feeding preferences.

Although these uncertainties likely contributed to deviations from actual trace element loads that were taken up by the scallops and/or associated with individual phytoplankton cells, the calculations corroborate previously hypothesized uptake mechanisms. In the case of Ba and Mo, a sufficient amount of those trace elements was available for the scallops to induce the formation of Ba/Ca_{shell} peaks and Mo/Ca_{shell} peaks in the studied year. Moreover, the calculations demonstrated that physiological parameters of the bivalve can strongly affect the element-to-calcium ratios in its shell, which need to be considered when using trace element profiles as quantitative proxies.

Table S4.1 Information about 12 *Pecten maximus* specimens analyzed in this study. 'Habitat' specifies if a specimen lived in a cage (1 m above the sediment) or directly on the sediment surface. Three cage-lived samples (Shell A-C) were analyzed for their barium, molybdenum and lithium contents using 'LA-ICP-MS' and three shells from the sediment (Shell D-F). All additional shells were solely used for growth readings ('GR') in order to generate robust averaged growth curves from shells collected from the cage ($n = 6$) and the sediment($n = 6$). Average limits of detection were about 0.03 µmol mol^{-1} for Ba/Ca$_{shell}$, 0.01 µmol mol^{-1} for Mo/Ca$_{shell}$ and 3.17 µmol mol^{-1} for Li/Ca$_{shell}$. Relative standard deviation in percent ('RSD') were calculated from measurements of the certified reference material NIST SRM 612. The pressed carbonate powder pellet USGS MACS-3 was used as a quality control material and obtained values were compared with published values (59.6 µg g^{-1} for Ba, 1.21 µg g^{-1} for Mo and 62.9 µg g^{-1} Li; GeoReM database).

Sample ID	Date of collection	Habitat	Analyses	Ba/Ca$_{shell}$		Mo/Ca$_{shell}$		Li/Ca$_{shell}$	
				RSD (%)	MACS3 (µg g^{-1})	RSD (%)	MACS3 (µg g^{-1})	RSD (%)	MACS3 (µg g^{-1})
Shell A	14.10.2021	Cage	GR + LA–ICP–MS	0.7	58.0 ± 5.4	0.7	1.2 ± 0.1	1.2	52.3 ± 4.2
Shell B	04.10.2021	Cage	GR + LA–ICP–MS	1.7	55.3 ± 0.9	2.1	1.3 ± 0.1	1.8	53.1 ± 1.6
Shell C	14.10.2021	Cage	GR + LA–ICP–MS	1.1	55.1 ± 4.7	1.1	1.3 ± 0.2	0.4	54.9 ± 3.6
Shell 1	04.10.2021	Cage	GR	—	—	—	—	—	—
Shell 2	04.10.2021	Cage	GR	—	—	—	—	—	—
Shell 3	04.10.2021	Cage	GR	—	—	—	—	—	—
Shell D	04.10.2021	Sed.	GR + LA–ICP–MS	0.9	55.8 ± 1.7	1.0	1.4 ± 0.2	0.9	52.3 ± 4.2
Shell E	11.10.2021	Sed.	GR + LA–ICP–MS	1.2	55.4 ± 1.6	1.9	1.2 ± 0.1	1.4	52.3 ± 4.2
Shell F	04.10.2021	Sed.	GR + LA–ICP–MS	1.3	55.6 ± 2.2	1.2	1.2 ± 0.1	1.4	52.3 ± 4.2
Shell 4	04.10.2021	Sed.	GR	—	—	—	—	—	—
Shell 5	11.10.2021	Sed.	GR	—	—	—	—	—	—
Shell 6	11.10.2021	Sed.	GR	—	—	—	—	—	—

Table S4.2 Monthly Shapiro–Wilk test results to check for normality distribution of average shell growth data obtained from cage and sediment shells. Month-wise Bartlett's test for diagnosing homoscedasticity between cage and sediment shells.

Month (2021)	Shapiro–Wilk test Cage shells		Shapiro–Wilk test Sediment shells		Bartlett test Cage vs Sediment
	Statistic	p	Statistic	p	p
May	0.97	0.59	0.96	0.28	0.43
June	0.94	0.09	0.97	0.56	0.11
July	0.96	0.28	0.95	0.12	0.51
August	0.99	0.95	0.97	0.58	0.82
September	0.97	0.58	0.97	0.54	0.80

Table S4.3 Two-way ANOVA test results. 'Month' accounts for temporal influence, i.e., monthly (May–September) differences, and 'Location' denotes for differences in growth rates between cage and sediment living shells.

Factor	Degrees of freedom (df)	Sum of squares	Mean squares	F	p
Month	4	60490.13	15122.53	50.04	4.03×10^{-32}
Location	1	51827.21	51827.21	171.50	3.34×10^{-31}
Month:Location	4	17232.85	4308.21	14.26	1.19×10^{-10}
Residual	295	89147.32	302.19	—	—

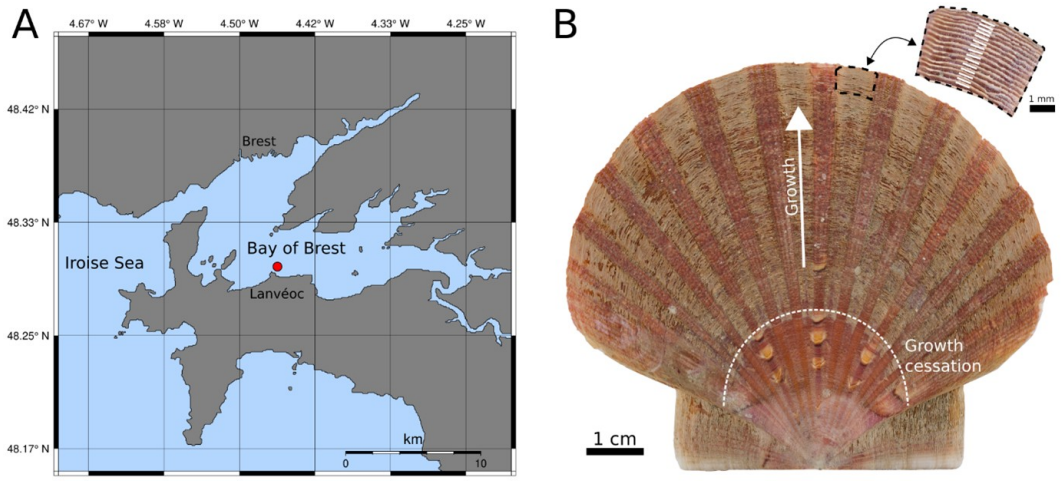

Figure S4.1 Map showing the Bay of Brest (northwest France) and location where the scallop specimens were hatched and collected (red circle; Pointe de Lanvéoc) (**A**). Left valve of a *P. maximus* specimen (prior to the removal of overlapping calcitic striae) and magnification of a shell portion close to the ventral margin (after removing overlapping striae) with white lines (magnified shell portion) indicating how individual LA-ICP-MS scans were positioned on the shell surface (**B**).

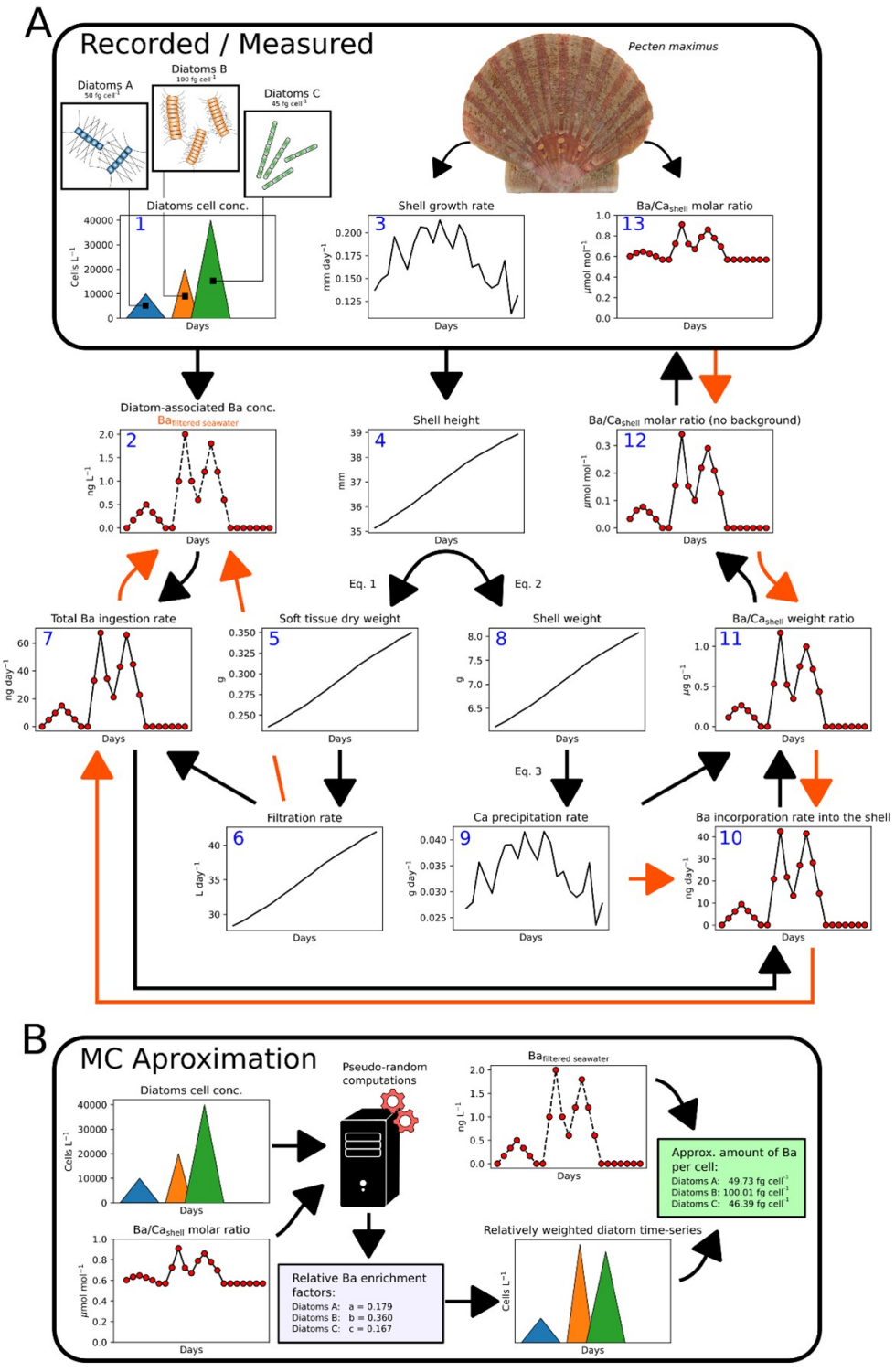

Figure S4.2 Simplified example of the hypothesized relationship between diatom-

Figure S4.2 (continued) associated Ba (three diatom species in this example) and measured Ba/Ca_{shell} profiles, modified after and based on the calculations proposed by Thébault et al. (2009a). Black arrows in **A** depict the connection and contribution from cellular Ba in diatoms to the obtained Ba/Ca_{shell} profiles. Orange arrows in **A** illustrate the steps performed to approximate the total uptake of Ba by the scallops and the amount of diatom-associated Ba in the filtered seawater from the measured Ba/Ca_{shell} profile. **B** illustrates how the Monte Carlo (MC) method (described in Fröhlich et al., 2022a) was included to estimate the cellular Ba content of individual diatom species, i.e., approximating the Ba/Ca_{shell} profiles by iteratively testing a large number of pseudo-randomly generated weighting factors. These species-specific weighting factors served as an indication of the relative Ba enrichment associated with each diatom species. This information was used together with the previously estimated $Ba_{filtered\ seawater}$ (**A**) to compute absolute cellular Ba concentrations of each diatom species.

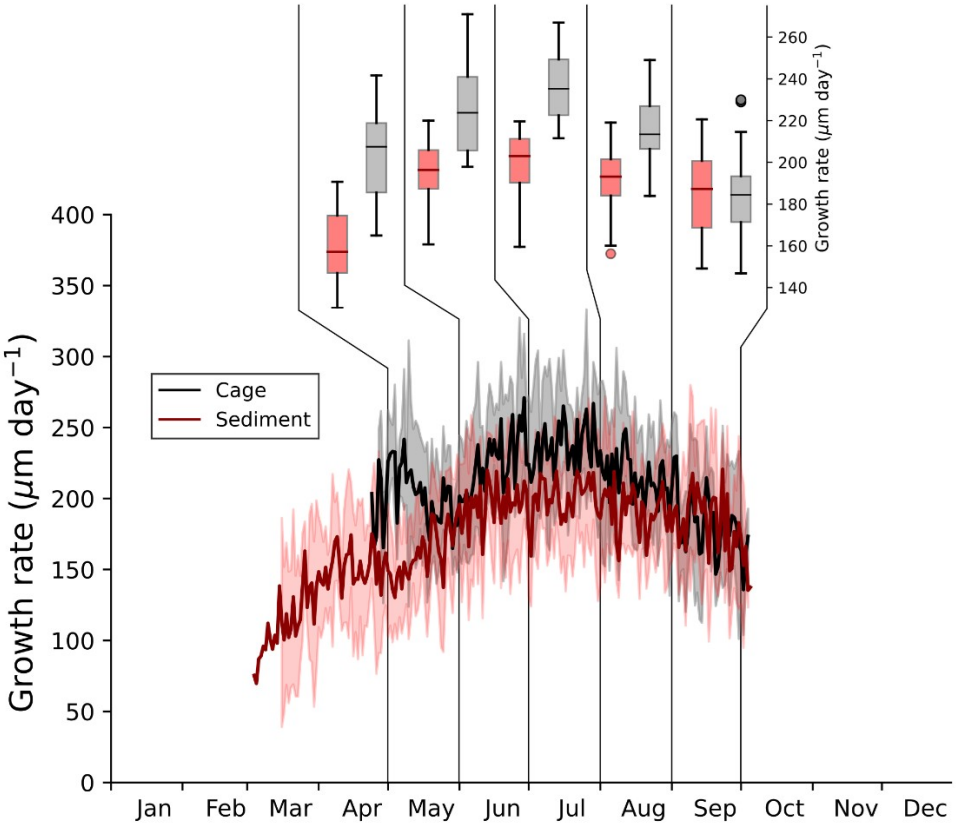

Figure S4.3 Growth rates measured in six specimens of *P. maximus* shells living in a cage (1 m above the sediment) and six specimens grown on the sediment surface. Bold lines correspond to the average growth rates ($\pm 1\sigma$) for cage and sediment shells and box plots indicate monthly differences in measured growth rates.

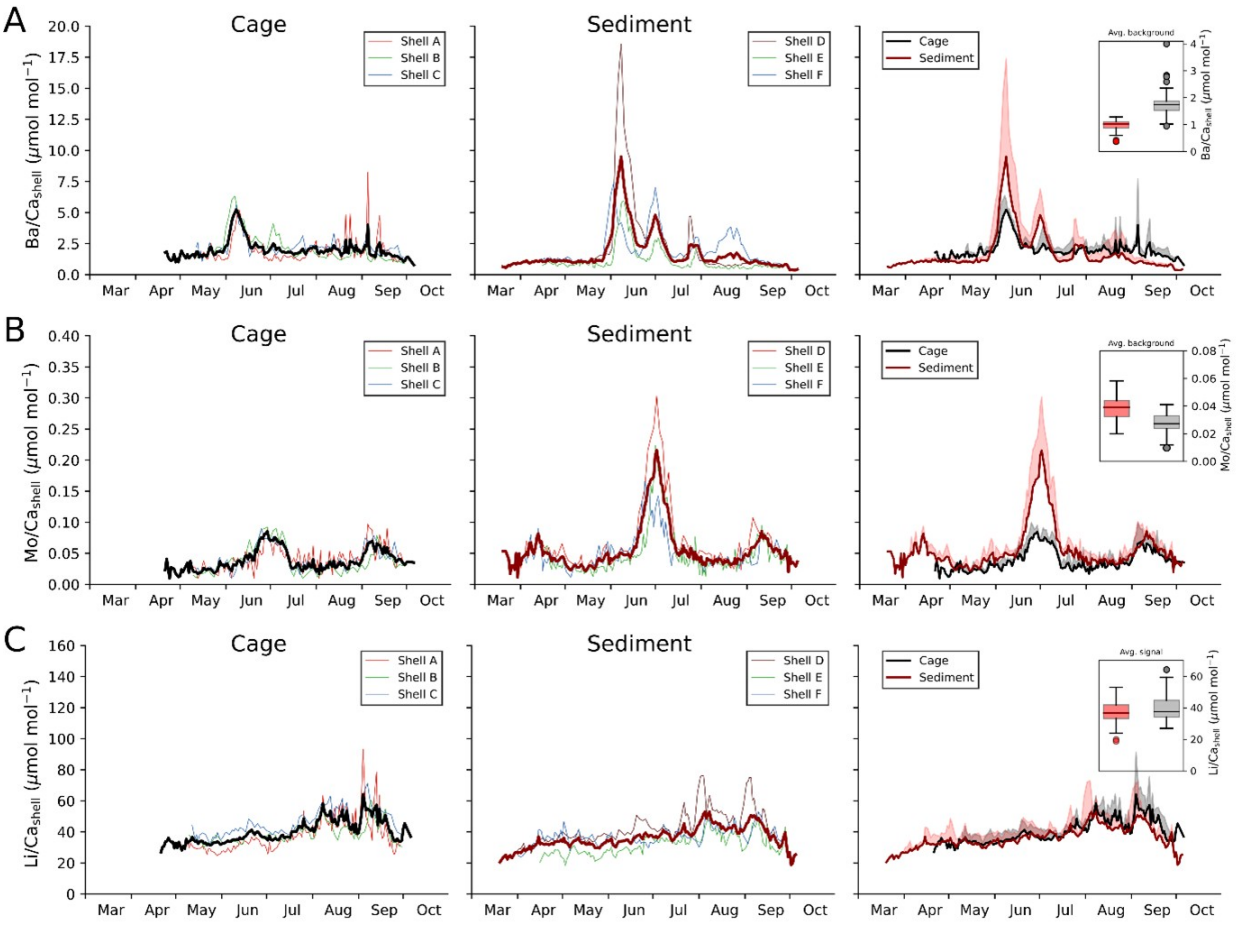

Figure S4.4 Ba/Ca$_{shell}$ (**A**), Mo/Ca$_{shell}$ (**B**) and Li/Ca$_{shell}$ (**C**) measured in three *P. maximus* specimens grown inside a cage (Shell A–C; left panel) and on the sediment surface (Shell D–F; center panel) during 2021. Average molar element-to-calcium chronologies represented as bold lines. For better visualization, the average profiles ($+1\sigma$) from cage and sediment shells were plotted together (right panel). Box plots indicate for differences in the background signals between cage and sediment shells of average Ba/Ca$_{shell}$ and Mo/Ca$_{shell}$ profiles and the average signal of Li/Ca$_{shell}$ ratios.

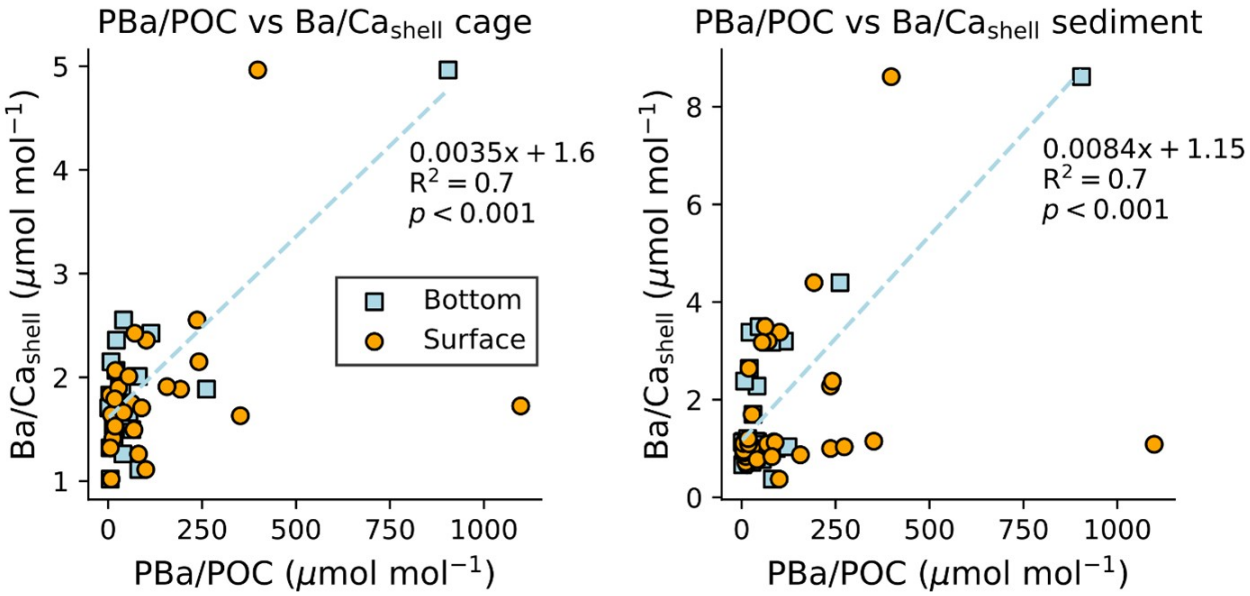

Figure S4.5 Cross-plots of PBa/POC ratios measured in bottom and surface waters vs. average Ba/Ca$_{shell}$ profiles from cage and sediment shells. Ba/Ca$_{shell}$ profiles were resampled to match the resolution of the PBa/POC data. Significant (Pearson) correlations only existed between PBa/POC levels measured in bottom waters and Ba/Ca$_{shell}$ profiles and the linear regression model is indicated as a blue line.

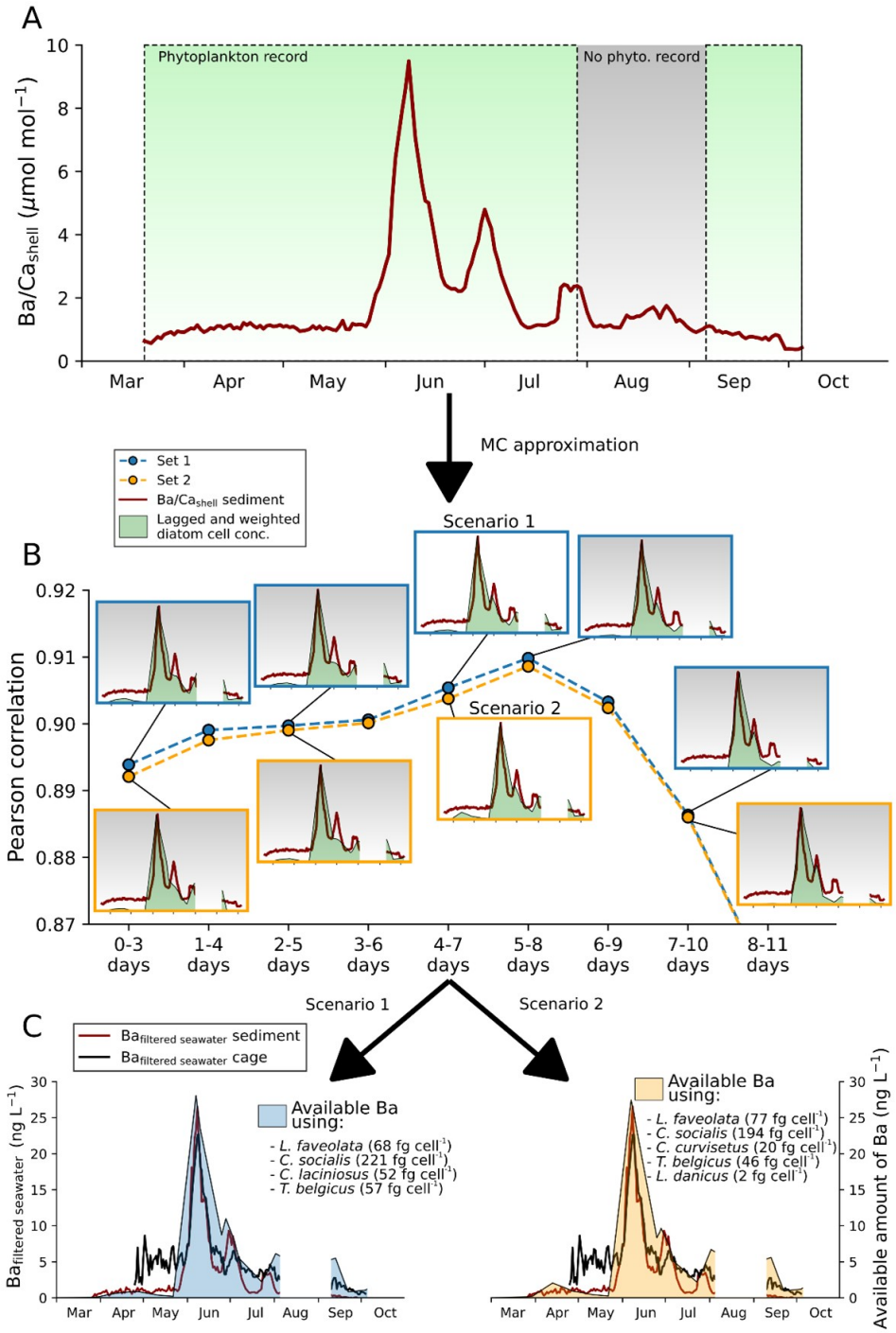

Figure S4.6 The average Ba/Ca$_{shell}$ profile obtained from sediment-grown shells (**A**) was used to approximate the potential contribution of the most abundant diatom taxa observed in the water column to the Ba/Ca$_{shell}$ peaks. Since no phytoplankton record

Figure S4.6 (continued) was available between late July to early September, the Monte Carlo (MC) approximations were performed by excluding this time period (gray area in **A**). Pearson correlation coefficients indicated for the best combination (small subplots illustrating the respective result of the temporally shifted and weighted diatom time-series) that were tested for different time lags (**B**). Considering the growth rates and filtration rates (i.e., 5 L h^{-1} g^{-1} soft tissue dry weight), the $Ba_{filtered\ seawater}$ concentration was estimated (**C**). Using scenario 1 and scenario 2, the diatom-associated amount of Ba was estimated following the assumption that the ingestion of diatoms triggered the formation of the measured Ba/Ca_{shell} peaks (see calculations described in Fig. S4.2).

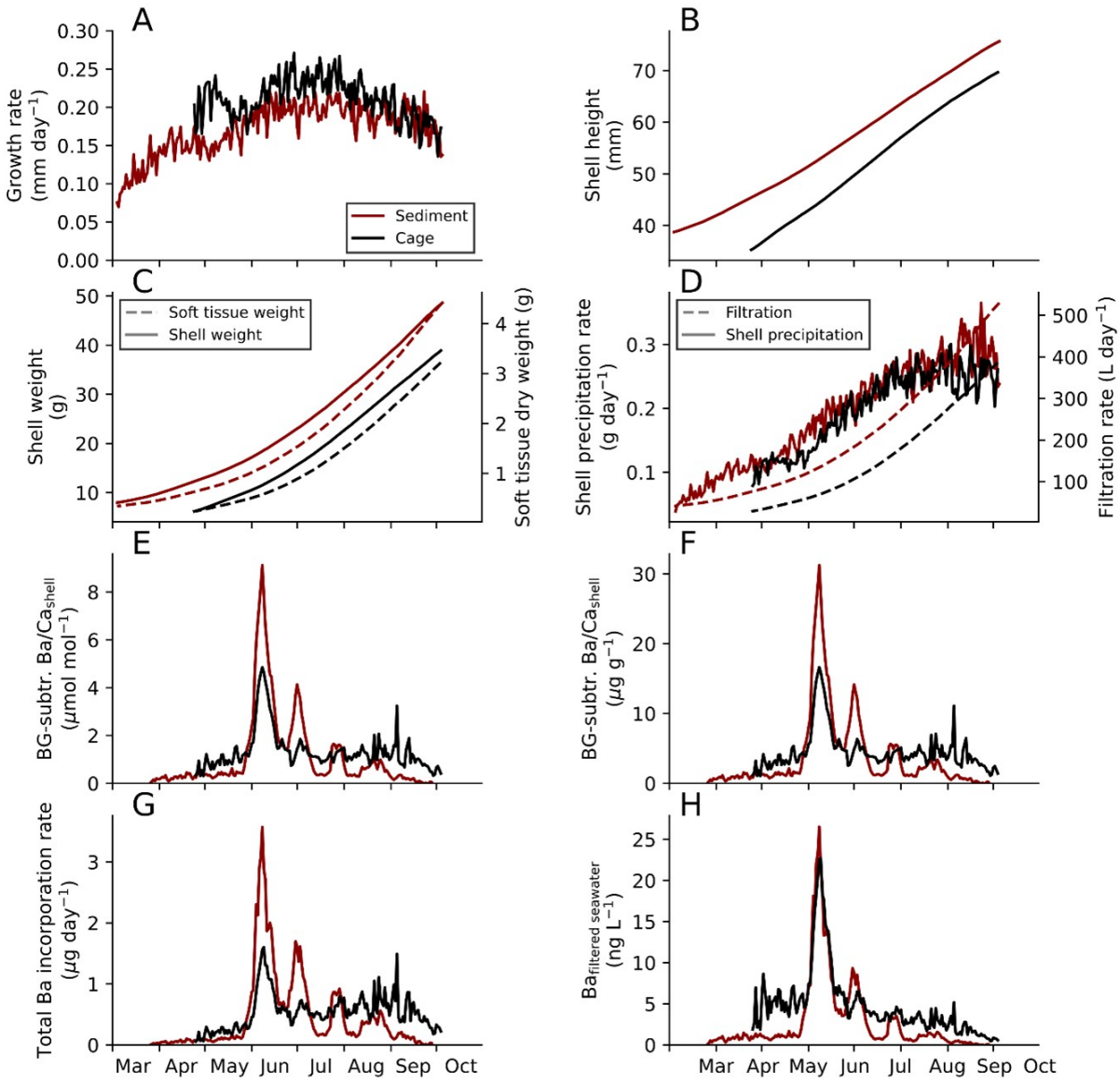

Figure S4.7 Average growth rates measured in sediment shells and cage shells (**A**; step 3 in Fig. S4.2) were used to calculate daily shell heights (**B**; step 4 in Fig. S4.2) and approximate the shell weight and soft tissue dry weight (**C**; step 8 and 5 in Fig. S4.2) following the allometric relationships from Lorrain et al. (2004). Estimated filtration rates (at 5 L h^{-1} g^{-1} soft tissue dry weight; step 6 in Fig. S4.2) and shell precipitation rates (**D**). Background subtracted averaged Ba/Ca$_{shell}$ profiles (**E**; step 12 in Fig. S4.2) were converted into weight ratios (**F**; step 11 in Fig. S4.2) and used to approximate absolute Ba incorporation rates (**G**; step 7 in Fig. S4.2). Together with the daily filtration rate, the Ba$_{filtered\ seawater}$ was estimated (**H**; step 2 in Fig. S4.2).

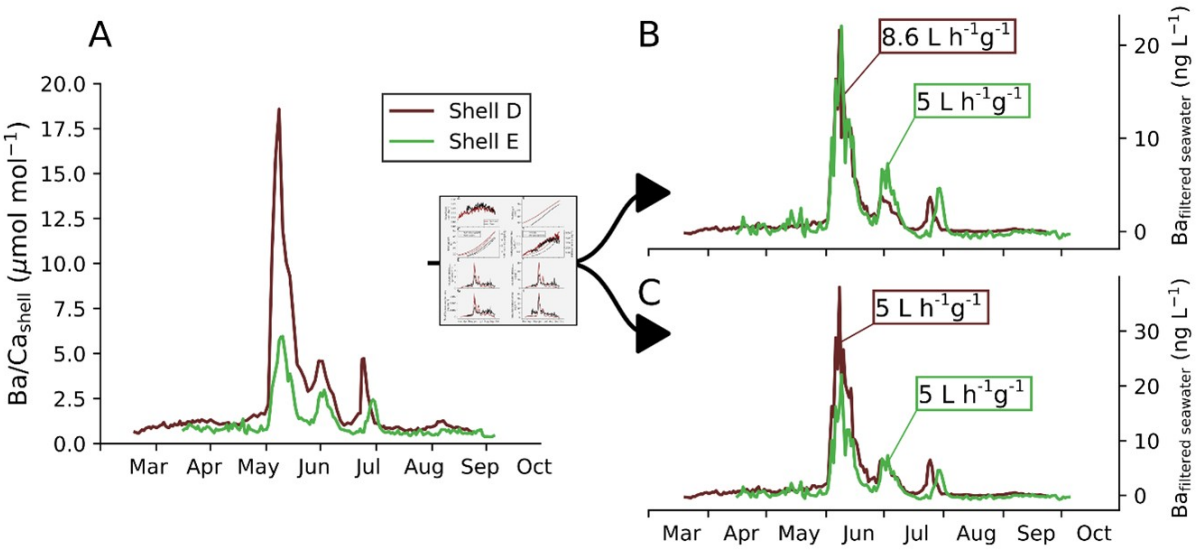

Figure S4.8 Differences in the Ba/Ca$_{shell}$ profile of Shell D and Shell E that grew on the sediment (**A**). After considering the individual growth rates and filtration rates (following the steps performed in Fig. S4.2 and S4.7), the Ba$_{filtered\ seawater}$ amount was approximated (**B** and **C**). Subplot **B** illustrates a likely scenario in which Shell D possessed a slightly higher weight-standardized filtration rate compared to Shell E. According to this filtration scenario, both scallops would have filtered the same amount of Ba from the seawater during the large bloom in early June (e.g., induced by a large diatom bloom). This indicates to what extent small differences in filtration rates can affect Ba$_{filtered\ seawater}$ concentrations. For comparison, the Ba$_{filtered\ seawater}$ amount is depicted assuming a similar weight-standardized filtration rate for both shells (**C**).

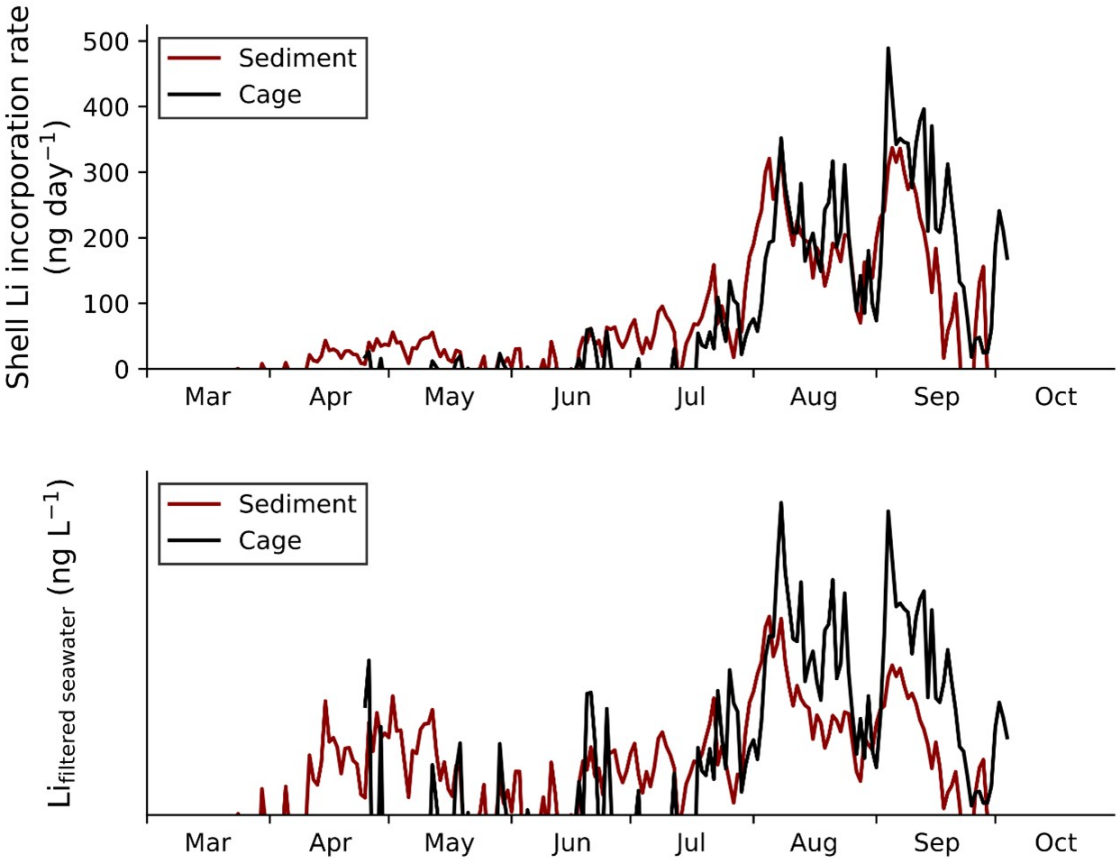

Figure S4.9 Estimated Li incorporation rate into the shell for cage and sediment shells (upper panel) calculated using the Li/Ca_{shell} elemental ratios together with the daily Ca precipitation rate. Note that the Li/Ca_{shell} background level was approximated, using the growth rate dependency described by Thébault and Chauvaud (2013), and subtracted from the measured Li/Ca_{shell} profiles to account for excess Li/Ca_{shell}. Relative amount of Li that was filtered by scallops from the cage and from the sediment (lower panel) considering a similar soft tissue dry weight-normalized filtration rate. Absolute values for the Li content in the filtered seawater could not be calculated as the relative Li distribution among soft tissue and shell is unknown.

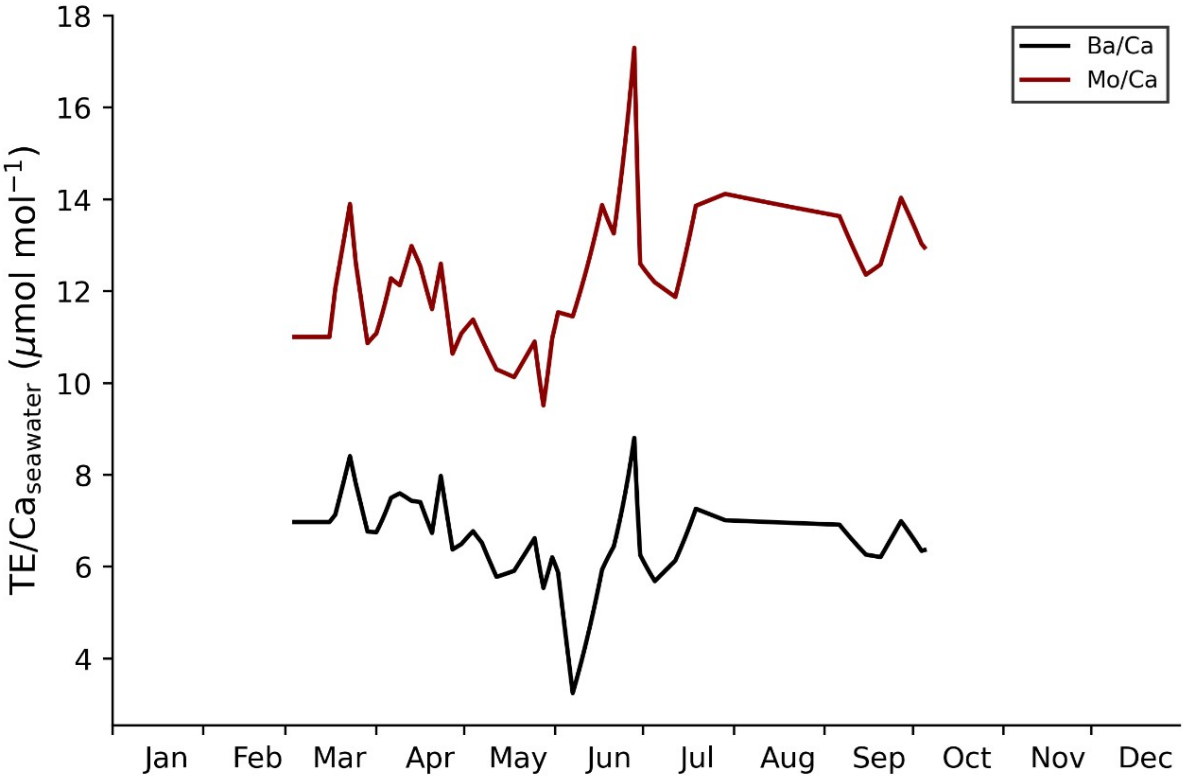

Figure S4.10 Dissolved Ba/Ca$_{seawater}$ and Mo/Ca$_{seawater}$ ratio measured in the water at the study locality.

References

Alldredge, A. L., Gotschalk, C. C., 1989. Direct observations of the mass flocculation of diatom blooms: Characteristics, settling velocities and formation of diatom aggregates. Deep Sea Research Part A, Oceanographic Research Papers 36, 159–171.

Alldredge, A. L., Gotschalk, C., 1988. In situ settling behavior of marine snow. Limnology and Oceanography 33, 339–351.

Barats, A., Amouroux, D., Chauvaud, L., Pécheyran, C., Lorrain, A., Thébault, J., Church, T. M., Donard, O. F., 2009. High frequency barium profiles in shells of the great scallop *Pecten maximus*: A methodical long-term and multi-site survey in Western Europe. Biogeosciences 6, 157–170.

Barats, A., 2006. Micro analyse quantitative des éléments traces dans la calcite de la coquille Saint Jacques (*Pecten maximus*) par Ablation Laser ICP-MS: une archive journalière de la biogéochimie des environnements côtiers tempérés. Diss. Université de Pau et des Pays de l'Adour.

Barats, A., Amouroux, D., Pécheyran, C., Chauvaud, L., Thébault, J., Donard, O. F. X., 2010. Spring molybdenum enrichment in scallop shells: A potential tracer of diatom productivity in temperate coastal environments (Brittany, NW France). Biogeosciences 7, 233–245.

Barats, A., Pécheyran, C., Amouroux, D., Dubascoux, S., Chauvaud, L., Donard, O. F. X., 2007. Matrix-matched quantitative analysis of trace-elements in calcium carbonate shells by laser-ablation ICP-MS: Application to the determination of daily scale profiles in scallop shell (*Pecten maximus*). Analytical and Bioanalytical Chemistry 387, 1131–1140.

Barbier, E. B., Hacker, S. D., Kennedy, C., Koch, E. W., Stier, A. C., Silliman, B. R., 2011. The value of estuarine and coastal ecosystem services. Ecological Monographs 81, 169–193.

Bates, S. S., Hubbard, K. A., Lundholm, N., Montresor, M., Leaw, C. P., 2018. *Pseudo-nitzschia*, *Nitzschia*, and domoic acid: New research since 2011. Harmful Algae 79, 3–43.

Beninger, P. G., Decottignies, P., Rincé, Y., 2004. Localization of qualitative particle selection sites in the heterorhabdic filibranch *Pecten maximus* (Bivalvia: Pectinidae). Marine Ecology Progress Series 275, 163–173.

Bishop, J. K. B., 1988. The barite-opal-organic carbon association in oceanic particulate matter. Nature 332, 341–343.

Chauvaud, L., Donval, A., Thouzeau, G., Paulet, Y. M., Nézan, E., 2001. Variations in food intake of *Pecten maximus* (L.) from the Bay of Brest (France): Influence of environmental factors and phytoplankton species composition. Comptes Rendus de l'Académie des Sciences - Series III - Sciences de la Vie 324, 743–755.

Chauvaud, L., Thouzeau, G., Paulet, Y. M., 1998. Effects of environmental factors on the daily growth rate of *Pecten maximus* juveniles in the Bay of Brest (France). Journal of Experimental Marine Biology and Ecology 227, 83–111.

Clark, G. R., 2005. Daily growth lines in some living pectens (Mollusca: Bivalvia), and some applications in a fossil relative: Time and tide will tell. Palaeogeography, Palaeoclimatology, Palaeoecology 228, 26–42.

Collier, R. W., 1985. Molybdenum in the Northeast Pacific Ocean. Limnology and Oceanography 30, 1351–1354.

Coplen, T. B., Böhlke, J. K., De Bièvre, P., Ding, T., Holden, N. E., Hopple, J. A., Krouse, H. R., Lamberty, A., Peiser, H. S., Révész, K., Rieder, S. E., Rosman, K. J. R., Roth, E., Taylor, P. D. P., Vocke, R. D., Xiao, Y. K., 2002. Isotope-abundance variations of selected elements (IUPAC Technical Report). Pure and Applied Chemistry 74, 1987–2017.

Dehairs, F., Chesselet, R., Jedwab, J., 1980. Discrete suspended particles of barite and the barium cycle in the open ocean. Earth and Planetary Science Letters 49, 528–550.

Dellwig, O., Beck, M., Lemke, A., Lunau, M., Kolditz, K., Schnetger, B., Brumsack, H. J., 2007. Non-conservative behaviour of molybdenum in coastal waters: Coupling geochemical, biological, and sedimentological processes. Geochimica et Cosmochimica Acta 71, 2745–2761.

Eppley, R. W., Coatsworth, J. L., Solórzano, L., 1969. Studies of nitrate reductase in marine phytoplankton. Limnology and Oceanography 14, 194–205.

Field, C. B., Behrenfeld, M. J., Randerson, J. T., Falkowski, P., 1998. Primary production of the biosphere: Integrating terrestrial and oceanic components. Science 281, 237–240.

Fisher, N. S., Guillard, R. R. L., Bankston, D. C., 1991. The accumulation of barium by marine phytoplankton grown in culture. Journal of Marine Research 49, 339–354.

Fröhlich, L., Siebert, V., Huang, Q., Thébault, J., Jochum, K. P., Schöne, B. R., 2022a. Deciphering the potential of Ba/Ca, Mo/Ca and Li/Ca profiles in the bivalve shell *Pecten maximus* as proxies for the reconstruction of phytoplankton dynamics. Ecological Indicators 141, 109121.

Fröhlich, L., Siebert, V., Walliser, E. O., Thébault, J., Jochum, K. P., Chauvaud, L., Schöne, B. R., 2022b. Ba/Ca profiles in shells of *Pecten maximus* – A proxy for specific primary producers rather than bulk phytoplankton. Chemical Geology 593, 120743.

Ganeshram, R. S., François, R., Commeau, J., Brown-Leger, S. L., 2003. An experimental investigation of barite formation in seawater. Geochimica et Cosmochimica Acta 67, 2599–2605.

Gillikin, D. P., Dehairs, F., Lorrain, A., Steenmans, D., Baeyens, W., André, L., 2006. Barium uptake into the shells of the common mussel (*Mytilus edulis*) and the potential for estuarine paleo-chemistry reconstruction. Geochimica et Cosmochimica Acta 70, 395–407.

Gillikin, D. P., Lorrain, A., Paulet, Y. M., André, L., Dehairs, F., 2008. Synchronous barium peaks in high-resolution profiles of calcite and aragonite marine bivalve shells. Geo-Marine Letters 28, 351–358.

Hallegraeff, G. M., 1993. A review of harmful algal blooms and their apparent global increase. Phycologia 32, 79–99.

Hillebrand, H., Dürselen, C. D., Kirschtel, D., Pollingher, U., Zohary, T., 1999. Biovolume calculation for pelagic and benthic microalgae. Journal of Phycology 35, 403–424.

Ho, T. Y., Quigg, A., Finkel, Z. V., Milligan, A. J., Wyman, K., Falkowski, P. G., Morel, F. M. M., 2003. The elemental composition of some marine phytoplankton. Journal of Phycology 39, 1145–1159.

Iglesias-Rodriguez, M. D., Halloran, P. R., Rickaby, R. E. M., Hall, I. R., Colmenero-Hidalgo, E., Gittins, J. R., Green, D. R. H., Tyrrell, T., Gibbs, S. J., von Dassow, P., Rehm, E., Armbrust, E. V., Boessenkool, K. P., 2008. Phytoplankton calcification in a high-CO_2 world. Science 320, 336–340.

Jochum, K. P., Garbe-Schönberg, D., Veter, M., Stoll, B., Weis, U., Weber, M., Lugli, F., Jentzen, A., Schiebel, R., Wassenburg, J. A., Jacob, D. E., Haug, G. H., 2019. Nano-powdered calcium carbonate reference materials: Significant progress for microanalysis? Geostandards and Geoanalytical Research 43, 595–609.

Jochum, K. P., Stoll, B., Herwig, K., Willbold, M., 2007. Validation of LA-ICP-MS trace element analysis of geological glasses using a new solid-state 193 nm Nd:YAG laser and matrix-matched calibration. Journal of Analytical Atomic Spectrometry 22, 112–121.

Jochum, K. P., Weis, U., Stoll, B., Kuzmin, D., Yang, Q., Raczek, I., Jacob, D. E., Stracke, A., Birbaum, K., Frick, D. A., Günther, D., Enzweiler, J., 2011. Determination of reference values for NIST SRM 610-617 glasses following ISO guidelines. Geostandards and Geoanalytical Research 35, 397–429.

Kubanek, J., Hicks, M. K., Naar, J., Villareal, T. A., 2005. Does the red tide dinoflagellate *Karenia brevis* use allelopathy to outcompete other phytoplankton? Limnology and Oceanography 50, 883–895.

Laing, I., 2004. Filtration of king scallops (*Pecten maximus*). Aquaculture 240, 369–384.

Leighton, D. L., 1979. A growth profile for the rock scallop *Hinnites multirugosus* held at several depths off La Jolla, California. Marine Biology 51, 229–232.

Lewitus, A. J., Horner, R. A., Caron, D. A., Garcia-Mendoza, E., Hickey, B. M., Hunter, M., Huppert, D. D., Kudela, R. M., Langlois, G. W., Largier, J. L., Lessard, E. J., RaLonde, R., Rensel, J. E. J., Strutton, P. G., Trainer, V. L., Tweddle, J. F., 2012. Harmful algal

blooms along the North American west coast region: History, trends, causes, and impacts. Harmful Algae 19, 133–159.

Lobus, N. V., Kulikovskiy, M. S., Maltsev, Y. I., 2021. Multi-element composition of diatom *Chaetoceros* spp. from natural phytoplankton assemblages of the Russian Arctic Seas. Biology 10, 1009.

Longerich, H. P., Jackson, S. E., Günther, D., 1996. Laser ablation inductively coupled plasma mass spectrometric transient signal data acquisition and analyte concentration calculation. Journal of Analytical Atomic Spectrometry 11, 899–904.

Lorenzen, C. J., 1966. A method for the continuous measurement of *in vivo* chlorophyll concentration. Deep-Sea Research and Oceanographic Abstracts 13, 223–227.

Lorenzen, C. J., 1967. Vertical distribution of chlorophyll and phaeo-pigments: Baja California. Deep-Sea Research and Oceanographic Abstracts 14, 735–745.

Lorrain, A., Paulet, Y. M., Chauvaud, L., Dunbar, R. B., Mucciarone, D., Fontugne, M., 2004. δ^{13}C variation in scallop shells: Increasing metabolic carbon contribution with body size? Geochimica et Cosmochimica Acta 68, 3509–3519.

Lorrain, A., Paulet, Y. M., Chauvaud, L., Savoye, N., Nézan, E., Guérin, L., 2000. Growth anomalies in *Pecten maximus* from coastal waters (Bay of Brest, France): Relationship with diatom blooms. Journal of the Marine Biological Association of the United Kingdom 80, 667–673.

MacDonald, B. A., 1986. Production and resource partitioning in the giant scallop *Placopecten magellanicus* grown on the bottom and in suspended culture. Marine Ecology Progress Series 34, 79–86.

MacDonald, B. A., Bajdik, C. D., 1992. Orientation and distribution of individual *Placopecten magellanicus* (Gmelin) in two natural populations with differing production. Canadian Journal of Fisheries and Aquatic Sciences 49, 2086–2092.

Marali, S., Schöne, B. R., Mertz-Kraus, R., Griffin, S. M., Wanamaker, A. D., Butler, P. G., Holland, H. A., Jochum, K. P., 2017. Reproducibility of trace element time-series (Na/Ca, Mg/Ca, Mn/Ca, Sr/Ca, and Ba/Ca) within and between specimens of the bivalve *Arctica*

islandica – a LA-ICP-MS line scan study. Palaeogeography, Palaeoclimatology, Palaeoecology 484, 109–128.

Marino, R., Howarth, R. W., Chan, F., Cole, J. J., Likens, G. E., 2003. Sulfate inhibition of molybdenum-dependent nitrogen fixation by planktonic cyanobacteria under seawater conditions: A non-reversible effect. Hydrobiologia 500, 277–293.

Masuzawa, T., Suzuki, T., Seki, K., Kosugi, T., Hibi, Y., Yamamoto, M., Takada, J., Matsushita, R., Yanada, M., 1999. Multielement compositions of marine phytoplankton samples from coastal areas of japan by instrumental neutron activation analysis. Biological Trace Element Research 71, 331–342.

McConnaughey, T. A., Gillikin, D. P., 2008. Carbon isotopes in mollusk shell carbonates. Geo-Marine Letters 28, 287–299.

Menden-Deuer, S., Lessard, E. J., 2000. Carbon to volume relationships for dinoflagellates, diatoms, and other protist plankton. Limnology and Oceanography 45, 569–579.

Mendoza, Y., Freites, L., Lodeiros, C. J., López, J. A., Himmelman, J. H., 2003. Evaluation of biological and economical aspects of the culture of the scallop *Lyropecten* (*Nodipecten*) *nodosus* in suspended and bottom culture. Aquaculture 221, 207–219.

Mori, C., Beck, M., Striebel, M., Merder, J., Schnetger, B., Dittmar, T., Pahnke, K., Brumsack, H. J., 2021. Biogeochemical cycling of molybdenum and thallium during a phytoplankton summer bloom: A mesocosm study. Marine Chemistry 229, 103910.

Morris, I., Syrett, P. J., 1963. The development of nitrate reductase in *Chlorella* and its repression by ammonium. Archiv für Mikrobiologie 47, 32–41.

Palmer, R. E., 1980. Behavioral and rhythmic aspects of filtration in the bay scallop, *Argopecten irradians concentricus* (Say), and the oyster, *Crassostrea virginica* (Gmelin). Journal of Experimental Marine Biology and Ecology 45, 273–295.

Pan, Y., Subba Rao, D. V., Mann, K. H., Li, W. K. W., Harrison, W. G., 1996. Effects of silicate limitation on production of domoic acid, a neurotoxin, by the diatom *Pseudo-nitzschia multiseries*. II. Continuous culture studies. Marine Ecology Progress Series 131, 235–243.

Poppeschi, C., Charria, G., Daniel, A., Verney, R., Rimmelin-Maury, P., Retho, M., Goberville, E., Grossteffan, E., Plus, M., 2022. Interannual variability of the initiation of the phytoplankton growing period in two French coastal ecosystems. Biogeosciences 19, 5667–5687.

Richard, M., 2009. Analyse de la composition élémentaire de *Pecten maximus* par HR-ICP-MS Element 2 : développements méthodologiques et interprétations écologiques. Diss. Université de Bretagne Occidentale-Brest.

Roth, I., Riley, J. P., 1971. The distribution of trace elements in some species of phytoplankton grown in culture. Journal of the Marine Biological Association of the United Kingdom 51, 63–72.

Schöne, B. R., Tanabe, K., Dettman, D. L., Sato, S., 2003. Environmental controls on shell growth rates and δ^{18}O of the shallow-marine bivalve mollusk *Phacosoma japonicum* in Japan. Marine Biology 142, 473–485.

Schöne, B. R., Huang, X., Zettler, M. L., Zhao, L., Mertz-Kraus, R., Jochum, K. P., Walliser, E. O., 2021. Mn/Ca in shells of *Arctica islandica* (Baltic Sea) – A potential proxy for ocean hypoxia? Estuarine, Coastal and Shelf Science 251, 107257.

Schöne, B. R., Marali, S., Jantschke, A., Mertz-Kraus, R., Butler, P. G., Fröhlich, L., 2023. Can element chemical impurities in aragonitic shells of marine bivalves serve as proxies for environmental variability? Chemical Geology 616, 121215.

Shumway, S. E., Cucci, T. L., Lesser, M. P., Bourne, N., Bunting, B., 1997. Particle clearance and selection in three species of juvenile scallops. Aquaculture International 5, 89–99.

Shumway, S. E., Selvin, R., Schick, D. F., 1987. Food resources related to habitat in the scallop *Placopecten magellanicus*. Journal of Shellfish Research 6, 89–95.

Siebert, V., Moriceau, B., Fröhlich, L., Schöne, B. R., Amice, E., Beker, B., Bihannic, K., Bihannic, I., Delebecq, G., Devesa, J., Gallinari, M., Germain, Y., Grossteffan, É., Jochum, K. P., Le Bec, T., Le Goff, M., Liorzou, C., Leynaert, A., Marec, C., Picheral, M., Rimmelin-Maury, P., Rouget, M. L., Waeles, M., Thébault, J., 2023. HIPPO environmental monitoring: impact of phytoplankton dynamics on water column chemistry and

the sclerochronology of the king scallop (*Pecten maximus*) as a biogenic archive for past primary production reconstructions. Earth System Science Data 15, 3263–3281.

Spilling, K., Olli, K., Lehtoranta, J., Kremp, A., Tedesco, L., Tamelander, T., Klais, R., Peltonen, H., Tamminen, T., 2018. Shifting diatom-dinoflagellate dominance during spring bloom in the Baltic Sea and its potential effects on biogeochemical cycling. Frontiers in Marine Science 5, 327.

Stecher, H. A., Krantz, D. E., Lord, C. J., Luther, G. W., Bock, K. W., 1996. Profiles of strontium and barium in *Mercenaria mercenaria* and *Spisula solidissima* shells. Geochimica et Cosmochimica Acta 60, 3445–3456.

Stecher, H. A., Kogut, M. B., 1999. Rapid barium removal in the Delaware estuary. Geochimica et Cosmochimica Acta 63, 1003–1012.

Sternberg, E., Tang, D., Ho, T. Y., Jeandel, C., Morel, F. M. M., 2005. Barium uptake and adsorption in diatoms. Geochimica et Cosmochimica Acta 69, 2745–2752.

Strohmeier, T., Strand, Ø., Cranford, P., 2009. Clearance rates of the great scallop (*Pecten maximus*) and blue mussel (*Mytilus edulis*) at low natural seston concentrations. Marine Biology 156, 1781–1795.

Subba Rao, D. V., Pan, Y., Mukhida, K., 1998. Production of domoic acid by *Pseudo-nitzschia multiseries* Hasle, affected by lithium. Marine Ecology 19, 31–36.

Sun, J., Liu, D., 2003. Geometric models for calculating cell biovolume and surface area for phytoplankton. Journal of Plankton Research 25, 1331–1346.

Tabouret, H., Pomerleau, S., Jolivet, A., Pécheyran, C., Riso, R., Thébault, J., Chauvaud, L., Amouroux, D., 2012. Specific pathways for the incorporation of dissolved barium and molybdenum into the bivalve shell: An isotopic tracer approach in the juvenile great scallop (*Pecten maximus*). Marine Environmental Research 78, 15–25.

Tachihana, S., Nagao, N., Katayama, T., Hirahara, M., Yusoff, F. M., Banerjee, S., Shariff, M., Kurosawa, N., Toda, T., Furuya, K., 2020. High productivity of eicosapentaenoic acid and fucoxanthin by a marine diatom *Chaetoceros gracilis* in a semi-continuous culture. Frontiers in Bioengineering and Biotechnology 8, 602721.

Tardy, Y., Krempp, G., Trauth, N., 1972. Le lithium dans les minéraux argileux des sédiments et des sols. Geochimica et Cosmochimica Acta 36, 397–412.

Thébault, J., Chauvaud, L., 2013. Li/Ca enrichments in great scallop shells (*Pecten maximus*) and their relationship with phytoplankton blooms. Palaeogeography, Palaeoclimatology, Palaeoecology 373, 108–122.

Thébault, J., Chauvaud, L., Clavier, J., Fichez, R., Morize, E., 2006. Evidence of a 2-day periodicity of striae formation in the tropical scallop *Comptopallium radula* using calcein marking. Marine Biology 149, 257–267.

Thébault, J., Chauvaud, L., L'Helguen, S., Clavier, J., Barats, A., Jacquet, S., Pécheyran, C., Amouroux, D., 2009a. Barium and molybdenum records in bivalve shells: Geochemical proxies for phytoplankton dynamics in coastal environments? Limnology and Oceanography 54, 1002–1014.

Thébault, J., Jolivet, A., Waeles, M., Tabouret, H., Sabarot, S., Pécheyran, C., Leynaert, A., Jochum, K. P., Schöne, B. R., Fröhlich, L., Siebert, V., Amice, E., Chauvaud, L., 2022. Scallop shells as geochemical archives of phytoplankton-related ecological processes in a temperate coastal ecosystem. Limnology and Oceanography 67, 187–202.

Thébault, J., Schöne, B. R., Hallmann, N., Barth, M., Nunn, E. V., 2009b. Investigation of Li/Ca variations in aragonitic shells of the ocean quahog *Arctica islandica*, northeast Iceland. Geochemistry, Geophysics, Geosystems 10, Q12008.

Toullec, J., Moriceau, B., Vincent, D., Guidi, L., Lafond, A., Babin, M., 2021. Processes controlling aggregate formation and distribution during the Arctic phytoplankton spring bloom in Baffin Bay. Elementa 9, 00001.

Toullec, J., Vincent, D., Frohn, L., Miner, P., Le Goff, M., Devesa, J., Moriceau, B., 2019. Copepod grazing influences diatom aggregation and particle dynamics. Frontiers in Marine Science 6, 751.

Turner, J. T., Tester, P. A., 1997. Toxic marine phytoplankton, zooplankton grazers, and pelagic food webs. Limnology and Oceanography 42, 1203–1213.

Vitousek, P. M., Aber, J. D., Howarth, R. W., Likens, G. E., Matson, P. A., Schindler, D. W., Schlesinger, W. H., Tilman, D. G., 1997. Human alteration of the global nitrogen cycle: Sources and consequences. Ecological Applications 7, 737–750.

Wang, W. X., Fisher, N. S., Luoma, S. N., 1995. Assimilation of trace elements ingested by the mussel *Mytilus edulis*: Effects of algal food abundance. Marine Ecology Progress Series 129, 165–176.

Wasmund, N., Kownacka, J., Göbel, J., Jaanus, A., Johansen, M., Jurgensone, I., Lehtinen, S., Powilleit, M., 2017. The diatom/dinoflagellate index as an indicator of ecosystem changes in the Baltic Sea 1. Principle and handling instruction. Frontiers in Marine Science 4, 22.

Westberry, T., Behrenfeld, M. J., Siegel, D. A., Boss, E., 2008. Carbon-based primary productivity modeling with vertically resolved photoacclimation. Global Biogeochemical Cycles 22, 1–18.

Widdows, J., Moore, M. N., Lowe, D. M., Salkeld, P. N., 1979. Some effects of a dinoflagellate bloom (*Gyrodinium aureolum*) on the mussel, *Mytilus edulis*. Journal of the Marine Biological Association of the United Kingdom 59, 522–524.

Winder, M., Sommer, U., 2012. Phytoplankton response to a changing climate. Hydrobiologia 698, 5–16.

Worm, B., Barbier, E. B., Beaumont, N., Duffy, J. E., Folke, C., Halpern, B. S., Jackson, J. B. C., Lotze, H. K., Micheli, F., Palumbi, S. R., Sala, E., Selkoe, K. A., Stachowicz, J. J., Watson, R., 2006. Impacts of biodiversity loss on ocean ecosystem services. Science 314, 787–790.

Yamamoto, T., Oh, S. J., Kataoka, Y., 2004. Growth and uptake kinetics for nitrate, ammonium and phosphate by the toxic dinoflagellate *Gymnodinium catenatum* isolated from Hiroshima Bay, Japan. Fisheries Science 70, 108–115.

Zhao, L., Schöne, B. R., Mertz-Kraus, R., 2017. Controls on strontium and barium incorporation into freshwater bivalve shells (*Corbicula fluminea*). Palaeogeography, Palaeoclimatology, Palaeoecology 465, 386–394.

5 Influence of sampling strategy, alignment method and growth morphology on the temporal contextualization of high-resolution geochemical data

---

Lukas Fröhlich[1], Qian Huang[1], Bernd R. Schöne[1],

[1] *Johannes Gutenberg University, Mainz, Germany*

Reference:

Fröhlich, L., Huang, Q., Schöne, B. R., 2025. Influence of sampling strategy, alignment method and growth morphology on the temporal contextualization of high-resolution geochemical data. Palaeogeography, Palaeoclimatology, Palaeoecology 674, 113003.

As presented in the previous chapters, high-resolution geochemical data are crucial to reconstruct short-term phytoplankton dynamics from bivalve shells (e.g., using Ba/Ca_{shell} profiles). In this chapter, the sampling of geochemical data and their temporal alignment was explored from a theoretical perspective for shells from slower growing bivalves (e.g., *A. islandica*). This allowed to evaluate and develop sclerochronological techniques that are essential to employ long-living bivalves as high-resolution geochemical proxy archives. The findings of this study highlight the extent to which sampling strategy, alignment method, and growth morphology affect the accuracy of temporally contextualized information extracted from biogenic archives. This manuscript was published in the journal 'Palaeogeography, Palaeoclimatology, Palaeoecology'. My contribution to this manuscript was the conceptualization, formal analysis, methodology, visualization and writing of the original draft. This work was funded by the European Research Council (ERC) under the European Union's Horizon 2020 Research and Innovation Program (grant agreement No 856488—ERC Synergy project "SEACHANGE: Quantifying the impact of major cultural transitions on marine ecosystem functioning and biodiversity").

Author contributions:

LF – Conceptualization, Formal analysis, Methodology, Visualization, Writing - original draft, Writing - review and editing

QH – Validation, Investigation, Data curation, Conceptualization, Writing - original draft

BRS – Resources, Project administration, Formal analysis, Funding Acquisition, Supervision, Validation, Writing - review and editing

Abstract

High-resolution proxy reconstructions of physical and ecological variables in aquatic environments are commonly derived from biogenic archives such as bivalve shells. Interpretation of geochemical data measured in circular-shaped sample spots placed along shell cross-sections requires precise temporal alignment. The latter can be challenging, because differences in growth rate, morphology and sampling methods introduce biases to the reconstructed signals. This study systematically evaluates the impact of different sampling strategies and alignment methods on the reconstruction of environmental signals, i.e., temperature oscillations and phytoplankton blooms. Synthetic environmental signals and digital shell models of the bivalve *Arctica islandica* were used to numerically simulate how environmental variables are recorded during shell growth. A novel alignment method is presented, demonstrating significantly improved reconstruction accuracy when compared to traditional techniques. The new method enhances the reliability of proxy-based environmental reconstructions using biogenic archives and offers new insights into highly dynamic environmental signals such as phytoplankton blooms.

5.1 Introduction

The accretionary growth of biogenic carbonates, such as fish otoliths, corals and mollusk shells encode environmental signals as geochemical properties during growth (e.g., Tzadik et al., 2017; Peharda et al., 2021). If the periodicity of incremental growth is known, geochemical proxies (stable isotopes, element chemical properties etc.) can be contextualized temporally (Thébault et al., 2009). These sclerochronological analyses enable the high-resolution reconstruction of environmental conditions in the past, including seasonal to multi-decadal changes in temperature, salinity and primary production (e.g., Butler et al., 2013; Jolivet et al., 2015; Reynolds et al., 2022). Collecting the sample material generally requires the abrasion or ablation of the mineralized hard parts. A common practice is to mill or drill powder from calcium carbonates or to ablate material in-situ using a powerful laser for element chemical analyses. Usually, distinct marks remain on the sampled surface. Smaller samples generally produce higher-resolution time-series. However, aligning such records is particularly challenging, because (1) the growth rate of organisms varies on seasonal timescales (Jones and Quitmyer, 1996; Goodwin et al., 2001), (2) the geometry of the growth patterns (increment shapes) can introduce bias produced by unevenly sampled material, (3) the size of the sample spots in relation to the corresponding increment widths varies throughout the ontogeny of the organism (see Goodwin et al., 2001; Goodwin et al., 2003). If the growth patterns, the shape of the growth increments and the sampling methods are not properly considered, temporal misalignments of geochemical samples can occur, leading to misinterpretations of the reconstructed environmental signals.

Herein, we evaluated the impact of sampling strategies and temporal alignment methods on the reconstruction of sub-annual environmental signals in relation to variable growth increment morphologies. We present a new approach for temporally aligning proxy data determined in biogenic hard parts (exemplarily in bivalve shells) to improve the accuracy of translating geochemical data from a distance- into a time-domain. We used the long-lived bivalve, *Arctica islandica*, given its legacy of providing long-term paleoclimate records (Jones, 1980; Weidman et al., 1994; Marchitto et al., 2000; Wanamaker et al., 2008; Butler et al., 2013) and high-resolution paleoenvironmental variables (Schöne and Huang, 2021; Schöne et al., 2022a; Schöne et al., 2022b; Höche et al., 2023). The major challenge is to assess the accuracy of the reconstructed chronologies because either the environmental data are unavailable or provide a temporal resolution differing from that of the shell archive. To

overcome these uncertainties, we first generated synthetic data mimicking the environmental fluctuations of sea surface temperature (SST) and phytoplankton abundance. Then, we developed 2D digital shell models that numerically simulated the process of the time and growth rate-dependent incremental shell formation, based on empirical shell morphology and growth data of *A. islandica*. These digital models facilitated the numerical discretization of shell formation by splitting annual increments into numerous small, sub-annual microgrowth steps, each representing an equal time interval (hereafter referred to as microgrowth increments). Note that these microgrowth increments do not refer to internal or external forcings producing sub-annual increments, e.g., based on tides or circadian rhythms, but were defined by arbitrarily short time steps, a necessary approach to discretize the overall continuous process of shell formation. Given that the absolute timing of each growth step was defined, the underlying synthetic time-series were used to assign environmental signals to the microgrowth increments of the shell models. This approach simulated the process of recording environmental signals as geochemical properties into the shell. Since the underlying variable, the hypothetical geochemical response and the shell geometry were mathematically described, digital sampling experiments were performed to test different sampling strategies. By using different alignment methods, the reconstructed signals were then compared to synthetic environmental signals allowing to quantify the accuracy of the reconstructions. Although this study focused on bivalve shells, the principles derived herein can apply to a variety of other biogenic archives that grow on periodic bases and can help to improve future sclerochronological studies.

5.2 Material and methods

5.2.1 Digital shell models

The morphology of the outer shell layer (OSL) of *A. islandica* shells (NE Iceland; see Marali and Schöne, 2015) were modeled in two dimensions based on empirical data of three cross-sections (Shell A, Shell B and Shell C; Fig. 5.1). The shell modeling procedure can be described as follows. (1) Cross-sections of *A. islandica* that were immersed in Mutvei's solution (cf. Schöne et al., 2005) and digitalized (Fig. 5.1A-D) using a stereomicroscope (Zeiss Stemi 508) equipped to a DSLR camera (Canon EOS RP) and a Schott VisiLED MC1000 sectoral dark-field light source. The microscope images were digitally stacked (Microsoft

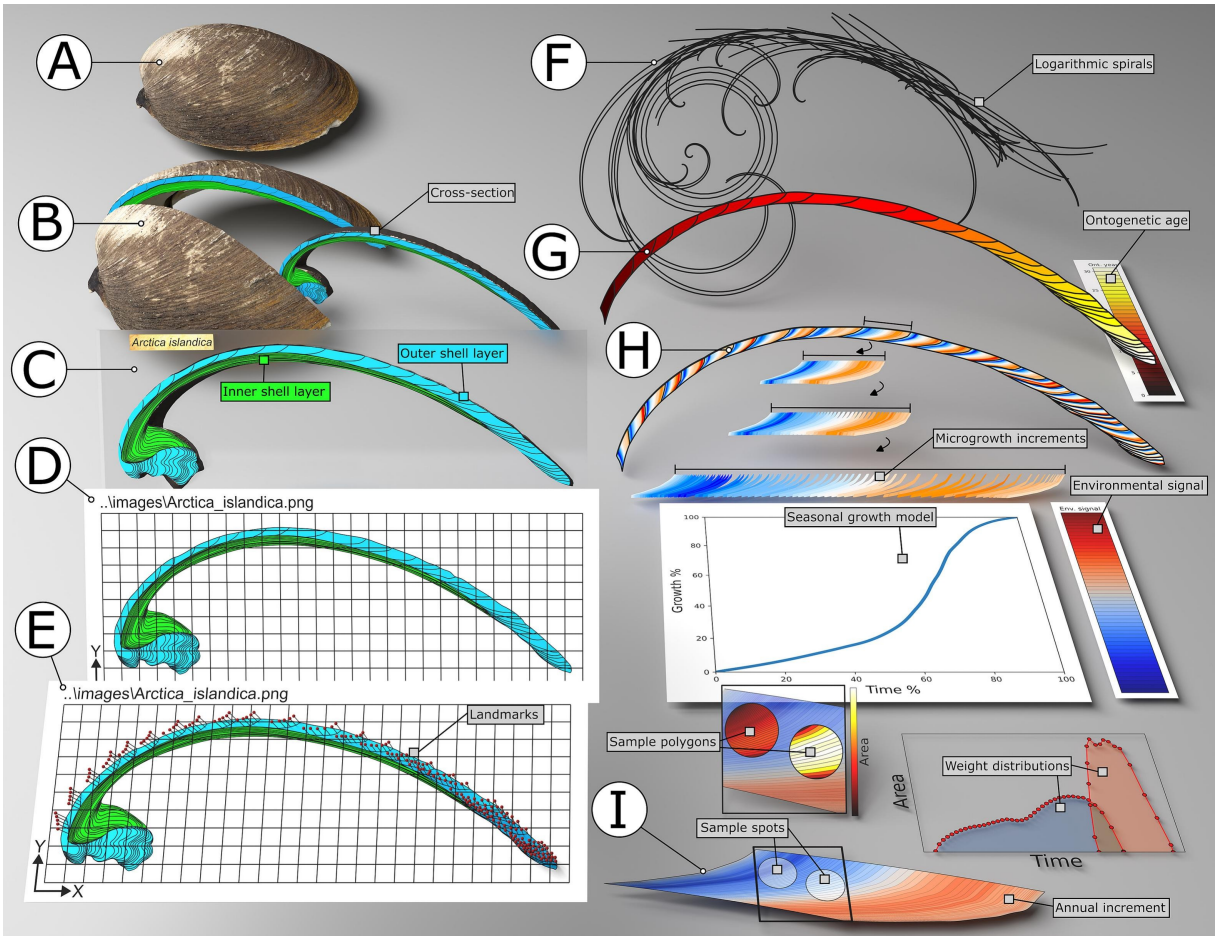

Figure 5.1 Schematic illustration of the steps used to digitally construct shell cross-section. An *Arctica islandica* valve (**A**) was cut along the axis of maximum growth to obtain a several mm-thick cross-section (**B**). This cross-sectioned shell slab was then attached to a glass slide (**C**) and stained with Mutvei solution to enhance the visibility of the growth patterns. The cross-section was photographed with a digital camera (**D**) and landmarks (pixel coordinates) were positioned along the shapes of the annual growth lines (**E**), i.e., of the OSL. Logarithmic spirals were constructed according to the stacking increment model of Ubukata (2001) using the landmark coordinates (**F**). The spirals connected the inner and outer edges of each annual increment (**G**). Microgrowth increments were interpolated between the start and the end of annual growth lines following the inner and outer spirals (**H**). The width of the microgrowth increments were determined by the seasonal growth model and an underlying signal assigned to each growth increment. Two sample spots (indicated as circles) exemplarily positioned within an annual increment (**I**). As the microgrowth increments were numerically described, the area of an increment that is covered by a sample spot can be calculated and the weights of each microgrowth increment can be deduced. Although the two samples do not overlap spatially, there is a clear temporal overlap between them.

Image Composite Editor) generating high-resolution composite images of the cross-sections. (2) Landmarks were then positioned along the clearly visible annual growth lines (Fig. 5.1E) and their pixel coordinates were retrieved. (3) Subsequently, the growth geometry for each annual increment was then digitally reconstructed according to the principles of the 'stacking increments model' presented by Ubukata (2001), which describes the accretionary shell growth of the outer shell layer as the result of 'stacking increments' where the geometry of a given increment determines the geometry and dimension of the successive increment (Supporting Information Fig. S5.1). To construct a stacking increments model, four growth parameters need to be defined (cf. Ubukata, 2001), namely, the ratio between the movement of the pallial line and the growth of the mantle (G); the ratio between the amount of deposited shell material at the outer edge and the growth of the mantle (C); the ratio between the amount of shell accretion at the pallial line (inner edge) and the growth of the mantle (C'); the magnitude of a given growth step (ε). At this stage, the growth fronts are represented by simple straight lines and can be represented by the vector $\overrightarrow{L}$ defined between two points P_1 and P_2 in Cartesian coordinates (Supporting Information Fig. S5.1), with the length of the growth front at time step s (L_s) defined as the magnitude of $\overrightarrow{L}$:

$$L_s = \left\| \overrightarrow{L} \right\| = \sqrt{(x_2 - x_1)^2 + (y_2 - y_1)^2} \tag{5.1}$$

with $\overrightarrow{P_1} = \begin{pmatrix} x_1 \\ y_1 \end{pmatrix}$, $\overrightarrow{P_2} = \begin{pmatrix} x_2 \\ y_2 \end{pmatrix}$. The remaining variables can be calculated by:

$$\begin{gathered} \varepsilon L_s G = \varepsilon \times L_s \times G, \\ \varepsilon L_s C = \varepsilon \times L_s \times C, \\ \text{and} \\ \varepsilon L_s C' = \varepsilon \times L_s \times C' \end{gathered} \tag{5.2}$$

The dimension of the successive growth front of the following discrete time step $s + \Delta s$ is then defined by

$$L_{s+\Delta s} = (1 + \varepsilon) L_s - \varepsilon L_s G \tag{5.3}$$

In the next step, the vector $\overrightarrow{L}$ is scaled to the length $\varepsilon L_s G$ to determine the position of P_G along the line segment $P_1 P_2$. Similarly, the vector $\overrightarrow{L}_\perp$ perpendicular to $\overrightarrow{L}$ is scaled to $\varepsilon L_s C$ as well as to $\varepsilon L_s C'$ and anchored at, respectively, P_2 and P_G to calculate the position of both

P_C and $P_{C'}$ (Supporting Information Fig. S5.1). Here, the position of $P_{C'}$ equals the inner point of the newly generated growth front P_3. Finally, P_4 can be calculated as the end of a line segment with the length $L_{s+\Delta s}$ starting at P_3 and intersecting P_C. The resulting points P_3 and P_4 describe the geometry of the growth front at $s+\Delta s$ and serve as new starting points for the following iteration, i.e., $P_{1s+\Delta s}$ and $P_{2s+\Delta s}$. If the growth parameters are constant, the shape of the stacking increments necessarily follows logarithmic spirals (Ubukata, 2001), allowing to calculate the spirals for the inner and outer edges (Fig. 5.1F and Supporting Information Fig. S5.1) of the OSL. In this study, a stacking increments model was constructed for each individual annual increment. Therefore, the growth parameters G, C, C' and ε had to be identified for each model. This was achieved by using the landmarks with known coordinates that were placed on digital microscope images of cross-sections positioned along annual growth lines (Supporting Information Fig. S5.2A). Since the stacking increments model generates straight instead of curved growth lines, the shape of the growth front was not considered at this stage but was addressed in a subsequent step (see below). Thus, the first and the last landmark of the growth lines served as the end points P_1, P_2, P_3 and P_4 of a given annual increment (Supporting Information Fig. S5.2B and C) from which the growth parameters were calculated. P_G was determined from $\overrightarrow{L}_\perp$ that intersects with $P_{C'}$ $(= P_3)$ from which $\varepsilon L_s G$ and $\varepsilon L_s C'$ was calculated. Likewise, P_C was found as the intersection of $\overrightarrow{L}_\perp$ starting at P_2 and the line P_3P_4 allowing to determine $\varepsilon L_s C$. Additionally, L_s and $L_{s+\Delta s}$ are defined as the magnitude of $\overrightarrow{P_1P_2}$ and $\overrightarrow{P_3P_4}$ (Fig. S5.2F). Finally, the increment-specific growth parameters were obtained by:

$$\varepsilon = \left(\frac{L_{s+\Delta s} + \varepsilon L_s G}{L_s}\right) - 1$$
$$G = \frac{\varepsilon L_s G}{\varepsilon \times L_s}, \quad C = \frac{\varepsilon L_s C}{\varepsilon \times L_s} \quad \text{and} \quad C' = \frac{\varepsilon L_s C'}{\varepsilon \times L_s} \tag{5.4}$$

According to these parameters, the stacking increments model was used to construct the logarithmic spirals that describe the outer and the inner edge of the respective annual increment (Supporting Information Fig. S5.3). The origin of the inner and outer spirals was numerically approximated by reverting the process of stacking increments model, i.e., calculating the geometry of the increment of a former instead of a successive time step, resulting in progressively smaller increments. Here, we iteratively minimized the Euclidean

distance D between P_1 and P_2 to approximate the origin, so that

$$\lim_{n\to\infty} D_n = \lim_{n\to\infty} \left\| \overrightarrow{P_{2,n}} - \overrightarrow{P_{1,n}} \right\| \approx 0 \tag{5.5}$$

where $\overrightarrow{P_{1,n}}$ and $\overrightarrow{P_{2,n}}$ represent the position of P_1 and P_2 at iteration n. From this origin point, the radial distance r_1 and r_2 as well as the angles θ_1 and θ_2 were calculated (Supporting Information Fig. S5.3E and F). Given a logarithmic spiral defined in polar coordinates as

$$r = ae^{b\theta}, \tag{5.6}$$

the parameters a and b can be calculated using the angle difference (θ_Δ) between θ_1 and θ_2 (Fig. S5.3G):

$$\begin{aligned} b &= \frac{\ln\left(\frac{r_1}{r_2}\right)}{\theta_\Delta}, \\ a &= \frac{r_1}{e^{b\theta_1}} \end{aligned} \tag{5.7}$$

depicting the scaling factor and the growth rate of the spiral, respectively. Accordingly, the inner and outer spirals can be constructed, with the start of the annual increment being defined by θ_1 and the end by θ_2 (Supporting Information Fig. S5.3H and I). Finally, the last steps generated the sub-annual microgrowth increments for each annual increment by taking their logarithmic growth into account (Supporting Information Fig. S5.4). Therefore, the landmarks of the annual growth lines were connected to the outer and inner spiral producing a closed polygon covering the entire annual increment (Supporting Information Fig. S5.4A). According to the seasonal growth model of *A. islandica* (taken from Höche et al., 2022), the percentage of shell growth was determined for each sub-annual time step (Supporting Information Fig. S5.4B). This allowed to resample the inner and outer spiral based on their arc lengths (between θ_1 and θ_2). Since the shape of the growth lines (i.e., start and end growth line of each increment) were described by heterogeneously distributed landmarks, a smoothing step was included (Supporting Information Fig. S5.4C). This was done by normalizing the growth lines, so that the first landmark is located at (0,0) and the last at (1,0) (Supporting Information Fig. S5.4C), enabling the equidistant resampling of those lines. Then, the start and end growth lines were smoothed by fitting cubic splines to the

resampled points. These cubic splines were discretized equidistantly producing a sequence of points that were transformed back to their original position between the inner and the outer spirals (Supporting Information Fig. S5.4D). To generate a gradual transition from the inner spiral to the outer spiral, the parameters a and b were linearly interpolated, resulting in n intermediate logarithmic spirals that smoothly morphed between the inner and the outer spirals. These spirals were resampled according to their arc lengths and the seasonal growth model (Supporting Information Fig. S5.4E). The smoothed start and end growth lines were then cut into $n+1$ segments and equidistantly resampled (Supporting Information Fig. S5.4F and G). This resulted in pairs of segments, each containing an equal number of points, with segments on the starting growth line corresponding to segments on the ending growth line. By linearly interpolating the resampled points between a start segment and an end segment and position them between the two neighboring spirals, it was possible to generate clearly defined boundaries for the individual microgrowth increments that smoothly change their shape from the starting growth line, across the annual increment toward the end growth line (Supporting Information Fig. S5.4H and I).

This method allowed to numerically simulate the accretionary growth of *A. islandica* by discretizing the continuous growth into microgrowth steps. For the digital shell models, a resolution of 2000 microgrowth increments per annual increment was used. The geometry of each individual microgrowth increment was therefore represented as a two-dimensional polygon (see Fig. 5.1H, I), which enabled the digital resampling of specific shell portions to imitate the extraction of geochemical samples (Fig. 5.1I). The corresponding value, i.e., the geochemical signal measured, was then determined as the weighted sum of the values that were assigned to each microgrowth increment (Fig. 5.1I). The corresponding weights were determined by calculating the intersecting area between the microgrowth increments and the sample spot geometry, relative to the total area of the sample (Fig. 5.1I). As the microgrowth increments are temporally constrained, each sample spot obtained a unique time-dependent weight distribution (Fig. 5.1I). All calculations and statistics were performed using Python (3.12.3).

5.2.2 Synthetic environmental signals

Two environmental signals (SST and phytoplankton abundance; Fig. 5.2A) were generated to assign discretized values to individual microgrowth increments (see section 5.2.1). These

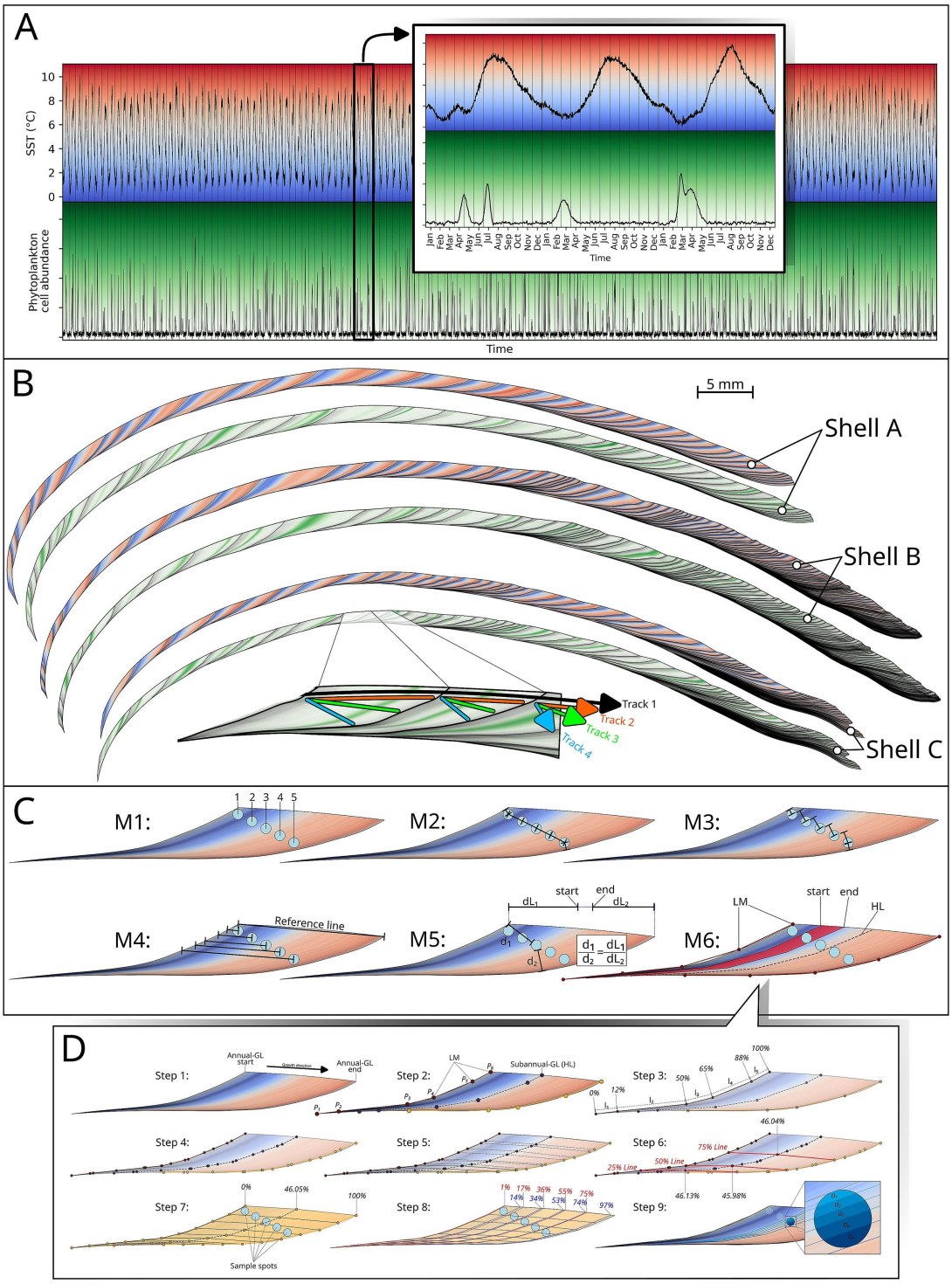

Figure 5.2 Synthetically generated sea surface temperature (SST) and relative phytoplankton cell abundance time-series (**A**). Numerical models of the shell cross-sections (**B**)

Figure 5.2 (continued) were constructed based on empirical data from the outer shell layer of three *Arctica islandica* shells collected in northeast Iceland. Color variations in the shell models represent the environmental signals (from **A**) that were recorded in the shell during each moment of growth in the form of isochronous, subannual microgrowth increments. Tracks 1 to 4 schematically illustrate the relative positioning within the cross-sections of four different sampling tracks along which non-overlapping, digital sample spots (300 and 80 µm diameter) were placed. To temporally constrain each sampling spot, six different alignment methods were applied and tested (**C**). Panel **D** depicts the steps performed for alignment method 6 (M6). GL = growth lines; HL = helping lines; LM = landmarks. Information on the different alignment methods is provided in the Materials and Method section.

data were produced from randomly generated base signals with additional noise (e.g., Smith et al., 2023). The SST time-series (Fig. 5.2A) was based on monthly instrumental SST data from Iceland (Grímsey and Raufarhöfn; Hanna et al., 2006). An SST chronology was randomly generated using monthly averages, fitted with cubic splines and complemented with stochastic noise. The noise component was generated using the discrete Ornstein–Uhlenbeck differential equation aiming to imitate random environmental fluctuations (Smith et al., 2023). The dataset simulated a seasonally oscillating environmental signal. Conversely, the synthetic phytoplankton abundance (Fig. 5.2A) aimed to model individual blooms, as they can be reconstructed from barium-to-calcium ratios (e.g., Marali et al., 2017; Doré et al., 2020; Fröhlich et al., 2022; Schöne et al., 2023). Such profiles were characterized by variable peak magnitudes (between spring and summer) that episodically interrupt the constant background level (e.g., Gillikin et al., 2008). This behavior was modeled using Gaussian functions (Zhai et al., 2012), where the number of peaks (between 0 and 2), their timing (early spring to late summer), height, and width (5 to 20 days) were randomly determined. By generating 135 years of synthetic time-series, multiple environmental patterns were encompassed.

According to the formation time of the microgrowth increments, discretized signals were assigned to corresponding increments (Fig. 5.2B). This allowed to effectively imitate the incremental recording of environmental variables throughout shell growth. We assumed that (1) no time lag existed between the occurrence of the environmental signal and its encoding in the shell, (2) the archived values represent the corresponding environmental signals and (3) that the value assigned to a microgrowth increment is constant and does not change across its geometry.

5.2.3 Digital sampling experiments

Different digital sampling strategies were conducted to test how various positions of spots within an annual growth increment affect the accuracy of the signal reconstructions. The experiments differed by the direction of the sampling tracks that were used to equidistantly position sample spots (Supporting Information Fig. S5.5 to S5.7). Experiments 1 to 4 (abbreviated as Exp. 1 - Exp. 4) include sampling tracks (Fig.5.2B) that were placed parallel to the outer shell surface (Exp. 1) to tracks that are almost perpendicular to the tangent of the direction of growth (Exp. 4). Criteria for positioning the samples were that spots do not overlap spatially and that a minimum of three samples fit into one annual increment. All experiments were performed using circular sample geometries with a diameter of 300 µm sampling resolution for (i.e., a typical sampling resolution for δ^{18}O and δ^{13}C analyses; Trofimova et al., 2021) and 80 µm (i.e., a typical sampling resolution for element analyses; Fröhlich et al., 2023).

5.2.4 Temporal alignment methods

To compare the reconstructed signal with the underlying signal, the samples were temporally aligned using six different alignment methods (Fig. 5.2C; Table 5.1). For all these alignment methods, the sample spot positions within increments (i.e., growth percentage; %gr) were determined and translated into a temporal framework using a seasonal growth model for *A. islandica* (Höche et al., 2022). The alignment method 1 (M1) was based on the number of sample spots placed within an increment according to which corresponding %gr were calculated by dividing the respective growth increment into equally spaced steps (see Fig. 5.2C). Alignment method 2 (M2) involved digital image analysis to measure the distance between a spot center and a successive spot center as well as the shortest distance to the annual growth lines at the start and end for the first and last samples, respectively. Corresponding %gr then was calculated as the ratio between the cumulative distance to a spot center and the total length considering all segment distances. Alignment method 3 (M3) was also based on the distance between spot centers, but it involved calculations of the shortest distance between a hypothetical sub-annual growth line (visible or non-visible) intersecting a spot center and a subsequent spot center. Alignment method 4 (M4) was based on the shortest distance between a spot center and the annual start growth line. Then, this distance was related to the total width of the increment defined as the distance between the

Table 5.1 Overview and short descriptions of the alignment methods tested in this study. The principles of each alignment method are depicted in Fig. 5.2C and D.

Alignment method	Description	Features
M1	Equally sized growth steps determined by the number of sample spots within an increment.	Simple use, alignment of spot center, equidistant spacing assumed
M2	Shortest distance between successive spot centers and annual growth lines.	Distance measurements, alignment of spot center
M3	Shortest distance between spot center and sub-annual growth line intersecting preceding spot center.	Distance measurements, alignment of spot center, sub-annual growth line identification
M4	Distance between sample spots and annual growth line compared to the length of a reference line spanning from the annual start and end growth line.	Distance measurements, alignment of spot center, distances related to increment width
M5	Shortest distances of sample spot boundaries to annual start and end growth line projected onto a reference line.	Distance measurements, approximating time intervals covered by sample spots
M6	Growth increment morphology approximated. Annual and sub-annual growth lines digitally reconstructed using landmarks. Geometric interpolation steps used to estimate position and coverage of individual samples.	Digital image analysis required, increment shape considered using landmark coordinates, geometric operations required, temporal weight distributions approximated

growth lines at the start and end as measured on the outer edge of the OSL. Alignment method 5 (M5) was modified after the procedure presented by Vihtakari et al. (2016). The measured shortest distances between the perimeter of a sample spot and the growth lines at the start (d_1) and end (d_2) were projected on a distance axis (i.e., the distance between the growth lines at the start and end) as dL_1 and dL_2 so that the ratio d_1/d_2 equaled dL_1/dL_2. This allowed to approximate a time interval covered by a sample spot, unlike M1–M4 which associate a sample spot to a single time value. Similarly, alignment method 6 (M6; Fig. 5.2D and Supporting Information Fig. S5.8), a novel approach developed in this study, approximated the start time and the end time covered by a sample spot. Briefly, this method is based on nine steps. (1) The identification of annual growth lines and, if possible, sub-annual disturbance lines that act as helping lines (i.e., guidelines that help to describe the increment morphology). (2) The positioning of landmarks with known (pixel) coordinates along the growth lines to digitally capture the shape of the increments. (3) Each landmark is then converted into a percentage of the total growth line length based on the individual segments, i.e., the lines between successive landmarks. These percentages were stored and 25 %, 50 % and 75 % added. (4) Each growth line and helping lines is resampled (linear interpolation) according to the percentages, ensuring that each line contains knots with equal percentages. (5) As each growth line provides a similar number of knots, these landmarks can be connected between different growth lines producing lines spanning across the entire increment, i.e., connecting the start and end growth line. (6) If helping lines are used, the 25 %, 50 % and 75 % connection lines can be employed to determine at which percentage the helping line intersects these connection lines. Taking the mean percentage allows the approximation of the %gr that is represented by a helping line. Accordingly, a specific %gr can be assigned to each growth line (i.e., the starting growth line is 0 %gr, the ending growth line is 100 %gr, and each helping line falls between 0 %gr and 100 %gr). (7) The geometry and position of the sample spots is determined. (8) The connecting lines (see step 5) are then used as guidelines to linearly interpolate the shell growth at every %gr between the annual start and end growth line. For example, the growth line at 50 %gr can be reconstructed by finding the 50 %gr position on each connection line and by connecting these points with simple line segments. This step allows to approximate the start as well as the end %gr of a sample spot by taking the shape of the increment into account. (9) After the start and end %gr was defined, the corresponding %gr range can be subdivided into multiple slices using simple linear interpolation. This produces distinct polygons that intersect the entire sample

spot. By calculating the area of the individual polygons within the sample spot (the sum of all polygon areas equals to the area of the sample spot), the relative contribution of each slice with a known %gr to the measured value can be approximated. Finally, the use of the seasonal growth model allows to convert the %gr into absolute calendar dates and therefore time dependent weight distributions can be approximated.

Table 5.2 Averaged Pearson correlation coefficients calculated between the reconstructed signals and the underlying environmental signals (SST and phytoplankton abundance) for all digital experiments (Exp. 1 to Exp. 4) and alignment methods (M1 to M6).

	M1	**M2**	**M3**	**M4**	**M5**	**M6**
Exp. 1	0.93	**0.95**	0.93	0.90	0.68	0.99
Exp. 2	**0.96**	**0.95**	**0.96**	**0.92**	0.68	**1.00**
Exp. 3	0.94	0.94	0.94	0.86	0.69	0.99
Exp. 4	0.88	0.88	0.81	0.81	**0.74**	0.99

5.3 Results

5.3.1 Accuracy of sampling and alignment strategies

All experiments and temporal alignment strategies resulted in generally high degrees of correlations between the synthetic environmental data and the reconstructed signals (Figs. 5.3, 5.4 and Supporting Information Fig. S5.9, S5.10), with a mean Pearson correlation coefficient of 0.89 ± 0.08 (1σ). On average, SST signal reconstructions provided better correlations than the reconstructions of the phytoplankton signal, i.e., $r = 0.96$ and 0.82, respectively. Comparing the two different spot sizes revealed slightly lower average correlations for 300 µm spots ($r = 0.88$) than for 80 µm spots ($r = 0.90$). All sampling strategies showed relatively similar results with Exp. 2 being the highest correlation ($r = 0.91$), followed by Exp. 1 ($r = 0.90$) and Exp. 3 ($r = 0.89$) and finally, Exp. 4 with the lowest correlation coefficient of 0.85. M6 was the most accurate temporal alignment method, with an average Pearson correlation coefficient of 0.99 ± 0.01 (1σ). Both alignment methods (M1 and M2) resulted in correlations of 0.93 followed by M3 and M4 with 0.91 and 0.87, respectively. The least accurate reconstructions were obtained using alignment method M5 with a Pearson correla-

tion of 0.70 ± 0.20 (1σ). Assessing the differences among sampling strategies with respect to alignment methods (Table 5.2) demonstrated that sampling techniques of Exp. 2 resulted in the most accurate reconstructions in combination with M1, M2, M3, M4 and M6. Only alignment method M5 performed best in combination with sampling strategy of Exp. 4.

5.4 Discussion

5.4.1 Sampling strategies

The sampling strategies tested in this study (Exp. 1 to 4) provided generally high degrees of correlations between the synthetic environmental data and the reconstructed signals (Figs. 5.3 and 5.4). Nevertheless, small differences in the resulting accuracies existed among the sampling techniques. The results demonstrate that placing the sample spots within growth increments, i.e., without intersecting annual growth lines and parallel to the shell surface (Exp. 2), generated the most accurate reconstructions. This is because sampling tracks placed along the outer portion of the OSL (Fig. 5.2B; Track 2) allow to fit more samples into an increment resulting in a higher temporal resolution (i.e., lower time-averaging) compared to Exp. 3 and 4. Moreover, avoiding spots intersecting annual growth lines enhances the precision of the alignment, because slowly growing shell portions, like those that are close to annual growth lines, result in largely time-averaged signals. A problem that has received little attention in the sclerochronological literature is temporal overlap of samples even if they do not overlap spatially (Fig. 5.1), introducing reconstruction biases. Using the digital shells, it was possible to calculate the similarity of a sample spot with its preceding sample spot (Supporting Information Fig. S5.11). Interestingly, the experiments showed (Supporting Information Fig. S5.11) that samples can share more than 50 % of the (geochemical) information with a previous sample, especially during times of faster shell growth, which in turn is determined by the seasonal growth model. However, these similarities differed among sampling strategies. When positioning samples following Exp. 1 and 2, spots will largely overlap. By increasing the angle of the sampling track relative to the outer shell surface (Exp. 3 and 4), the extent of overlap can be minimized (Supporting Information Fig. S5.12). Those overlaps are controlled by the increment morphology, the distance between individual samples and the spot diameter, which also influence the temporal resolution. Conclusively, the average accuracy of reconstructed signals was highest for the Exp. 2

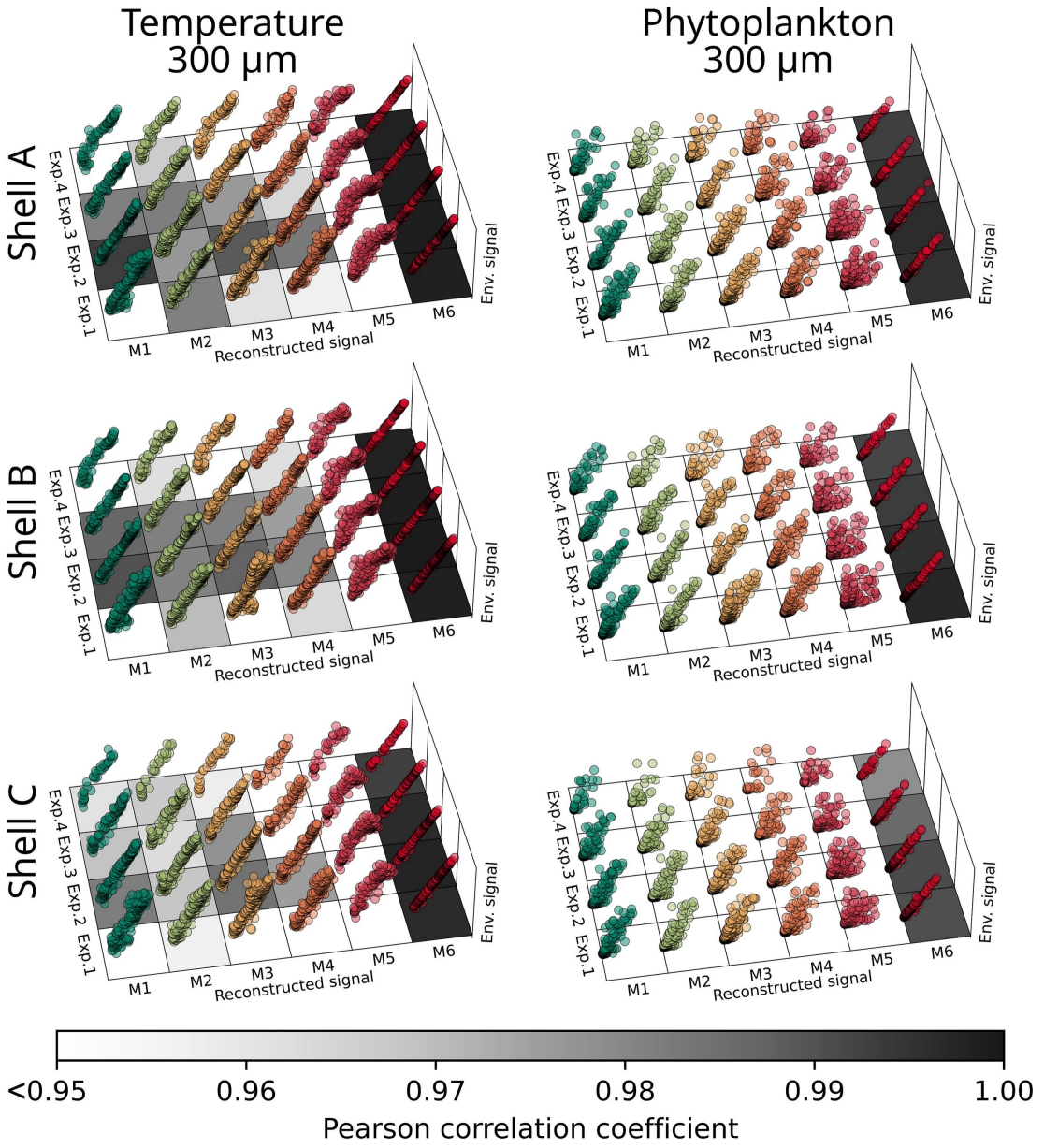

Figure 5.3 Reconstruction accuracies of the digital sampling experiments using 300 µm wide sample spots. The correlation plots are calculated between the reconstructed signals and the underlying synthetic environmental signals, i.e., the sea surface temperature (left) and phytoplankton abundance (right) for the three different digital shell models (Shell A, Shell B and Shell C). Each subplot shows the correlation of a specific sampling experiment (Exp. 1 to 4) in combination with one of the six different temporal alignment methods (M1 to M6). The color-coded patch below each individual experiment denotes the Pearson correlation coefficient of the respective experiment, i.e., darker colors indicate stronger correlations (all values are provided in the Supporting Information Fig. S5.9).

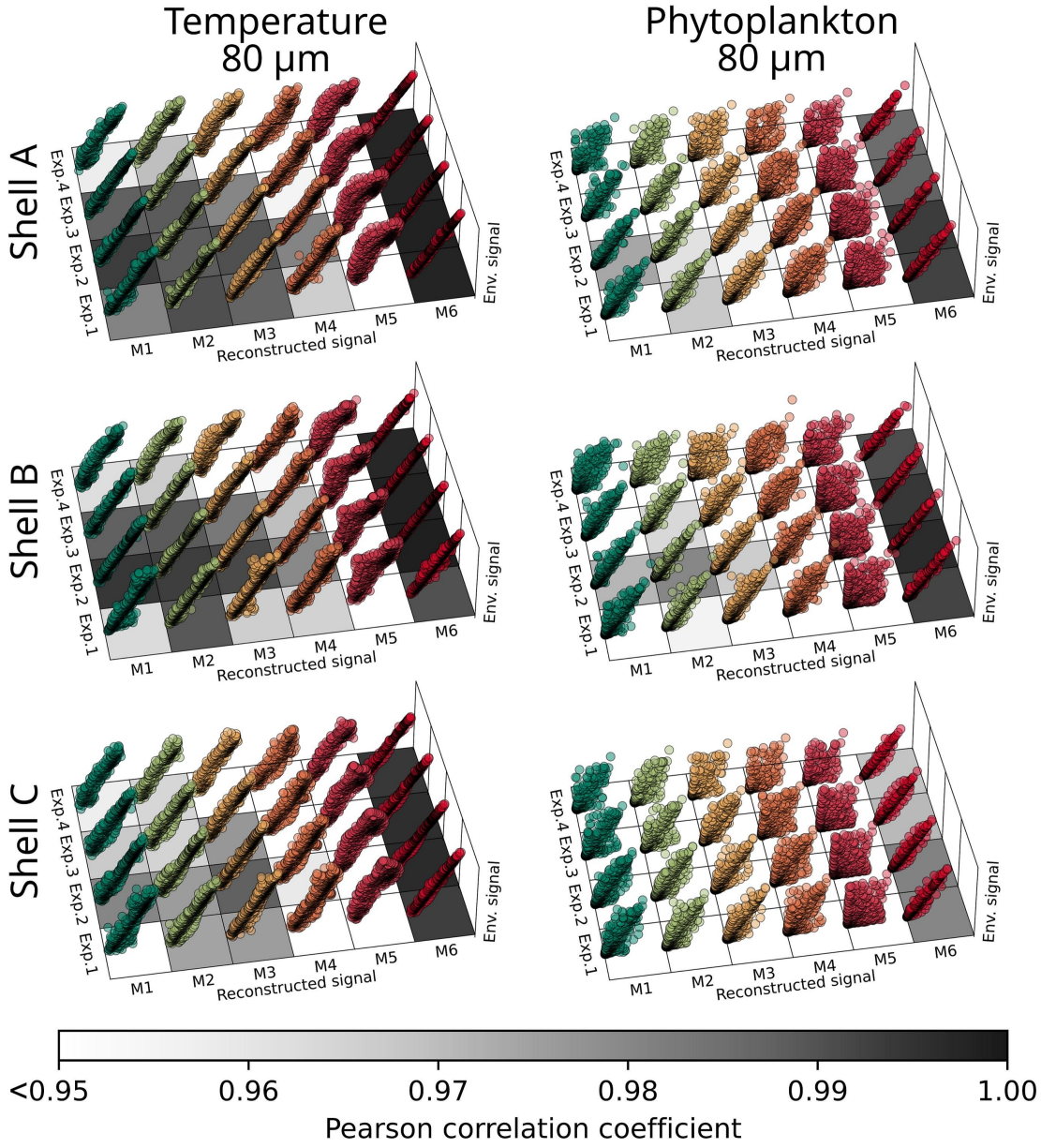

Figure 5.4 Reconstruction accuracies of the digital sampling experiments using 80 µm wide sample spots. The correlation plots are calculated between the reconstructed signals and the underlying synthetic environmental signals, i.e., the sea surface temperature (left) and phytoplankton abundance (right) for the three different digital shell models (Shell A, Shell B and Shell C). Each subplot shows the correlation of a specific sampling experiment (Exp. 1 to 4) in combination with one of the six different temporal alignment methods (M1 to M6). The color-coded patch below each individual experiment denotes the Pearson correlation coefficient of the respective experiment, i.e., darker colors indicate stronger correlations (all values are provided in the Supporting Information Fig. S5.10).

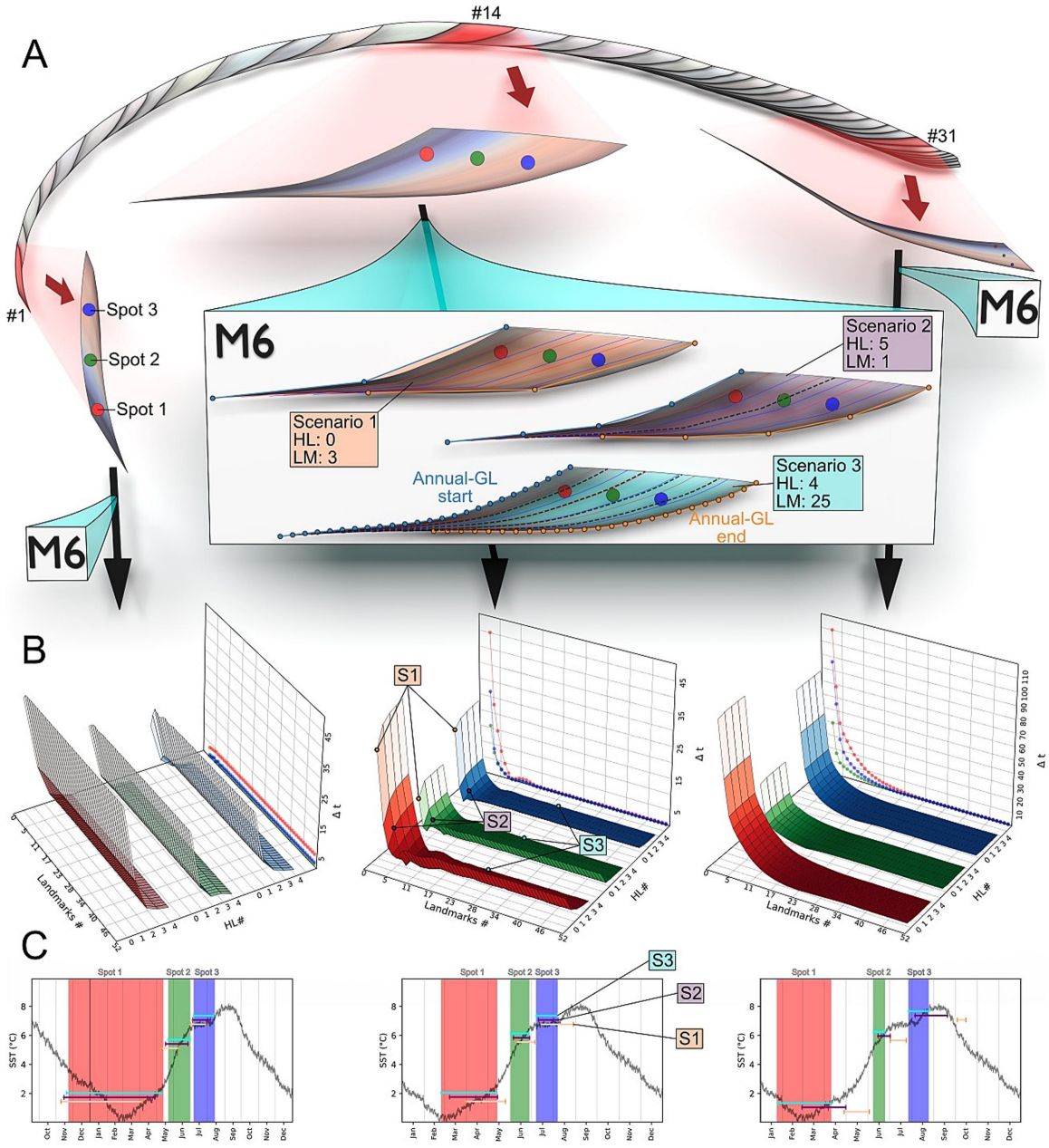

Figure 5.5 Temporal alignment method M6 applied on three sample spots (Spot 1, 2 and 3) positioned in ontogenetically different growth increments, i.e., year 1, 14 and 31 (**A**). As the accuracy of this method is influenced by the number of helping lines (HL) and the number of landmarks (LM) that were used, different configurations that were tested, with three different scenarios (S1, S2, S3) on increment #14 exemplarily depicted in the center box in **A**. The temporal difference (Δt) between the reconstructed ranges and the true ranges was determined by calculating the square root of the sum of the squared differences between the start and end time. The effect of landmark and helping

Figure 5.5 (continued) line number on Δt for all three sample spots are shown in **B**. Reconstructed ranges for Spot 1, 2 and 3 according to scenarios S1 (orange), S2 (purple) and S3 (cyan) indicated as horizontal lines (**C**). Note that for a clearer representation a small offset along the y-axis was added to the samples. Ranges that are covered by each sample are indicated as vertical color-coded bars.

caused by more samples per increment but coincided with larger temporal overlaps. These temporal overlaps should be carefully considered in geochemical analyses by adjusting the sampling technique as well as the temporal alignment method (see section 5.4.2).

5.4.2 Temporal alignment methods

While the sampling strategies yielded closely similar correlation coefficients (section 5.4.1), the alignment method comparison revealed larger differences. Therefore, the accuracy of reconstructed geochemical chronologies suggests to be mostly influenced by the temporal alignment method rather than the sampling strategy. On average, all tested alignment methods (Fig. 5.2C) demonstrably resulted in high correlations between the reconstructed and the environmental signal (Figs. 5.3 and 5.4), indicating all methods appear to be applicable to align geochemical data (Supporting Information Fig. S5.13 and S5.14). If the analysis aims to accurately reconstruct sub-seasonal signals, a careful selection of the alignment method becomes crucial. One significant step toward improving the alignment techniques is the approximation of the temporal ranges covered by individual sample spots (i.e., M5 and M6). Yet, appropriate reconstruction accuracies can be achieved using the temporal alignment M1 to M4, especially when the underlying signal is characterized by gradual, seasonal oscillations like the SST time-series rather than highly dynamic and abrupt changes (i.e., phytoplankton time-series). However, M1 to M4 associate the centroid of spots to single dates rather than ranges (Fig. 5.2C), which can result in strongly misaligned signals and produce biases. In contrast, the time encapsulated within samples was approximated by M5 but, interestingly, resulted in weaker reconstruction accuracies. This outcome suggests that projecting the distance between annual growth lines and sample spots onto a reference line (Fig. 5.2C) can produce biases in the temporal alignment. However, this influence may differ among bivalve species with different growth morphologies, i.e., the growth line shapes of the herein tested *A. islandica* shells may be more affected by this temporal alignment method compared to shapes of other taxa (e.g., *Serripes groenlandicus* for which this method was

initially developed by Vihtakari et al., 2016). In addition, the temporal ranges (between the start and end time of sample spot) determined by M5 were used to calculate the average environmental signal within that time window. As the correlations were computed between the sample signals and those averaged environmental signals, the findings suggest that temporal ranges alone are insufficient to produce accurate high-resolution reconstructions. Temporal alignment method M6 produced by far the most accurate reconstructions (Fig. 5.3). This method linearly interpolated the growth morphology by following the shape of each increment. If the shape is known, the past ventral margins, i.e., previous growth fronts, can be reconstructed for each time step during growth. Along with the spot perimeter, temporally constrained weight distributions can be approximated allowing to mathematically treat temporally overlapping samples. Moreover, M6 appeared to be a robust alignment method showing consistently high correlations, irrespective of the used sampling strategy.

5.4.3 Methodological reflections

To obtain realistic data, the digital shell models were mathematically reconstructed using empirical data. However, the underlying rules, such as logarithmic shell growth (Ubukata, 2001), simplify the complex and chaotic nature of growth and variable environmental conditions affecting shell morphology (Schöne, 2013). The growth was modeled using a defined seasonal growth model allowing no deviations, despite reported inter-annual differences (Höche et al., 2022; Schöne et al., 2022b). A homogeneous distribution of geochemical signals within individual microgrowth increments was assumed although small geochemical heterogeneities may occur among contemporaneously formed shell material, e.g., due to microstructural differences between sub-layers of the bivalve shell (Shirai et al., 2014; Brosset et al., 2022). The impact of these uncertainties on temporal alignment accuracy needs further research. However, we assume that chaotic perturbations would equally affect the reconstruction accuracy of all alignment methods and, thus, our conclusion that M6 is a robust method may remain valid.

The increment shape and width – subject to change through ontogeny (Fig. 5.5A; Supporting Information Fig. S5.15) – influence the number of landmarks and helping lines considered in M6. Testing multiple configurations (Fig. 5.5B) demonstrated that for broad, curved increments, which can be typically observed in shell portions formed during early ontogeny, the number of helping lines is the dominant factor for accuracy. In contrast, for increments

in ontogenetically older shell portions, characterized by longer growth lines and narrower increments, the number of landmarks significantly impacts alignment results (Fig. 5.5C). Therefore, M6 could have achieved even higher accuracies if more helping lines were considered within the numerical simulations.

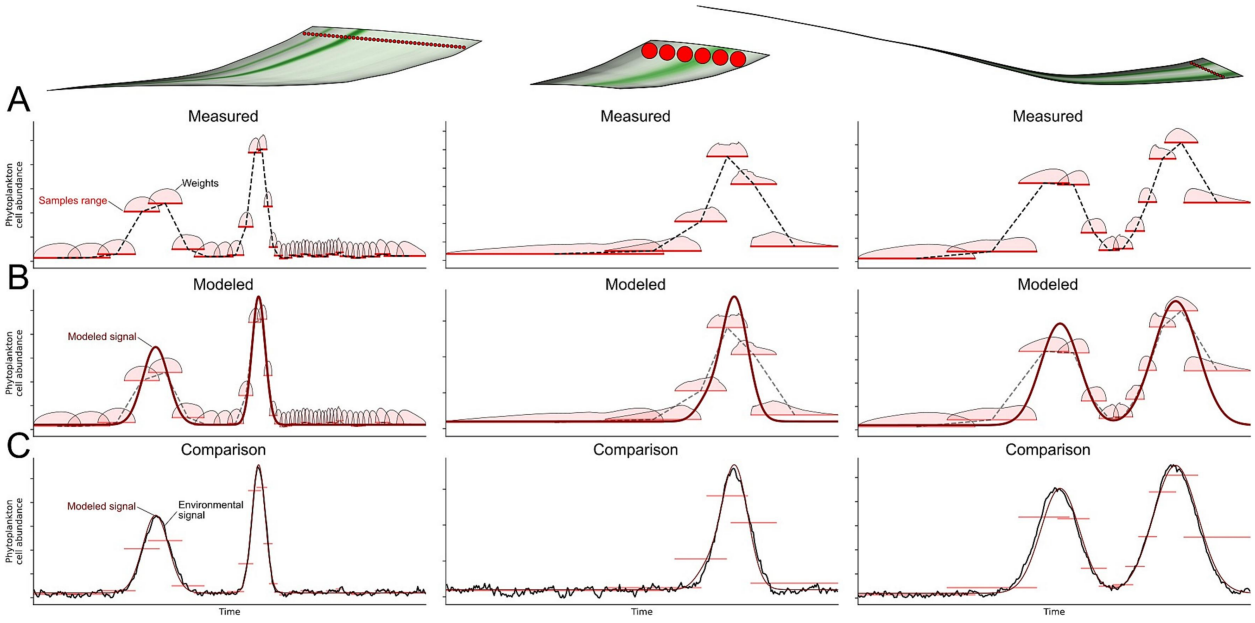

Figure 5.6 Exemplary reconstruction of the underlying phytoplankton signal based on sample spots taken from three increments (left to right). The color intensities within the growth increments correspond to the signal archived in the microgrowth increments (**A**). Red circles indicate the sample spot positions and diameter, i.e., 80 µm (left and right) and 300 µm (center). Temporal ranges of sample spots shown as horizontal, red lines with corresponding weight distribution, as approximated by alignment method M6. The underlying signal, as modeled on the basis of Gaussian functions using numerical optimization algorithms and the approximated sample weights, represented as darkred curves (**B**). Comparison of modeled to environmental signal is shown in **C**.

5.4.4 Modeling geochemical profiles – an outlook

The main purpose of developing M6 was to improve the high-resolution reconstruction of dynamic paleoenvironmental signals, e.g., phytoplankton blooms (e.g., Thébault et al., 2022). In this context, the approximations of temporally constrained weights can provide useful information. Specifically, the timing and magnitude of phytoplankton blooms, as recorded in geochemical profiles (e.g., Poitevin et al., 2022), can be modeled using time-averaged samples and corresponding weights (Fig. 5.6). Since the phenology of a plankton bloom can be described by Gaussian functions (Zhai et al., 2012), a numerical optimization algorithm (e.g., L-BFGS-B) can be used to identify the best fit by minimizing the sum of least squares between weighted and predicted values. This approach can be complemented by a Monte Carlo process that iteratively tests randomly selected initial parameters. This approach was tested on Shell A for different increments and spot sizes. As expected, the measured, raw signals tend to underestimate the peak magnitudes due to time-averaging effects (Fig. 5.6A). However, the fitted models differ from the time-series produced by the sample ranges (Fig. 5.6B) and showed remarkable similarities to the underlying environmental signals (Fig. 5.6C). Applying this modeling approach with the previously proposed method (M6) offers a promising opportunity to accurately reconstruct the absolute height and timing of the peaks, potentially enabling a reliable reconstruction of past phytoplankton dynamics.

5.5 Conclusion

This study systematically tested the influence of different sclerochronological sampling strategies as well as temporal alignment methods on the fidelity of high-resolution reconstructions of geochemical signals encoded in incrementally growing biogenic archives. This was achieved by employing digital models of cross-sections that were empirically constructed from *A. islandica* shells with synthetically generated environmental signals. The discretization of the continuous process of shell formation into numerous, extremely small microgrowth steps allowed the evaluation of how different alignment methods affect the temporal contextualization of geochemical data. Numerical simulations underscored the critical role of both sampling strategies and alignment methods in enhancing the reliability of paleoenvironmental reconstructions. Specifically, placing sample spots parallel to the shell surface without

intersecting annual growth lines demonstrably resulted in the most accurate sampling strategy in combination with most alignment techniques. In comparison to conventional methods, the new temporal alignment method significantly improved the accuracy. This improvement was achieved because the sample spot geometry, the shape of growth lines and the increment morphology was considered within this temporal alignment approach. An artifact of high-resolution geochemical sampling is that sample spots can temporally overlap, as demonstrated by the numerical simulations. The new alignment method can account for these overlaps because all time slices that are encompassed by individual samples can be approximated. Furthermore, temporally constrained weights, as approximated by the alignment method, allowed highly accurate reconstructions of dynamic events such as phytoplankton blooms. Although the method was exemplarily demonstrated on shells of *A. islandica*, the underlying principles and methods developed in this study are not limited to this species but broadly applicable for a wide range of high-resolution biogeochemical archives.

5.6 Supporting Information

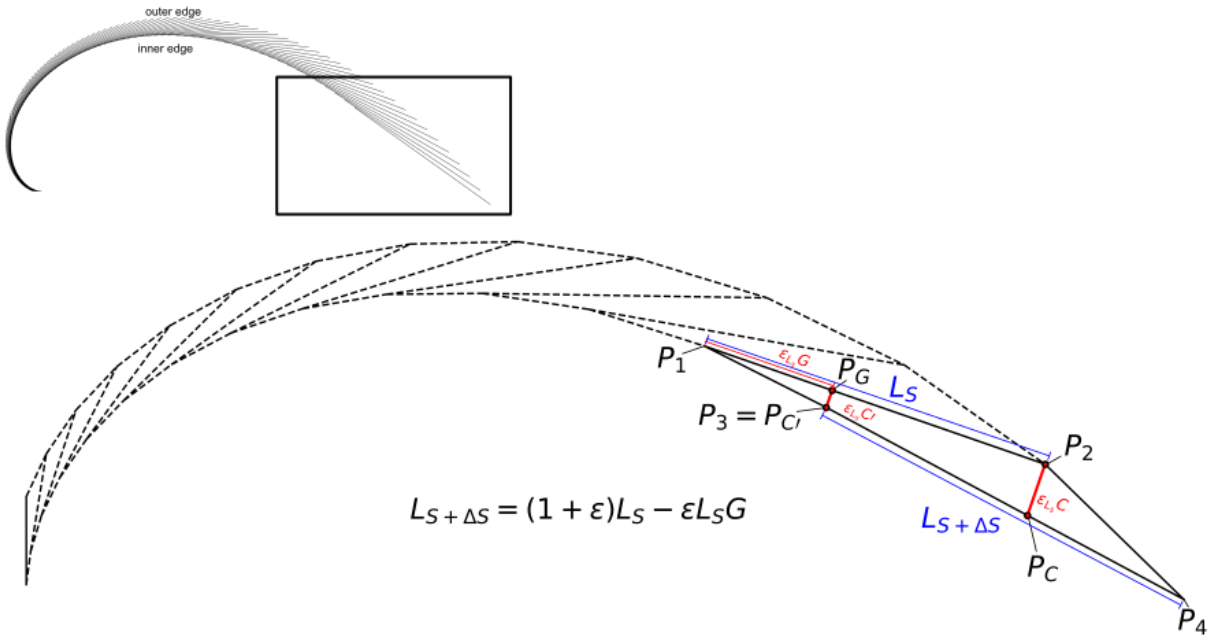

Figure S5.1 Illustration of the underlying stacking increments model developed by Ubukata (2001) with the relevant parameters required for constructing the two-dimensional shell growth of the outer shell layer.

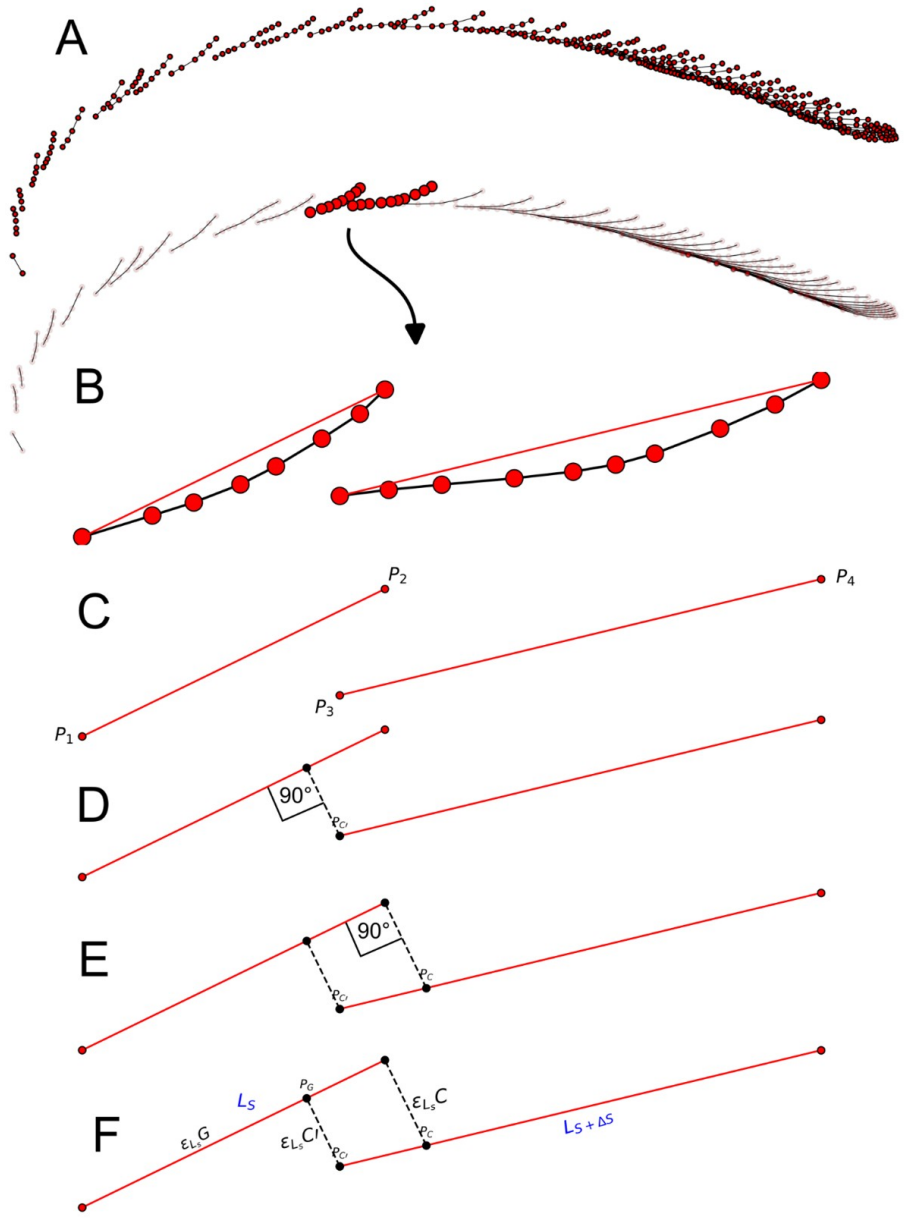

Figure S5.2 Example of landmarks heterogeneously positioned along annual growth lines (**A**) with a magnification of two annual growth lines encapsulating an annual growth increment (**B**-**F**). To construct the stacking increments model, the growth lines were simplified as straight lines (**B** and **C**). The end point P_3 equaled to $P_{C'}$ from which a connecting line was constructed that is perpendicular to the line P_1P_2 (**D**). Similarly, a perpendicular line starting at P_2 and intersecting P_3P_4 defined the position of P_C (**E**). According to these geometries (**F**) the growth parameters used for the stacking increments model were deduced (see main text).

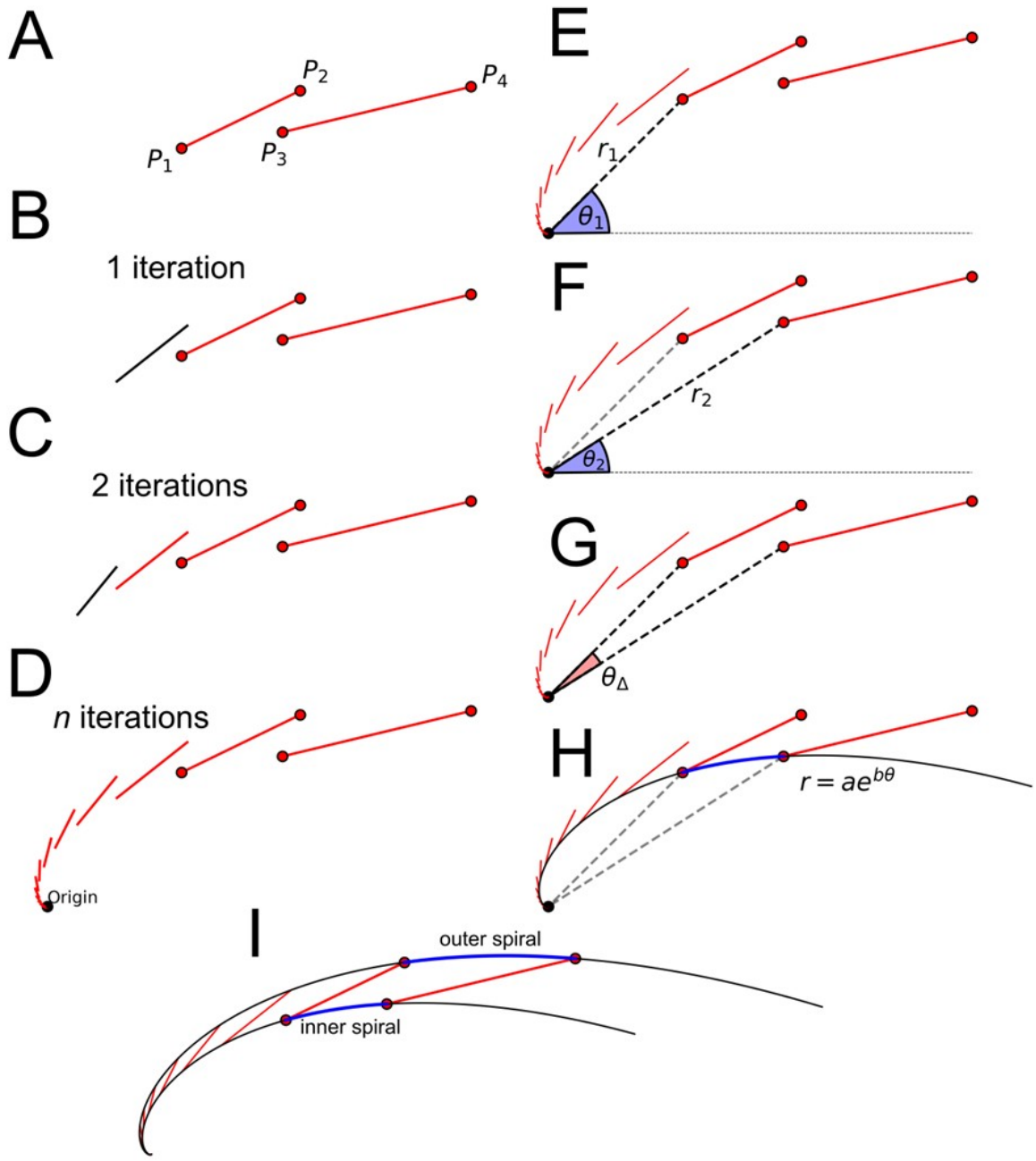

Figure S5.3 Based on the growth parameters of the stacking increments model (calculated according to Fig. S5.2), the simplified growth lines (**A**) were used to iteratively back calculate the origin of the logarithmic spirals (**B** to **D**) that are inherited in the stacking increments model. After the position of the origin was numerically approximated, the logarithmic spirals for the inner and the outer edge were generated (**E** to **I**; see main text for details).

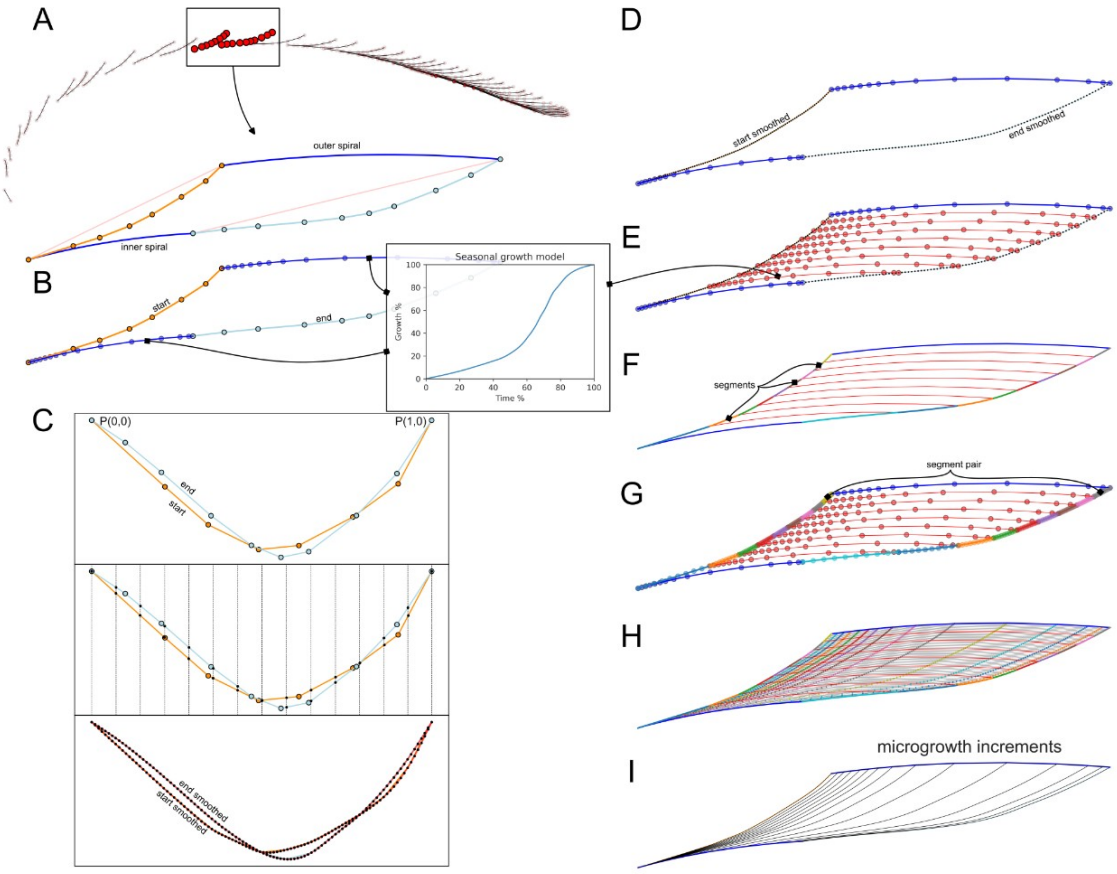

Figure S5.4 Visualization of the method used to interpolate the growth line morphology across an annual increment by considering its underlying logarithmic shell growth. The inner and outer edge (dark blue curves) are described as logarithmic spirals (**A**). These spirals were resampled according to the seasonal growth model and their arc lengths (**B**). Start (orange) and end (light blue) growth lines were normalized, resampled and smoothed using cubic splines (**C**), resulting in smoothed start and end growth lines between the inner and outer edge (**D**). Interpolating the logarithmic spirals (red) and resample them using the seasonal growth model (**E**). Calculate individual segments of the smoothed start and end growth line that are enclosed within two neighboring spirals (**F**). Resample these pair of segments (**G**), interpolate their shape between the start segments and the end segments and place them between the resampled logarithmic spirals (**H**). This method allowed to reconstruct sub annual microgrowth increments which shape is gradually adapting from the start growth line to the end growth line, i.e., left to right (**I**).

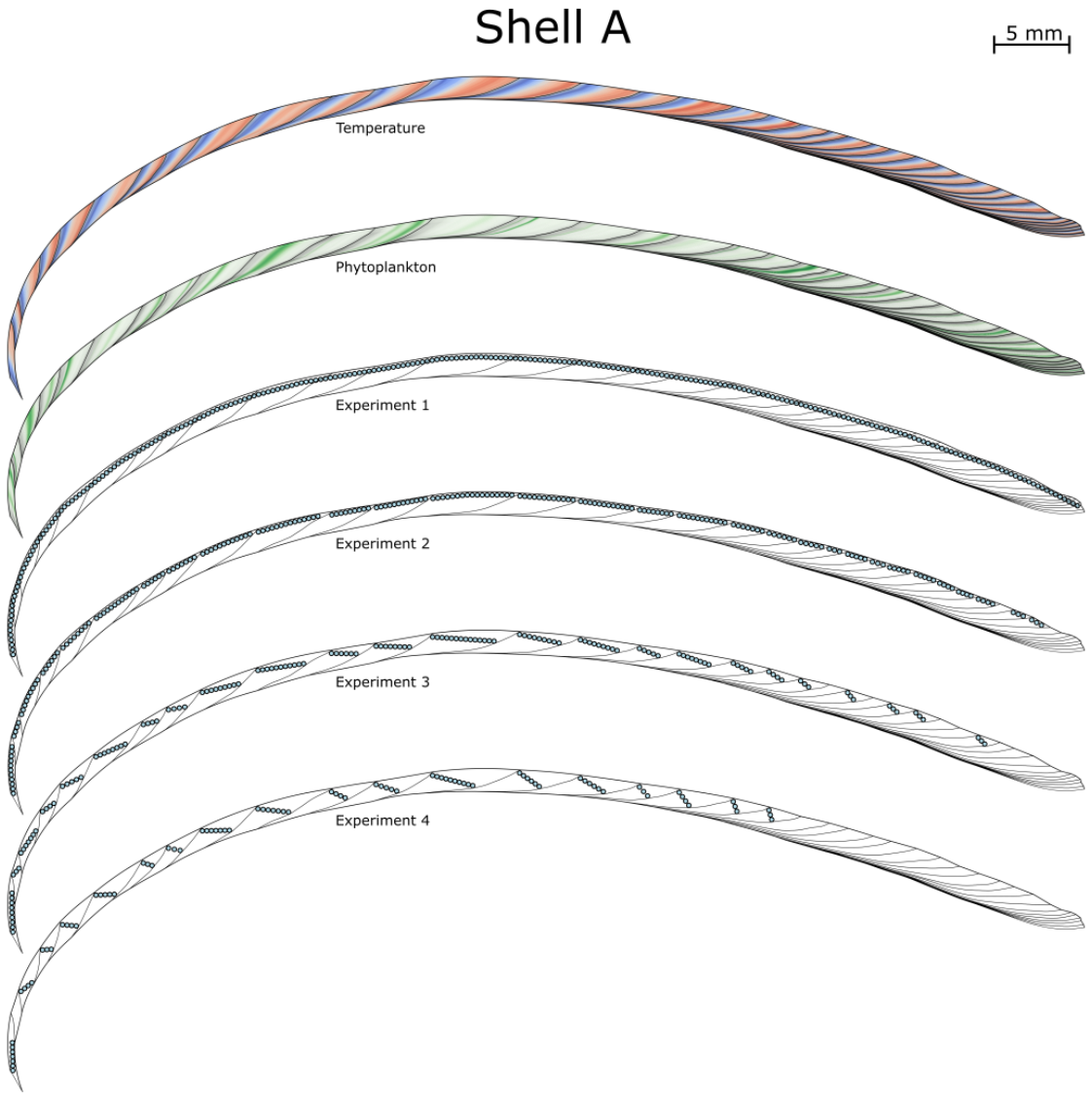

Figure S5.5 Digital shell model produced for Shell A with color-coded temperature (SST) and phytoplankton abundance signals (first two subplots). Experiment 1 to 4 illustrate the relative positioning and orientation of sample spots with a diameter of 300 µm.

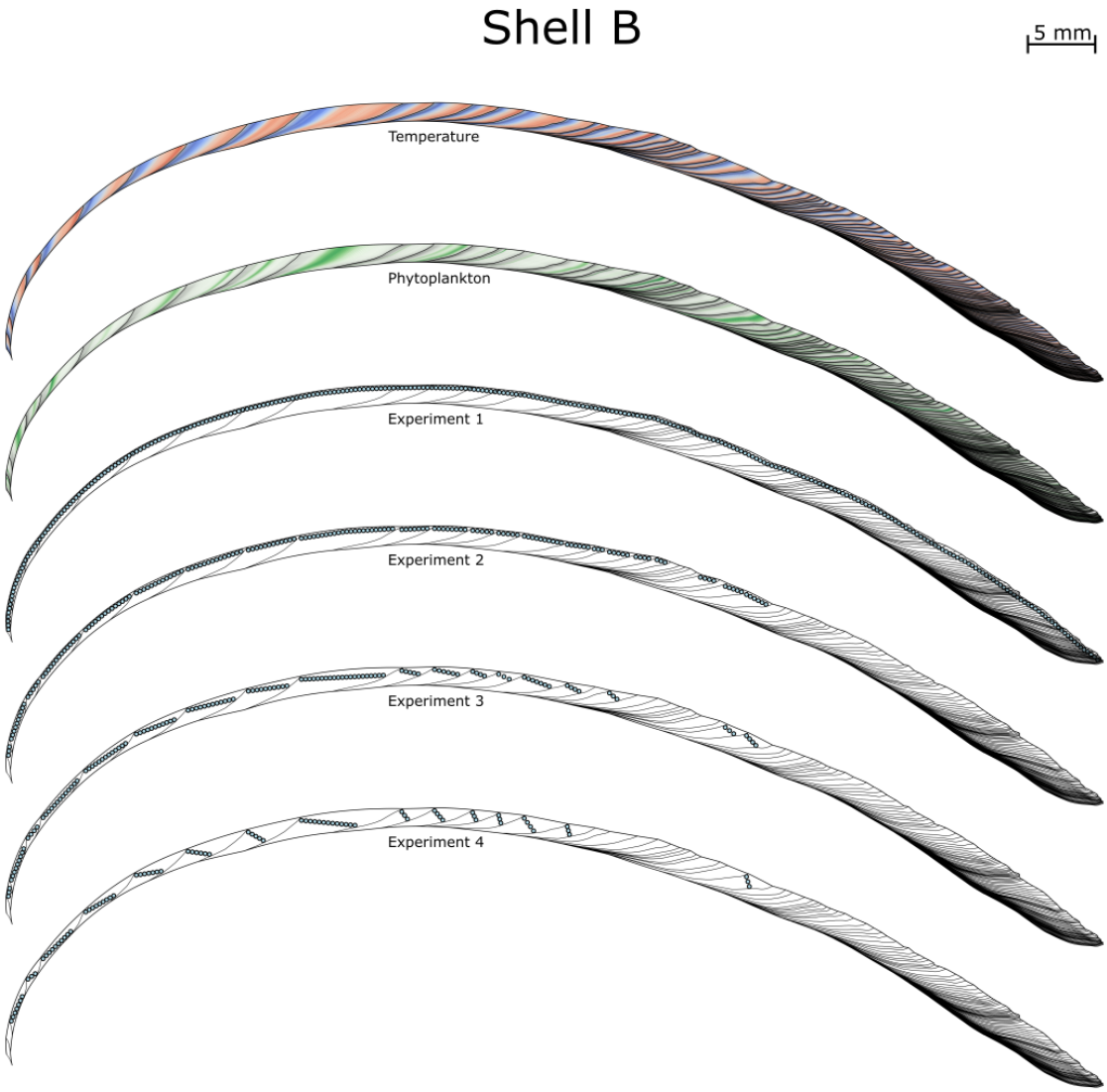

Figure S5.6 Digital shell model produced for Shell B with color-coded temperature (SST) and phytoplankton abundance signals (first two subplots). Experiment 1 to 4 illustrate the relative positioning and orientation of sample spots with a diameter of 300 µm.

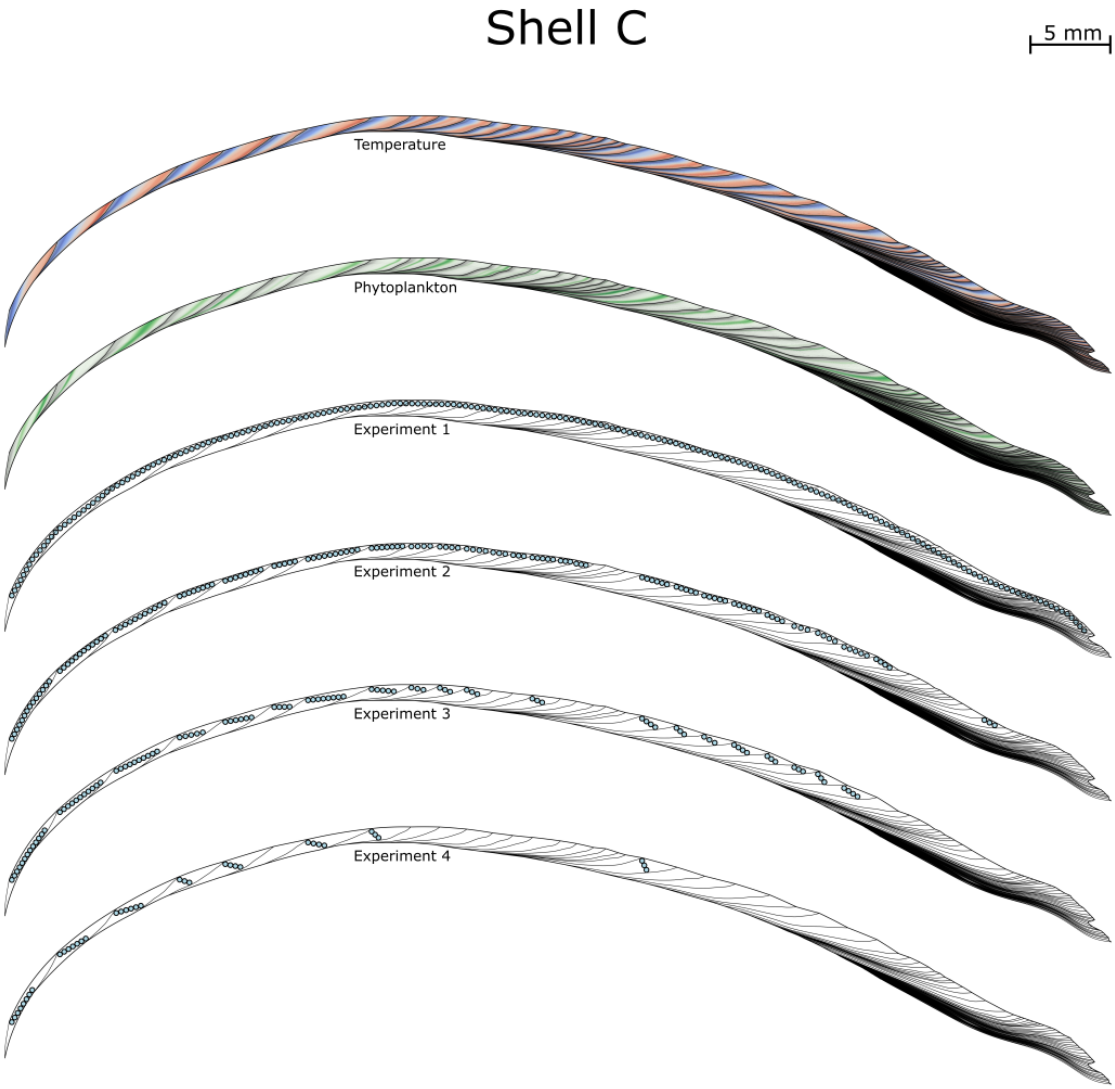

Figure S5.7 Digital shell model produced for Shell C with color-coded temperature (SST) and phytoplankton abundance signals (first two subplots). Experiment 1 to 4 illustrate the relative positioning and orientation of sample spots with a diameter of 300 µm.

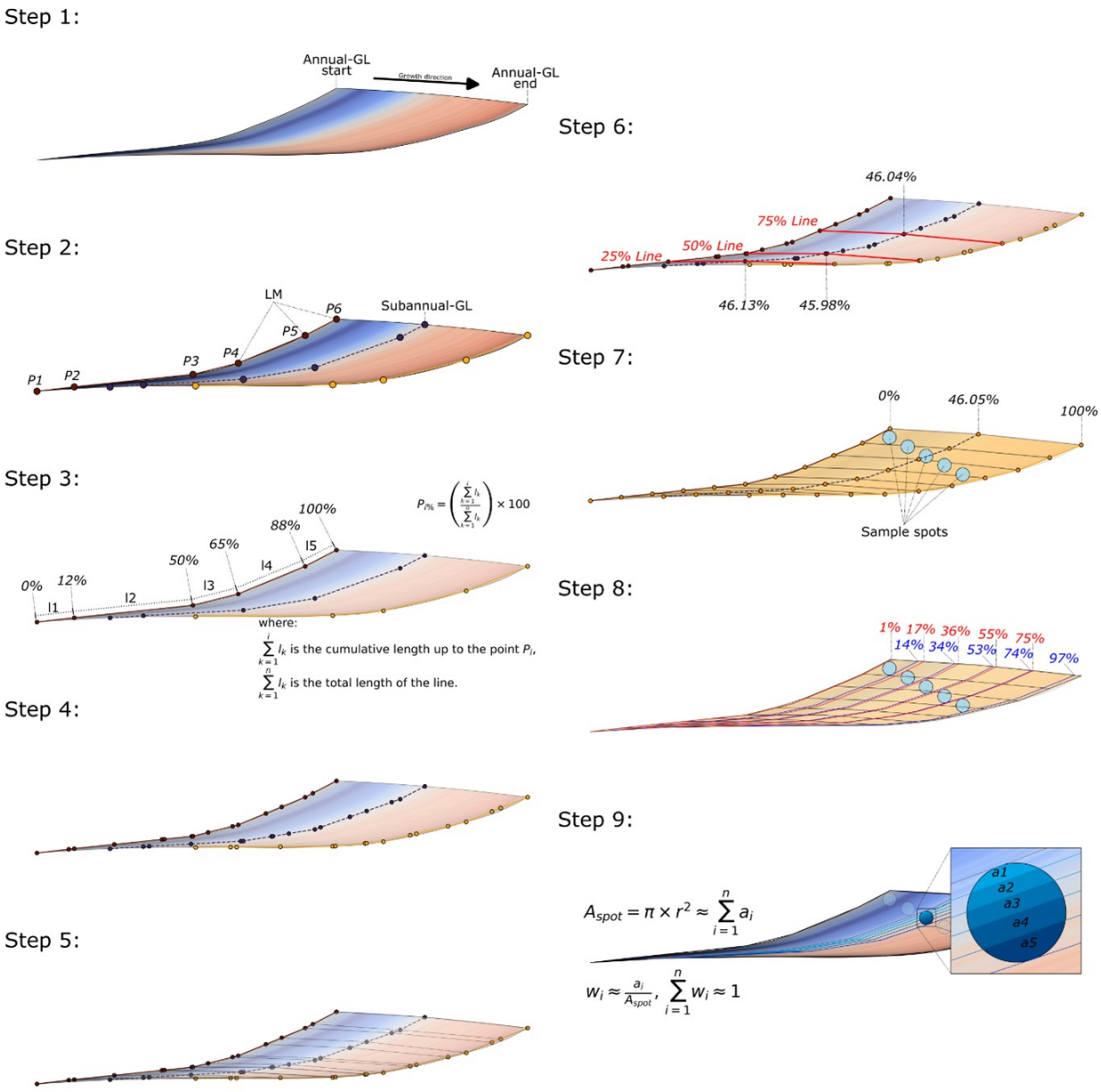

Figure S5.8 Steps involved in the temporal alignment method M6. Identify the growth lines (GL) that define the annual increment, i.e., the start and end growth line (Step 1). Using digital image analyses tools to mark the shape and curvature of each GL by positing landmarks (LM) along their geometry. Likewise, mark sub-annual growth lines (disturbance lines), if visible within the increments (Step 2). Calculate the percentage of each landmark segment (l_i) using the ratio between cumulative length up to the given landmark at position i and the total length of the growth line (Step 3). Resample each

Figure S5.8 (continued) growth line by linearly interpolating according to the previously determined percentages so that all growth lines contain a similar number of knots (Step 4). If not included, add knots at 25%, 50% and 75%. Generate connecting line segments between the knots of equal percentages (Step 5). If sub-annual GL were marked, calculate at which percentage the 25%, 50% and 75% connection lines intersect with the sub-annual GL (Step 6). This step allowed to assign an approximated growth percentage to the sub-annual GL which served as helping lines. Identify the position of the sample spots within the increment (Step 7). By linearly interpolating along the connecting lines, it is feasible to approximate the hypothetical microgrowth lines at each point within the increment (Step 8) allowing to identify at which growth percentage a sample spot starts (red values in Step 8) and ends (blue values in Step 8). Approximated growth percentages can then be converted into a time-domain using a seasonal growth model. Moreover, following the method illustrated in Step 9, it is possible to approximate the temporally constrained weight distribution for each sample spot, by sub sampling between the start and end growth percentage of a sample spot by generating smaller slices intersecting the sample spot.

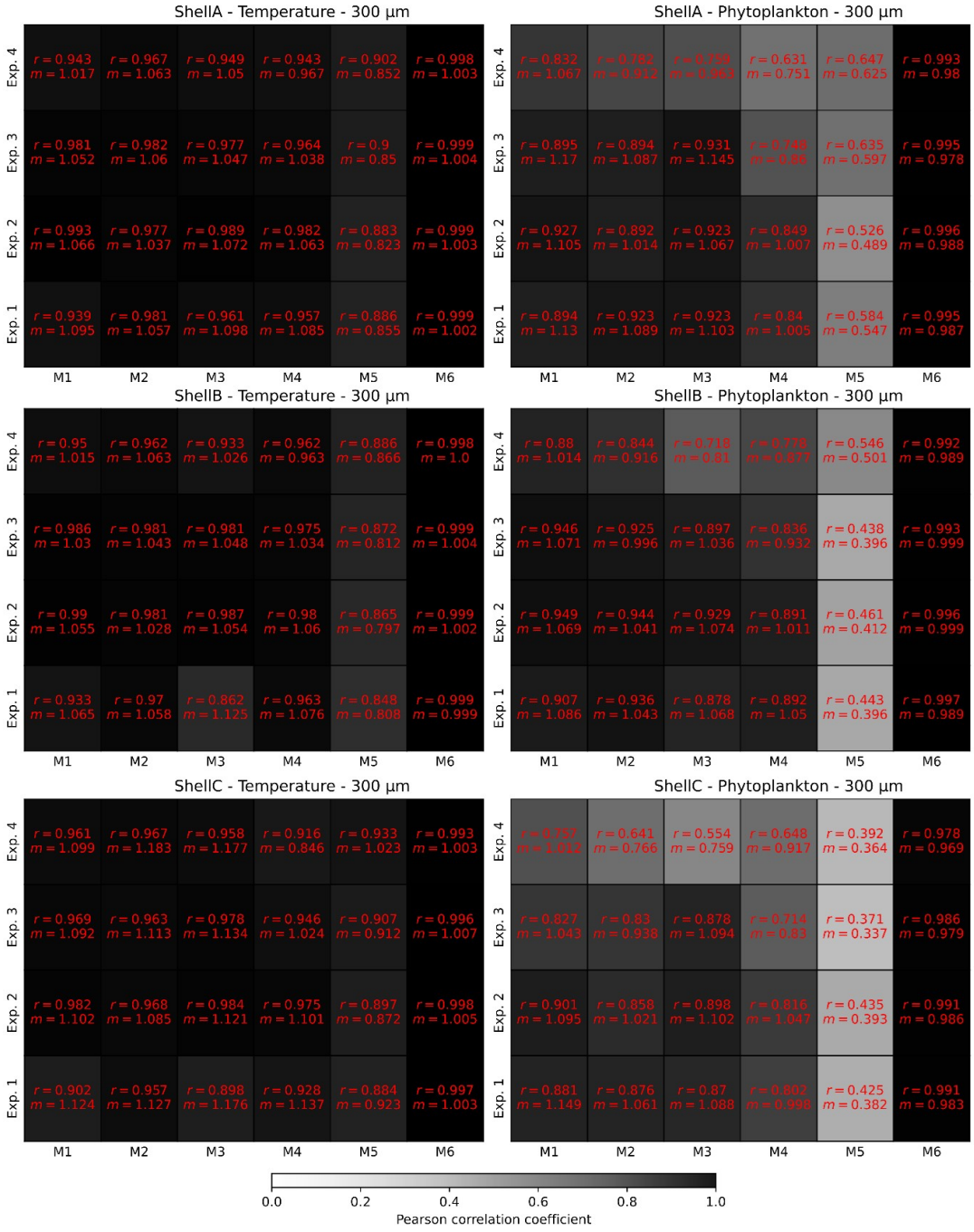

Figure S5.9 Resulting accuracies (Pearson correlation coefficients r) between reconstructed signals and underlying (synthetic) data obtained by the different sampling experiments in combination with the different alignment methods, using circular sample spots of 300 µm diameter. Grey scale indicates the strength of the Pearson correlations. Additionally, the slope m of the linear regression model is provided.

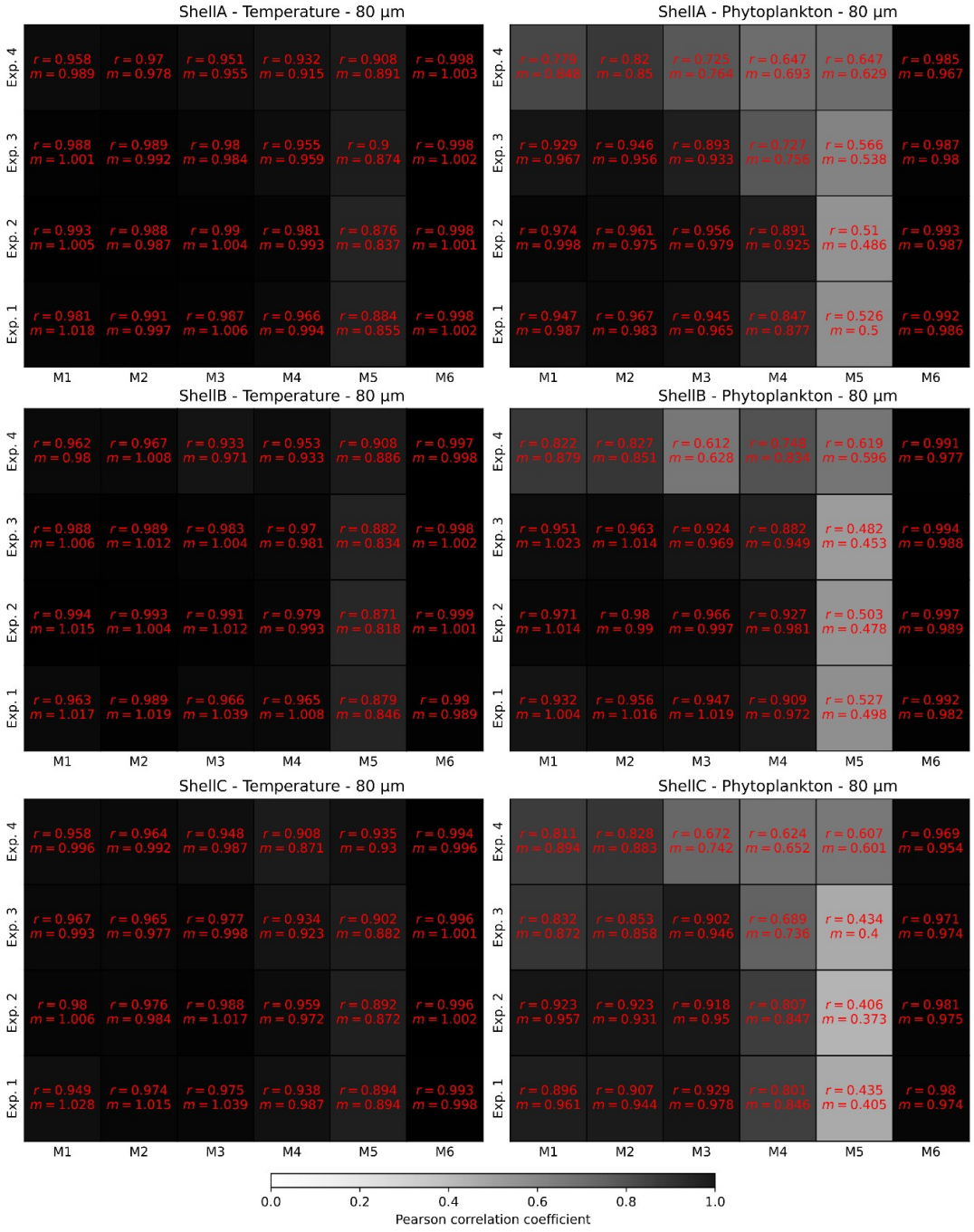

Figure S5.10 Resulting accuracies (Pearson correlation coefficients r) between reconstructed signals and underlying (synthetic) data obtained by the different sampling experiments in combination with the different alignment methods, using circular sample spots of 80 µm diameter. Grey scale indicates the strength of the Pearson correlations. Additionally, the slope m of the linear regression model is provided.

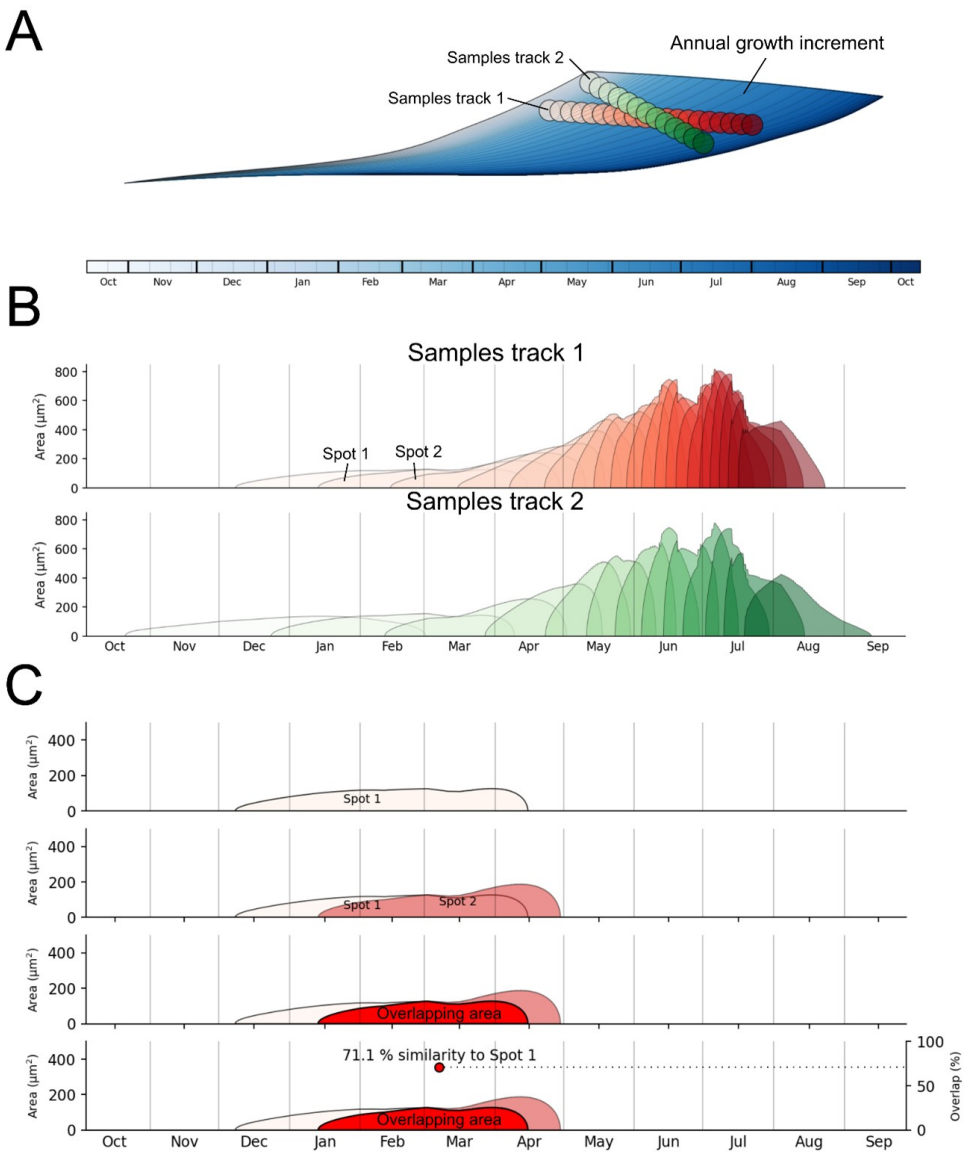

Figure S5.11 To illustrate the degree of overlap between sample spots, two hypothetical sample tracks were placed across an annual growth increment (**A**). The temporally constrained weight distributions of each spot, which is proportional to the area of a microgrowth increment within a sample spot, are illustrated in **B**. Demonstrably, sample spots are overlapping temporally, although no spatial overlap exists (e.g., compare first sample spot of track 1 with first sample spot of track 2). This demonstrates that sample spots can contain similar geochemical information although different shell portions were sampled. To quantify the degree of similarity among spots, the overlapping area between two sample spots were calculated and divided by the total area of the former (**C**). Hence, the resulting percentage describes how similar spot 2 is relative to spot 1.

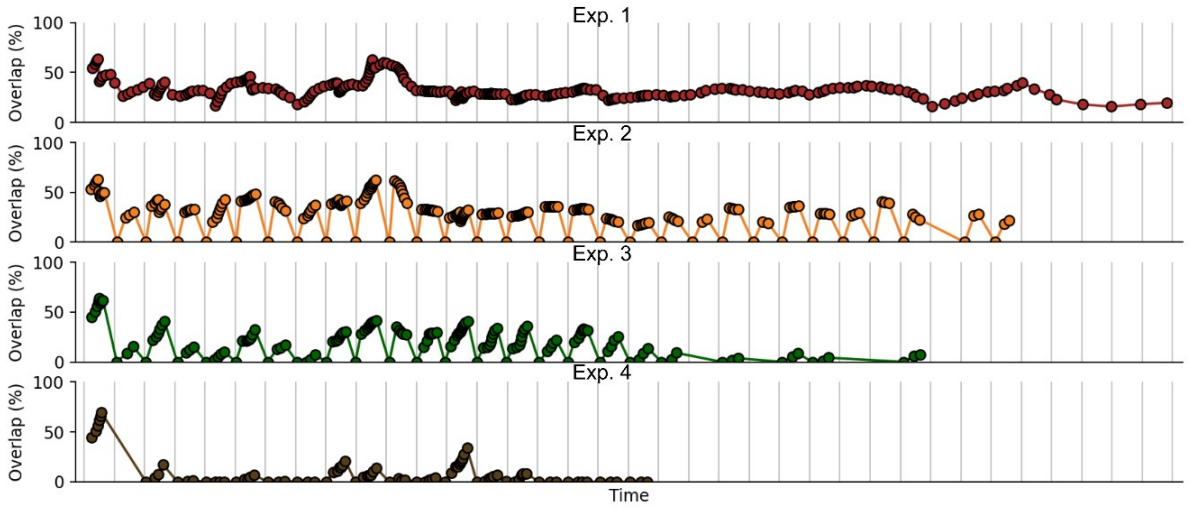

Figure S5.12 Degree of overlapping between successive sample spots (based on the method of Fig. S5.11C) for Shell A and sample spots with 300 µm diameter. The subplots show the results for the four different sampling strategies of Exp. 1 to 4.

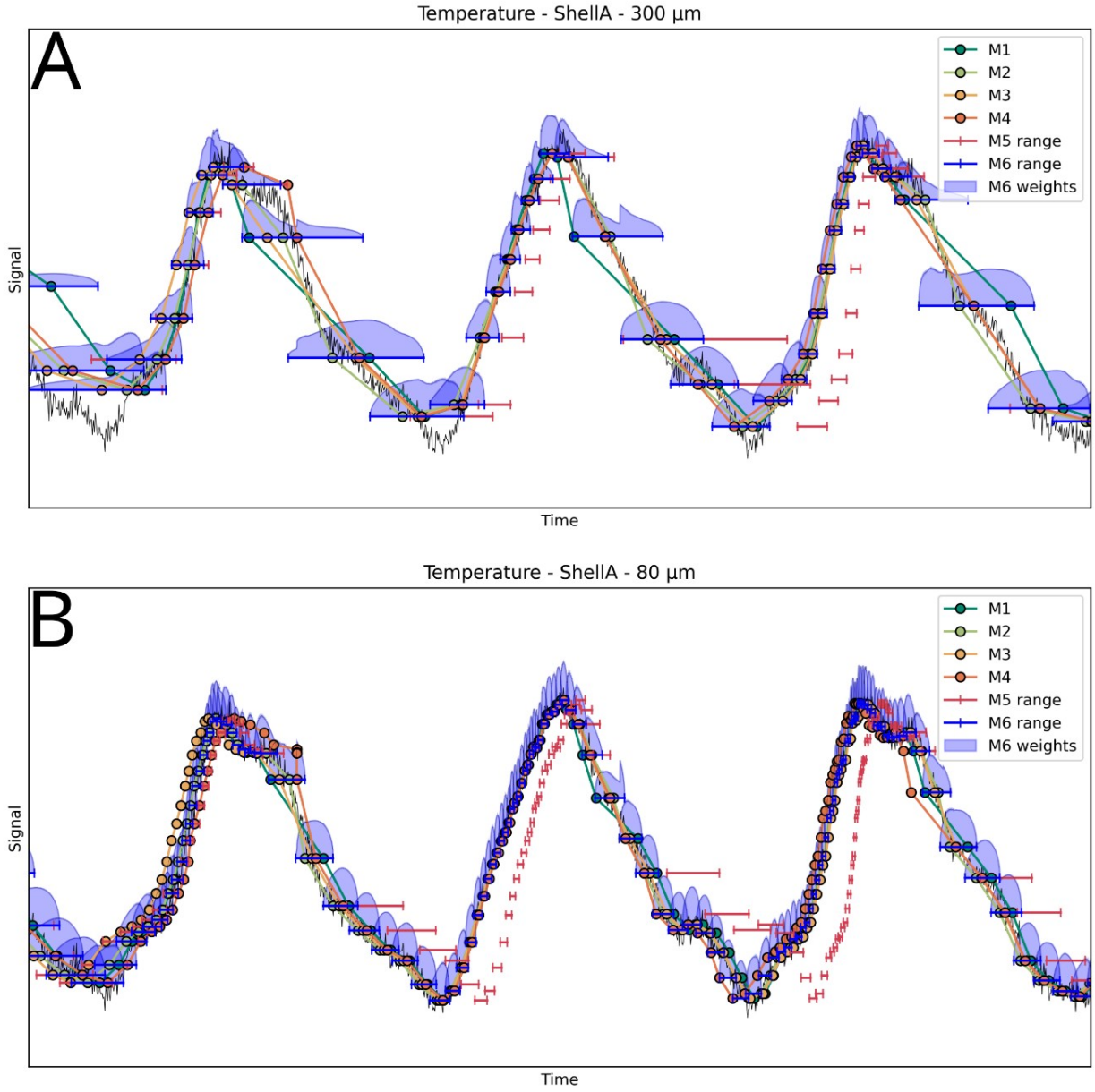

Figure S5.13 Temporally aligned temperature signal using 300 µm (**A**) and 80 µm (**B**) spot sizes, digitally sampled from Shell A using the sampling strategy of Experiment 1 (see Fig. S5.5). Note that alignment method M1 to M4 temporally contextualize the spot center positions, while M5 and M6 approximate temporal ranges covered by sample spots. Furthermore, M6 approximates temporally constrained weight distributions (blue area) according to the increment morphology, the growth model and the sample geometry.

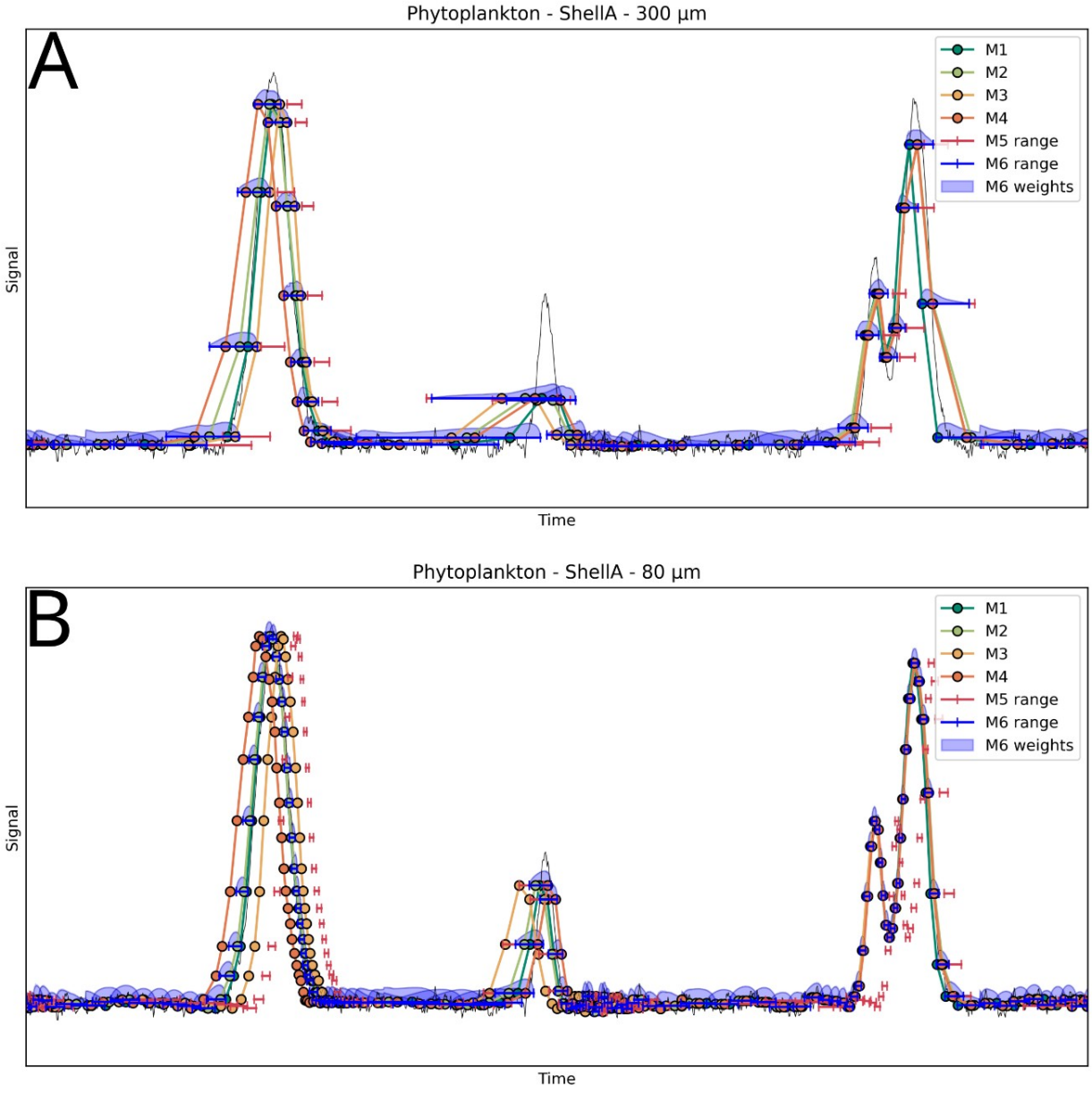

Figure S5.14 Temporally aligned phytoplankton abundance signal using 300 µm (**A**) and 80 µm (**B**) spot sizes, digitally sampled from Shell A using the sampling strategy of Experiment 1 (see Fig. S5.5). Note that alignment method M1 to M4 temporally contextualize the spot center positions, while M5 and M6 approximate temporal ranges covered by sample spots. Furthermore, M6 approximates temporally constrained weight distributions (blue area) according to the increment morphology, the growth model and the sample geometry.

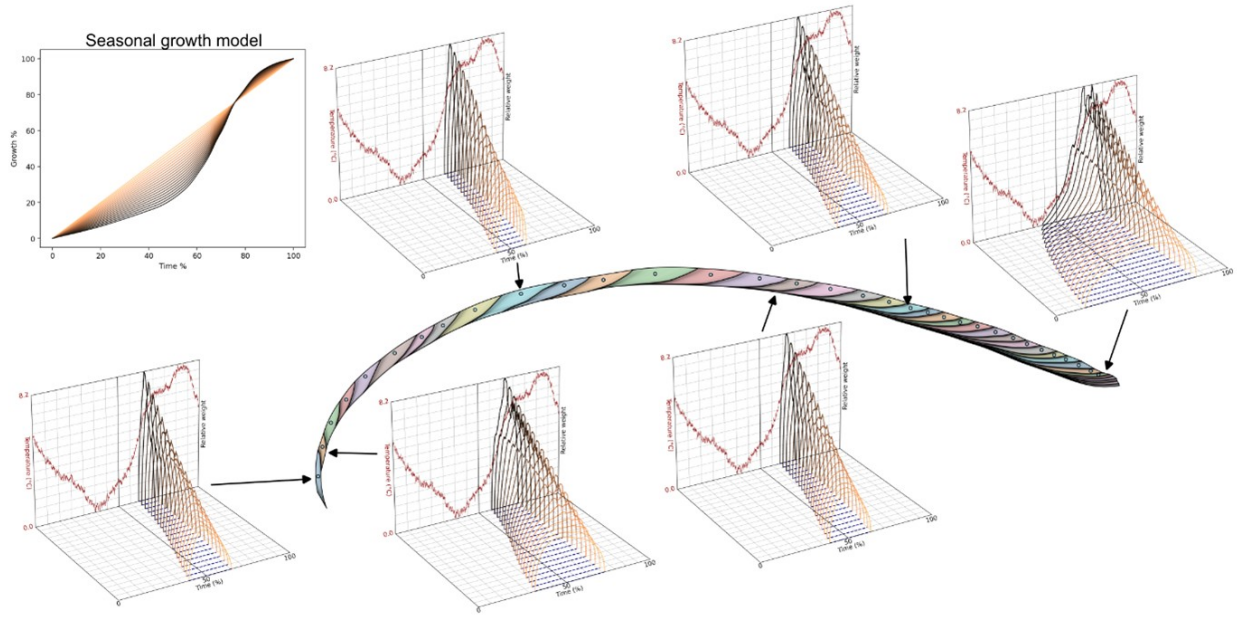

Figure S5.15 Variability of time-dependent weight distributions for sample spots (300 µm) taken from the center of different annual growth increments. Additionally, the effect of the seasonal growth model complexity onto the weight distributions is shown, color-coded from a simple constant growth (orange) to a more complex (black) growth pattern.

References

Brosset, C., Höche, N., Shirai, K., Nishida, K., Mertz-Kraus, R., Schöne, B. R., 2022. Strong coupling between biomineral morphology and Sr/Ca of *Arctica islandica* (Bivalvia) – Implications for shell Sr/Ca-based temperature estimates. Minerals 12, 500.

Butler, P. G., Wanamaker, A. D., Scourse, J. D., Richardson, C. A., Reynolds, D. J., 2013. Variability of marine climate on the North Icelandic Shelf in a 1357-year proxy archive based on growth increments in the bivalve *Arctica islandica*. Paleogeography, Palaeoclimatology, Palaeoecology 373, 141–151.

Doré, J., Chaillou, G., Poitevin, P., Lazure, P., Poirier, A., Chauvaud, L., Archambault, P., Thébault, J., 2020. Assessment of Ba/Ca in *Arctica islandica* shells as a proxy for phytoplankton dynamics in the Northwestern Atlantic Ocean. Estuarine, Coastal and Shelf Science 237, 106628.

Fröhlich, L., Siebert, V., Huang, Q., Thébault, J., Jochum, K. P., Schöne, B. R., 2022. Deciphering the potential of Ba/Ca, Mo/Ca and Li/Ca profiles in the bivalve shell *Pecten maximus* as proxies for the reconstruction of phytoplankton dynamics. Ecological Indicators 141, 109121.

Fröhlich, L., Siebert, V., Huang, Q., Thébault, J., Moriceau, B., Jochum, K. P., Schöne, B. R., 2023. Uptake of barium, molybdenum, and lithium and incorporation into scallop shells: Refining proxies for primary production dynamics. Limnology and Oceanography 68, 2544–2561.

Gillikin, D. P., Lorrain, A., Paulet, Y. M., André, L., Dehairs, F., 2008. Synchronous barium peaks in high-resolution profiles of calcite and aragonite marine bivalve shells. Geo-Marine Letters 28, 351–358.

Goodwin, D. H., Flessa, K. W., Schöne, B. R., Dettman, D. L., 2001. Cross-calibration of daily growth increments, stable isotope variation, and temperature in the Gulf of California bivalve mollusk *Chione cortezi*: Implications for paleoenvironmental analysis. PALAIOS 16, 387–398.

Goodwin, D. H., Schöne, B. R., Dettman, D. L., 2003. esolution and fidelity of oxygen isotopes as paleotemperature proxies in bivalve mollusk shells: Models and observations. PALAIOS 18, 110–125.

Hanna, E., Jónsson, T., Ólafsson, J., Valdimarsson, H., 2006. Icelandic coastal sea surface temperature records constructed: Putting the pulse on air–sea–climate interactions in the northern North Atlantic. Part I: Comparison with HadISST1 open-ocean surface temperatures and preliminary analysis of long-term patterns and anomalies of SSTs around Iceland. Journal of Climate 19, 5652–5666.

Höche, N., Walliser, E. O., Schöne, B. R., 2022. Microstructural mapping of *Arctica islandica* shells reveals environmental and physiological controls on biomineral size. Frontiers in Earth Science 9, 781305.

Höche, N., Zettler, M. L., Huang, X., Schöne, B. R., 2023. Shell microstructures (disturbance lines) of *Arctica islandica* (Bivalvia): A potential proxy for severe oxygen depletion. Frontiers in Marine Science 10, 1219716.

Jolivet, A., Asplin, L., Strand, Ø., Thébault, J., Chauvaud, L., 2015. Coastal upwelling in Norway recorded in great scallop shells. Limnology and Oceanography 60, 1265–1275.

Jones, D. S., Quitmyer, I. R., 1996. Marking time with bivalve shells: Oxygen isotopes and season of annual increment formation. PALAIOS 11, 340–346.

Jones, D. S., 1980. Annual cycle of shell growth increment formation in two continental shelf bivalves and its paleoecologic significance. Paleobiology 3, 331–340.

Marali, S., Schöne, B. R., Mertz-Kraus, R., Griffin, S. M., Wanamaker, A. D., Matras, U., Butler, P. G., 2017. Ba/Ca ratios in shells of *Arctica islandica* – Potential environmental proxy and crossdating tool. Palaeogeography, Palaeoclimatology, Palaeoecology 465, 347–361.

Marali, S., Schöne, B. R., 2015. Oceanographic control on shell growth of *Arctica islandica* (Bivalvia) in surface waters of Northeast Iceland – Implications for paleoclimate reconstructions. Palaeogeography, Palaeoclimatology, Palaeoecology 420, 138–149.

Marchitto, T. M., Jones, G. A., Goodfriend, G. A., Weidman, C. R., 2000. Precise temporal correlation of Holocene mollusk shells using sclerochronology. Quaternary Research 53, 236–246.

Peharda, M., Schöne, B. R., Black, B. A., Corrège, T., 2021. Advances of sclerochronology research in the last decade. Palaeogeography, Palaeoclimatology, Palaeoecology 570, 110371.

Poitevin, P., Roy, V., Galbraith, P. S., Chaillou, G., 2022. Insights into coastal phytoplankton variations from 1979 to 2018 derived from Ba/Ca records in scallop shells (*Chlamys islandica*) from a fishing ground in the northern Gulf of St. Lawrence. Marine Environmental Research 181, 105734.

Reynolds, D. J., von Biela, V. R., Dunton, K. H., Douglas, D. C., Black, B. A., 2022. Sclerochronological records of environmental variability and bivalve growth in the Pacific Arctic. Progress in Oceanography 206, 102864.

Schöne, B. R., Huang, Q., 2021. Ontogenetic δ^{15}N trends and multidecadal variability in shells of the bivalve mollusk, *Arctica islandica*. Frontiers in Marine Science 8, 748593.

Schöne, B. R., Huang, X., Jantschke, A., Mertz-Kraus, R., Zettler, M. L., Liu, D., Yu, K., 2022a. High-resolution reconstruction of dissolved oxygen levels in the baltic sea with bivalves – a multi-epecies comparison (*Arctica islandica*, *Astarte borealis*, *Astarte elliptica*). Frontiers in Marine Science 9, 820731.

Schöne, B. R., Marali, S., Mertz-Kraus, R., Butler, P. G., Wanamaker, A. D., Fröhlich, L., 2022b. Importance of weighting high-resolution proxy data from bivalve shells to avoid bias caused by sample spot geometry and variability in seasonal growth rate. Frontiers in Earth Science 10, 889115.

Schöne, B. R., 2013. *Arctica islandica* (Bivalvia): A unique paleoenvironmental archive of the northern North Atlantic Ocean. Global and Planetary Change 111, 199–225.

Schöne, B. R., Dunca, E., Fiebig, J., Pfeiffer, M., 2005. Mutvei's solution: An ideal agent for resolving microgrowth structures of biogenic carbonates. Palaeogeography, Palaeoclimatology, Palaeoecology 228, 149–166.

Schöne, B. R., Marali, S., Jantschke, A., Mertz-Kraus, R., Butler, P. G., Fröhlich, L., 2023. Can element chemical impurities in aragonitic shells of marine bivalves serve as proxies for environmental variability? Chemical Geology 616, 121215.

Shirai, K., Schöne, B. R., Miyaji, T., Radarmacher, P., Krause, R. A., Tanabe, K., 2014. Assessment of the mechanism of elemental incorporation into bivalve shells (*Arctica islandica*) based on elemental distribution at the microstructural scale. Geochimica et Cosmochimica Acta 126, 307–320.

Smith, T., Zotta, R. M., Boulton, C. A., Lenton, T. M., Dorigo, W., Boers, N., 2023. Reliability of resilience estimation based on multi-instrument time series. Earth System Dynamics 14, 173–183.

Thébault, J., Jolivet, A., Waeles, M., Tabouret, H., Sabarot, S., Pécheyran, C., Leynaert, A., Jochum, K. P., Schöne, B. R., Fröhlich, L., Siebert, V., Amice, E., Chauvaud, L., 2022. Scallop shells as geochemical archives of phytoplankton-related ecological processes in a temperate coastal ecosystem. Limnology and Oceanography 67, 187–202.

Thébault, J., Schöne, B. R., Hallmann, N., Barth, M., Nunn, E. V., 2009. Investigation of Li/Ca variations in aragonitic shells of the ocean quahog *Arctica islandica*, northeast Iceland. Geochemistry, Geophysics, Geosystems 10, Q12008.

Trofimova, T., Andersson, C., Bonitz, F. G. W., Pedersen, L. E. R., Schöne, B. R., 2021. Reconstructing early Holocene seasonal bottom-water temperatures in the northern North Sea using stable oxygen isotope records of *Arctica islandica* shells. Paleogeography, Palaeoclimatology, Palaeoecology 567, 110242.

Tzadik, O. E., Curtis, J. S., Granneman, J. E., Kurth, B. N., Pusack, T. J., Wallace, A. A., Hollander, D. J., Peebles, E. B., Stallings, C. D., 2017. Chemical archives in fishes beyond otoliths: A review on the use of other body parts as chronological recorders of microchemical constituents for expanding interpretations of environmental, ecological, and life-history changes. Limnology and Oceanography: Methods 15, 238–263.

Ubukata, T., 2001. Stacking increments: A new model and morphospace for the analysis of bivalve shell growth. Historical Biology 15, 303–321.

Vihtakari, M., Renaud, P. E., Clarke, L. J., Whitehouse, M. J., Hop, H., Carroll, M. L., Ambrose, W. G., 2016. Decoding the oxygen isotope signal for seasonal growth patterns in Arctic bivalves. Palaeogeography, Palaeoclimatology, Palaeoecology 446, 263–283.

Wanamaker, A. D., Heinemeier, J., Scourse, J. D., Richardson, C. A., Butler, P. G., Eiríksson, J., Knudsen, K. L., 2008. Very long-lived mollusk confirm 17th century AD tephra-based radiocarbon reservoir ages for north Icelandic shelf waters. Radiocarbon 50, 399–412.

Weidman, C. R., Jones, G. A., Kyger, 1994. The long-lived mollusc *Arctica islandica*: A new paleoceanographic tool for the reconstruction of bottom temperatures for the continental shelves of the northern North Atlantic Ocean. Journal of Geophysical Research 99, 18305–18314.

Zhai, L., Gudmundsson, K., Miller, P., Peng, W., Gufinnsson, H., Debes, H., Hátún, H., White, G. N., Walls, R. H., Sathyendranath, S., Platt, T., 2012. Phytoplankton phenology and production around Iceland and Faroes. Continental Shelf Research 37, 15–25.

6 Summary and perspectives

The findings presented throughout this thesis provided new insights into how the geochemical impurities of Ba, Mo and Li in shells of *Pecten maximus* reflect phytoplankton dynamics and environmental variability of the surrounding water. By combining daily resolved trace element profiles from shell collected over multiple years with detailed environmental monitoring data, this work further refined the understanding and applicability of Ba/Ca_{shell}, Mo/Ca_{shell} and Li/Ca_{shell} as potential paleoenvironmental proxies for phytoplankton bloom events. The statistical framework developed and applied herein enables the comparison of shell geochemical chronologies with variations of phytoplankton abundance from multiple species, allowing to identify the phytoplankton taxa that potentially influenced the shell chemistry. The methodologies and findings presented herein advance the use of bivalve shells as high-resolution multi-proxy archives, particularly for reconstructing ecologically important yet complex variables such as phytoplankton dynamics.

The first manuscript, (**Chapter 2**) demonstrated that the peaks in the Ba/Ca_{shell} time-series measured in scallop shells are primarily linked to blooms of specific phytoplankton taxa, particularly diatoms, rather than bulk primary production (i.e., chlorophyll *a* concentrations) or the total cell abundance of diatoms or dinoflagellates. When considering a short time lag of several days, patterns in the Ba/Ca_{shell} profiles reflect the abundance of certain phytoplankton species, aligning with the idea of a selective feeding behavior of *P. maximus*. Further, a high running similarity between Ba/Ca_{shell} profiles and phytoplankton dynamics after applying species-specific weighting factors indicated that the cellular Ba content varies among different phytoplankton taxa. These results emphasized that the direct association of Ba/Ca_{shell} profiles with general indicators of total primary productivity can be misleading. Thus, the study substantiated the urgent need for thorough calibrations with detailed understanding about the phenology of the primary producers surrounding the bivalves to disentangle the processes driving the formation of Ba/Ca_{shell} peaks. Additionally, the statistical approach introduced in this chapter provides a valuable tool to assess the relationship between the geochemical proxies like Ba/Ca_{shell} peaks and multi-dimensional phytoplankton community data.

The second manuscript (**Chapter 3**) extended the geochemical analyses by including Mo/Ca_{shell} and Li/Ca_{shell} data in addition to Ba/Ca_{shell} profiles. By employing a pseudo-random sampling approach that evaluated potential species-specific contributions of phytoplankton taxa to obtained geochemical profiles as well as potential time lags, this study supports the notion that trace element peaks in Ba/Ca_{shell}, Mo/Ca_{shell} and Li/Ca_{shell} profiles

have a dietary origin. Aligning with Chapter 2, a time lag of ca. one to two weeks between phytoplankton blooms and the timing of shell peak formation was identified. Ba/Ca_{shell} peaks were associated with the abundance of ingestible diatom and dinoflagellate taxa. Mo/Ca_{shell} peaks agreed with the timing and magnitude of blooms of the dinoflagellate *Gymnodinium* spp. and possibly diatom aggregation events. Li/Ca_{shell} peaks were related to large diatom blooms of *Chaetoceros* spp. or neurotoxin-containing blooms of *Pseudo-nitzschia*. While corroborating previously proposed hypotheses on the formation of trace element peaks, the distinct underlying mechanisms between the three trace elements, involving different phytoplankton taxa, highlight the potential of Ba/Ca_{shell}, Mo/Ca_{shell} and Li/Ca_{shell} as complementary indicators. Thus, different aspects of the phytoplankton community structure are potentially captured by the trace element variations, promoting shells of *P. maximus* as valuable multi-proxy archives.

The third manuscript (**Chapter 4**) further explored the uptake of Ba, Mo and Li from the environment by the scallops and their subsequent incorporation into the shell carbonate. Through an in-situ controlled experiment comparing the shell chemistry of caged specimens, suspended above the (sediment-water interface) SWI, with naturally living scallop shells from the seafloor, this work disentangled the influences from processes inside the water column with those potentially occurring at SWI. The synchronous occurrence of Ba/Ca_{shell} and Mo/Ca_{shell} enrichments in all specimens, together with concurrent particulate Ba and Mo variations, indicated that both elements were bound to particulate organic matter, transported within the water column, and incorporated in scallop shells via trophic uptake. These findings aligned well with the proposed uptake mechanisms deduced from the preceding chapters, with Ba/Ca_{shell} peaks being largely affected by the abundance of specific Ba-enriched diatoms and Mo/Ca_{shell} peaks influenced by blooms of the dinoflagellate *Gymnodinium* spp., associated with high levels of Mo-containing enzymes. Furthermore, differences in trace-element peak magnitudes between cage-grown and benthic-living scallop shells could be attributed to physiological factors such as growth and filtration rates that can modulate shell geochemistry, an effect that needs to be considered when interpreting such proxy signals in future studies.

The final study (**Chapter 5**) addressed sclerochronological techniques required for the reliable reconstruction of short-term environmental variabilities, like phytoplankton blooms, from geochemical proxy archives. This was achieved by evaluating how different sampling and alignment strategies affect the accuracy of environmental reconstructions from mollusk

shells. Using digital models, exemplarily based on shells of *Arctica islandica*, that numerically simulated the incremental shell growth of the bivalves, this study demonstrated that both sampling strategy and temporal alignment method significantly influence the accuracy of shell-based environmental reconstructions from geochemical proxies. Furthermore, an improved alignment method was introduced that accounts for temporally overlapping sample spots and growth increment morphologies, offering a robust temporal contextualization of geochemical data compared to conventional techniques. The methodological framework presented in this study facilitates the application of high-resolution geochemical proxy information extracted from slow-growing bivalve shells, thereby strengthening their reconstruction capabilities of highly dynamic environmental variables such as phytoplankton dynamics.

In conclusion, this work demonstrated that variations in the profiles of Ba/Ca_{shell}, Mo/Ca_{shell} and Li/Ca_{shell} archived in shells of *P. maximus* from the Bay of Brest were strongly linked to phytoplankton dynamics of the water column. The underlying mechanisms responsible for the formation of short-term trace element enrichments in these shells could be attributed to distinct phytoplankton-associated processes, of which each proxy captured complementary aspects of the primary producer dynamics. Accordingly, *P. maximus* shells emerge as powerful geochemical multi-proxy archives for the reconstruction of past phytoplankton dynamics, providing information highly relevant to marine science, paleoecology, paleoclimatology as well as fisheries research. At the same time, this work also demonstrated some of the challenges involved in calibration and the potential application of these proxies. As shown here, the complex interplay between phytoplankton phenology, community compositions and species interactions in combination with the physiological characteristics of the bivalves (e.g., filtration rate, element uptake and temporally delayed incorporation into the shell material), makes it difficult to establish direct correlations between shell chemistry and phytoplankton dynamics. Especially, when trace element enrichments are associated with the occurrence of multiple phytoplankton species, as observed for Ba/Ca_{shell} peaks, detailed monitoring data and robust statistical evaluation become necessary to deduce potential patterns that account for species-specific trace element loads across different phytoplankton taxa. The application of such proxies would likewise rely on the statistical evaluation of the timing and magnitude of Ba/Ca_{shell} peaks and how they change through time. For instance, frequency analyses of peak occurrence could indicate shifts in the diatom composition towards species that contain either more or less cell-related Ba. Such interpretations can be further complemented when combined with Mo/Ca_{shell} and Li/Ca_{shell} profiles. Mo/Ca_{shell} can

indicate for the presence of nitrate-assimilating dinoflagellates or provide indirect information on the nutrient status of the water, as nutrient-limited conditions trigger phytoplankton aggregation episodes which can be recorded in Mo/Ca_{shell} profiles. Mass sedimentations of diatom cells following large blooms could be indicated by Li/Ca_{shell} peaks which, however, require further detailed calibrations.

The outcomes of this work direct future research in multiple ways. Key phytoplankton taxa identified in Chapters 2 to 4 (e.g., *Chaetoceros*, *Gymnodinium*, *Pseudo-nitzschia*) can be integrated in controlled feeding experiments to validate the proposed mechanisms that cause enhanced trace element uptake by *P. maximus*. Eventually, such phytoplankton can be grown under various environmental conditions, such as variable dissolved trace element concentrations, pH or iron availability, that reportedly affect element accumulations on phytoplankton cells (Sternberg et al., 2005). Likewise, culturing phytoplankton exposed to different nitrogen sources, i.e., ammonium vs nitrate, can facilitate the understanding of Mo cycling in the water and the formation of Mo/Ca_{shell} peaks in more detail. Rolling tank experiments offer a great opportunity to produce phytoplankton aggregates of varying sizes and under controlled conditions. Testing which aggregate size range are effectively filtered by scallops, in combination with measurements of their chemical properties, would provide valuable insights into the role of aggregation events onto the observed Mo/Ca_{shell} profiles. In general, more data on cellular trace element concentrations among phytoplankton species and their spatial variability across different ecological settings will be extremely beneficial for future studies and are crucial for the quantitative application of respective geochemical proxies. Since the Li/Ca_{shell} profiles measured in the scallop shells from the studied years exhibited only a single distinct peak, hypotheses regarding peak formation could be proposed, yet they could hardly be tested and confirmed. Therefore, more work is certainly needed regarding the peak formation in Li/Ca_{shell} profiles and their relationship with primary producers.

Apart from calibration research, an important step will be to extend the testing and application of these geochemical proxies to (sub)fossil shell material. Evidently, a key requirement of a valuable geochemical archive for paleoenvironmental reconstructions is the availability of well-preserved (sub)fossil material from different time periods. Although information about the historical distribution and abundance of *P. maximus* shells is limited, several studies have reported the occurrence of shell remains from various archeological sites. Interestingly, single valves of *P. maximus* were excavated at Neanderthal-associated caves in southeast

Spain, dating back to ca. 50000 years BP (Zilhão et al., 2010). These remains suggest that the great scallop not only served as a dietary source but also fulfilled a cultural, symbolic purpose (Álvarez-Fernández, 2015). Other records of *P. maximus* remains were reported from shell middens, settlements and grave sites across the European coast of Spain, France, Scotland to Scandinavia, dating throughout the Holocene (e.g., Johansson, 2005; Bertin, 2015; Dupont and Marchand, 2021; Dupont et al., 2023). The cultural significance of scallop shells, particularly as a pilgrimage symbol since the 11th century, also contributed to an increased presence in the archeological record (Johansson, 2005; Pérez-Ramallo et al., 2023). Although many of these remains have been transported and lack geographic provenance, well-dated and site-specific *P. maximus* shells could offer a unique opportunity to reconstruct past phytoplankton dynamics at high-resolution and explore human influences on marine ecosystems. Applying Ba/Ca_{shell}, Mo/Ca_{shell}, and Li/Ca_{shell} analyses to archaeological shells could reveal long-term trends in bloom intensity, their seasonal timing and nutrient status of the ecosystem, ultimately tracing how phytoplankton community composition has shifted through natural and anthropogenic changes over time.

The findings from this work, specifically the underlying mechanism governing the geochemical variability in *P. maximus* shells, are likely transferable to phylogenetically close bivalve species across a broad range of environmental settings. For example, conducting similar studies on *Pecten jacobaeus* shells from the Mediterranean Sea would further strengthen the understanding of the proposed trace element uptake mechanisms identified for *P. maximus* shells. Extending the application of Ba/Ca_{shell}, Mo/Ca_{shell} and Li/Ca_{shell} to other bivalve species likewise represents an important direction for future studies. For instance, the extremely long-lived bivalve *A. islandica* frequently exhibits distinct Ba/Ca_{shell} peaks (e.g., Marali et al., 2017; Doré et al., 2020), offering the great potential to study multi-decadal variations of Ba-enriched primary producers, based only on a few shells. However, the slow shell growth and the lower temporal resolution of geochemical samples demand careful consideration about sampling strategies and temporal alignment methods prior to the interpretation of peak timing and magnitudes, particularly when sub-annual changes such as specific phytoplankton bloom dynamics are of interest.

References

Álvarez-Fernández, E., 2015. Marine resource exploitation during the Middle and early Upper Paleolithic in Europe: Overview of the available evidence. Palethnologie. Archéologie et sciences humaines 7, 188–205.

Bertin, L., 2015. Exploitation of mother of pearl in the Middle Ages, Clos d'Ugnac archaeological site (Pennautier, Aude, France): Malacological study, consumption, exploitation and utilization of the nacre. Quaternary International 375, 145–152.

Doré, J., Chaillou, G., Poitevin, P., Lazure, P., Poirier, A., Chauvaud, L., Archambault, P., Thébault, J., 2020. Assessment of Ba/Ca in *Arctica islandica* shells as a proxy for phytoplankton dynamics in the Northwestern Atlantic Ocean. Estuarine, Coastal and Shelf Science 237, 106628.

Dupont, C., Baudry, A., Daire, M. Y., Barillé, L., 2023. A technical adaptation? Shell dye extraction on the eve of the roman conquest in Gaul (Port-Blanc, Hoedic island, France). PALEO. Revue d'archéologie préhistorique Hors-série, 144–161.

Dupont, C., Marchand, G., 2021. New paradigms in the exploitation of Mesolithic shell middens in Atlantic France: The example of Beg-er-Vil, Brittany. Quaternary International 584, 59–71.

Johansson, B. M., 2005. Mollusc shells in swedish archaeology – occurrence, significance and potentials. Lund Archaeological Review 8, 89–130.

Marali, S., Schöne, B. R., Mertz-Kraus, R., Griffin, S. M., Wanamaker, A. D., Matras, U., Butler, P. G., 2017. Ba/Ca ratios in shells of *Arctica islandica* – Potential environmental proxy and crossdating tool. Palaeogeography, Palaeoclimatology, Palaeoecology 465, 347–361.

Pérez-Ramallo, P., Lorenzo-Lizalde, J. I., Staniewska, A., Aiestaran, M., Aguirre, J., Sesma, J. S., Marzo, S., Lucas, M., Ilgner, J., Chivall, D., Higham, T., Rodríguez-Varela, R., Götherström, A., Etxeberria, F., Grandal-d'Anglade, A., Alexander, M., Roberts, P., 2023. To the field of stars: Stable isotope analysis of medieval pilgrims and populations along

the Camino de Santiago in Navarre and Aragon, Spain. Journal of Archaeological Science: Reports 48, 103847.

Sternberg, E., Tang, D., Ho, T. Y., Jeandel, C., Morel, F. M. M., 2005. Barium uptake and adsorption in diatoms. Geochimica et Cosmochimica Acta 69, 2745–2752.

Zilhão, J., Angelucci, D. E., Badal-García, E., d'Errico, F., Daniel, F., Dayet, L., Douka, K., Higham, T. F. G., Martínez-Sánchez, M. J., Montes-Bernárdez, R., Murcia-Mascarós, S., Pérez-Sirvent, C., Roldán-García, C., Vanhaeren, M., Villaverde, V., Wood, R., Zapata, J., 2010. Symbolic use of marine shells and mineral pigments by Iberian Neandertals. Proceedings of the National Academy of Sciences 107, 1023–1028.